Durham University

Durham E-Theses

Simulating feedback on galaxy formation by jets from spinning black holes

FILIP HUSKO

How to cite:

HUSKO, FILIP (2024) Simulating feedback on galaxy formation by jets from spinning black holes. Doctoral thesis, Durham University.

Use policy

The full-text may be used and/or reproduced, and given to third parties in any format or medium, without prior permission or charge, for personal research or study, educational, or not-for-profit purposes provided that:

- a full bibliographic reference is made to the original source
- a https://etheses.durham.ac.uk/id/eprint/15844/ is made to the metadata record in Durham E-Theses
- the full-text is not changed in any way

The full-text must not be sold in any format or medium without the formal permission of the copyright holders.

Please consult the full Durham E-Theses policy for further details.

Academic Support Office, The Palatine Centre, Durham University, Stockton Road, Durham, DH1 3LE
e-mail: e-theses.admin@durham.ac.uk Tel: +44 0191 334 6107
https://etheses.durham.ac.uk

Simulating feedback on galaxy formation by jets from spinning black holes

Filip Huško

A Thesis presented for the degree of
Doctor of Philosophy

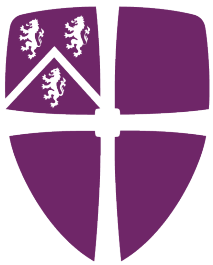

Physics Department
Durham University
United Kingdom
January 2025

Abstract

In the last few decades, it has become apparent that energy release from supermassive black holes (BHs), in the form of active galactic nuclei (AGN) feedback, is an important physical process that affects galaxy formation and evolution. Modern theoretical models of galaxy formation and evolution almost always include AGN feedback, since it appears to be necessary in order to reproduce massive elliptical galaxies with little star formation. The EAGLE cosmological hydrodynamical simulations of galaxy formation used thermal isotropic feedback from BHs that was intended to represent the effects of radiatively driven quasar winds. In this thesis I present an expanded AGN feedback model that includes three different accretion and feedback regimes, with each BH being in a different regime depending on its accretion rate. I add a kinetic jet feedback mode that is present at all accretion rates, but is strongest at low and very high accretion rates. In each regime I also include the effects of accretion disc winds, implemented as thermal isotropic feedback, but with different efficiencies, representing different launching mechanisms. BH spin is modeled in a self-consistent manner, including different physics in each accretion regime, as well as BH spindown by jets. It is used to determine the feedback efficiencies and the jet directions, based on the most recent results from general-relativistic magneto-hydrodynamical (GRMHD) simulations. This BH spin evolution and AGN feedback model has been implemented into the SWIFT numerical code.

The majority of the results in this thesis concern tests of the above model, in the form of hydrodynamical simulations ran using SWIFT. These tests were intentionally done on idealized set-ups of galaxy groups and clusters, to allow controlled studies of the effects of changes to the AGN feedback scheme. I began by performing simple tests of single constant power jet episodes, launched into constant density ambient media, with the aim of validating the numerical code, especially motivated by the fact that these were the first such simulations of jets done using smoothed particle hydrodynamics (SPH). I found that the simulated properties of the jets and the lobes they inflate closely match analytical predictions, and their basic properties are well converged to resolution as poor as a few hundred particles per lobe. I then

performed similar tests in a more realistic ambient medium, with a density profile and held in hydrostatic equilibrium by gravity. I focused on the late-time evolution and the interaction between jet-inflated bubbles and the intracluster medium (ICM). These interactions were complex, with multiple physical processes at play. The main finding was that most of the initially injected energy ended up in heating and expanding the ICM, therefore increasing its (negative) gravitational potential energy.

In the second half of the thesis, I present results of tests done in a similar set-up, but with self-consistent BH accretion and feedback, coupled with the EAGLE galaxy formation and evolution model. These tests assumed Bondi accretion onto the BH, and used the aforementioned BH spin evolution model to track the BH spin. The BH spin was then used for jet feedback, for both its direction and efficiency. The tests spanned a range of halo masses, from galaxy group to galaxy cluster scales, as well as a wide range of central ICM temperatures (representing the spectrum of cool-core to non-cool-core clusters). In all cases, jet feedback was successful at quenching star formation in the central galaxies, or at least significantly reducing it relative to the case of no AGN feedback. Similar tests were performed with the fiducial thermal isotropic feedback model, as well as a hybrid model, where kinetic jets are used at low accretion rates, and thermal isotropic feedback at high accretion rates. Kinetic jets were found to be generally more efficient at quenching than thermal isotropic feedback, but the hybrid model was the most promising.

The suite of tests presented in this thesis provided a necessary validation to the model. The model is planned to be used in the next generation of large, cosmological hydrodynamical simulations that will succeed the EAGLE simulations. The results presented here will also be helpful for the easier interpretation of AGN feedback effects in such cosmological simulations.

Declaration

The work in this thesis is based on research carried out at the Physics Department, Durham University, United Kingdom. No part of this thesis has been submitted elsewhere for any other degree or qualification. Chapters 3, 4, 5 and 6 have been published in similar form as the following papers:

Chapter 3: Huško, F. & Lacey, C. G. (2023), MNRAS, 520, 5090,

Chapter 4: Huško, F. & Lacey, C. G. (2023), MNRAS, 521, 4375,

Chapter 5: Huško, F.; Lacey, C. G.; Schaye, J ; Schaller, M.; Nobels, F. S. J. (2022), MNRAS, 516, 3750,

Chapter 6: Huško, F.; Lacey, C. G.; Schaye, J ; Nobels, F. S. J. (2022), Schaller, M. (2024), MNRAS, 527, 5988.

Copyright © 2025 by Filip Huško.

"The copyright of this thesis rests with the author. No quotations from it should be published without the author's prior written consent and information derived from it should be acknowledged".

Acknowledgements

I would like to thank Vernesa Smolčić and Vibor Jelić for their support and encouragement during my first years in academia. I would also like to thank Joop Schaye and Matthieu Schaller, who began working with me during my PhD, and offered their time and guidance despite their being no obligation to do so, and us being at different institutes. Thanks Joop for all the prompt and detailed suggestions! Thanks Matthieu for all the help with coding and SWIFT, especially in the beginning! Thanks to Bert Vandenbroucke for the same.

Most of all, I would like to thank Cedric G. Lacey. Thank you for providing the opportunity to do an internship with you at Durham, and for being available in the subsequent year, for discussions and work on our papers, even though there was no formal reason to do so. This was a critical time−my scientifically formative years, so it was very useful to be able to work together during this period. Thanks to Carlton M. Baugh for the same reasons! Thank you, Cedric, for inviting me to do a PhD with you as my supervisor, meeting with me regularly, and being available and prompt whenever I needed advice, or if something needed to be done. These may seem like minor things, but I do not take it for granted, having heard of so many cases where supervisors neglect their students. Most of all, thanks for all the guidance during the PhD itself! You have instilled in me a sense of and value for scientific rigor, objectivity, and thoroughness, that I wish was more wide-spread in science. I will consider this invaluable for the rest of my career!

Finally, I would like to thank my friends and family. My friends in Durham: Martina, Carolina, Hannah, Tom... It would not have been the same without you! My friends in Croatia: Niko, Nina, Davor, Bartol, Roman, Mislav, Silvio. Thanks for always being there, and staying my friends, despite the distances between us. To my parents: thanks for being encouraging, and not suppressing my weird career aspiration that I had from such a young age. To my family overall: thanks for all the support!

Contents

Abstract **ii**

Declaration **iv**

Acknowledgements **v**

List of Figures **xii**

List of Tables **xxxiv**

1 Introduction **1**

1.1 Galaxies in observations and theory 1

1.1.1 The earliest observations of other galaxies 1

1.1.2 Types and properties of galaxies 2

1.1.3 ΛCDM: the standard model of cosmology and structure formation 3

1.1.4 The formation and growth of galaxies in ΛCDM 4

1.1.5 Modern galaxy formation and evolution models 6

1.2 Observations and theory of active galactic nuclei 8

1.2.1 Discovery of quasars and radio galaxies 8

1.2.2 The impact of active galactic nuclei on their host galaxies in observations . . . 9
1.2.3 The theory of accretion . . . 12
1.2.4 The theory of active galactic nuclei jet launching . . . 15
1.3 Simulating galaxy formation and evolution with AGN jet feedback . . . 17
1.3.1 The need for AGN feedback in models . . . 17
1.3.2 AGN feedback and jets in cosmological hydrodynamical simulations of galaxy formation and evolution . . . 18
1.3.3 The potential benefits of including jets from AGN . . . 19
1.3.4 Idealized simulations of AGN jets . . . 20
1.4 Overview of the thesis . . . 23

2 A hybrid black hole accretion and feedback model 24
2.1 Summary of the model . . . 24
2.2 Black hole accretion rates . . . 26
2.3 The interchanging of accretion/feedback modes . . . 29
2.4 Feedback efficiencies . . . 31
2.5 Evolving the magnitude of black hole spin . . . 38
2.6 Choosing the sign of BH spin . . . 41
2.7 Evolving the direction of BH spin . . . 43
2.8 Final spin and mass loss to gravitational waves after BH mergers . . . 47
2.9 Additional time-step criteria . . . 48
2.10 Jet launching scheme . . . 50
Appendix 2.A: Innermost stable circular orbit (ISCO) . . . 51
Appendix 2.B: Variable accretion efficiencies . . . 51
Appendix 2.C: Slim disc wind efficiency formula . . . 52

3 Idealized hydrodynamical tests of active galactic nuclei jets using smoothed particle hydrodynamics 56
3.1 Introduction . . . 56
3.2 Jet and lobe evolution in the self-similar regime . . . 58
3.3 Numerical implementation . . . 60

3.3.1 Jet launching scheme 61
3.3.2 Physical setup 62
3.3.3 Simulations 64
3.3.4 Definition of jet lobe 67
3.3.5 Measuring the energetics and jet/lobe lengths and radii 70
3.4 Results: general properties of simulated jets 70
3.4.1 Ballistic jets 70
3.4.2 General properties of jets in the self-similar phase 72
3.4.3 Evolution of the jet-inflated lobe length and width 76
3.4.4 Jet, lobe and ambient medium energetics 78
3.4.5 Comparison with previous simulations 79
3.5 Results: comparison of jets with varying parameters 82
3.5.1 Varying the jet power 83
3.5.2 Varying the half-opening angle 85
3.5.3 Varying the launching velocity 85
3.5.4 Varying the mass resolution 88
3.5.5 Varying the mass resolution - implications for cosmological simulations 89
3.5.6 Power-law ambient medium density profiles 92
3.6 Summary and conclusions 96

4 Idealized simulations of the jet-intracluster medium interaction 98
4.1 Introduction 98
4.2 Simulations 100
4.2.1 Physical setup 100
4.2.2 Jet launching 101
4.2.3 Seeding of particle positions 101
4.2.4 Parameter choices and variations 102
4.3 General characteristics of jet-inflated bubbles 103
4.3.1 Jet launching and lobe inflation 103
4.3.2 Bubble inflation 105
4.3.3 Bubble and ICM energetics 106

4.3.4 Effects of jet-inflated bubbles on gas profiles 110
4.4 The uplift of ambient gas behind jet-inflated bubbles 112
4.4.1 General properties of gas at late times 114
4.4.2 The masses and volumes of the drift and wake 115
4.4.3 Direct comparison with a theoretical model 116
4.5 Jet-inflated bubbles with varying parameters 124
4.5.1 Varying the jet power 125
4.5.2 Varying both the jet power and launching velocity 128
4.5.3 Varying the jet launching velocity 128
4.5.4 Varying the jet half-opening angle 129
4.5.5 Impact of numerical resolution 129
4.5.6 Impact of hydrodynamical scheme 129
4.6 Conclusions 130

5 Spin-driven jet feedback in idealised simulations of galaxy groups and clusters 132

5.1 Introduction 132
5.2 Numerical implementation and physical set-up 133
5.2.1 Black hole feedback model 133
5.2.2 Numerical code and subgrid physics 135
5.2.3 Black hole accretion 136
5.2.4 The numerical algorithm for spin evolution 137
5.2.5 Jet launching 138
5.2.6 Dark matter, stars and gas 140
5.2.7 Simulations 142
5.3 Results: The quenching of galaxies across the mass scale 145
5.3.1 Galaxy group 145
5.3.2 Low-mass galaxy cluster 148
5.3.3 High-mass galaxy cluster 154
5.4 Jet feedback in more detail 159
5.4.1 Uplift of filaments 160
5.4.2 Structure of the cold gas 162

5.4.3 Driving of shocks and sound waves . . . 163
5.4.4 Impact of jet feedback on profiles of gas-related quantities . . 164
5.4.5 Impact of parameter variations on the cooling and feedback cycle of galaxies . . . 165
5.5 Summary and conclusions . . . 170
Appendix 5.A: Black hole spin alignment timescale . . . 173
Appendix 5.B: Additional parameter variations . . . 177
5.B.1 Direction of jet launching: opening angle and inclination . . . 177
5.B.2 Impact of ICM properties . . . 177
5.B.3 Impact of other variations . . . 181

6 Winds versus jets: a comparison of black hole feedback modes 183
6.1 Introduction . . . 183
6.2 Simulations, methods and set-up . . . 187
6.2.1 Implementation of AGN feedback . . . 188
6.2.2 Physical set-up . . . 191
6.2.3 Simulations . . . 192
6.2.4 Observational sample of entropy profiles . . . 194
6.3 Results I: feedback with black hole spin evolution . . . 197
6.3.1 Feedback powers . . . 200
6.3.2 Impact of feedback on galaxy growth . . . 204
6.3.3 Evolution of black hole properties . . . 207
6.3.4 Entropy profiles . . . 212
6.4 Results II: simplified feedback . . . 214
6.4.1 General results . . . 215
6.4.2 Varying the implementation of feedback . . . 220
6.5 Summary and conclusions . . . 229
Appendix 6.A: Effects of jet redirection and precession . . . 233
Appendix 6.B: Mass flux associated with accretion and feedback . . . 236
Appendix 6.C: Fraction of black hole growth at low vs. high Eddington ratios . . . 237
Appendix 6.D: Dimensionless entropy profiles . . . 238

Appendix 6.E: Periodicity between jet episodes 240

7 Conclusions and future work **242**

7.1 Ongoing and future work 246

List of Figures

1.1 The large-scale structure of dark matter in the Millennium dark-matter-only simulation (Springel 2005). 5

1.2 Schematic of jets interacting with the ambient medium (the ICM in a galaxy cluster), adopted from Bourne & Sijacki (2017). This shows the main features of such interactions: 1) the unshocked, fast-moving jet, 2) shocked jet material forming a lobe/cocoon and 3) the bow shock propagating into the ambient medium. 22

2.1 An illustration of our accretion disc model, adopted from Müller (2004). At low Eddington ratios ($f_{\rm Edd} < 0.01$), the accretion disc is largely thick and hot (the ADAF flow), with very little mass inflow, and most of the energy outflow taking the form of relativistic jets. At moderate accretion rates ($0.01 < f_{\rm Edd} < 1$), the accretion disc is thin and outflows are largely radiation-driven. At super-Eddington rates, the disc again becomes thick, and has both relativistic jets and disc-driven winds. We also include jets at moderate Eddington ratios, with their efficiency increasing sharply as the BH approaches and exceeds the Eddington rate. 27

2.2 The state of the accretion disc that we assume in the model, depending on values of the BH spin parameter a and the Eddington ratio $f_{\rm Edd,0} = \dot{M}_{\rm BH,acc,0}/\dot{M}_{\rm Edd}$. Note that we use the large-scale accretion rate $\dot{M}_{\rm BH,acc,0}$ and not the net accretion rate $\dot{M}_{\rm BH}$ in this definition. The Eddington rate used in the definition is spin-dependent, due to a non-constant radiative efficiency. 30

2.3 The feedback efficiencies used in the model. The top row shows the efficiencies on a linear scale, while the bottom row uses a logarithmic scale for the $y-$axis. The left-hand panels shows wind efficiencies, while the right-hand panels show jet efficiencies. The winds are implemented as thermal isotropic feedback, representing energy-driven winds shocked on subgrid scales. For thin discs, the radiative efficiency depends on spin and is given by Eqn. (1.2), and a fraction $\epsilon_{\rm f}$ (assumed to be 0.1 for this figure) of that couples to the gas to launch a wind (with a total efficiency given by the red line). The slim disc also launches winds, but with a much different dependence on spin (Eqn.2.5) due to additional MHD effects and an interaction of radiation with jets. The winds from the thick disc are launched on account of MHD effects and thermal pressure, with an efficiency given by Eqn. (2.3) and shown as the blue line. For the jet efficiency we use the same formula for all accretion regimes (Eqn. 2.7), with a fully-MAD value of dimensionless magnetic flux ϕ (Eqn.2.4) used for the thick disc, while for the thin and slim discs, ϕ is strongly dependent on the Eddington ratio $f_{\rm Edd}$ (Eqn. 2.6) and is much smaller than $\phi_{\rm MAD}$ unless the slim disc is strongly super-Eddington. Note the difference in the $y-$axis range compared to the left-hand panel. . . . 32

2.4 The feedback efficiencies used in the model, the same as shown in Fig. 2.3. However, here we plot both the wind efficiencies (red lines) and jet efficiencies (blue lines) in the same panels, but for different accretion regimes (thick disc - top row, thin disc - middle row, slim disc - bottom row). The left-hand and right-hand columns show linear and logarithmic versions of the same plots, respectively. For other details, see caption of Fig. 2.3. 34
2.4 The spinup/spindown function in our model. These are given by Eqn. (2.19) for the thick disc (blue line) and Eqn. (2.20) for the thin and slim discs (red and orange lines). For the latter, we show the spinup/spindown function for several values of $f_{\rm Edd}$. 42
2.5 The accretion efficiency in the thick disc as a function of the Eddington ratio $f_{\rm Edd} = \dot{M}_{\rm BH,acc,0}/\dot{M}_{\rm Edd}$, assuming different values of the parameter s (see text for details) and sound speed $c_{\rm s}$ of the ambient medium. This accretion efficiency is given by Eqn. (2.47), where the Bondi radius $R_{\rm B}$ is replaced by $\min(R_{\rm B}, R_{\rm tr})$, and in which $R_{\rm tr}$ is the transition radius between the thin and thick disc (Eqn. 2.48). 53
2.6 The slim disc wind efficiencies used in our model (left-hand panel), obtained using data from the simulations performed by Ricarte et al. (2023). The points show average values of the wind efficiency for each individual simulation performed by Ricarte et al. (2023), where the $x-$axis values are the average dimensionless magnetic fluxes ϕ for each of those simulations. The wind efficiencies are obtained as described in the text. The lines represent the fitting function given by Eqn. (2.50), which includes an explicit dependence on magnetic flux, which is most apparent for the zero spin case. The right-hand panel shows the remaining dependence on BH spin, $f(a)$, which we fit using Eqn. (2.51) (see text for how we obtain the individual values of that function). 55

3.1 Visualisations of the gas temperature distribution for a ballistic jet (effective half-opening angle $\theta_j = 0°$, top) and a jet in the self-similar evolutionary phase (half-opening angle $\theta_j = 10°$, bottom) at different times. All other parameters correspond to our fiducial choice, given in the first row of Table 6.1. Colours represent the temperature of the gas, as given by the colour bar. The panels show slices 10 kpc in depth. 68

3.2 Visualisations of the gas temperature distribution in our highest resolution jet simulation, with particle mass $m_{gas} = 5.73 \times 10^3$ $M_\odot$, at different times. All other parameters correspond to our fiducial choice, given in the first row of Table 6.1. Colours represent the temperature of the gas, as given by the colour bar. The panels are 10 kpc in depth. 71

3.3 Top: properties of our highest resolution jet simulation after 96 Myr (with a mass resolution $m_{gas} = 5.73 \times 10^3$ $M_\odot$, while other parameters correspond to our fiducial choice, given in the first row of Table 6.1). Bottom: properties of a simulation with a slightly lower resolution, $m_{gas} = 1.81 \times 10^4$ $M_\odot$, a smaller opening angle $\theta_j = 5°$ and a larger jet velocity $v_j = 30000$ km/s, after 48 Myr. Each panel is 10 kpc in depth and shows different gas properties, as given by the titles and legends. 73

3.4 Time evolution of the jet lobe length and radius, as well as the bow shock radius (solid and dotted lines, as marked), in our standard simulation (first row of Table 6.1). These are compared to predictions from Kaiser & Best (2007) for the lobe (dashed lines; Eqn. 3.5). . . . 77

3.5 Energetics of our standard jet simulation (see the first row of Table 6.1 for a list of parameters), at $t = 100$ Myr. *Top:* Evolution of the total energies in the jet lobe and ambient medium. Blue lines represent kinetic energy, while red lines are the thermal energy. The sums for the lobe and ambient medium are given by the black lines. The grey lines represent the total injected energy and the total change in the energy of the lobes and the ambient medium. These two lines overlap, showing that energy is numerically conserved. *Bottom:* Kinetic, thermal and total energy densities per unit length along the jet axis, normalised by the total jet length. 80

3.6 Comparison of jets simulated with different parameters (see Table 6.1 for the range of variations), after 100 Myr of evolution. The standard set of parameters is: $P_\mathrm{j} = 10^{46}$ erg/s, $\theta_\mathrm{j} = 10°$, $v_\mathrm{j} = 15000$ km/s and $m_\mathrm{gas} = 1.81 \times 10^5$ $\mathrm{M}_\odot$. When varying one parameter, all others remain fixed. From top to bottom, each row contains variations of: jet power, half-opening angle, launching velocity and mass resolution. The colours show gas temperature, according to the colour bars. The panels are 10 kpc in depth. 84

3.7 Jet and lobe length as a function of time for simulations with various parameters. The standard set of parameters is: $P_\mathrm{j} = 10^{46}$ erg/s, $\theta_\mathrm{j} = 10°$, $v_\mathrm{j} = 15000$ km/s $m_\mathrm{gas} = 1.81 \times 10^5$ $\mathrm{M}_\odot$, and the range of variations is given in Table 6.1. Each panel represents a different variation of parameters, as visible in the legends (top left - jet power, top right - half-opening angle, bottom left - launching velocity, bottom right - mass resolution). Orange lines represent theoretical predictions from Kaiser & Best (2007). Where we show only one line, there should be no change of jet length with the parameter being varied. 86

3.8 Comparison of jets simulated with varying numerical resolutions (see top of each panel, these are typical resolutions employed in cosmological simulations of galaxy clusters or large-volume cosmological simulations). The number of particles in each jet varies from ≈ 450 to ≈ 14000. Other jet parameters used are the same as the fiducal case, see Table 6.1. The panels show the jets after 100 Myr of evolution. The colours show gas temperature, according to the colour bar. The panels are 10 kpc in depth. 89

3.9 Comparison of the evolution of jets launched into power-law ambient density profiles (see top-right-hand corner of the first panel in each row). Other jet-related parameters used are listed in the last row of Table 6.1. The colours show gas temperature, according to the colour bar. The panels are 25 kpc in depth. 94

3.10 Comparison of jet-inflated lobe lengths and radii in simulations with power-law ambient density profiles (see top-left corner of each panel). Other jet-related parameters used are listed in the last row of Table 6.1. The solid lines show measured lengths and radii from the simulations, while the dashed lines give equivalent predictions for self-similar jet-inflated lobe expansion from Kaiser & Best (2007). 95

4.1 Visualizations of jet launching in our highest resolution simulation ($m_{\rm gas} = 10^4$ M$_\odot$), through temperature maps at different times (top) and maps of various properties (as labeled), at $t = 50$ Myr (bottom). The panels measure 400×120 kpc^2, in slices with a depth of 15 kpc. The jets are active for 40 Myr with a (total) power of 3.16×10^{45} erg/s. Jet particles are kicked conically within half-opening angles of 15°, and with launching velocities of 20000 km/s. The total gas mass, its distribution and the external potential correspond to a dark matter halo with a virial mass of 10^{14} M$_\odot$. 104

4.2 Bubble inflation and propagation in our highest resolution simulation ($m_{\rm gas} = 10^4$ M$_\odot$), at different times. The top half of the simulation is shown through volume renderings of the temperature, in order to highlight the 3D structure of the bubbles. The bottom half shows slices 30 kpc in depth. The panels measure 1200×360 kpc^2. See caption of Fig. 4.1 for details of the jet launching and external medium. 107

4.3 Jet/bubble and ambient medium energetics in our highest resolution simulation ($m_{\rm gas} = 10^4$ M$_\odot$), at different times. We define all jet particles as the bubble, even before the bubble has formed. See caption of Fig. 4.1 for details of the jet launching and external medium. . . . 109

4.4 Impact of the jets and bubbles on the radial profiles of gas (top left), temperature (top right), pressure (bottom left) and entropy (bottom right). These results are for our highest resolution simulation ($m_{\rm gas} = 10^4$ M$_\odot$), at different times as per the legend. See caption of Fig. 4.1 for details of the jet launching and external medium. 111

4.5 Impact of the jets and bubbles on the radial profiles of gas (top left), temperature (top right), pressure (bottom left) and entropy (bottom right). These results are for our highest resolution simulation ($m_{\rm gas} = 10^4$ M$_\odot$), at $t = 800$ Myr. We show the profiles using all particles (black), using particles only within 10 degrees of the jet-launching axis (blue), and outside 30 degrees of the jet launching axis. See caption of Fig. 4.1 for details of the jet launching and external medium. 113

4.6 Slices through the gas (30 kpc depth) showing the structure of the jet bubbles and their surroundings, at a resolution level of $m_{\rm gas} = 10^4$ M$_\odot$, and 800 Myr after the start of the simulation. The panels measure 1200×360 kpc^2. Each panel shows a different property, as in the panel titles. See caption of Fig. 4.1 for details of the jet launching and ambient medium. 114

4.7 Bubble, drift and wake masses and volumes (see main text for definitions and methods of measurement) in our highest resolution simulation, as functions of time. See caption of Fig. 4.1 for details of the jet launching and the ambient medium. 117

4.8 Measurement of the drift, wake and entrainment coefficients (see main text for definitions and methods of measurement) in our highest resolution simulation, as functions of time. See text or caption of Fig. 4.1 for details of the jet launching and ambient medium. 120

4.9 Bubble properties measured from our highest resolution simulation (see main text for methodology), as functions of bubble position (black lines). The panels show density (top left), radius (top right), and velocity (bottom). These are compared with predicted values from the theoretical model by Pope et al. (2010). The initial conditions for this model are our measured values at 100 Myr. In the bottom left panel, different lines represent model predictions with different effects included; the blue line represents buoyancy and adiabatic expansion, while all other lines, with the exception of magenta, model one additional effect (as per the legend). In the bottom right panel, lines of those same colours represent each effect included successively. Magenta lines represent model predictions with all effects included. Numerical coefficients for each effect are given in the legends. In the top two panels we do not show model predictions with drag, entrainment, drift or the wake, as they do not influence bubble densities or radii. See caption of Fig. 4.1 for details of the jet launching and ambient medium. 121

4.10 Renderings of the gas temperature in simulations with varying physical parameters (first row - jet power, second row - jet power and launching velocity, third row - launching velocity, fourth row - half-opening angle). The standard set of parameters is $P_{\rm j} = 3.16 \times 10^{45}$ erg/s, $v_{\rm j} = 2 \times 10^4$ km/s and $\theta_{\rm j} = 15°$. In each case of a varying parameter(s), we show the visualizations at a specific time of interest for that variation (top right corner in each panel). The relevant parameter(s) being varied in each simulation is shown above each panel. The jet duration is 50 Myr, and the numerical resolution $m_{\rm gas} = 10^5$ $\rm M_\odot$. 126

4.11 Renderings of the gas temperature in simulations with varying numerical resolution (top row) and hydrodynamical scheme (bottom row). The jet-related parameters used in these simulations are $P_{\rm j} = 3.16 \times 10^{45}$ erg/s, $v_{\rm j} = 2 \times 10^4$ km/s and $\theta_{\rm j} = 15°$, $T_{\rm j} = 50$ Myr. The numerical resolution or scheme being used in each simulation is shown above each panel. 127

5.1 Gas temperature projections (mass-weighted mean) in our fiducial simulation (see Table 6.1 for details) of the galaxy group halo ($M_{200} = 10^{13}$ $\rm M_\odot$) at different times. The images show a region 1 Mpc across and 200 kpc in depth. They show initially strong jets that inflate lobes and launch bow shocks, a weaker, precessing jets at intermediate times, and a very weak jet at late times. 146

5.2 Jet power and star formation rate in the $M_{200} = 10^{13}$ $\rm M_\odot$ simulations with varying resolution (left), initial SMBH spin (middle) and initial central temperatures (right). The details of the fiducial case, relative to which these variations are made, are given in Table 6.1 (purple line in each panel, underlined parameter in each panel legend). The dotted black lines represent the upper limit of the specific star formation rate required to classify a galaxy as quenched. 148

5.3 Gas temperature projections (mass-weighted mean) in our fiducial simulation (see Table 6.1 for details) of the low-mass galaxy cluster ($M_{200} = 10^{14}$ $M_\odot$) at different times. The images show a region 1 Mpc across and 200 kpc in depth. They show the variety of jet morphologies featured during and between multiple cooling flows. The video version of this plot is available to view at https://youtu.be/Edf2hS7HU70. 149

5.4 Time dependence of the quenching/feedback process in the low-mass galaxy cluster simulations ($M_{200} = 10^{14}$ $M_\odot$) with varying mass resolution (top row), initial SMBH spin (middle row) and initial central temperatures (bottom row). The left-hand panels show the jet power, while the right-hand panels show the star formation rate. Insets in the left-hand panels show the injected jet energy and magnitude of SMBH spin. The insets in the right-hand panels show the cold gas mass. The details of the fiducial case, relative to which these variations are made, are given in Table 6.1 (purple and orange lines in the top/middle and bottom panels, respectively; underlined parameter in each panel legend). The dotted black lines represent the upper limit of the specific star formation rate required to classify a galaxy as quenched. 151

5.5 Gas temperature projections (mass-weighted mean) in our fiducial simulation (see Table 6.1 for details) of the high-mass galaxy cluster ($M_{200} = 10^{15}$ $M_\odot$) at different times. The images show a region 1.2 Mpc across and 400 kpc in depth. They show the variety of jet and bubble morphologies in this simulation, as well as jet reorientation. The video version of this plot is available to view at https://youtu.be/2herQHMnrZs. 156

5.6 Time dependence of the quenching/feedback process in the high-mass galaxy cluster simulations ($M_{200} = 10^{15}$ $M_\odot$) with varying mass resolution (top row), initial SMBH spin (middle row) and initial central temperatures (bottom row), as per the legends in the right-hand panels. The left-hand panels show the jet power, while the right-hand panels show the star formation rate. Insets in the left-hand panels show the magnitude of SMBH spin and the angle between the spin vector and $z-$axis. The insets in the right-hand panels show the cold gas mass. The details of the fiducial case, relative to which these variations are made, are given in Table 6.1 (purple and orange lines in the top/middle and bottom panels, respectively; underlined parameter in each panel legend). The dotted black lines represent the upper limit of the specific star formation rate required to classify a galaxy as quenched. The yellow line in the top panel is discontinued at ≈ 12 Gyr since this simulation (the highest-resolution one) was not run for the full 16 Gyr. 158

5.7 Gas properties (mass-weighted means) at different times in our fiducial simulation (see Table 6.1 for details) of the high-mass galaxy cluster ($M_{200} = 10^{15}$ $M_\odot$). Each image is 800 kpc across, and shows slices 200 kpc in depth. Insets show a zoom-in of the central 50 kpc (10 kpc in depth). From left to right we show the temperature, entropy, shock/sound wave indicator and X-ray surface brightness (see text for details). From top to bottom we show different times. The video version of the X-ray plots is available to view at https://youtu.be/113F4ndbm1c. 161

5.8 Profiles of gas density, tempreature and entropy from our fiducal high-mass galaxy cluster simulation at medium resolution ($M_{200} = 10^{15}$ $M_\odot$, $m_g = 6.4 \times 10^6$ $M_\odot$, see Table 6.1 for details). The initial profiles are shown by dotted lines, while thick solid lines are the median profiles using individual snapshots, which are shown with thin solid lines. The purple and orange lines show median profiles for our simulated cluster when it is cool-core (CC) and non-cool-core (NCC), respectively. The cluster is classified as the former if its central entropy (within $r < 10$ kpc) satisfies $K_0 < 30$ keVcm^2, and the latter if $K_0 > 30$ keVcm^2. This definition follows the observational sample of Cavagnolo et al. (2009); their median CC and NCC entropy profiles are shown with dashed purple and orange lines, respectively 166

5.9 Time dependence of the quenching/feedback process in the high-mass galaxy cluster simulations ($M_{200} = 10^{15}$ $M_\odot$) with varying parameters/choices, as per the legends in the right-hand panels. In the top row we vary the jet launching velocity, and in the middle row the choice of which particles are kicked from the SMBH smoothing kernel. The bottom row shows a case with the jets fixed along the $z-$axis, with the jet power calculated using a fixed efficiency (see legend). The left-hand panels show the jet power, while the right-hand panels show the star formation rate. Insets in the left-hand panels show the magnitude of SMBH spin and the angle between the spin vector and $z-$axis in the top and middle panel, and the total injected jet energy in the bottom panel. The insets in the right-hand panels show the cold gas mass. The details of the fiducial case, relative to which these variations are made, are given in Table 6.1 (purple line in each panel and underlined parameter in each panel legend, with the exception of the bottom row). The dotted black lines represent the upper limit of the specific star formation rate required to classify a galaxy as quenched. 168

5.10 The alignment of an initially misaligned SMBH spin vector, calculated using two different approaches. We show the $x-$ component of the angular momentum direction vector, i.e. the component in the direction of the outer accretion disc. The initial SMBH spin is $a = 0.5$, and it is directed along the $z-$axis. The SMBH mass is $M_{\rm BH} = 10^7$ $\rm M_\odot$, and the SMBH is accreting with a constant $\dot{m} = 0.1$. Black lines show the predicted alignment from the differential equation approach, using equations (5.4) and (5.6), while blue lines show predictions using our warp increment approach, with equation (5.7). The solid blue line shows the predicted alignment using the derived warp alignment timescale (equation 5.7), while the dashed blue line shows the prediction from the same approach, but using the alignment timescale from the differential equation approach, given by equation (5.6). The agreement between the black and dashed blue lines shows that the two approaches are (almost) equivalent. 178

5.11 Time dependence of the quenching/feedback process in the high-mass galaxy cluster simulations ($M_{200} = 10^{15}$ $\rm M_\odot$) with varying half-opening angles of the jet (top) and initial inclinations of the SMBH spin vector, relative to the angular momentum of the halo (bottom). The left-hand panels show the jet power, while the right-hand panels show the star formation rate. Insets in the left-hand panels show the magnitude of SMBH spin and the angle between the spin vector and $z-$axis. The insets in the right-hand panels show the cold gas mass. The fiducial simulation is the one with half-opening angle $\theta_{\rm j} = 10^\circ$ and inclination $\theta_0 = 0^\circ$ (purple and blue line, respectively, in the top and bottom panels); other details of the fiducial setup are given in Table 6.1. The dotted black lines represent the upper limit of the specific star formation rate required to classify a galaxy as quenched. 179

5.12 Time dependence of the quenching/feedback process in the high-mass galaxy cluster simulations ($M_{200} = 10^{15}$ $M_\odot$) with varying spin parameters (top) and metallicity profiles of the ICM (bottom). The left-hand panels show the jet power, while the right-hand panels show the star formation rate. Insets in the left-hand panels show the magnitude of SMBH spin and the angle between the spin vector and z-axis. The insets in the right-hand panels show the cold gas mass. The fiducial simulation is the one with an ICM spin parameter of $\lambda_g = 0.05$ and constant metallicity $Z = 0.3Z_\odot$ (orange and purple lines, respectively, in the top and bottom panels); other details of the fiducial setup are given in Table 6.1. The dotted black lines represent the upper limit of the specific star formation rate required to classify a galaxy as quenched. 180

5.13 Time dependence of the quenching/feedback process in high-mass galaxy cluster simulations ($M_{200} = 10^{15}$ $M_\odot$) with varying gravitational softening lengths at fixed mass resolution (top) and particle position seeding (bottom). The left-hand panels show the jet power, while the right-hand panels show the star formation rate. Insets in the left-hand panels show the magnitude of SMBH spin and the angle between the spin vector and z-axis. The insets in the right-hand panels show the cold gas mass. The fiducial simulation is the one with a gravitational softening length of of $\epsilon_g = 1.2$ kpc and random particle seeding (purple line in each panel); other details of the fiducial setup are given in Table 6.1. The dotted black lines represent the upper limit of the specific star formation rate required to classify a galaxy as quenched. 182

6.1 A visualization of the gas temperature at four representative times in our hybrid simulation (with both kinetic jets and thermal isotropic feedback, interchanging at an Eddington ratio $f_{\rm Edd,crit} = 0.01$) of the high-mass galaxy cluster ($M_{200} = 10^{15}$ $\rm M_\odot$). The colours indicate the projected, mass-weighted gas temperature, as indicated by the colour bar, and we include all gas in a 50 kpc-deep slice. The left-hand panels show times when kinetic jet feedback dominates, while the right-hand panels show times when thermal isotropic feedback is dominant. The bottom two panels show that both types of feedback lead to spherical shock waves. At all times shown here, ambient gas uplifted by feedback-induced outflows is visible in the form of cool filamentary structures. 198

6.2 Comparison of the cooling and feedback cycle in simulations using the BH spin evolution model for our idealized galaxy group ($M_{200} = 10^{13}$ $M_\odot$), low-mass cluster ($M_{200} = 10^{14}$ $M_\odot$) and high-mass cluster ($M_{200} = 10^{15}$ $M_\odot$), from left to right. From top to bottom we show the kinetic jet power, the thermal heating power, the cold gas masses ($T < 2 \times 10^4$ K) and the star formation rates. The details of these simulations are given in § 6.2.2 and Table 6.1 (in terms of physical set-up and halo mass) as well as § 6.2.3 and Table 6.2 (in terms of the feedback implementation). The model uses the thin, radiatively-efficient accretion disc with thermal isotropic feedback (orange lines) and/or the thick, advection-dominated accretion disc with kinetic jet feedback (blue lines). The purple lines show cases with hybrid feedback, in which the feedback and accretion modes interchange at an Eddington ratio $f_{\rm Edd,crit} = 0.01$ (below this value kinetic jets are used, above it thermal isotropic feedback). The feedback powers are calculated using adaptive time bins such that during each bin, 10 feedback events (heating or kicking particles) occurred. The cold gas masses and star formation rates are calculated as moving averages in 5 Myr-wide bins. The arrows indicate averages over the 8 Gyr simulation run time. 201

6.3 The properties of the BHs and their evolution in simulations using the BH spin evolution model. From top to bottom, we show the BH masses, the Eddington fractions, the BH spin magnitudes, the angles between the BH spin vectors and the $z-$axis, and the jet and radiative efficiencies. All quantities except the feedback efficiencies are sampled every 5 Myr. The feedback efficiencies are sampled every 1 Myr and then a moving average in a 5 Myr-wide bin is calculated using only times when the BH is in the appropriate accretion state (the thick disc for the jet efficiency and the thin disc for the radiative efficiency), and they are weighted by the accretion rate. The arrows indicate averages over the 8 Gyr simulation run time. Everything else is the same as in Fig. 6.2. 208

6.4 The radial gas entropy profiles (volume-weighted) of the ICM using the BH spin evolution model, from the same set of simulations as in Figs. 6.2 and 6.3. The solid lines show medians calculated using 160 snapshots between $t = 0$ and $t = 8$ Gyr, while the shadings indicate the $16^{\rm th} - 84^{\rm th}$ percentile ranges. The profiles in the initial conditions are shown with the dashed lines. The observational data sets are described in § 6.2.4. The profiles from Johnson et al. (2009) and Sun et al. (2009) are converted from their dimensionless form to physical form for the two left-hand panels separately, which is why these data differ in the two panels. The sample from Cavagnolo et al. (2009) is split onto cool-core (CC) and non-cool-core (NCC) clusters. 211

6.5 The feedback cycle for our simulations with fixed feedback efficiencies (as well as fixed jet directions in the jet feedback case, where they are launched in the $z-$direction). The left-hand panels show results for the low-mass galaxy cluster case ($M_{200} = 10^{14}$ $M_\odot$), while the right-hand ones show the results for the high-mass galaxy cluster ($M_{200} = 10^{15}$ $M_\odot$). In the top panels we show the feedback powers, while the bottom panels show the SFRs. For the jet case, we perform fiducial simulations that have velocities high enough to lead to the inflation of hot lobes of gas (blue lines), as well as lower-velocity ones (purple lines) that instead have an equal energy per kicking event as the thermal isotropic simulations (orange lines). The feedback powers are calculated using adaptive time bins such that during each bin, 10 feedback events (heating or kicking particles) occurred, while the star formation rates are calculated as moving averages using 5 Myr-wide bins. The arrows indicate averages over the 8 Gyr simulation run time. Further details of the simulations are given in § 6.2.3 and Table 6.3. 216

6.6 Radial gas profiles (volume-weighted) of the ICM for the same set of simulations as shown in Fig. 6.5. From top to bottom we show the electron number density, the temperature and the entropy. The solid lines are medians calculated using 160 snapshots between $t = 0$ and $t = 8$ Gyr, while the shadings indicate the $16^{\rm th} - 84^{\rm th}$ percentile ranges. The profiles in the initial conditions are shown with dashed lines. The observational data sets are described in § 6.2.4. The sample from Cavagnolo et al. (2009) is split onto cool-core (CC) and non-cool-core (NCC) clusters. 218

6.7 A mosaic of different jet (top row) and isotropic (bottom row) feedback simulations with varying feedback parameters, for the low-mass galaxy cluster ($M_{200} = 10^{14}$ $M_\odot$). The colours indicate the gas temperature, as shown by the colour bar, and we include all gas in a 50 kpc-deep slice. The panels all show the same spatial scales. The simulation times shown here are generally different since the timing of the feedback activity is highly chaotic. For both the jets and isotropic feedback we vary: 1) the fraction of energy injected as thermal as opposed to kinetic (values of 0, 0.5 and 1), shown on the left-hand side, and 2) the energy increment received by the particles (by factors of $\sqrt{10} \approx 3.16$), shown on the right-hand side. The variations of the jet energy type use a jet velocity of 1.5×10^4 km s^{-1} (or its corresponding heating temperature if feedback is mixed or purely thermal), while the corresponding isotropic variations use a corresponding temperature increase of $\Delta T = 10^9$ K. The variations of the energetics are done for kinetic feedback in the jet case and thermal feedback in the isotropic case. 221

6.8 Impact of parameter variations on the feedback cycle for both jet (left) and isotropic (right) feedback as measured through the feedback power and the star formation rate (insets in each panel), for the low-mass galaxy cluster ($M_{200} = 10^{14}$ $M_\odot$ halo). The feedback powers are calculated using adaptive time bins such that during each bin, 10 feedback events (heating or kicking particles) occurred, while the star formation rates are calculated as averages in bins with a fixed width of 5 Myr. The arrows indicate averages over the 8 Gyr simulation run time. The dotted horizontal lines in the inset panels show the SFR at which the BCG is classified as marginally quenched (sSFR = 0.01 Gyr^{-1}). The details of the simulations are given in § 6.2.3 and Table 6.3. The parameters that are varied are shown in the legend of each panel, and they are: 1) the fraction of energy injected in thermal as opposed to kinetic form (top row, values of 0, 0.5 and 1), 2) the kicking/heating energy increments, given by the choice of jet velocity and heating temperature (middle row, by factors of $10^{1/4} \approx 1.78$ and $\sqrt{10} \approx 3.16$, which corresponds to logarithmic intervals of 0.25 and 0.5 dex, respectively) and 3) the feedback efficiency (bottom row, by factors of 10). The fiducial cases are those with thermal isotropic and kinetic jet feedback, using efficiencies of $\epsilon = 0.01$, heating temperatures of $\Delta T = 10^{8.5}$ K and jet velocities of $v_\mathrm{j} = 1.5 \times 10^4$ km s^{-1}. These parameters are underlined in the legend of each panel. 223

6.9 Impact of parameter variations on the gas entropy profiles (volume-weighted) of the ICM using both jet (left) and isotropic (right) feedback, for the low-mass galaxy cluster ($M_{200} = 10^{14}$ $M_\odot$). The solid lines are medians calculated using 160 snapshots between $t = 0$ and $t = 8$ Gyr, while the shadings indicate the $16^{\mathrm{th}} - 84^{\mathrm{th}}$ percentile ranges. The fiducial parameters (underlined and printed in each panel), as well as the parameters being varied, are the same as shown in Fig. 6.8 and described in its caption. The observational data sets are described in § 6.2.4. 226

6.10 Time dependence of the jet powers (left) and star formation rates (right) in the high-mass galaxy cluster ($M_{200} = 10^{15}$ $M_\odot$) simulations that feature jet redirection, compared with a case that has a fixed jet direction (along the $z-$axis). In the top panels we compare with a case that features jet redirection using the spin evolution model. The bottom panels show several cases where the jets are held fixed in a direction that randomly changes, with the period of these redirections shown in the legend. The arrows indicate averages over the 8 Gyr simulation run time. The parameters of the simulations correspond to the sixth row of Table 6.3. 233

6.11 Same as Fig. 6.10, but showing cases with precessing rather than redirecting jets. From top to bottom we show several cases with different periods of jet precession. In each row (i.e. at every fixed precession period) we also vary the precession angle. 234

6.12 Ratio of total mass accreted (top row), launched into the jets (middle row) and heated (bottom row) by the BH, and the total stellar mass formed. The arrows indicate averages over the 8 Gyr simulation run time. This figure is an extension of Fig. 6.2. 236

6.13 BH mass growth that occurs at low Eddington ratios ($f_{\rm Edd} < 0.01$) as a fraction of the total mass growth, for our simulations with BH spin evolution. This figure is an extension of Fig. 6.3. 238

6.14 Dimensionless entropy profiles for our simulations with BH spin evolution. This figure may be considered an alternative to Fig. 6.4. Note that we define the entropy K_{500} using the actual baryon fractions of our simulated haloes, rather than the cosmic baryon fraction (the usual choice). We find that this leads to better agreement between the profiles at large distances. 239

6.15 Time dependence of quantities related to the quenching/feedback process in our fiducial $M_{200} = 10^{14}$ $M_\odot$ simulation with fixed jet feedback (the parameters are given in the third row of Table 6.3). From top left to bottom right we show the jet power, SFR, cooling time at several radii (see legend) and cooling time to dynamical time ratio for the same radii. These plots show that the periodicity between jet/cooling episodes is set by the cooling time of the gas with $t_{\rm cool}/t_{\rm dyn} \approx 10$, due to all gas with that ratio below 10 undergoing cooling. 240

List of Tables

3.1 List of all simulations and the parameters we use. In the first row we specify the parameters of our fiducial simulation with a constant-density ambient medium. In the second row we specify the parameters that are varied for this same case. In the final row we specify the parameters of the case with a power-law ambient density profile. The parameters are, in order: 1) $m_{\rm gas}$ - mass resolution, 2) $P_{\rm j}$ - jet power, 3) $v_{\rm j}$ - jet velocity, 4) $\theta_{\rm j}$ - jet half-opening angle, 5) ambient medium density ρ - constant value or power law slope and 6) $T_{\rm j}$ - jet duration. 67

5.1 List of all simulations. In the first three rows we specify the parameters of our fiducial simulations for each of the three halo masses we have simulated. We then specify the ranges of variations of all other parameters in the next three rows. The parameters are, in order: 1) M_{200} - halo mass, 2) $m_{\rm gas,0}$ - central gas resolution in terms of particle mass, 3) T_0 - central gas temperature, 4) a_0 - magnitude of initial SMBH spin, 5) $\epsilon_{\rm j}$ - jet efficiency; constant value or $\epsilon_{\rm j}(a)$, the spin-dependent efficiency given by equation (2.7), 6) $v_{\rm j}$ - jet launching velocity, 7) Scheme - which particles within the SMBH smoothing kernel are kicked from the SMBH, F: farthest, C: closest, S: closest to the axis of the spin vector (in terms of angular distance), L: lowest density. 144

6.1 List of parameters for the initial conditions (first eight columns) and numerical resolution (last two columns) of our idealized galaxy group and cluster simulations. These are, in order: 1) M_{200} - halo mass, 2) r_{200} - halo virial radius, 3) NFW halo concentration parameter $c_{\rm NFW}$, 4) baryonic mass fraction within R_{500}, $f_{\rm b,500}$, 5) central gas temperature T_0, 6) stellar mass of the BCG, 7) Hernquist scale length (half-light radius) of the galaxy, 8) mass of the central BH, 9) spin of the BH, 10) central gas mass resolution, 11) gravitational softening length. 192

6.2 List of simulations performed with the BH spin evolution model (see Chapter 2). For each halo mass, three simulations were performed with different feedback and accretion modes. In the hybrid mode, the thin disc and thermal isotropic feedback is used when the BH is accreting with $f_{\rm Edd} > f_{\rm Edd,crit} = 0.01$, while the thick disc and kinetic jets are used otherwise. The details of these simulations are given below. 193

6.3 List of simulations performed with simplified feedback prescriptions (without BH spin evolution, i.e. with fixed feedback efficiencies and jets in the direction of the $z-$axis). Three simulations were performed for the low- and high-mass galaxy clusters. For the low-mass galaxy cluster, further variations of all the parameters were performed in a total of 16 simulations. The parameters of these simulations are given in the last two rows. * Th. - thermal, Mix. - mixed (half thermal, half kinetic), Kin. - kinetic. 195

CHAPTER 1

Introduction

1.1 Galaxies in observations and theory

1.1.1 The earliest observations of other galaxies

Until the beginning of the 20th century, it was thought that our galaxy was the only such collection of baryonic matter (i.e. gas, stars, dust). With the observations performed by Hubble (1926a) at the Mount Wilson Observatory, other galaxies were resolved and studied in some detail, leading to the realization that our galaxy is not unique. Other galaxies had been observed before (e.g. the ones in the Messier catalogue), and some are visible to the naked eye (e.g. the Andromeda galaxy or the Small and Large Megallenic clouds), but only as nebulae that are not obviously collections of stars.

Hubble further discovered that most galaxies (if they are sufficiently distant) are receding from us (Hubble 1929), with a velocity that grows with distance. This behaviour is thus known as Hubble's law. It results in the redshifting of the light emitted by these galaxies, and is caused by the isotropic and homogenous expansion of the Universe. These observations showed that the Universe is not static. Concurrent with Einstein's discovery of general relativity (Einstein 1916), they led

to the birth of modern cosmology, and the study of the origin (the Big Bang) and evolution of the Universe as whole.

Early observations of galaxies also revealed that the rotational velocities of their stars do not agree with the visible amount of matter at large distances (Oort 1932, Babcock 1939, Volders 1959, Roberts & Whitehurst 1975). In addition, Zwicky (1933) found that missing matter is necessary to explain observations of galaxy clusters (which cannot be bound unless there is orders of magnitude more matter than is visible to telescopes). The early observations of galaxy rotation curves were further confirmed in a more statistical fashion by Bosma (1978) and Rubin et al. (1980), showing that neutral gas and stars, respectively, orbit with roughly constant velocities regardless of the distance from the centre of their galaxy. These observations were interpreted as being due to a large amount of mass that is not visible to telescopes (dubbed dark matter).

1.1.2 Types and properties of galaxies

Galaxies of different morphological types were discovered early (Hubble 1926b - Hubble sequence), with the main distinction existing between spiral (disc) and elliptical (spheroidal) galaxies. The statistical study of galaxies and their properties began in earnest in the second half of the 20th century, due to the increasing power of telescopes and observational instruments. As detailed observations of galaxies grew in number and sophistication (e.g. Efstathiou et al. 1988, Loveday et al. 1992, York et al. 2000, Colless et al. 2001), it became clear that there is great diversity in galaxy populations and their dynamics. The most important distinction between different galaxies is their luminosity, or stellar mass, both of which may span orders of magnitude. This ranges from dwarf galaxies that are a thousand times less massive than our own galaxy (which itself has a stellar mass of $M_* \approx 6 \times 10^{10}$ $\mathrm{M}_\odot$; see e.g. Licquia & Newman 2015), to large galaxies in the centres of galaxy clusters; brightest-cluster-galaxies or BCGs, that are up to a hundred times more massive than our own galaxy; see e.g. Erfanianfar et al. 2019).

Modern galaxy surveys (e.g. the GAMA survey; Driver et al. 2011) allow the precise and statistical measurements of galaxy abundances (e.g. as a function of lu-

minosity in various bands; e.g. Loveday et al. 2012, or stellar mass; e.g. Baldry et al. 2012), sizes (e.g. Lange et al. 2015) gas, metal and dust abundances (e.g. Catinella et al. 2010, Sanders et al. 2021 and Orellana et al. 2017 respectively), star formation rates (e.g. Davies et al. 2016), and morphological types (e.g. Moffett et al. 2016). High-redshift surveys give an idea of how these properties evolve with redshift (e.g. Madau et al. 1996). It is thus a challenge for the modern theory of galaxy formation and evolution to reproduce all these observations.

1.1.3 ΛCDM: the standard model of cosmology and structure formation

Understanding the formation and evolution of galaxies, from a theoretical perspective, is a complex problem that lies at an intersection of many branches of physics. At the heart of the problem is the question of structure formation. Structures form in an expanding and evolving Universe, and it is thus critical to embed any model of galaxy formation and evolution in a cosmological context.

Einstein's theory of general relativity (Einstein 1916) provides a theoretical framework in which the evolution of the Universe can be studied. His field equations can be used to derive the evolution of the Universe as a whole, under the assumption that it is homogenous and isotropic. If there is only radiation and matter permeating the Universe, Einstein's equations predict that the Universe's expansion, observed first by Hubble (Hubble 1926a), should slow down with time, and possibly reverse (depending on the total amount of matter in the Universe). However, observations of distant supernovae (Perlmutter et al. 1999) have revealed that the expansion of the Universe is accelerating, rather than slowing down. This is interpreted as being due to a constant energy density (or pressure) permeating the Universe (so called dark energy), which can be included in Einstein's equations of general relativity as the cosmological constant Λ. The existence of dark energy is also heavily favoured by observations of the cosmic microwave background (CMB, an afterglow of the Big Bang; Spergel et al. 2003) and large-scale cosmic structure (Blake et al. 2011).

Observations of rotation curves of galaxies (and of galaxy clusters) show that dark matter dominates over baryonic matter, and thus must be included in cos-

mological models (e.g. Zwicky 1933, Rubin et al. 1980). Different types of dark matter may exist: so-called cold, warm or hot, depending on when it becomes non-relativistic. Observations currently favour cold dark matter (de Bernardis et al. 2000), so it is the standard choice for most cosmological applications. In this form, using a cosmological constant Λ representing dark energy, and cold dark matter, the standard cosmological model is usually referred to as ΛCDM.

ΛCDM has been used to explain features in the CMB when the electrons and nuclei recombined to form neutral atoms soon after the Big Bang (Spergel et al. 2003). Reproducing the features in the CMB with a best-fitting ΛCDM model shows that, in the current Universe, dark matter is ≈ 6 times more abundant than normal matter, while dark energy is ≈ 3 times as abundant than all matter (in terms of energy density). The radiation energy density is negligible at the present time. Such a best-fitting ΛCDM model predicts that the Universe is ≈ 14 Gyr old.

1.1.4 The formation and growth of galaxies in ΛCDM

In the ΛCDM model, structures grow from density perturbations seeded very soon after the Big Bang, thought to originate from quantum fluctuations. These perturbations are imprinted onto the temperature of the CMB, and are thus observable. Denser regions become ever denser under the influence of their own gravity, and eventually collapse to form dark matter haloes that host galaxies. In Fig. 1.1 we show an image of the large-scale structure of the universe, as found in the Millennium Simulation (Springel 2005). The dark matter forms a cosmic web made up of walls, filaments and nodes, with dark matter haloes located in all of these structures, but the most massive and rarest ones (hosting galaxy clusters) inhabiting the largest nodes.

At high redshifts $z \approx 100$, the density perturbations permeating the Universe are true perturbations (in the sense that they represent a small deviation from the mean density). Up to this redshift, their growth can be studied using linear theory (Bardeen 1980). However, beyond this redshift, they become denser, and their evolution becomes nonlinear. In this regime, the study of the formation and evolution of structures can be done using either analytical approximations (e.g. the

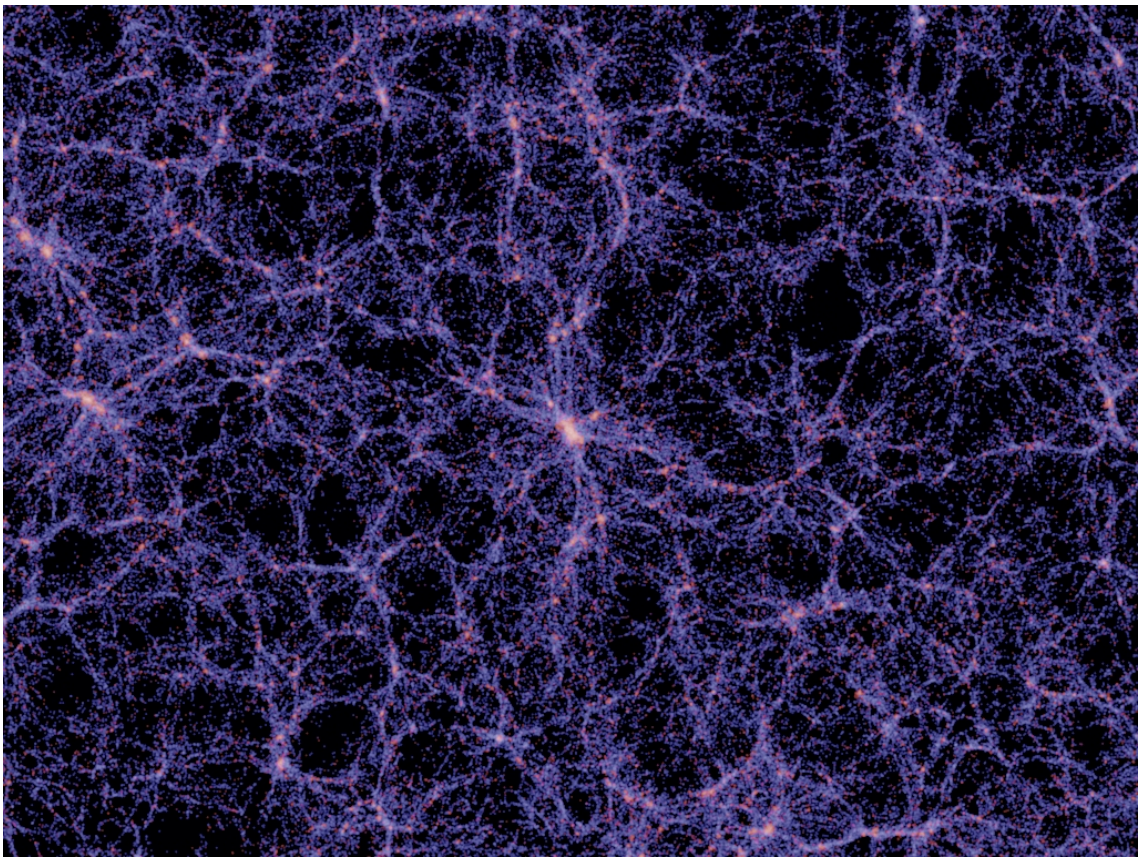

Figure 1.1: The large-scale structure of dark matter in the Millennium dark-matter-only simulation (Springel 2005).

Press & Schechter 1974 formalism) or N-body simulations. The former is a useful approach for dark matter structure formation and evolution, but less so for galaxies, since there are many intertwined physical processes at play that influence their formation and evolution.

The first structures that form are dark matter haloes, that are characterised by approximate virial equilibrium. These haloes host gas, but also start accreting it in the form of filaments from the cosmic web. This gas eventually starts cooling, and once it reaches very low temperatures $T \approx$few hundred K, it starts to form the first stars. Thus, the birth of galaxies commences. The details of this process are not very well understood at the earliest redshifts, due to our poor knowledge of the properties of the first stars. The recently-launched JWST telescope has also hinted at the possibility that supermassive black holes may be hosted by galaxies from the very beginning (e.g. Maiolino et al. 2023), and could even form before a galaxy's first stars have formed.

Once galaxies have formed in their haloes, they grow through gas cooling and star formation, but also hierarchical merging. Less massive haloes of dark matter merge to form progressively more massive haloes, eventually leading to the most massive virialized structures in the Universe, galaxy clusters hosting thousands of galaxies embedded in a vast halo of hot gas (e.g. Lacey & Cole 1993). The galaxies themselves also merge in this process, typically under the influence of infall due to dynamical friction (e.g. Boylan-Kolchin et al. 2008).

1.1.5 Modern galaxy formation and evolution models

The description laid out in the previous subsection allows us to answer the broadest questions about galaxy formation, but it does not provide detailed predictions of galaxies' properties and their statistics. In the modern era of astronomy, as alluded to earlier, the statistical power of surveys has allowed measurements of many of these properties to be made to within a few per cent accuracy. Modern theoretical models of galaxy formation thus try to match these observations. However, matching observations to such detail requires relatively complex modeling, as galaxy formation and evolution depends on many physical processes.

Most modern galaxy formation and evolution models employ numerical simulations, in which a number of computational elements, representing a single or various types of matter, are evolved according to a coupled system of differential equations, typically under the influence of at least gravity. Such simulations can be used to model various processes, e.g. a galaxy merger (White 1978) or the infall of a satellite galaxy in a more massive halo due to dynamical friction (Boylan-Kolchin et al. 2008). In the context of galaxy formation and evolution, the simplest type of numerical simulations are cosmological dark-matter-only (DMO) simulations: N-body simulations in which structure formation (dark matter halo formation and growth) is resolved in an expanding Universe (e.g. Frenk et al. 1988). The main three approaches to modelling galaxy formation and evolution are: 1) semi-analytical models, 2) semi-empirical models and 3) hydrodynamical simulations. All three approaches use numerical simulations, with the first two using N-body DMO simulations, while the latter also simulates baryons directly.

In the first two approaches, galaxies themselves are not resolved and do not exist in the simulation directly. They are instead evolved in post-processing, i.e. after all dark matter haloes have been identified in an N-body simulation. Galaxies are then assumed to be hosted by these haloes and are evolved according to certain processes. In semi-analytical models (e.g. Hernquist 1990, Croton et al. 2006, Bower et al. 2006, Lacey et al. 2016, Lagos et al. 2018), these processes are of a physical nature, and they include: 1) radiative cooling, 2) chemistry (element abundance modeling), 3) dust modeling, 4) star formation, 5) stellar feedback, 6) feedback from black holes, 7) galaxy mergers and disc instabilities. In semi-empirical models (e.g. Behroozi et al. 2013, Moster et al. 2018), the complexities of many of these processes are avoided. Instead of directly modeling them, in such approaches, dark matter haloes are assumed to be hosting a galaxy with a particular star formation rate, that may depend on the stellar/halo mass and redshift. In addition to some dynamical modeling (galaxy mergers), this is sufficient to evolve and predict the stellar mass of galaxies, but not any further quantities.

The most popular recent approach is hydrodynamical cosmological simulations (e.g. Vogelsberger et al. 2014, Schaye et al. 2015, Kaviraj et al. 2017, Davé et al. 2019,

Dubois et al. 2021). In this approach, baryonic resolution elements (cells or particles containing gas, stars and black holes) are evolved alongside dark matter. Thus, all of the physical processes modelled in semi-analytical models, such as radiative cooling, element and dust modelling, star formation and its feedback, black hole growth and its feedback, are employed in hydrodynamical simulations 'on the fly'. This makes hydrodynamical simulations the most complex approach to galaxy formation and evolution, certainly from the perspective of computational expense, but it has the advantage that galaxies are resolved as structures within the simulations. As a result, the predictive power of the simulations is greater, and the simulations can be more easily used as a laboratory to study the interplay of the many physical processes at play.

In all three approaches to galaxy formation and evolution, the models must be calibrated to some observed data. This is due to all models having to use a certain number of unknown free parameters, representing our lack of full understanding of the baryonic processes being modelled. In hydrodynamical simulations, some of the processes are of a 'subgrid' nature, meaning they are not resolved (e.g. star formation or its feedback). In this case, the parameters associated with the implementation of that physical process may be of a completely numerical nature. In either case, the calibration is typically done to observed data at $z = 0$, and the data in question is typically: 1) the stellar mass function, 2) the galaxy size - stellar mass relation and 3) the black hole mass - stellar mass relation, or some subset of these.

1.2 Observations and theory of active galactic nuclei

1.2.1 Discovery of quasars and radio galaxies

As the power of optical telescopes grew sharply in the second half of the last century, alongside galaxies, a new class of objects was also discovered: 'quasars' (quasi-stellar objects, so named because they appear as point sources in images; Schmidt 1963). However, from their spectra, it became apparent that these objects are distant, and

not in our galaxy (Kellermann et al. 1969). This also meant that they are very bright, in order to be observable at such distances (observations in this century are finding them at redshifts up to $z \approx 10$, Shen et al. 2020). With time, it became clear that there is only one compelling way to explain their power: the presence of a black hole, which can extract energy very efficiently out of accreting matter, and radiate it outwards (e.g. Shakura & Sunyaev 1973, Novikov & Thorne 1973).

In addition to quasars, the first radio telescopes also detected very powerful and resolved large-scale radio emission around so-called radio galaxies (Schmidt 1968). These objects were eventually realized to be synchrotron-emitting plasma that is typically outside galaxies (Bicknell 1995), and that takes the shape of jets and lobes. Like with quasars, black holes became a compelling explanation for these radio sources, since the power associated with them is extremely high.

Other than this indirect evidence, the existence of supermassive black holes (SMBHs) was first inferred through a dynamical analysis of the core of the M87 galaxy (Young et al. 1978), with the SMBH mass estimated at $M_{\rm BH} \approx 5 \times 10^9$ $\rm M_\odot$. A similar analysis was done for own galaxy's core (Sgr A*) some time later (Genzel et al. 1994), estimating a SMBH mass of $M_{\rm BH} \approx 3 \times 10^6$ $\rm M_\odot$. Even later, direct observations of orbital motions of individual stars were able to show that there must be an object with a mass $M \approx 4 \times 10^6$ $\rm M_\odot$ contained in a very small volume in our galaxy's centre (Gillessen et al. 2009). This could conceivably only be a SMBH. This was recently confirmed by observations with the Event Horizon Telescope, both for Sgr A* (Akiyama et al. 2022) and M87 (Event Horizon Telescope Collaboration et al. 2021), showing images of the black holes' shadows, directly confirming the existence of supermassive black holes. The masses of the two SMBHs, as measured by the EHT, are $M_{\rm BH} = 6.5 \pm 0.7 \times 10^9$ $\rm M_\odot$ and $M_{\rm BH} = 4 \pm 0.8 \times 10^6$ $\rm M_\odot$ for M87 and Sgr A*, respectively, in good agreement with earlier dynamical measurements.

1.2.2 The impact of active galactic nuclei on their host galaxies in observations

The evidence that supermassive black holes can influence their galaxies, in the form of active galactic nuclei (AGN), has been elusive. While the observations of both

quasars and radio jets/lobes has increased in quality and quantity to the present day (e.g. Schmidt 1968, Becker et al. 1995, Shimwell et al. 2017), it is hard to demonstrate the direct effect they have on their host galaxies. Measurements of black hole masses have shown that there is a relatively tight relation between black hole mass and a galaxy's bulge mass, and even tighter relation between the black hole mass and the central stellar velocity dispersion (Kormendy & Ho 2013, McConnell & Ma 2013). This correlation implies that black holes grow in tight relation with the galaxy's growth, but it does not prove that such growth impacts the galaxy, only that they may have a common fuel supply.

Outflows are found in many galaxies hosting quasars, likely caused by radiation pressure driving winds (e.g. Fiore et al. 2017, Nomura et al. 2016). These winds are thought to have a strong impact on their host galaxies, by ejecting both some of the inter-stellar medium (ISM) and gas on larger scales out of their host dark matter haloes. However, there is no evidence that the host galaxies are quenched by these outflows at the time of observation. As shown by some recent simulations (Ward et al. 2022), this is likely the case because black holes are fed by the very gas associated with star formation, so finding a black hole in the process of driving outflows is only likely if the galaxy is star-forming. Radio galaxies, on the other hand, have been found to be very common in massive galaxies that are already quenched (Sabater et al. 2019). This again, however, does not prove that radio galaxies are causing quenching, since they could merely be more common in quenched and gas-poor systems (in which lower BH accretion rates could make a radio-loud AGN more likely; Heckman & Best 2014).

Observations of galaxy clusters, however, reveal the most compelling evidence for AGN feedback at work. The majority of baryonic matter in galaxy clusters is located in the intracluster medium (ICM), a diffuse and hot (X-ray emitting; $T > 10^7$ K) gaseous halo which roughly traces the dark matter distribution (Pratt et al. 2009, Sun et al. 2009, Lin et al. 2012). Observations of the ICM in X-rays reveal the existence of cavities, regions marked by a lack of X-ray emission (e.g. Bîrzan et al. 2004, McNamara et al. 2005, Wise et al. 2007). These cavities are coincident with bubbles and lobes inflated by jets, visible in radio frequencies (Blandford & Königl

1979, Urry & Padovani 1995). The jets are thought to be launched from AGN hosted by the central galaxies in the clusters (Ghisellini et al. 1993, Biretta et al. 1999).

The central region of the ICM (inner few hundred kpc) is dense and cool enough that the cooling time is often significantly shorter than the Hubble time (Hudson et al. 2010). As a result, we would expect the central galaxy of many galaxy clusters to harbour very high rates of cool gas deposition and star formation. However, other than a few exceptions (O'Dea et al. 2008, McDonald et al. 2015), this is usually not the case (Edge & Stewart 1991, Fabian 1994, McDonald et al. 2018). Furthermore, observations of emission lines, expected in the presence of a cooling flow, are consistent with low cooling rates (Peterson et al. 2003, Bregman et al. 2006). The central galaxies of galaxy clusters are typically 'red and dead', like most other massive elliptical galaxies (Wiklind et al. 1995, Salim et al. 2007, Young et al. 2011, Whitaker et al. 2012, Davis et al. 2019).

In order to keep the central galaxies of galaxy clusters devoid of significant cool gas and star formation, energy release from the central BH has been suggested as a mechanism that counters cooling flows (Tabor & Binney 1993, Ciotti & Ostriker 1997). Specifically, AGN jets have been proposed as the heating mechanism that is responsible (Fabian 2012, Werner et al. 2019, Eckert et al. 2021). The power required to create the X-ray cavities (a proxy for the jet power) has been found to be correlated with the X-ray luminosity of the ICM (Rafferty et al. 2006, Nulsen et al. 2009, Hlavacek-Larrondo et al. 2012a, Russell et al. 2013). It is also sufficient to offset cooling, indicating that AGN feedback in the form of relativistic jets is a plausible mechanism of star formation quenching, by depriving the central galaxies of the required cool gas.

Jets have also been observed in systems that are smaller than galaxy clusters, such as galaxy groups (Sancisi et al. 1987, Baldi et al. 2009, Randall et al. 2011, Werner et al. 2019, Eckert et al. 2021) and remnants of galaxy mergers (Heckman et al. 1986, Merritt & Ekers 2002, Ivison et al. 2012, Shabala et al. 2017). More surprisingly, they have also been observed in disc galaxies (Ledlow et al. 2001, Singh et al. 2015, Nesvadba et al. 2021, Webster et al. 2021) and dwarf galaxies (Pakull et al. 2010, Mezcua et al. 2019, Yang et al. 2020, Davis et al. 2022), indicating that

their effects may be widespread.

1.2.3 The theory of accretion

In order to extract energy from matter near a supermassive black hole, the matter must first reach very close to it. The question of how black holes accrete is thus critical. The simplest accretion model is that of Bondi-Hoyle-Lytetton accretion (BHL hereafter; Bondi & Hoyle 1944, Bondi 1952a). This solution describes spherical, initially subsonic accretion of homogenous gas without angular momentum, under the influence of the black hole's gravity, which radially pulls the gas inwards. It is thought to approximately describe not just accretion onto supermassive black holes, but also stellar-mass black holes, protostars and protoplanets. The accretion rate in the BHL solution is given by

$$\dot{M}_{\rm BHL} = 4\pi \frac{G^2 M_{\rm BH}^2 \rho}{(c_{\rm s}^2 + v^2)^{3/2}}, \tag{1.1}$$

where $M_{\rm BH}$ is the black hole mass, ρ and $c_{\rm s}$ the density and sound speed of the ambient medium (at infinity) and v the velocity of the BH relative to the gas.

The main unrealistic assumption made in deriving the BHL accretion rate is that gas has no angular momentum. In reality, we always expect gas to have some finite angular momentum, so the flow must circularize at some radius. Extensions have been made to the BHL rate, that take into account both the gas' vorticity (angular momentum), as well as the fact that it can be clumpy, supersonic and turbulent (Krumholz et al. 2005, Krumholz et al. 2006). However, qualitatively, the behaviour of the solution is similar to the BHL one. The BHL solution, or its extensions, cannot explain quasars. The main reason is that the dynamical time-scale of accretion, at a given radius, is much too short compared to the cooling time-scale. Another issue is that gas needs to be viscously heated to radiate sufficiently, but the heating rate is very low if one assumes only atomic interactions.

Shakura & Sunyaev (1973), however, found a solution that can describe well observations of quasars, and that is to this day used in many AGN models. In this solution, which describes the so-called 'standard accretion disc', the source of

viscosity is not explicitly derived. Instead, the kinematic viscosity ν is set equal to $\nu = \alpha c_{\rm s} H$, $c_{\rm s}$ is the sound speed at a given radius within the disc, and H the radius-dependant scale height of the disc. α is a numerical constant, typically taken to be of order 0.1, which parametrizes the model. The model is therefore often referred to as the '$\alpha-$disc'. Note that while the source of viscosity is not explicitly explained in this model, it is thought to be caused by large-scale magnetic fields that permeate the accretion disc.

In the Shakura & Sunyaev (1973) disc (or its relativistic, spinning counterpart: Novikov & Thorne 1973), the accretion disc is thin ($H/R \approx 0.001 - 0.01$) and dense, and has a short cooling time. The radial velocity is very small compared to the Keplerian velocity $v_{\rm r} \approx \alpha(H/R)v_{\rm K}$, while the orbital velocity is essentially Keplerian. Thus, the gas has enough time to radiate away all of the heat generated by viscous stresses. As the gas loses energy, it falls towards smaller radii, but it does so over many Keplerian orbits. The amount of energy radiated by the gas can be obtained by comparing its total energy at infinity and that at some inner radius $R_{\rm in}$. This is the radius at which orbits are no longer circular and stable, and within which the gas falls into the black hole rapidly (before the gas has time to radiate away its internal energy). Such a radius, usually referred to as the innermost stable circular orbit (ISCO), is predicted to exist by Einstein's theory of general relativity. Specifically, both the solution for a non-spinning (Schwarzschild 1916) and a spinning black hole (Kerr 1963) predict the existence of such a radius.

For a non-spinning black hole, $R_{\rm ISCO} = 6R_{\rm G}$, where $R_{\rm G}$ is the gravitational radius of the black hole, given by $R_{\rm G} = M_{\rm BH}G/c^2$, G and c being Newton's gravitational constant and the speed of light, respectively. For a spinning black hole, $R_{\rm ISCO}$ varies with the dimensionless spin parameter $a = J_{\rm BH}c/M_{\rm BH}^2 G$, where $J_{\rm BH}$ is the angular momentum of the BH. Spin can theoretically be in the range $a \in [-1, 1]$, where negative signs indicate retrograde accretion (of matter that is counteraligned relative to the BH's spin axis). In reality, however, spin is thought to have an effective upper limit of $a_{\rm max} \approx 0.998$ due to effects of photon emission (Thorne 1974). The expression for $r_{\rm ISCO}$ ($R_{\rm ISCO}/R_{\rm G}$) as a function of spin is given in Appendix 2.A (in Chapter 2). We also give an expression for the specific angular momentum

at $r_{\rm ISCO}$. Here we give the expression for the radiative efficiency (defined as $\epsilon_{\rm r} = L_{\rm bol}/\dot{M}_{\rm BH,acc}c^2$, where $\dot{M}_{\rm BH,acc}$ is the net accretion rate though the BH event horizon) of the thin disc:

$$\epsilon_{\rm r}(a) = 1 - e_{\rm ISCO}(a) = 1 - \sqrt{1 - \frac{2}{3r_{\rm ISCO}(a)}}, \tag{1.2}$$

where $e_{\rm ISCO}$ is the specific binding energy at $r_{\rm ISCO}$ in units of c^2. The radiative efficiency for the case of zero spin is $\epsilon_{\rm r} \approx 5\%$, while the variation across the $a \in [-0.998, 0.998]$ range is monotonic and spans $\epsilon_{\rm r} \in [4\%, 32\%]$. Such high radiative efficiencies can readily explain observations of quasars, and more generally, bright AGN.

The feedback on galaxies from thin accretion discs surrounding SMBHs can occur through several mechanisms, including: 1) direct radiative heating of gas on galaxy scales (e.g. Choi et al. 2012), 2) the launching of a wind on the scale of the accretion disc as a result of magnetic fields or radiation pressure on gas (e.g. Nomura et al. 2016, Fiore et al. 2017, Mizumoto et al. 2021, Quera-Bofarull et al. 2023), 3) the launching of a wind on galaxy scales as a result of radiation pressure on dust (e.g. Pier & Krolik 1992).

Observations of radio galaxies require further consideration, as the existence of jets is not explained by the above models. Observations have found that galaxies exhibiting radio jets or lobes predominantly host dormant AGN, that are quite massive but not very bright (e.g. Heckman & Best 2014). These AGN clearly cannot be described by the standard, thin accretion disc solution. Narayan & Yi (1994) found the solution for a hot accretion flow, which is essentially the extension of a BHL-like flow from large scales down to the event horizon (see also the general-relativistic counterpart). In this solution, both radial and orbital velocities are significant fractions of the Keplerian value. The accretion flow is geometrically thick ($H/R \approx 0.5$, we will thus refer to it as the 'thick disc') and optically thin. It is diffuse, with most of the internal energy advected inwards before it has time to radiate away. The radiative efficiency of the disc is thus low.

The thick accretion disc appears at low (dimensionless) accretion rates corre-

sponding to Eddington ratios of $f_{\rm Edd,0} = \dot{M}_{\rm BH,acc,0}/\dot{M}_{\rm Edd} \lesssim 0.01$, where the Eddington accretion rate is given by

$$\dot{M}_{\rm Edd} = \frac{L_{\rm Edd}}{\epsilon_{\rm r} c^2} = 4\pi \frac{G M_{\rm BH} m_{\rm p}}{\epsilon_{\rm r} \sigma_{\rm T} c}. \tag{1.3}$$

Here, $m_{\rm p}$ is the proton mass, $\sigma_{\rm T}$ the Thomson cross-section and $\epsilon_{\rm r}$ the spin-dependent radiative efficiency of the thin accretion disc (see § 1.2.3). $\dot{M}_{\rm BH,acc,0}$ is the large-scale accretion rate onto the SMBH (before the matter settles down to an accretion disc, this may be given by e.g. the BHL rate). As we will discuss in the next subsection, the generation of very efficient AGN jets can readily occur in the thick disc due to a combination of a magnetic dynamo and advection of magnetic fields. Since observations find most radio jets to be hosted by black holes accreting with low accretion rates, this accretion regime appears to be a compelling explanation (McNamara & Nulsen 2012). In addition to jets, energetically weaker winds are expected to be launched from these accretion disc winds, and they probably take away the vast majority of the accreting mass (Begelman 2012).

The vast majority of black holes in the local Universe, as well as at higher redshifts, are thought to be in either the thin or thick accretion regime (Weinberger et al. 2017a). However, for some black holes, at certain times it is possible that accretion proceeds at super-Eddington rates (e.g. as a result of a galaxy merger, or for black holes hosted by protoclusters at very high redshifts). At super-Eddington rates, the slim disc solution is valid (Wang & Zhou 1999). This accretion regime is largely similar to the thick disc, so it may also launch strong jets (see next subsection), with the main difference being that radiation pressure is dominant over gas pressure. As a result, disc winds are also expected from the slim disc.

1.2.4 The theory of active galactic nuclei jet launching

According to the model of Blandford & Znajek (1977) (BZ), magnetic fields present due to an accretion disc plunge into the SMBH's ergosphere and corotate due to the frame dragging of space-time caused by the rotation of a black hole. This results in a net outward flux of energy and angular momentum. The power of the jet that

is launched in the BZ process scales as $P_{\rm jet} \propto \Omega_{\rm H}^2 \Phi_{\rm H}^2$ at low BH spin, where $\Omega_{\rm H}$ is the angular velocity of the event horizon, and $\Phi_{\rm H}$ is the net poloidal magnetic flux threading the horizon. The largest source of uncertainty in modeling jet powers comes from the strength of the magnetic field, which determines the flux $\Phi_{\rm H}$.

In the last two decades, general-relativistic magneto-hydrodynamical (GRMHD) simulations of thick discs have been performed (Narayan et al. 2003, Tchekhovskoy et al. 2010, McKinney et al. 2012), largely finding good qualitative agreement with the analytical solution of Narayan & Yi (1994). However, provided that the simulations are run for a significantly long time, the disc settles down to the equilibrium magnetically-arrested disc state (MAD, Narayan et al. 2003), in which the magnetic field near the BH horizon has reached its maximal steady-state value. The large poloidal magnetic field in the central regions of the disc 'chokes' the inward flow, causing the accretion to proceed in discrete blobs (or thin streams at very high resolution, see Ripperda et al. 2022). This configuration results from a strong dynamo effected, which boosts the poloidal magnetic field component even if only a toroidal one is initially present, coupled with advection of magnetic fields towards the centre alongside the advection of gas.

Simulations of the jet launching process in MAD systems have converged in terms of how much energy the jets extract from the SMBH (e.g. Tchekhovskoy et al. 2011, McKinney et al. 2012, Sadowski et al. 2014, Liska et al. 2020, Narayan et al. 2022). Recent observational estimates of the magnetic field in the thick disc surrounding the central SMBHs in M87 and our own galaxy confirm this (Event Horizon Telescope Collaboration et al. 2021). High-resolution and long-duration simulations have found that the MAD state is achieved even without any initial poloidal magnetic field, bolstering the theoretical expectation that all thick discs should be MAD (Liska et al. 2020). Simulations of thinner accretion discs have also found that the MAD state can be achieved in those systems (Liska et al. 2019), and the jet powers are then much higher than classically expected (Meier 2002). It is not clear, however, if the MAD state is readily reached for thin discs in reality. Slim discs, on the other hand, readily form jets, similar to the thick disc (Ricarte et al. 2023).

The jet power in the MAD state is proportional to the accretion rate and scales with BH spin roughly as $P_{\rm j} \propto a^2$, with an even steeper dependence at high (magnitudes of) spin. At $a = 0.5$, the jet efficiency is ≈ 30 per cent, while at $a = 1$, it is around 200 per cent (indicating a net decrease in the total mass-energy). The jet powers at $a < 0$ are lower than at $a > 0$, with the efficiencies never exceeding 100 per cent. In addition to the energy tapping, the jets also tap the angular momentum of the BH very efficiently, causing strong spindown. This is an effect that has historically not often been included in models (e.g. Fanidakis et al. 2011, Griffin et al. 2019), but it is crucial.

1.3 Simulating galaxy formation and evolution with AGN jet feedback

1.3.1 The need for AGN feedback in models

Around the turn of the millennium, X-ray observations of galaxy clusters showed that AGN feedback is likely preventing massive cooling flows from developing and causing the central galaxies to be extremely star-forming, as we discussed in § 1.2.2. Semi-analytical models of galaxy formation and evolution had been struggling up to this point with reproducing the bright end of galaxy luminosity functions: there were too many bright galaxies predicted when modern values of the cosmic baryon fraction were used (e.g. Somerville & Primack 1999, Benson et al. 2003). However, motivated by observations, semi-analytical models began incorporating AGN feedback. As was shown by e.g. Bower et al. (2006) and Croton et al. 2006 the bright end of the luminosity function can be reproduced if gas cooling in massive haloes is offset due to some heating source (assumed to be radio jets). Since then, nearly all semi-analytical models have been including the effects of AGN (e.g. Henriques et al. 2015, Lagos et al. 2018).

1.3.2 AGN feedback and jets in cosmological hydrodynamical simulations of galaxy formation and evolution

While semi-analytical models first included the effects of radio jets, AGN feedback also began to be included into hydrodynamical simulations of galaxies in the form of thermal isotropic heating of gas using a constant feedback efficiency (Springel 2005, Booth & Schaye 2009), intended to represent the effects of isotropic quasar winds. This choice was motivated largely by the fact that most growth of black holes occurs in the thin disc regime (where such feedback is appropriate), and that the radiative efficiency does not depend much on spin (unlike the jet efficiency). Furthermore, since the feedback is assumed to be isotropic, there is no need to track black hole spin. In reality, however, even quasar feedback is probably more complex than was assumed, with there being a strong dependence of the feedback efficiency on the (dimensionless) black hole accretion rate (e.g. Nomura et al. 2016, Quera-Bofarull et al. 2023), as well as some directionality that depends on black hole spin.

The first two successful large-scale hydrodynamical cosmological simulations of galaxy formation were Illustris (Vogelsberger et al. 2014) and EAGLE (Schaye et al. 2015). Both used thermal isotropic feedback (representing quasar feedback) at moderate Eddington ratios, with EAGLE employing it at all Eddington ratios, and Illustris only at higher Eddington ratios ($f_{\rm Edd,0} > 0.01$). At low Eddington ratios, in Illustris the effects of AGN jets were included by manual placement of hot bubbles of gas outside galaxies (see Sijacki et al. 2007). In recent years, hydrodynamical models have begun to incorporate explicit jet feedback (e.g. SIMBA: Davé et al. 2019, HorizonAGN: Dubois et al. 2014b, New-Horizon: Dubois et al. 2021).

The above simulations model jet feedback by kicking gas particles or cells close to the SMBH by velocities of order 10^4 km/s. The numerical resolution that can be achieved in such cosmological simulations is often thought to be insufficient to fully capture the impact of the jets (Bourne & Sijacki 2017, Weinberger et al. 2017b). In particular, low resolution simulations do not display instabilities in the jets, which could be important for their evolution and energetics (Perucho et al. 2006, Perucho et al. 2010). Recently, there has been considerable effort at including AGN jets in

a realistic manner, by modeling the evolution of BH spin (e.g. Dubois et al. 2014a, Fiacconi et al. 2018, Talbot et al. 2020). The inclusion of BH spin has a significant impact on AGN jet feedback by providing a direction, as well as a variable jet efficiency.

1.3.3 The potential benefits of including jets from AGN

The EAGLE galaxy formation model (Schaye et al. 2015, Crain et al. 2015) is based on the Booth & Schaye (2009) AGN feedback scheme developed for the OWLS simulations (Schaye et al. 2010). The EAGLE simulations used a fairly simple AGN feedback prescription: thermal isotropic feedback representing AGN-driven winds, using a constant feedback efficiency. Despite the simplicity, the model correctly predicted the number of galaxies as a function of mass (as measured through the stellar mass function or the stellar mass-halo mass relation; Schaye et al. 2015) and redshift (Furlong et al. 2015) as well as many galaxy properties (e.g. the metallicities and sizes; Schaye et al. 2015, molecular gas content; Lagos et al. 2015, and colours; Trayford et al. 2017).

The Hydrangea simulations used the EAGLE model to evolve a sample of galaxy clusters (Bahé et al. 2017a). Despite the EAGLE model working well for the overall population of galaxies, these simulations found that BCGs were too massive, from about a factor of two for low-mass clusters (halo masses of order 10^{14} $M_{\odot}$) to a factor of nearly ten for high-mass clusters (halo masses of order 10^{15} $M_{\odot}$). The same galaxies were also found to be too highly star-forming compared to observations. This problem possibly originates from overly strong cooling flows in the simulations, which could be a consequence of insufficient heating by thermal isotropic AGN feedback at large radii (e.g. > 100 kpc).

The C-EAGLE project (Barnes et al. 2017) also used the EAGLE model to simulate a broadened sample (relative to Hydrangea) of galaxy clusters. Mock X-ray observations (Barnes et al. 2017) showed that these clusters appear to have central entropies of the ICM that are too high (a problem confirmed by Altamura et al. 2023 on a separate sample of galaxy groups and clusters, using an updated version of the EAGLE model). This is also true for the temperature, and the reverse

is true for the density. A related problem is in the cool-core (CC) versus non-cool-core (NCC) dichotomy of clusters (e.g. Hudson et al. 2010): simulated clusters are likely too often NCC as compared to observed ones (the fraction of CC clusters is too low), although firm conclusions on this are complicated by varying definitions in the literature of what is a CC versus a NCC cluster (Barnes et al. 2018).

Including a more realistic feedback mechanism (representing the effects of relativistic jets) may be helpful in reproducing the observed entropy profiles in galaxy clusters, presumably by allowing more effective coupling of the feedback energy to larger radii instead of only to the core of the ICM. A similar modification may be beneficial in the IllustrisTNG model (see e.g. the results of the MillenniumTNG simulations, Pakmor et al. 2022). This is despite that model using kinetic feedback at low accretion rates (alongside thermal isotropic feedback at high accretion rates), and the reason may be that the feedback mechanism is also isotropic. As we will show in this thesis, kinetic isotropic and thermal isotropic feedback are fairly similar in their effects, at least in the context of idealized cluster simulations. The potential problems we have discussed may be present even for the SIMBA simulations (Davé et al. 2019), which also show somewhat too high entropies, albeit at intermediate radii rather than in the core of the ICM (Oppenheimer et al. 2021). While SIMBA includes AGN jets, they are launched in the direction of the angular momentum of the gas near the BH, which may not be very stable (especially in clusters and at low resolutions). As we will show in this thesis, the jet direction needs to be relatively stable for the jets to lead to significant differences compared to isotropic feedback.

1.3.4 Idealized simulations of AGN jets

In order to understand and model the effects of AGN jets in simulations of galaxy formation and evolution, it is important to perform more controlled, idealized simulations. This may be either idealized simulations of single episodes of injection (typically over a particular time with a constant jet power), or simulations where a single black hole does self-consistent feedback by accreting based on some accretion rate formula (e.g. the BHL rate) and producing feedback with some efficiency as a result. In either case, the focus is on the evolution of single systems, rather than a

population. These simulations may sometimes be zoom-in cosmological simulations of a particular object (e.g. Dubois et al. 2010, Bourne & Sijacki 2020), but are more typically idealized simulations where an object (e.g. a galaxy or intracluster medium of an idealized galaxy cluster) is set up in advance.

Early idealised simulations of single-episode AGN jet feedback often circumvented highly uncertain physics of jet launching, and instead manually placed bubbles of hot gas into the ICM (Churazov et al. 2001, Brüggen et al. 2002, Reynolds et al. 2006, Pavlovski et al. 2008, Sternberg & Soker 2008). The bubbles were then studied as they interacted with and rose through the ICM on account of buoyancy. More recent simulations of single-episode jet feedback have focused mostly on the active phase of the jets (although note that such simulations were already being performed in the 1990s, e.g. Falle 1991, Komissarov & Falle 1998). This has been possible due to significant improvements in the reliability of such simulations, which are a result of our better understanding of jet physics and numerical modeling, as well as improved computational capabilities. Such simulations may include only hydrodynamical aspects of the jets (e.g. Komissarov & Falle 1998, Hardcastle & Krause 2013, Horton et al. 2020). However, other aspects are often included, such as: relativistic physics (e.g. Walg et al. 2013, English et al. 2016, Choi 2017), magnetic fields (e.g. Hardcastle & Krause 2014, Tchekhovskoy & Bromberg 2016, Mukherjee et al. 2020), radiative cooling (e.g. Blondin et al. 1990, Stone et al. 1997, Guo et al. 2018) or cosmic rays (e.g. Guo & Mathews 2011, Ehlert et al. 2018, Yang et al. 2019). In Fig. 1.2 we show the schematic reprensentation (adopted from Bourne & Sijacki 2017) of supersonic jets interacting with the ambient medium (the ICM inside a galaxy cluster), as often seen in these idealized simulations. The jet is shocked at the jet head, where it causes a bow shock to propagate into the ambient medium, and the shocked jet material is displaced sideways or may even flow backwards (i.e. the backflow), forming a hot diffuse lobe (or cocoon).

The main focus of the above studies is often the jet energetics, i.e. how much energy is transferred to the ICM, where, how quickly and in what form (Morsony et al. 2010, Bourne & Sijacki 2017, Weinberger et al. 2017b, Bourne et al. 2019), as well as by what means (Perucho et al. 2010, Bambic & Reynolds 2019, Yang et al.

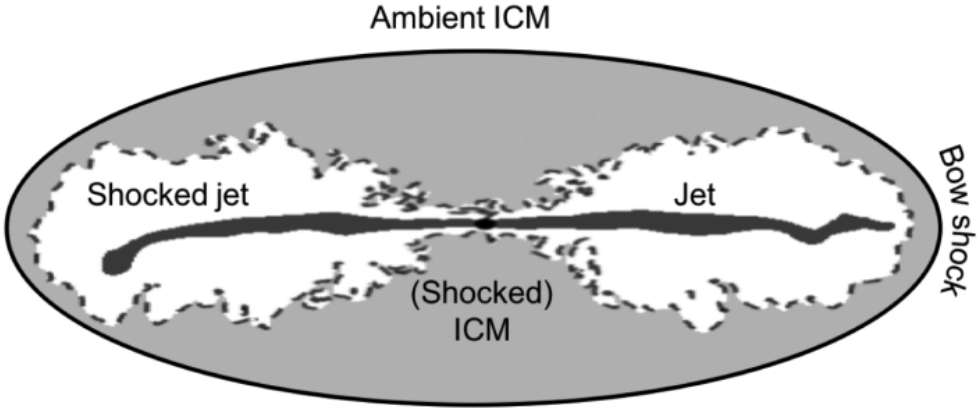

Figure 1.2: Schematic of jets interacting with the ambient medium (the ICM in a galaxy cluster), adopted from Bourne & Sijacki (2017). This shows the main features of such interactions: 1) the unshocked, fast-moving jet, 2) shocked jet material forming a lobe/cocoon and 3) the bow shock propagating into the ambient medium.

2019, Wang & Yang 2022). For our purposes, the main conclusion from most of these simulations is that jets effectively transfer their energy to the ambient medium (of order half the jet energy ends up in the ambient medium while the jet is active, and more soon after it is shut off). This energy injection is not only in the direction of the jets, but is somewhat more isotropic, since the transferral of the energy is mostly done through the bow shock (if the jets are strongly supersonic relative to the ambient medium).

The second category of interest is that of idealized jet simulations, with self-consistent accretion and where a central SMBH launches jets based on an accretion rate determined from gas properties near the SMBH. These simulations almost exclusively use adaptive mesh refinement (AMR), with spatial resolutions typically reaching $200-500$ pc (e.g. Gaspari et al. 2011, Li et al. 2015, Beckmann et al. 2019) in the centres of the simulated systems. The jet velocities used are of order 10^4 $\mathrm{km s^{-1}}$ (e.g. Gaspari et al. 2011, Yang & Reynolds 2016, Meece et al. 2017), and the jet efficiencies ϵ_j (related to the jet power P_j and SMBH accretion rate $\dot{M}_\mathrm{BH}$ through $\epsilon_\mathrm{j} = P_\mathrm{j}/\dot{M}_\mathrm{BH,acc}c^2$) are typically low, in the range $\epsilon_\mathrm{j} = 10^{-4}-10^{-2}$ (e.g. Gaspari et al. 2012, Yang & Reynolds 2016, Martizzi et al. 2019). The jets are usually launched in a fixed direction, but some studies have included precession imposed by hand

(e.g. Li et al. 2017, Meece et al. 2017). The jet powers achieved in these simulations are in the range $P_{\rm j} = 10^{45} - 10^{46}$ ergs^{-1} (e.g. Yang & Reynolds 2016, Li et al. 2017, Martin et al. 2019). The cold gas masses found in these simulations are often fairly large, $M_{\rm cold} = 10^{10} - 10^{11}$ M$_\odot$ or larger (e.g. Li & Bryan 2014a), probably due to low jet efficiencies. It is considerably harder to find common predictions among these simulations, since they may differ in many details. Broadly speaking, however, these simulations show that AGN jet feedback can successfully quench cooling flows in most galaxy clusters, with a broad range of AGN jet parameters. Massive galaxy clusters (with a DM halo mass of $\geq 10^{15}$ M$_\odot$) are, however, typically difficult to completely quench in such simulations.

1.4 Overview of the thesis

In this thesis, our aim is to develop and test a model for black hole spin evolution and AGN jet feedback, for use in cosmological hydrodynamical simulations of galaxy formation and evolution. In particular, we tailor our model to be used in successors of the EAGLE simulations. In Chapter 2 we present our model in full detail. In Chapter 3, we perform simple hydrodynamical tests of constant-power jets, for the first time ever in a smoothed particle hydrodynamics (SPH) code. In Chapter 4 we extend such simulations to more complex and realistic external media (a hydrostatic halo held in equilibrium by gravity), and focus on late-time evolution, and thus the interaction of the AGN-inflated lobes and bubbles with the ambient medium. In Chapters 5-6 we test our spin and jet feedback model in an idealized galaxy cluster, with self-consistent BH feeding and feedback. In Chapter 5 we focus on purely jet feedback, while in Chapter 6 we perform a thorough comparison with wind (thermal isotropic) feedback. In Chapter 7 we summarize and conclude.

CHAPTER 2

A hybrid black hole accretion and feedback model

2.1 Summary of the model

The EAGLE simulations used an AGN feedback model in which 10 per cent of the accreting mass-energy onto SMBHs was released as radiation, and a further 10 per cent of this radiative energy coupled to the gas near the SMBHs in the simulation as feedback energy (Schaye et al. 2015). Thus, 1 per cent of the mass-energy accreting onto SMBHs was released as feedback energy, injected into surrounding gas isotropically and in thermal form. In the BH growth and feedback model that we present here, we make two significant modifications relative to the fiducial EAGLE AGN model: 1) the introduction of BH spin and 2) the inclusion of an additional AGN feedback mode in the form of kinetic jets (alongside thermal isotropic feedback, representing the effects of winds that are shocked on subgrid scales). Modeling BH spin is necessary for the realistic inclusion of AGN jets, since jet directions and powers depend on BH spin (e.g. Tchekhovskoy et al. 2010).

In order to model BH spin in cosmological simulations, one needs to also assume subgrid models for accretion disc physics (Dubois et al. 2012, Fiacconi et al. 2018). Different accretion disc types need to be assumed at different accretion rates

(Eddington ratios) in order to model spin realistically. At the same time, different accretion discs are thought to lead to different forms of feedback. We assume different accretion states depending on the Eddington ratio, which we define as for this purpose as

$$f_{\rm Edd,0} = \frac{\dot{M}_{\rm BH,acc,0}}{\dot{M}_{\rm Edd}}. \tag{2.1}$$

Here, $\dot{M}_{\rm BH,acc,0}$ is the large-scale accretion rate, $\dot{M}_{\rm BH,acc,0}$. For most of the thesis, however, we use the Eddington ratio $f_{\rm Edd}$ defined in the same way, but with the large-scale accretion rate $\dot{M}_{\rm BH,acc,0}$ replaced by the net accretion rate onto the BH, $\dot{M}_{\rm BH,acc}$ (see the next subsection for subtleties associated with this difference). Note also that we use the spin-dependent Eddington accretion rate $\dot{M}_{\rm Edd}$ (see previous chapter) to define the Eddington ratio.

Our accretion disc model is illustrated schematically in Fig. 2.1, adopted from Müller (2004). The three accretion disc types we include in the model are as follows:

1. **Thick disc** at Eddington ratios $f_{\rm Edd,0} < 0.01$. This accretion flow is also known as the advection-dominated accretion flow (ADAF), hot accretion flow, RIAF (radiatively inefficient accretion flow), the hard state (in terms of X-ray spectra) and the low state (in terms of accretion rate). The disc is geometrically thick ($H/R \approx 0.5$) and optically thin. The gas in this disc is very hot and features advection which traps in most of the radiation, resulting in low luminosities. Gas orbits are not fully circular and instead have a significant radial component. The gas flow is continuous all the way down to the event horizon, with no abrupt change in properties at the innermost stable circular orbit ($R_{\rm ISCO}$). The poloidal magnetic flux at the event horizon of the black hole is very large, leading to strong jets. We take the solution for this disc from Narayan & Yi (1995).

2. **Thin disc** at Eddington ratios $0.01 < f_{\rm Edd,0} < 1$. This accretion disc is also known as the radiatively efficient, standard or Shakura-Sunyaev disc (SSD), as well as the soft or high state. The disc is geometrically thin (usually $H/R \in [0.001, 0.01]$) and optically thick, with a high radiative efficiency of order ≈ 10 per cent. Gas orbits are almost fully circular and extend down to $R_{\rm ISCO}$.

Within this inner radius, the orbits quickly become unstable. Jets are likely present, but their strength is not yet well constrained by either simulations or observations. This state is the one which was effectively assumed for all black holes in the EAGLE simulation (Schaye et al. 2015). We take the solution for this disc from Shakura & Sunyaev (1973).

3. **Slim disc** at Eddington ratios $f_{\rm Edd,0} > 1$. This accretion flow appears in the super-Eddington regime of accretion. The disc is geometrically fairly thick (H/R of order 0.1 to 0.5), but less so than the thick disc. It shares some features with both the thick and thin disc: it is both advection-dominated and radiatively efficient. It launches strong jets as well as being luminous (the efficiencies for jets and radiation are lower than in the thick and thin disc, respectively, but the accretion rate is higher, resulting in potentially higher jet powers and luminosities). We take the solution for this disc from Wang & Zhou (1999).

The modelling of accretion discs is highly dependent on assumptions about the kinematic viscosity ν in the discs, whose properties are largely unknown. All of the above models are so-called $\alpha-$discs, where α is a numerical parameter that is related to the kinematic viscosity ν through $\nu = \alpha c_{\rm s} H$. Here, $c_{\rm s}$ and H are the sound speed and height of the disc at a given radius, respectively. In the $\alpha-$disc models, α does not vary with radius, but is instead given by a constant value. We discuss our choice of α in § 2.3.

2.2 Black hole accretion rates

In many cosmological hydrodynamical simulations, including EAGLE, the BH growth and feedback model is agnostic to what occurs between the simulated scales, the accretion disc scales, and the very vicinity of the BH itself (the event horizon scale). In our model, we assume the existence of a subgrid accretion disc, as well as different feedback mechanisms. Unlike in the EAGLE model, the outflows can carry away so much mass that the net accretion rate close to the BH can be much less than that onto the accretion disc from larger scales. In addition, the outflows can

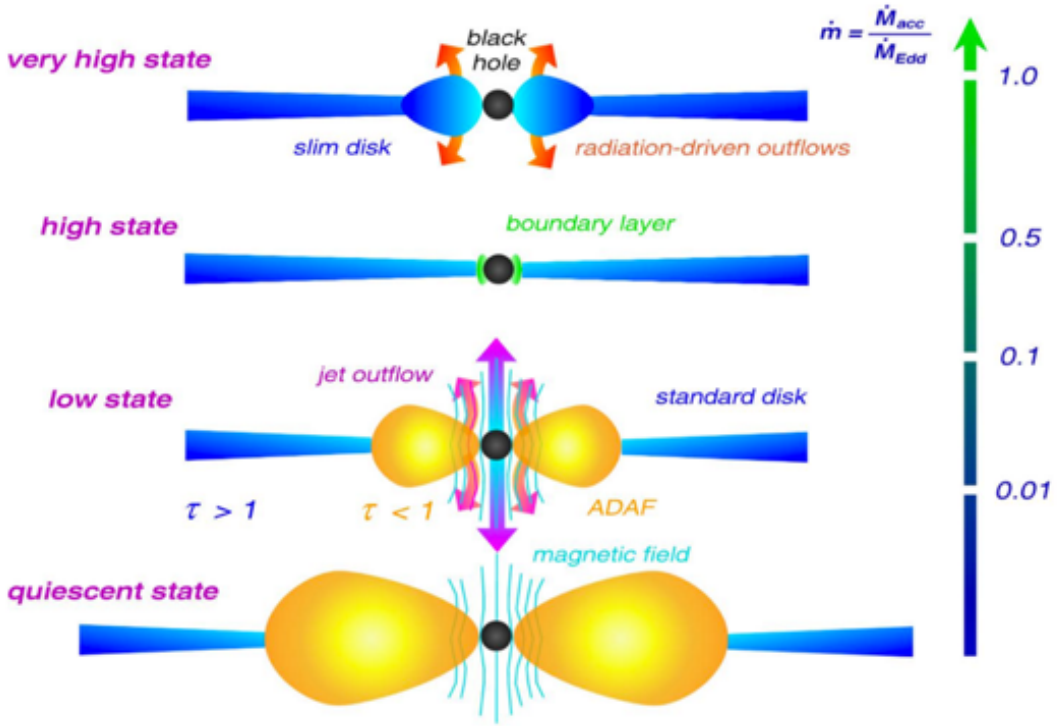

Figure 2.1: An illustration of our accretion disc model, adopted from Müller (2004). At low Eddington ratios ($f_{\rm Edd} < 0.01$), the accretion disc is largely thick and hot (the ADAF flow), with very little mass inflow, and most of the energy outflow taking the form of relativistic jets. At moderate accretion rates ($0.01 < f_{\rm Edd} < 1$), the accretion disc is thin and outflows are largely radiation-driven. At super-Eddington rates, the disc again becomes thick, and has both relativistic jets and disc-driven winds. We also include jets at moderate Eddington ratios, with their efficiency increasing sharply as the BH approaches and exceeds the Eddington rate.

be so energetic that there is net drop in BH mass as a result of accretion. These effects arise in the thick and slim disc, at very low and very high Eddington ratios, respectively.

Due to the above subtleties, we will, for clarity, refer to two different accretion rates in this Thesis. The first of the accretion rates is the large-scale one, $\dot{M}_{\rm BH,acc,0}$. This is the accretion rate onto a subgrid accretion disc that surrounds the BH, given by the BHL rate in this Thesis, but in general it may be given by other formulas (e.g. the torque-driven accretion rate as found by Hopkins & Quataert 2011).

The second accretion rate is $\dot{M}_{\rm BH,acc}$, the net accretion rate onto the BH horizon, i.e. the actual flow rate into the BH. This accretion rate is different from the large-scale one because the material accreting through the disc may be blown away by winds. This is a gradual process, so that the accretion rate actually depends on radius. At the final radius, the BH event horizon, the accretion rate onto the BH is smaller than the large-scale one by some efficiency factor. We may thus write $\dot{M}_{\rm BH,acc} = \epsilon_{\rm acc}\dot{M}_{\rm BH,acc,0}$, where $\epsilon_{\rm acc}$ is the accretion efficiency.

The actual change in BH mass is different from both of the above accretion rates. Given a large-scale accretion rate onto the accretion disc - BH system, $\dot{M}_{\rm BH,acc,0}$ (e.g. the BHL rate), the net change in BH mass is given by

$$\dot{M}_{\rm BH} = (1 - \epsilon_{\rm rad} - \epsilon_{\rm jet} - \epsilon_{\rm wind})\epsilon_{\rm acc}\dot{M}_{\rm BH,acc,0}. \tag{2.2}$$

Here, the efficiency terms are defined as $\epsilon_i = P_i/\dot{M}_{\rm BH,acc}c^2$, where P_i is the feedback power into a given channel i, and $\dot{M}_{\rm BH,acc} = \epsilon_{\rm acc}\dot{M}_{\rm BH,acc,0}$ is the net accretion rate onto the BH. Depending on the BH spin, the jet efficiency may be high enough that the net change in BH mass is negative, since the jets tap more energy out of the BH than is fed inwards by accretion.

Eqn. (2.2), as written in its current form, implies that all three processes (release of radiation, winds and jets) are independent of each other. In reality, the radiation and wind terms may be representing the same physical phenomenon, since radiation pressure is one of the ways of launching a wind. However, we keep all three terms separate, but with some caveats. We use the wind efficiency term $\epsilon_{\rm wind}$ to represent

the effects of winds (driven radiatively, thermally or through MHD effects) that are launched on the scale of the accretion disc. On the other hand, the radiative efficiency $\epsilon_{\rm rad}$ then represents all energy that is released from the disc in the form of radiation and which does not participate in the launching of a wind on the scales of the disc. It may, however, launch a wind on larger (e.g. galaxy) scales, as in the thin disc.

The feedback efficiencies are all calculated as functions of spin (Section 2.4), but the accretion efficiency may be either a constant parameter (with separate values of the thick and slim disc), or we may use a more complicated (and realistic) scaling relation (see Appendix 2.B), in which the accretion efficiency increases with the accretion rate.

2.3 The interchanging of accretion/feedback modes

The state of the accretion flow (thick, thin or slim disc) is assumed to depend on the dimensionless accretion rate, i.e. the Eddington ratio (which, to remind the reader, is defined using the large-scale accretion rate and the spin-dependent Eddington accretion rate). The transition between the thick (Narayan & Yi 1994) and thin (Shakura & Sunyaev 1973) discs should occur around $f_{\rm Edd,0} \approx \alpha^2$ (Narayan & Yi 1995). More recent calculations suggest that the properties of the thick disc already begin to change at $f_{\rm Edd} = 0.2\alpha^2$, and the transition appears to be complete by $f_{\rm Edd,0} = 0.7\alpha$ (Yuan & Narayan 2014). Between these two values, the disc takes on a transition state whose properties are not well understood. For conceivable values of α, which may be as low as 0.05 and as high as $0.1 - 0.4$ (King et al. 2007, Yuan & Narayan 2014), the transition state may occupy the range $0.001 - 0.3$ in $f_{\rm Edd,0}$. Observations of both X-ray binary spectra (Done et al. 2007) and AGN spectra (Noda & Done 2018) find this transition to occupy a narrower range of $f_{\rm Edd,0} = 0.01 - 0.03$. An analysis of the radiative and mechanical powers of AGN shows the transition to span the same range (Russell et al. 2013). We assume the lower end of this range to be the critical transition rate at which the two accretion states (the thin and thick disc) interchange; $f_{\rm Edd,0,crit} = 0.01$.

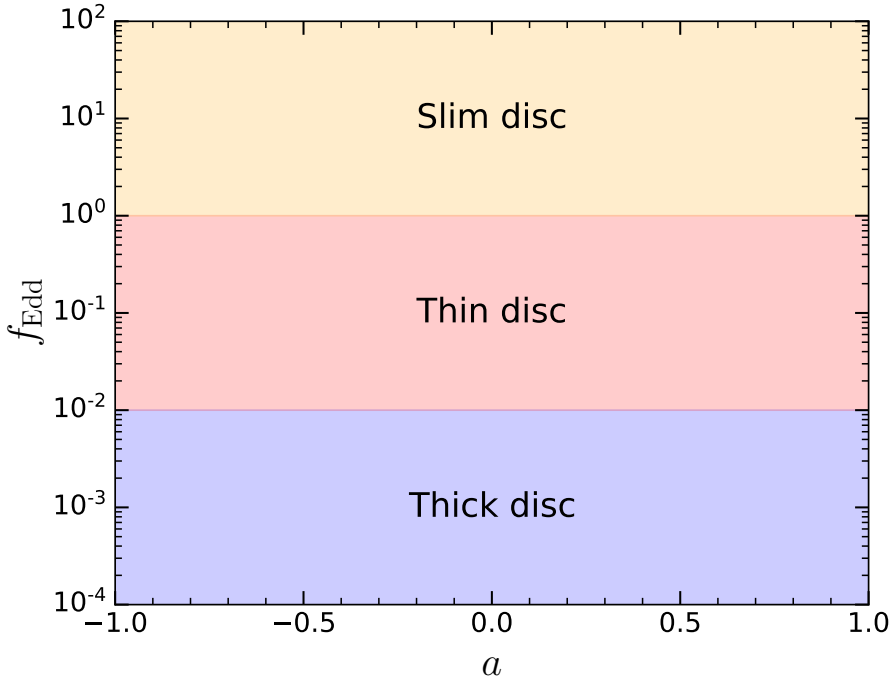

Figure 2.2: The state of the accretion disc that we assume in the model, depending on values of the BH spin parameter a and the Eddington ratio $f_{\rm Edd,0} = \dot{M}_{\rm BH,acc,0}/\dot{M}_{\rm Edd}$. Note that we use the large-scale accretion rate $\dot{M}_{\rm BH,acc,0}$ and not the net accretion rate $\dot{M}_{\rm BH}$ in this definition. The Eddington rate used in the definition is spin-dependent, due to a non-constant radiative efficiency.

Given this choice, we can set a value for the viscosity parameter α, which appears in many of the equations describing accretion disc structure that we will discuss. For this purpose we use the finding of numerical calculations that the transition spans the range between $0.2\alpha^2$ and 0.7α in $f_{\rm Edd,0}$ (Yuan & Narayan 2014). We assume that the geometric mean of these two boundaries corresponds to $f_{\rm Edd,crit,0} = 0.01$, which is true for $\alpha \approx 0.1$, so we set $\alpha = 0.1$ in this model.

We describe the accretion disc as slim (Wang & Zhou 1999) once the Eddington ratio $f_{\rm Edd,0} > 1$, i.e. once accretion is super-Eddington.

In Fig. 2.3 we show the dependence of the classification of accretion discs in our model on the BH spin parameter a and the Eddington ratio $f_{\rm Edd,0}$.

2.4 Feedback efficiencies

In this expanded model for AGN feedback we add a kinetic jet feedback mode, but we also modify the thermal isotropic feedback channel. In the fiducial EAGLE AGN model, the latter was used to represent the effects of kinetic winds that are driven radiatively and shocked on subgrid scales. The efficiency for this mode of feedback is given by $\epsilon_{\rm f}\epsilon_{\rm rad}$, where $\epsilon_{\rm rad}$ is the radiative efficiency (the fraction of accreting rest-mass energy released as radiation), which was taken to be constant and equal to 10 per cent in the EAGLE model. $\epsilon_{\rm f}$ is the coupling efficiency (also of order 10 per cent), which represents the fraction of the released radiation that efficiently couples to the gas, resulting in the launching of a kinetic wind.

The feedback efficiencies used in our model are shown in Fig. 2.3 and Fig.2.4. In the first figure we show the wind and jet efficiencies in separate panels, but different accretion regimes are shown in the same panels. In the second figure, we reverse that plotting strategy for clarity, and show separate panels for each accretion regime, but plot the wind and jet efficiencies in the same panels. In both figures, we show both linear and logarithmic versions of the panels for easier comparison between the different feedback modes.

In our model, at intermediate Eddington ratios that correspond to the thin disc ($0.01 < f_{\rm Edd,0} \lesssim 1$), we use the same formulation for radiatively-driven thin disc wind feedback, but we allow the radiative efficiency to depend on spin. We use the formula for a relativistic Keplerian accretion disc (Eqn. 1.2), which varies between $\epsilon_{\rm rad} \approx 4\%$ at $a = -0.998$ and $\epsilon_{\rm rad} \approx 30\%$ at $a = 0.998$. The total feedback efficiency (assuming $\epsilon_{\rm f} = 0.1$), is shown in Fig. 2.3 as the red line in the left-hand panel. The feedback efficiency varies from a nearly-constant 0.5 per cent at retrograde and mildly spinning prograde black holes ($a < 0.5$) to a maximum value of 3 per cent at $a = 0.998$, with a sharp increase beyond $a \approx 0.8 - 0.9$. As a comparison, the fiducial EAGLE model had a constant feedback efficiency of 1 per cent.

We also optionally implement winds in the thick and slim disc (using the same thermal isotropic feedback channel), but with different feedback efficiencies since

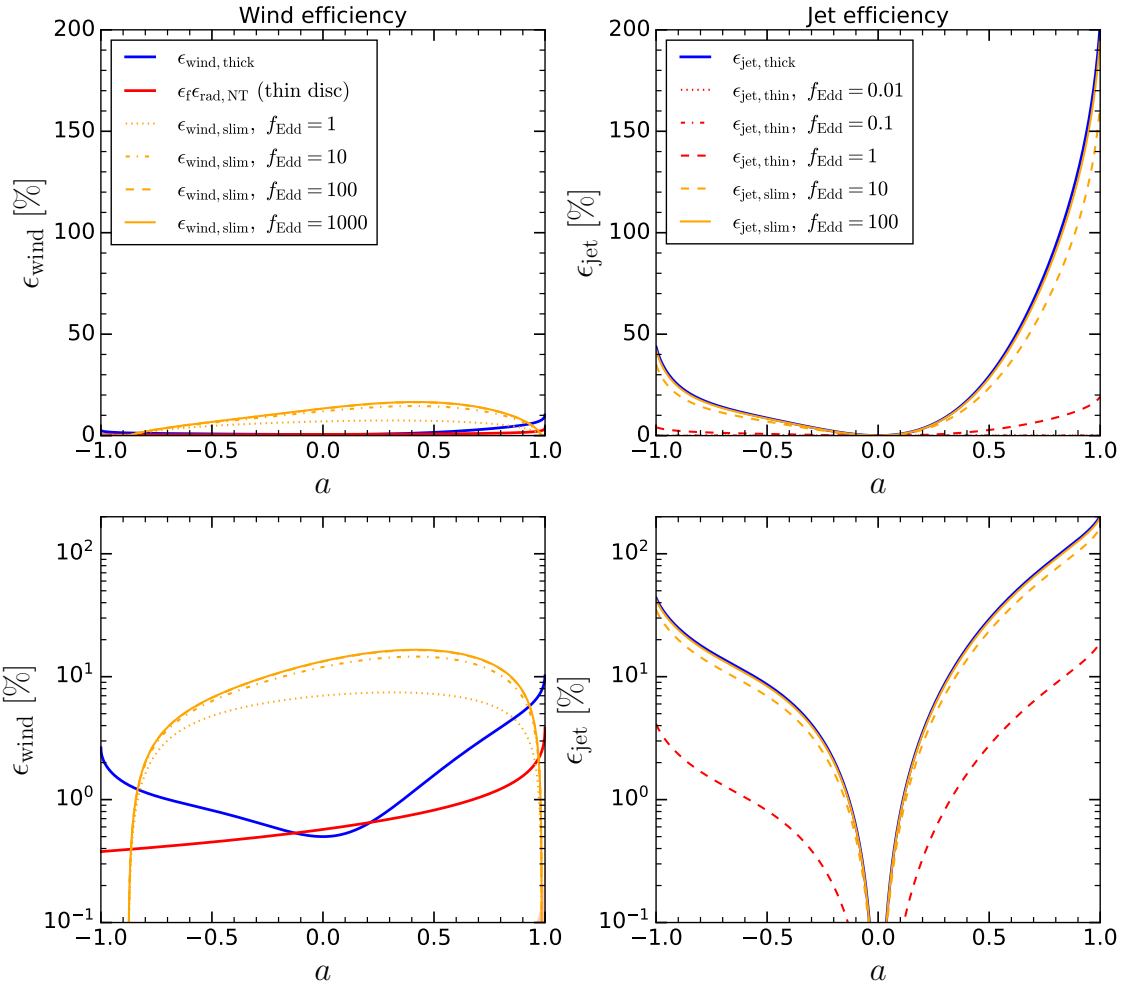

Figure 2.3: The feedback efficiencies used in the model. The top row shows the efficiencies on a linear scale, while the bottom row uses a logarithmic scale for the $y-$axis. The left-hand panels shows wind efficiencies, while the right-hand panels show jet efficiencies. The winds are implemented as thermal isotropic feedback, representing energy-driven winds shocked on subgrid scales. For thin discs, the radiative efficiency depends on spin and is given by Eqn. (1.2), and a fraction $\epsilon_{\rm f}$ (assumed to be 0.1 for this figure) of that couples to the gas to launch a wind (with a total efficiency given by the red line). The slim disc also launches winds, but with a much different dependence on spin (Eqn.2.5) due to additional MHD effects and an interaction of radiation with jets. The winds from the thick disc are launched on account of MHD effects and thermal pressure, with an efficiency given by Eqn. (2.3) and shown as the blue line. For the jet efficiency we use the same formula for all accretion regimes (Eqn. 2.7), with a fully-MAD value of dimensionless magnetic flux ϕ (Eqn.2.4) used for the thick disc, while for the thin and slim discs, ϕ is strongly dependent on the Eddington ratio $f_{\rm Edd}$ (Eqn. 2.6) and is much smaller than $\phi_{\rm MAD}$ unless the slim disc is strongly super-Eddington. Note the difference in the $y-$axis range compared to the left-hand panel.

these winds are of a different nature and launched in a different way. Note, however, that we assume that they are all energy-conserving and shocked on a subgrid scale (Costa et al. 2014). For the thick disc, we take results from general-relativistic magneto-hydrodynamical (GRMHD) simulations, which have converged in recent years and predict very similar properties for these discs (Tchekhovskoy et al. 2010, McKinney et al. 2012, Sadowski et al. 2013, Narayan et al. 2022). These all describe magnetically-arrested discs (MAD; Narayan et al. 2003) where the magnetic flux on the black hole horizon has saturated to some value that depends on spin.

In the thick disc, the same fraction of energy as that given by Eqn. (1.2) is released from accreting matter and ends up as heat in the system. While one may assume that all of it is advected inwards instead of released outwards, the aforementioned simulations find that these discs launch kinetic winds efficiently, on account of MHD effects and thermal pressure. We adopt the wind efficiency from Sadowski et al. (2013):

$$\epsilon_{\rm wind,thick}(a) = 0.005\left[1 + 0.3\left(\frac{\phi}{50}\right)\left(\frac{\Omega_{\rm H}}{0.2}\right)\right], \tag{2.3}$$

where $\phi = \Phi_{\rm H}/\sqrt{\dot{M}_{\rm BH,acc}R_{\rm G}^2 c}$ is the dimensionless magnetic flux threading the event horizon and $\Omega_{\rm H}$ the dimensionless angular velocity of the horizon, given by $\Omega_{\rm H} = a/2r_{\rm H}$, where $r_{\rm H} = 1 + \sqrt{1-a^2}$ is the dimensionless radius of the event horizon. For ϕ we adopt the expression as a function of spin from Narayan et al. 2022, which describes well all of these simulations:

$$\phi_{\rm MAD}(a) = -20.2a^3 - 14.9a^2 + 34a + 52.6. \tag{2.4}$$

The wind efficiency given by the above formulation is shown with a blue line in the left-hand panel of Fig. 2.3. It is at least as large as the wind one in the thin disc, and may be several times larger depending on the spin. Its effects are thus not negligible (although one needs to keep in mind that the accretion rates are lower in this mode than for the thin disc, as well as the fact that, unlike for the thin disc, we use an accretion efficiency for the thick disc, exactly because of the effects of these winds,

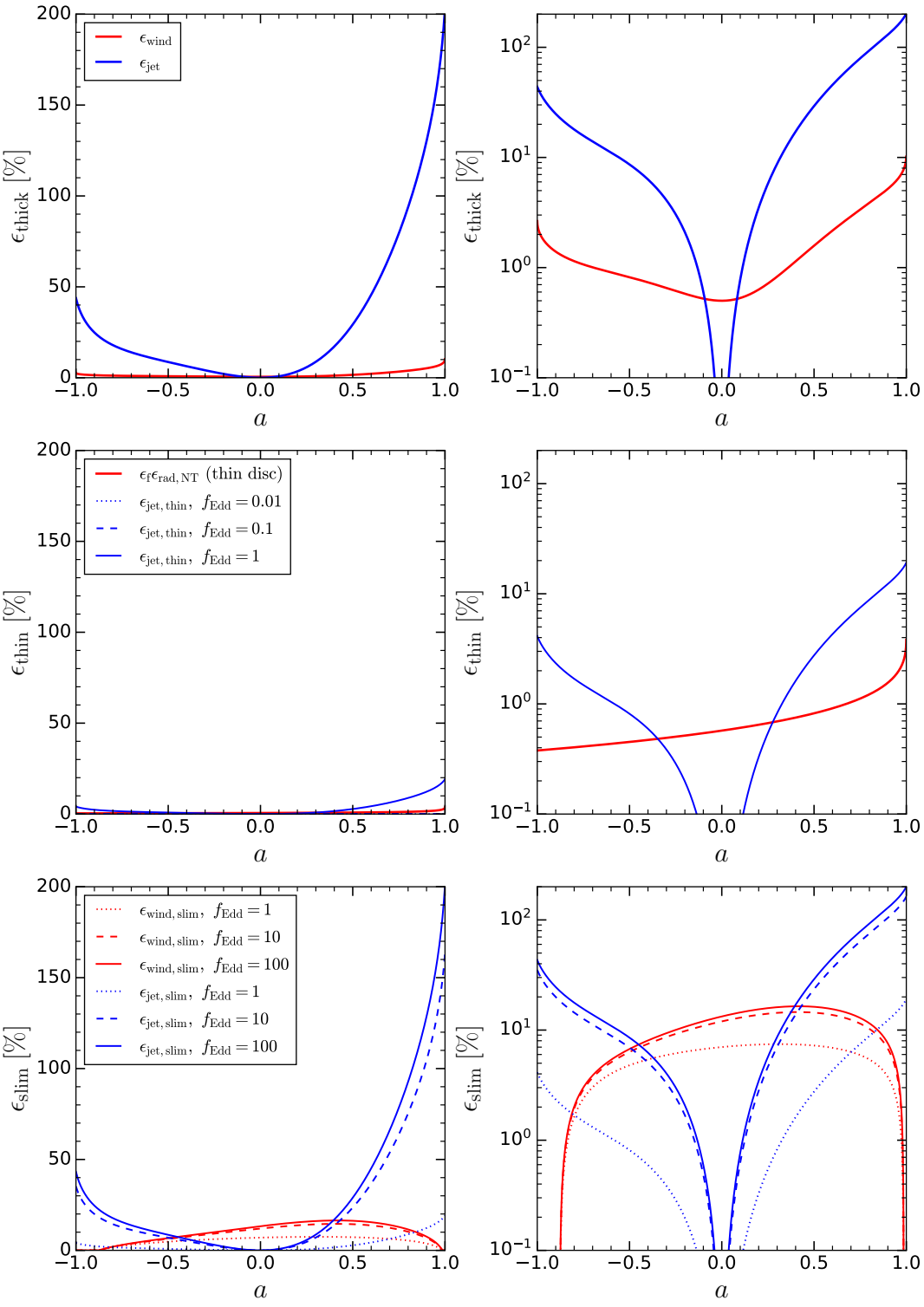

Figure 2.4: The feedback efficiencies used in the model, the same as shown in Fig. 2.3. However, here we plot both the wind efficiencies (red lines) and jet efficiencies (blue lines) in the same panels, but for different accretion regimes (thick disc - top row, thin disc - middle row, slim disc - bottom row). The left-hand and right-hand columns show linear and logarithmic versions of the same plots, respectively. For other details, see caption of Fig. 2.3.

onto which most of the accreting mass is loaded).

For slim discs, in our model we assume that they are quite similar to the thick disc in that they are geometrically thick and advection-dominated (Wang & Zhou 1999, Sadowski et al. 2014). The main difference is that radiation pressure is dominant over thermal pressure. We use results from Ricarte et al. (2023), who studied advection-dominated, MAD accretion discs at high accretion rates (including sub- and super-Eddington rates). In Appendix 2.C we detail our procedure for finding a formula for the wind efficiency from the results of Ricarte et al. (2023), since they do not provide such a formula. They do, however, provide a formula for the total MHD output in their simulations, which includes jets and winds. We thus calculate the wind efficiency by subtracting from their total MHD efficiency the jet efficiency, assuming the latter is given by a well-established formula that we discuss below (Eqn.2.7). Having done the subtraction, we find that the wind efficiency can be fit with the following formula (albeit with large scatter):

$$\epsilon_{\rm wind,slim}(a) = 0.065\left[1+\left(\frac{\phi_{\rm slim}}{50}\right)^2\right]\max\left(0, 1+\Omega_{\rm H}-8\Omega_{\rm H}^2\right). \tag{2.5}$$

Here, $\phi_{\rm slim}$ is the saturated dimensionless magnetic flux, which is found by Ricarte et al. (2023) to depend on the Eddington ratio as

$$\phi_{\rm slim} = \frac{(f_{\rm Edd}/1.88)^{1.29}}{1+(f_{\rm Edd}/1.88)^{1.29}}\phi_{\rm MAD}(a). \tag{2.6}$$

As is clear from the above formula, the dimensionless magnetic flux is generally smaller than the fully-MAD magnetic flux (Eqn. 2.4) unless the BH is accreting at highly super-Eddington rates ($f_{\rm Edd} \gg 1.88$). In that regime, the magnetic flux saturates to the fully-MAD value, and the accretion disc behaves quite similarly to the thick disc.

The wind efficiency of the slim disc is shown with orange lines in the left-hand panel of Fig. 2.3, for several values of $f_{\rm Edd}$ (note that this is the net Eddington ratio, not the large-scale one, $f_{\rm Edd,0}$). The increase and saturation with $f_{\rm Edd}$ (by $f_{\rm Edd} = 100$) are clearly visible. The efficiency is larger than both the thick and thin disc one for most values of spin. Unlike in the thin and thick disc, the wind efficiency

has a different shape (concave rather than convex). This is caused by the additional dependence on the angular velocity of the horizon present in Eqn. (2.5). Physically, this factor encapsulates the fact that in MAD discs with radiatively-driven winds, there is a strong dependence of the behaviour of radiation on the behaviour of jets. As found by some authors (e.g. Narayan et al. 2017), the presence of jets provides a funnel through which most of the radiation can then escape from the disc, rather than launching a wind. This explains the qualitative behaviour of decreasing wind efficiencies as one moves towards either $a = -1$ or $a = 1$ (note that the wind efficiency reaches a value of 0 at a finite value of spin $|a| < 1$).

In our model we assume that all accretion discs launch jets on account of energy (and angular momentum) extraction through the Blandford & Znajek (1977) (BZ) process. There have been many studies on jet launching from MAD thick discs, and recently it has been shown that the results (and fitting formulae) from these papers may also be applied to slim and thin discs (Ricarte et al. 2023). We assume the jet efficiency formula from Tchekhovskoy et al. (2010):

$$\epsilon_{\rm jet} = \frac{\kappa}{4\pi}\phi_{\rm BH}^2\Omega_{\rm BH}^2\left(1 + 1.38\Omega_{\rm BH}^2 - 9.2\Omega_{\rm BH}^4\right), \tag{2.7}$$

where κ is a numerical factor that depends on the initial geometry of the magnetic field (e.g. 0.054 for split-monopole vs. 0.044 for parabolic, we assume $\kappa = 0.05$). For the thick disc, we use the fully-MAD value of $\phi_{\rm MAD}$ for $\phi_{\rm BH}$ (Eqn.2.4), while for the thin and slim discs, we use the saturating, Eddington-ratio dependent value of $\phi_{\rm slim}$ (Eqn.2.6). For strongly super-Eddington rates, the jet efficiency of the slim disc is the same as that of the thick disc.

The jet efficiency given by the above formula is shown in the right-hand panel of Fig. 2.3 for all accretion disc types, and with blue lines in Fig. 2.4. For the thin and slim discs, we show cases with several Eddington ratios. For $f_{\rm Edd} \ll 1$ the jet efficiency is relatively negligible. By $f_{\rm Edd} = 1$ the jet efficiency for high values of spin is already larger than the wind efficiency of the thin or thick disc. For $f_{\rm Edd} = 10$ the full MAD efficiency is nearly reached, while it is fully reached by $f_{\rm Edd} = 100$. Note the very high values of the jet efficiency that are achieved at high spins and $f_{\rm Edd}$,

compared to the wind efficiencies (the $y-$axis is a factor of 10 times more extended than the one in the left-hand panel).

Finally, we note that as an option in the model, we implement radiative efficiencies for the thick and slim disc as well. These are used merely for the calculation of the bolometric AGN luminosities and are thus useful only for comparison with observations (i.e. we do not use them for feedback).

In the thick disc regime, most of the thermal energy is advected inwards towards the black hole before it has time to radiate away. This results in a low, but non-negligible radiative efficiency. This efficiency is mostly governed by radiative cooling rates of electrons through synchrotron, bremsstrahlung, and Compton processes. Numerical simulations have not focused on radiative efficiencies of thick discs, so we take the results from an early numerical study (Mahadevan 1997), in which cooling processes were studied in the context of the original thick disc solution Narayan & Yi (1994) (note that more recent results have been obtained; Xie & Yuan 2012, although their formulae are not as convenient for general numerical implementation).

The numerical study in question (Mahadevan 1997) found two different regimes: for $f_{\rm Edd} < f_{\rm Edd,crit,visc}$, viscous heating dominates the heating of electrons, whereas for $f_{\rm Edd,crit,visc} < f_{\rm Edd} < f_{\rm Edd,crit,thick}$, it is dominated by ion-electron heating. Here, $f_{\rm Edd,crit,visc}$ is the transitional value between the two thick disc regimes, and $f_{\rm Edd,crit,thick} = 0.01$ is the transitional accretion rate which separates thin and thick discs. The radiative efficiency in the viscous heating regime is given by

$$\epsilon_{\rm rad,thick} = 0.0002\epsilon_{\rm rad,NT}\left(\frac{\delta}{0.0005}\right)\left(\frac{1-\beta}{0.5}\right)\left(\frac{6}{r_{\rm ISCO}}\right), \tag{2.8}$$

and in the ion-electron heating regime by

$$\epsilon_{\rm rad,thick} = 0.2\epsilon_{\rm rad,NT}\left(\frac{f_{\rm Edd}}{\alpha^2}\right)\left(\frac{\beta}{0.5}\right)\left(\frac{6}{r_{\rm ISCO}}\right). \tag{2.9}$$

Here, β is the ratio of gas pressure and total pressure (which includes the magnetic pressure). A somewhat different parameter, $\beta_{\rm m}$, can be defined as the ratio of gas pressure and magnetic pressure (Yuan & Narayan 2014). The two parameters are related by $\beta = \beta_{\rm m}/(1+\beta_{\rm m})$. $\beta_{\rm m}$ is not an independent parameter; many simulations

have found that $\alpha\beta_{\rm m} \approx 0.5$ (Begelman et al. 2021, Yuan & Narayan 2014), which we adopt. δ represents the fraction of viscous energy dissipation directly transferred to the electrons, and is constrained in theoretical studies between 0.1 and 0.5 (Sharma et al. 2007, Yuan & Narayan 2014). Observations imply a value close to 0.2 (Yuan 2003, Liu & Wu 2013), which we adopt. The critical Eddington ratio between the two thick disc regimes can be found by ensuring that both formulae (Eqns. 2.8 and 2.9) yield the same radiative efficiency. This gives an accretion rate equal to

$$f_{\rm Edd,crit,visc} = 0.0002\left(\frac{\delta}{0.0005}\right)\left(\frac{1-\beta}{\beta}\right)\alpha^2, \tag{2.10}$$

which is equal to 1.28×10^{-3} for our assumed values of the different parameters.

For the slim disc, we take results based on numerical works (Sadowski 2009). We use the following fitting formula adopted for their results by (Madau et al. 2014):

$$\epsilon_{\rm rad,SD} = \frac{0.1}{f_{\rm Edd}} A(a)\left[\frac{0.985}{1.6/f_{\rm Edd} + B(a)} + \frac{0.015}{1.6/f_{\rm Edd} + C(a)}\right], \tag{2.11}$$

where the three spin-dependant functions are given by $A(a) = (0.9663{-}0.9292a)^{0.5639}$, $B(a) = (4.627 - 4.445a)^{0.5524}$ and $C(a) = (827.3 - 718.1a)^{0.7060}$.

2.5 Evolving the magnitude of black hole spin

The equation for the evolution of the angular momentum of the black hole can in the most general case be written as

$$\frac{{\rm d}\mathbf{J}_{\rm BH}}{{\rm d}t} = \left(\frac{{\rm d}\mathbf{J}}{{\rm d}t}\right)_{\rm acc} + \left(\frac{{\rm d}\mathbf{J}}{{\rm d}t}\right)_{\rm LT} + \left(\frac{{\rm d}\mathbf{J}}{{\rm d}t}\right)_{\rm EM} + \left(\frac{{\rm d}\mathbf{J}}{{\rm d}t}\right)_{\rm rad}, \tag{2.12}$$

where the four terms on the right-hand side represent the effects of accretion, Lense & Thirring (1918) (LT) torques, electromagnetic processes (launching of jets and winds) and torques due to radiation. We first assume that radiation is negligible and drop the last term (although we do indirectly include the effects of these torques by capping the spin to a value of 0.998, as already mentioned). Further, we assume a simplified picture in which LT torques act very quickly to bring the inner regions

of the accretion disc into either alignment or counteralignment with the current BH angular momentum vector (see next section for details). This then means that the LT torque term can be dropped (since these torques require misalignment between the disc and the BH). Furthermore, the entire equation can then be written in vectorless notation

$$\frac{\mathrm{d}J_{\rm BH}}{\mathrm{d}t} = \left(\frac{\mathrm{d}J}{\mathrm{d}t}\right)_{\rm acc} + \left(\frac{\mathrm{d}J}{\mathrm{d}t}\right)_{\rm EM}. \tag{2.13}$$

This equation can then be transformed into an equation for the evolution of the spin parameter. We begin by using $J_{\rm BH} = aM_{\rm BH}^2 G/c$ and the chain rule on the left-hand side of the above equation:

$$\frac{M_{\rm BH}^2 G}{c}\dot{a} + \frac{2M_{\rm BH}G}{c}a\dot{M}_{\rm BH} = L_{\rm in}\dot{M}_{\rm BH,acc} + \dot{J}_{\rm EM}, \tag{2.14}$$

where we have also written the rate of angular momentum gain through accretion as $\dot{J}_{\rm acc} = L_{\rm in}\dot{M}_{\rm BH,acc}$, where $L_{\rm in}$ is the specific angular momentum at some inner radius $R_{\rm in}$, at which orbits are unstable and at which gas begins to quickly plunge into the BH. $\dot{M}_{\rm BH,acc}$ is the net accretion rate though the BH event horizon, not accounting for radiative, wind or jet losses. Dividing the entire equation by $M_{\rm BH}\dot{M}_{\rm BH}G/c$ we further obtain

$$\frac{M_{\rm BH}}{\dot{M}_{\rm BH}}\dot{a} + 2a = \frac{L_{\rm in}c}{(1-\epsilon_{\rm tot})M_{\rm BH}G} + \frac{\dot{J}_{\rm EM}c}{\dot{M}_{\rm BH}M_{\rm BH}G}. \tag{2.15}$$

where $1-\epsilon_{\rm tot} = \dot{M}_{\rm BH}/\dot{M}_{\rm BH,acc}$. The first term of Eqn. (2.15) can be further rewritten as

$$\frac{M_{\rm BH}}{\dot{M}_{\rm BH}}\dot{a} = M_{\rm BH}\frac{\mathrm{d}a}{\mathrm{d}t}\frac{\mathrm{d}t}{\mathrm{d}M_{\rm BH}} = M_{\rm BH}\frac{\mathrm{d}a}{\mathrm{d}M_{\rm BH}} = \frac{M_{\rm BH}}{1-\epsilon_{\rm tot}}\frac{\mathrm{d}a}{\mathrm{d}M_{\rm BH,acc}}, \tag{2.16}$$

where we have used $\mathrm{d}M_{\rm BH} = (1-\epsilon_{\rm tot})\mathrm{d}M_{\rm BH,acc}$ in the last equality. We can now write Eqn. (2.15) as

$$M_{\rm BH}\frac{\mathrm{d}a}{\mathrm{d}M_{\rm BH,acc}} = \frac{L_{\rm in}c}{M_{\rm BH}G} - 2a(1-\epsilon_{\rm tot}) + (1-\epsilon_{\rm tot})\frac{\dot{J}_{\rm EM}c}{\dot{M}_{\rm BH}M_{\rm BH}G}. \tag{2.17}$$

We now write the spin evolution equation in its final form:

$$\frac{\mathrm{d}a}{\mathrm{d}M_{\rm BH,acc}/M_{\rm BH}} = \ell_{\rm in} - 2a(1-\epsilon_{\rm tot}) + s_{\rm EM}, \tag{2.18}$$

where we have defined the dimensionless specific angular momentum as $\ell_{\rm in} = L_{\rm in}/R_{\rm G}c$, and the term for the contribution to spinup/spindown from EM processes as $s_{\rm EM} = \dot{J}_{\rm EM}/\dot{M}_{\rm BH,acc}R_{\rm G}c$. The first term in Eqn. (2.18) is due to gas accretion onto the BH, the second one originates from the definition of the BH spin a through the presence of the BH mass as a factor, while the last term encapsulates electromagnetic effects (winds and jets, mostly the latter).

For the thick disc, instead of using Eqn. (2.18) explicitly in its current form, we use results from GRMHD simulations, to be consistent with what we assumed for feedback efficiencies. We assume the fitting function found by Narayan et al. (2022):

$$s_{\rm thick} = \left(\frac{{\rm d}a}{{\rm d}M_{\rm BH,acc}/M_{\rm BH}}\right)_{\rm thick} = 0.45 - 12.53a - 7.8a^2 + 9.44a^3 + 5.71a^4 - 4.03a^5. \tag{2.19}$$

As shown in Fig. 2.4, the right-hand-side of the above equation is positive for $a < 0.05$, leading to spinup, while it is negative for $a > 0.05$, leading to spindown. Thus, $a_{\rm eq} \approx 0.05$ is an equilibrium BH spin value at which accretion and jet/wind launching are balanced in terms of angular momentum flux into/out of the BH, such that the spin does not evolve (but note that the BH is growing in mass, and thus also angular momentum).

For the slim and thin disc, we use results from Ricarte et al. (2023), who find a fitting formula that smoothly interpolates between the thin disc regime without significant jet feedback (for $f_{\rm Edd}$ not close to super-Eddington values), and that where jet feedback essentially matches the thick disc (and so jet spindown should also be similar). Their formula is based on Eqn. (2.18), but they write it slightly differently:

$$s_{\rm thin/slim} = \left(\frac{{\rm d}a}{{\rm d}M_{\rm BH,acc}/M_{\rm BH}}\right)_{\rm thin/slim} = s_{\rm HD} - s_{\rm EM}, \tag{2.20}$$

where the first term is a pure hydrodynamical term, while the second is an electromagnetic term. $s_{\rm HD}$ is given in their approach by

$$s_{\rm HD} = \frac{s_{\rm thin} + s_{\rm min}\xi}{1+\xi}, \tag{2.21}$$

where $\xi = 0.017 f_{\rm Edd}$, $s_{\rm min} = 0.86 - 1.94a$ and $s_{\rm thin} = \ell_{\rm ISCO} - 2ae_{\rm ISCO}$ is the

spinup/spindown function of the 'pure' thin disc (with no outflows and outside the MAD regime), in which $\ell_{\rm ISCO}$ and $e_{\rm ISCO}$ are the (dimensionless) specific angular momentum and binding energy, respectively, at the ISCO (see Appendix 2.A). The EM term is given by

$$s_{\rm EM} = {\rm sgn}(a)\epsilon_{\rm EM}\left(\frac{1}{k\Omega_{\rm H}} - 2a\right), \tag{2.22}$$

where $\epsilon_{\rm EM} = \epsilon_{\rm jet} + \epsilon_{\rm wind}$ is the total (jet+wind) EM efficiency of the slim disc, and k is given by

$$k = \begin{cases} 0.23, & a < 0 \\ \min(0.35, 0.1 + 0.5a), & a > 0 \end{cases} \tag{2.23}$$

The slim disc spinup/spindown rate is shown in Fig. 2.5 for several values of $f_{\rm Edd}$. For sufficiently small $0.01 < f_{\rm Edd} \ll 1$, the spinup/spindown function is similar to that of the thin disc, and shows monotonic spinup to $a = 1$. As $f_{\rm Edd}$ increases, the impact of jets and winds on spindown becomes stronger, and the spinup/spindown function becomes more and more similar to the thick disc one (albeit there is some residual difference at $a < 0$, even for strongly super-Eddington slim discs).

2.6 Choosing the sign of BH spin

In our model, we assume that the effect of LT torques is effectively instantaneous (compared to the time-scale of accretion). In this picture, within the inner accretion disc, the BH's angular momentum always dominates and the accretion disc becomes either aligned or counter-aligned with the BH's spin vector through LT torques (or it may precess around the spin vector). In the case of counteralignment, we consider accretion to be retrograde and the BH spin negative. The thin disc develops a warp due to LT torques and is assumed to be perfectly aligned or counteraligned with the BH within a warp radius $R_{\rm warp}$, which is the radius out to which the 'communication' of the BH and the disc is effective (Bardeen & Petterson 1975), in terms of torques.

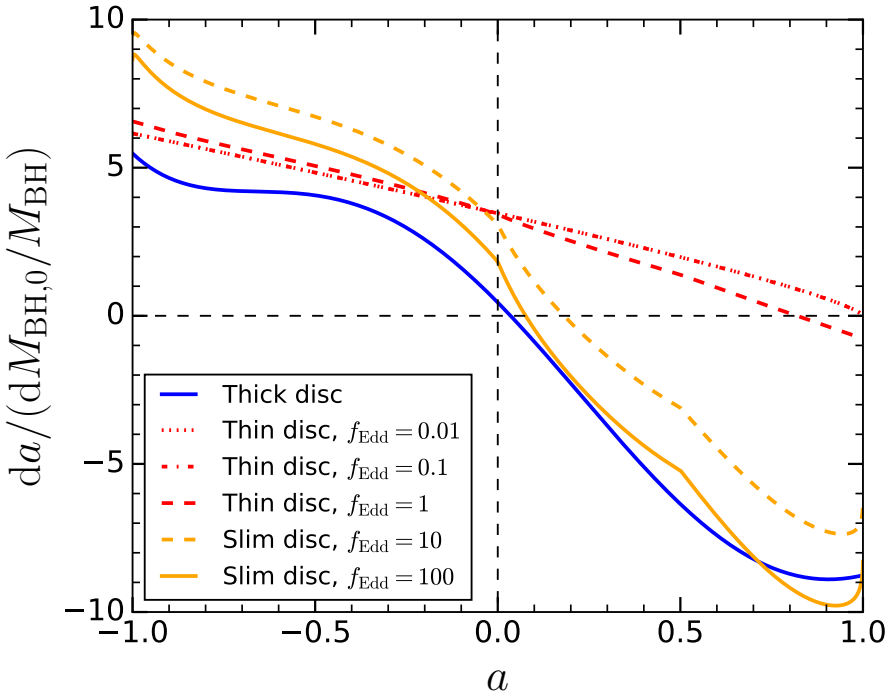

Figure 2.4: The spinup/spindown function in our model. These are given by Eqn. (2.19) for the thick disc (blue line) and Eqn. (2.20) for the thin and slim discs (red and orange lines). For the latter, we show the spinup/spindown function for several values of f_{Edd}.

Outside this radius, the accretion disc is undisturbed and aligned with the large-scale accretion flow.

For the thick and slim discs, the assumption of exact (counter-)alignment is invalid. Instead, the disc precesses about the BH spin vector. This precession occurs on very short time-scales, much shorter than the ones we are simulating. For this reason we may also assume (counter-)alignment of the thick disc, in a time-averaged sense. Thus, in our model, all accretion states are treated equally in this regard (but with different assumptions about the properties and structure of the accretion disc, which affects the size of the aligned or precessing region).

The sign of the BH spin (i.e. whether the disc aligns or counteraligns) is decided based on the criterion developed by King et al. (2005). In this prescription, the BH and the inner accretion disc are assumed to come into (counter-)alignment in such a way that the magnitude of the BH spin does not change, and that the total angular momentum (of the BH + inner accretion disc) is conserved. In this process, the BH spin vector aligns with the vector of the total angular momentum. The condition for counteralignment (and for spin to be negative) in this approach can be stated as follows:

$$\cos\theta < -\frac{J_{\rm warp}}{2J_{\rm BH}}, \tag{2.24}$$

where $\cos\theta = \hat{\mathbf{J}}_{\rm BH} \cdot \hat{\mathbf{J}}_{\rm d}$ is the misalignment between the BH and the large-scale angular momentum of the disc (i.e. outside $R_{\rm warp}$), whose direction is $\hat{\mathbf{J}}_{\rm d}$. $J_{\rm warp}$ is the total angular momentum of the inner accretion disc out to $R_{\rm warp}$.

2.7 Evolving the direction of BH spin

From a numerical standpoint, the direction of the BH spin is evolved in the following way. For each increment of mass $M_{\rm warp}$ consumed by the BH, the BH-inner accretion disc system is assumed to come into equilibrium (with the inner accretion disc aligned or counter-aligned with the BH), so that the direction of the angular momentum of both the BH and the inner accretion disc is parallel or anti-parallel to the direction of the total angular momentum $\mathbf{J}_{\rm tot} = \mathbf{J}_{\rm BH} + \mathbf{J}_{\rm warp}$. Here, $\mathbf{J}_{\rm warp} = J_{\rm warp}\hat{\mathbf{J}}_{\rm d}$ is the angular momentum of a single warp increment, which is assumed to be di-

rected along the angular momentum of the outer accretion disc (i.e. the large-scale accretion flow, which we calculate directly from the simulation). Note that we do not evolve the BH one warp increment at a time, but instead for a number of increments $N_{\rm warp} = \Delta M/M_{\rm warp}$ over each time-step, where $\Delta M = \dot{M}_{\rm BH,acc}\Delta t$ is the total mass to be consumed over a single time-step Δt.

In order to calculate $M_{\rm warp}$ and $J_{\rm warp}$, we require knowledge of 1) the warp radius $R_{\rm warp}$, 2) the surface density $\Sigma(R)$ and 3) the specific angular momentum $L(R)$. The warp mass $M_{\rm warp}$ is calculated simply as the integral over the surface density out to $R_{\rm warp}$, while the warp angular momentum $J_{\rm warp}$ includes the specific angular momentum $L(R)$ in the same integral. For the thin disc we assume Keplerian rotation, $L(R) = \sqrt{M_{\rm BH}GR}$, while for the thick and slim discs, the specific angular momentum is smaller by a numerical factor of order 0.5 (see discussion below, where we discuss the surface density of the thick and slim disc). We do not provide here the expressions for $M_{\rm warp}$ and $J_{\rm warp}$ for brevity, but we describe below our assumptions about $R_{\rm warp}$ and Σ.

The radius $R_{\rm warp}$, which separates the inner and outer accretion disc, can be calculated by equating the Lense-Thirring precession time-scale ($t_{\rm p} = 2\pi/\Omega_{\rm p}$, with $\Omega_{\rm p} = 2GJ_{\rm BH}/c^2R^3$ the precession rate) and the vertical warp propagation time-scale ($t_{\rm warp} = R^2/\nu_2$, with ν_2 the kinematic viscosity in the vertical direction) (Pringle 1992, Martin et al. 2007, Cielo et al. 2014). We use the relation $\dot{M} = 3\pi\nu_1\Sigma$ (for $R \gg R_{\rm ISCO}$, Fiacconi et al. 2018) to calculate ν_1, and therefore ν_2. For the thick and slim disc, we assume $\nu_2 = \nu_1$. For the thin disc, ν_2 can be related to ν_1 by $\nu_2 = \xi\nu_1$, with ξ a numerical factor (Lodato & Price 2010). The constant parameter ξ is often also expressed in the form α_2/α. Early theoretical calculations predicted $\alpha_2 = 1/2\alpha$ for small α (Papaloizou & Pringle 1983), which has also been confirmed by simulations (Lodato & Pringle 2007). Later simulations have found that higher-order corrections to this prediction may need to be included for realistic values of α (Lodato & Price 2010), such as $\alpha = 0.2$. These numerical results agree with an early theoretical prediction (Ogilvie 1999) which we assume here:

$$\xi = \frac{\nu_2}{\nu_1} = \frac{\alpha_2}{\alpha} = \frac{2}{\alpha^2}\frac{1+7\alpha^2}{4+\alpha^2}, \tag{2.25}$$

which reduces to $1/2\alpha^2$ for small α.

The warp radius, $R_{\rm warp}$, can be derived for the advection-dominated thick and slim discs as (see Ogilvie 1999):

$$R_{\rm warp,adv} = R_{\rm G}\left(\frac{384|a|}{25(H/R)^2}\right)^{2/5}. \tag{2.26}$$

Thus, it depends only on the magnitude of the current spin, the aspect ratio of the disc (and the BH mass through $R_{\rm G}$). For both the thick and slim disc we assume $H/R = 0.3$, based on GRMHD simulations (Narayan et al. 2022, Ricarte et al. 2023). This value is somewhat lower than the aspect ratio in the self-similar analytical solutions for these discs ($H/R \approx 0.4 - 0.5$ as in Narayan & Yi 1994, Wang & Zhou 1999, respectively). Regardless of these small differences, Eqn. (2.26) yields small warp radii (no larger than $\approx 10R_{\rm G}$), much smaller than the thin disc (see below). While we take the aspect ratio H/R from the GRMHD simulations, we assume surface densities based on the analytical solutions since they are more wieldy and easily accessible. These take the same form for the two types of accretion disc:

$$\Sigma_{\rm adv} = \frac{\dot{M}_{\rm BH,acc}}{2\pi R|v_{\rm r}|}, \tag{2.27}$$

where $v_{\rm r}$ is the radial inflow velocity of the gas, and the only source of difference between the expression for $\Sigma_{\rm adv}$ between the two discs. For the slim disc, $v_{\rm r} = -\alpha v_{\rm K}/\sqrt{5}$ (Wang & Zhou 1999), where $v_{\rm K} = \sqrt{M_{\rm BH}G/R}$ is the Keplerian velocity. For the thick disc we take $v_{\rm r} = -\alpha v_0 v_{\rm K}$ (Narayan & Yi 1994), where the parameter v_0 is not $1/\sqrt{5} \approx 0.45$ but is instead dependent on α through $v_0 = 3/(5+2\varepsilon)$, where $\varepsilon = (5/3-\gamma)/(\gamma-1)$, γ is the adiabatic index of the gas, related to the gas-to-total pressure ratio β by $\gamma = (8-3\beta)/(6-3\beta)$. Finally, β can be connected to α through the findings of GRMHD simulations (Yuan & Narayan 2014) as $\beta = 1/(1+2\alpha)$. v_0 depends on α only weakly; for $\alpha = 0.2$, we obtain $v_0 = 0.52$, very close to the value for the slim disc. Having introduced these dependencies, we are also in a position to state the specific angular momentum $L(R)$ for the thick and slim disc. For the slim disc, it is a factor $1/\sqrt{5} \approx 0.45$ smaller than the Keplerian value $\sqrt{M_{\rm BH}GR}$, while for the thick disc, it is $\Omega_0 = \sqrt{2\varepsilon/(5+2\varepsilon)}$ times the Keplerian value. For $\alpha = 0.2$,

$\Omega_0 \approx 0.37$, again close to the slim disc value.

For the thin disc, $R_{\rm warp}$ also depends on the surface density Σ, unlike for the thick and slim disc. The solution of the thin disc (Shakura & Sunyaev 1973), assumed in this model, describes three regions: a) an inner one where radiation pressure dominates the pressure and electron-electron scattering the opacity, which is often unstable and usually does not extend far out, b) a middle one where gas dominates the pressure and electron-electron scattering dominates the opacity and c) an outer one where gas also dominates the pressure, but the opacity is dominated by free-free absorption. We ignore region a) (because the mass and angular momentum associated with that region is relatively small for our purpose) and assume, for simplicity, that the entire thin accretion disc, at least out to $R_{\rm warp}$, can be described by either region b) or c). We have tested both assumptions and the choice between them appears to have little effect. However, we keep both choices as options in our model and specify them both here for clarity and completeness. Our fiducial choice is to the describe the disc using the region b). In region b), the surface density can be expressed as

$$\Sigma_{\rm TD,b} = 6.84 \times 10^5 \text{ g cm}^{-2} \alpha^{-4/5} f_{\rm Edd}^{3/5} \left(\frac{\epsilon_{\rm r}}{0.1}\right)^{3/5} \left(\frac{M_{\rm BH}}{10^8 M_\odot}\right)^{1/8} \left(\frac{R}{R_{\rm S}}\right)^{-3/5}, \quad (2.28)$$

(Collin-Souffrin & Dumont 1990) whereas in region c)

$$\Sigma_{\rm TD,c} = 3.41 \times 10^4 \text{ g cm}^{-2} \alpha^{-4/5} f_{\rm Edd}^{7/10} \left(\frac{\epsilon_{\rm r}}{0.1}\right)^{7/10} \left(\frac{M_{\rm BH}}{10^8 M_\odot}\right)^{1/20} \left(\frac{R}{R_{\rm S}}\right)^{-3/4} \quad (2.29)$$

(see appendix in Fiacconi et al. 2018). Here, $R_{\rm S} = 2R_{\rm G}$ is the Schwarzschild radius. Using these surface densities, the warp radii can be calculated as

$$R_{\rm warp,TD,b} = 3410 R_S a^{5/8} \xi^{-5/8} \alpha^{-1/2} f_{\rm Edd}^{-1/4} \left(\frac{\epsilon_{\rm r}}{0.1}\right)^{-1/4} \left(\frac{M_{\rm BH}}{10^8 M_\odot}\right)^{1/8} \quad (2.30)$$

for region b) (Griffin et al. 2019) and

$$R_{\rm warp,TD,c} = 2629 R_{\rm S} a^{4/7} \xi^{-4/7} \alpha^{-16/35} f_{\rm Edd}^{-6/35} \left(\frac{\epsilon_{\rm r}}{0.1}\right)^{-6/35} \left(\frac{M_{\rm BH}}{10^8 \,{\rm M}_\odot}\right)^{4/35} \quad (2.31)$$

for region c). The latter is equivalent to equation A8 from Fiacconi et al. 2018 (but with a different definition of ξ; we use $\xi = \nu_2/\nu_1$, whereas they use $\xi = (\nu_2/\nu_1)2\alpha^2$).

Thin accretion discs can extend to large enough distances that they are prone to the effects of self-gravity (see Lodato 2007 for a review). At large enough radii, the gravity due to the disc locally becomes comparable to that due to the BH. Here we assume that the disc extends out to a radius $R_{\rm sg}$ where the Toomre instability parameter, $Q = \Omega c_{\rm s}/\pi G\Sigma$, is equal to the critical value of 1. This equation, the Toomre instability criterion, be solved to obtain

$$R_{\rm sg,TD,b} = 6460 R_S \alpha^{28/51} f_{\rm Edd}^{-18/51} \left(\frac{\epsilon_{\rm r}}{0.1}\right)^{-18/51} \left(\frac{M_{\rm BH}}{10^8 M_\odot}\right)^{-49/51} \tag{2.32}$$

for region b) and

$$R_{\rm sg,TD,c} = 2456 R_S \alpha^{28/45} f_{\rm Edd}^{-22/45} \left(\frac{\epsilon_{\rm r}}{0.1}\right)^{-22/45} \left(\frac{M_{\rm BH}}{10^8 M_\odot}\right)^{-52/45} \tag{2.33}$$

for region c) (Fiacconi et al. 2018). For $Q < 1$ (i.e. $R > R_{\rm sg}$), the disc is prone to local gravitational instabilities and it likely undergoes gravitational collapse/fragmentation and star formation. In the case that $R_{\rm sg} < R_{\rm warp}$, we simply assume that the entire accretion disc is (counter-)aligned and use $R_{\rm sg}$ instead of $R_{\rm warp}$ in all equations where $R_{\rm warp}$ makes an appearance.

2.8 Final spin and mass loss to gravitational waves after BH mergers

The final spin of a BH-BH merger remnant is dependant on the mass ratio of the BHs, q = $M_{\rm BH,2}/M_{\rm BH,1} < 1$ as well as the three vectors relevant for this situation: the two spin vectors, $\mathbf{a_1}$ and $\mathbf{a_2}$ of the BHs, as well as the orbital angular momentum of the system about the centre of mass, $\mathbf{L}$. We use a fitting formula specifically tailored for use in cosmological simulations (Barausse & Rezzolla 2009):

$$\mathbf{a}_{\rm fin} = \frac{1}{(1+q)^2}(\mathbf{a}_1 + \mathbf{a}_2 q^2 + \mathbf{l} q), \tag{2.34}$$

where $\mathbf{l}$ is a vector whose direction is the same as that of the orbital angular momentum $\mathbf{L}$ (in the centre-of-mass frame), while its magnitude is given by

$$\begin{aligned} |\mathbf{l}| &= \frac{s_4}{(1+q^2)^2}\left(|\mathbf{a}_1|^2 + |\mathbf{a}|_1^2 q^4 + 2\,|\mathbf{a}_1||\mathbf{a}_2|\,q^2\cos\phi\right) + \\ &+ \left(\frac{s_5\mu+t_0+2}{1+q^2}\right)\left(|\mathbf{a}_1|\cos\theta + |\mathbf{a}_2|\,q^2\cos\xi\right) + 2\sqrt{3} + t_2\mu + t_3\mu^2. \end{aligned} \tag{2.35}$$

Here, $\mu = q/(1+q)^2$ is the symmetric mass ratio, and $s_4 = -0.1229$, $s_5 = 0.4537$, $t_0 = -2.8904$, $t_2 = -3.5171$, $t_3 = 2.5763$. The three cosines depend on the angles between the different vectors which play a role in the merger: $\cos\phi = \hat{\mathbf{a}_1}\cdot\hat{\mathbf{a}_2}$, $\cos\theta = \hat{\mathbf{a}_1}\cdot\hat{\mathbf{l}}$, $\cos\xi = \hat{\mathbf{a}_2}\cdot\hat{\mathbf{l}}$.

Given the information available within the model, we could in principle calculate the recoil velocity of the remnant, as well as the total mass fraction lost to gravitational waves. We do not implement the former at this stage since the model will be used in simulations (successors of EAGLE) that cannot reliably track the movement of black holes in their host galaxies. However, we do implement the latter. We use results from numerical relativity simulations (Barausse et al. 2012) and write the final mass of the remnant as:

$$M_{\rm BH,fin} = (M_{\rm BH,1}+M_{\rm BH,2})\Big\{1-[1-e_{\rm ISCO}(\tilde{a})]\mu-4\mu^2[4p_0+16p_1\tilde{a}(\tilde{a}+1)+e_{\rm ISCO}(\tilde{a})-1]\Big\}, \tag{2.36}$$

where $p_0 = 0.04827$, $p_1 = 0.01707$ and $e_{\rm ISCO}(\tilde{a})$ is the dimensionless specific binding energy (the expression can be read off from Eqn. 1.2) at the innermost stable circular orbit calculated using an effective spin variable defined as

$$\tilde{a} = \frac{|\mathbf{a_1}|\cos\theta + |\mathbf{a_2}|\cos\xi}{(1+q)^2}. \tag{2.37}$$

2.9 Additional time-step criteria

Given the changes to the BH model in the form of AGN jets and BH spin evolution, a few additional time-step criteria need to be implemented. The minimum of these time-steps is taken to actually evolve the BH, alongside the other time-steps already

used for the BH in the code. We introduce a jet-related time-step that is given by:

$$\Delta t_{\rm jet} = \frac{\Delta E_{\rm jet}}{P_{\rm jet}}. \tag{2.38}$$

This time-step ensures that the BH is woken up by the time it needs to 'hand out' a pair of kicks. In the above equation, $P_{\rm jet}$ is the current, instantenous jet power, while $\Delta E_{\rm jet} = 2 \times m_{\rm ngb} v_{\rm jet}^2$ is the energy to be handed out to a pair of particles, with $m_{\rm ngb}$ the average gas particle mass in the BH's kernel, and $v_{\rm jet}$ the target jet velocity.

We also introduce two time-steps related to the angular momentum of the BH. The first of these ensures that the magnitude of spin does not change too much over a single time-step, and it is given by

$$\Delta t_{\rm a} = 0.1 \frac{|a| M_{\rm BH}}{s \dot{M}_{\rm BH,acc}}, \tag{2.39}$$

where $s = {\rm d}a/({\rm d}M_{\rm BH,acc}/M_{\rm BH})$ is the spinup/spindown function discussed in § 2.5, given by Eqns. (2.19) and (2.20). The numerical factor 0.1 quantifies how finely we want to evolve spin; it ensures that the value of spin changes no more than 10 per cent (relative to the current value) over the next time-step.

We also introduce a time-step related to the redirection of the spin vector. Since the spin vector may be redirected very quickly relative to its magnitude (due to LT torques), this criterion is separate to the one mentioned above. This time-step is given by

$$\Delta t_{\rm a} = 0.1 \frac{M_{\rm warp} J_{\rm BH}}{\dot{M}_{\rm BH,acc} J_{\rm warp} \sin\theta}, \tag{2.40}$$

where θ is the angle between the current BH spin vector and the angular momentum of gas in the accretion disc on large scales. The numerical prefactor is again present to ensure a fine enough evolution of the spin vector direction. In particular, in the case that the spin vector and the gas angular momentum are perpendicular ($\sin\theta = 1$), this criterion will lead to a change of no more than $\approx 5^\circ$ in the spin vector direction per time-step.

2.10 Jet launching scheme

For each BH, we parametrize the choice of when and how to kick gas particles in the form of a target jet velocity $v_{\rm j}$. We express the energy being received by the particles through the target jet velocity as $\Delta E = 2 \times m_{\rm g} v_{\rm j}^2/2$, where $m_{\rm g}$ is the gas particle mass and the multiplication by two is present since we always kick in pairs. We do not kick particles perfectly along the jet direction (which is parallel or anti-parallel with the BH spin vector for each BH), but instead implement a finite half-opening angle $\theta_{\rm j}$ (e.g. 10°). This is accomplished by assigning a new kick direction every time a kick event occurs; this direction is given by a unit vector $\mathbf{n}_{\rm j}$ that is drawn randomly and uniformly in solid angle within a cone with a half-opening angle $\theta_{\rm j}$ directed along the chosen jet direction (either aligned with the BH spin vector or the $z-$axis). Since we always kick in pairs, the above procedure is done for one particle in the 'positive' direction (along the jet direction) and for another particle in the 'negative' direction (anti-parallel with the jet direction).

We kick particles by increasing their velocity (in the frame of each BH) by $\Delta \mathbf{v} = \Delta v \mathbf{n}_{\rm j}$. The magnitude of the velocity increase Δv is chosen in such a way that the kinetic energy of each particle increases exactly by $\Delta E/2$. Conservation of kinetic energy gives

$$\frac{1}{2} m_{\rm g} (\mathbf{v}_i + \Delta \mathbf{v})^2 - \frac{1}{2} m_{\rm g} \mathbf{v}_i^2 = \frac{\Delta E}{2}, \tag{2.41}$$

where $\mathbf{v}_i$ is the initial velocity. This equation can be solved for the magnitude of the velocity increase Δv, yielding

$$\Delta v = \sqrt{v_{\rm i,j}^2 + v_{\rm j}^2} - v_{\rm i,j}, \tag{2.42}$$

where $v_{\rm i,j} = \mathbf{v}_i \cdot \mathbf{n}_{\rm j}$ is the initial velocity projected onto the kick direction. This equation implies that the change in the particle velocity is always smaller than the target velocity, i.e. $\Delta v < v_{\rm j}$, if the initial velocity is non-zero. However, we use fairly large values of $v_{\rm j}$ that are at least a factor of 10 larger than the initial particle velocities, so in practice $\Delta v \approx v_{\rm j}$.

Appendix 2.A: Innermost stable circular orbit (ISCO)

The radius of the innermost stable circular orbit (ISCO) is given by $R_{\rm ISCO} = r_{\rm ISCO} R_{\rm G}$, where $r_{\rm ISCO}$ is the dimensionless radius of the ISCO. $r_{\rm ISCO}$ depends on spin as

$$r_{\rm ISCO} = 3 + Z_2 \mp \sqrt{(3 - Z_1)(3 + Z_1 + 2Z_2)}, \tag{2.43}$$

where the minus and plus sign are for prograde and retrograde accretion, respectively, and Z_1 and Z_2 are functions of spin given by

$$Z_1(a) = 1 + \left(1 - a^2\right)^{1/3} \left[\left(1 + |a|\right)^{1/3} + \left(1 - |a|\right)^{1/3}\right] \tag{2.44}$$

and

$$Z_2(a) = \sqrt{3a^2 + Z_1}. \tag{2.45}$$

The specific angular momentum at the ISCO is given by $L_{\rm ISCO} = M_{\rm BH} G \ell_{\rm ISCO}/c$, where $\ell_{\rm ISCO}$ is a dimensionless function of spin:

$$\ell_{\rm ISCO}(a) = \frac{2}{3\sqrt{3}}\left(1 + 2\sqrt{3r_{\rm ISCO} - 2}\right). \tag{2.46}$$

Appendix 2.B: Variable accretion efficiencies

In addition to modelling the accretion efficiency $\epsilon_{\rm acc}$ as a constant parameter, we implement a more realistic approach as an option within the model (Nemmen & Tchekhovskoy 2015). In this alternative, the efficiency depends on the ratio of the gravitational radius $R_{\rm G}$ and the Bondi radius $R_{\rm B} = 2M_{\rm BH}G/c_{\rm s}$, where $c_{\rm s}$ is the sound speed of the gas near the BH. In particular:

$$\epsilon_{\rm acc} = \left(\frac{100 R_{\rm G}}{R_{\rm B}}\right)^s = \left(\sqrt{10}\frac{c_{\rm s}}{c}\right)^{2s}. \tag{2.47}$$

If this equation is used, each black hole has a different accretion efficiency. The value of s is likely in the range $s = 0.3 - 1$ (Nemmen & Tchekhovskoy (2015)).

A yet more realistic approach would be to replace the Bondi radius $R_{\rm B}$ in Eqn. (2.47) with the outer radius of the thick accretion disc $R_{\rm o}$, which may be

equal to the Bondi radius if the thick disc represents the entire accretion flow, or it may correspond to $R_{\rm tr}$, the transition radius between the thick and thin disc (in this scenario, the disc is thick at $R < R_{\rm tr}$ and thin at $R \in [R_{\rm tr},\ R_{\rm B}]$). As the accretion rate drops, the thick disc extends to larger and larger distances since the transition radius $R_{\rm tr}$ depends on the large-scale accretion rate $\dot{M}_{\rm BH,acc,0}$. According to numerical calculations (e.g. Narayan & Yi 1995), the transition radius is given by

$$R_{\rm tr} = 2.82 \times 10^8 \frac{\alpha^4 \epsilon_{\rm ADAF}^2}{\beta(5+2\epsilon_{\rm ADAF})^6} \frac{1}{f_{\rm Edd}^2} R_{\rm G} = 1.724 \frac{R_{\rm G}}{f_{\rm Edd}^2}, \tag{2.48}$$

where we have assumed $\alpha = 0.2$ for the second equality.

This strong dependence ($R_{\rm tr} \propto 1/f_{\rm Edd}^2$) gives $R_{\rm tr} \approx 10^4 R_{\rm G}$ if $f_{\rm Edd} = 0.01$ (the disc is marginally thick), and $R_{\rm tr} \approx 10^6 R_{\rm G} \approx R_{\rm B}$ if $f_{\rm Edd} = 10^{-3}$. In the former case, the accretion efficiency is of order 10^{-1}, while in the latter, it is of order 10^{-3} (dependent on the assumed value of s). For $f_{\rm Edd} \lesssim 10^{-3}$, at least in this approach, the entire disc is thick. If this scaling relation between $R_{\rm tr}$ and $f_{\rm Edd}$ is assumed, the accretion efficiency depends only on $f_{\rm Edd}$ (given a choice of α), as $\epsilon_{\rm acc} \propto f_{\rm Edd}^{2s}$ (although the Bondi radius provides a floor to the accretion efficiency through Eqn. (2.47). In Fig. 2.5 we show the accretion efficiency as a function of $f_{\rm Edd}$ for different values of s and $c_{\rm s}$. The floor values shown in the plot are given by the ratio $(100R_{\rm G}/R_{\rm B})^s$, and they appear when $R_{\rm tr} > R_{\rm B}$.

Appendix 2.C: Slim disc wind efficiency formula

The GRRMHD simulations performed by Ricarte et al. (2023) span a wide range of accretion rates (sub- and super-Eddington) as well as multiple values of spin. The accretion rates are variable, but they vary around some mean value, which is effectively an input for their simulations. The authors provide data on the average dimensionless magnetic flux threading the horizon, ϕ, which reaches some saturated value if the system has reached the MAD limit (in which case the saturated value of ϕ depends on BH spin a and accretion rate, or Eddington ratio $f_{\rm Edd}$).

For each simulation, the authors also provide an average value of the total MHD efficiency $\epsilon_{\rm tot}$, measured at $5R_{\rm G}$. This efficiency should represent the total output

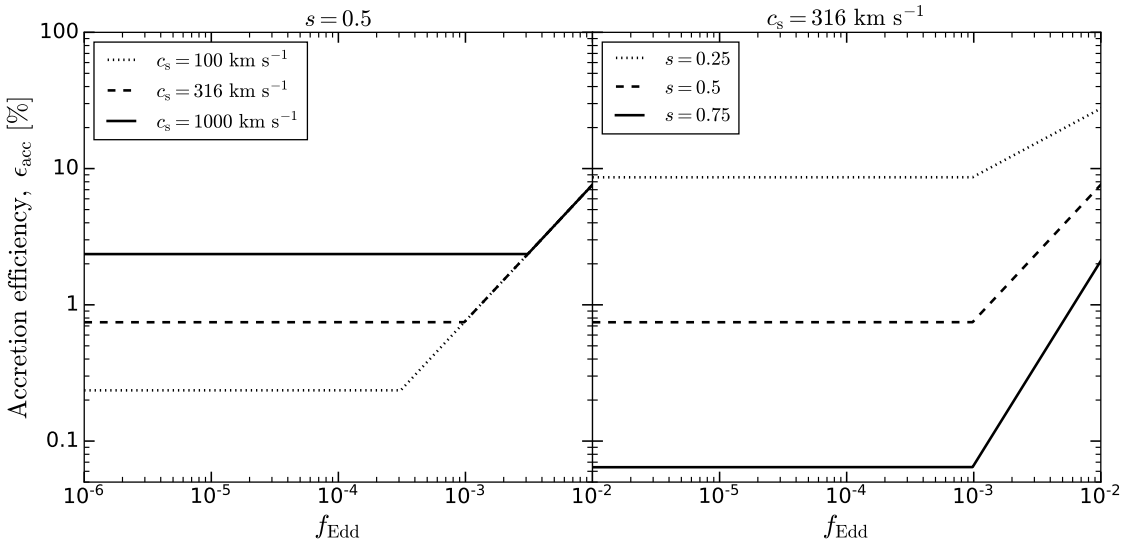

Figure 2.5: The accretion efficiency in the thick disc as a function of the Eddington ratio $f_{\rm Edd} = \dot{M}_{\rm BH,acc,0}/\dot{M}_{\rm Edd}$, assuming different values of the parameter s (see text for details) and sound speed $c_{\rm s}$ of the ambient medium. This accretion efficiency is given by Eqn. (2.47), where the Bondi radius $R_{\rm B}$ is replaced by $\min(R_{\rm B},\, R_{\rm tr})$, and in which $R_{\rm tr}$ is the transition radius between the thin and thick disc (Eqn. 2.48).

in both jets and winds. We thus find the value of the wind efficiency, not provided by the authors, for each simulation by subtracting from their total efficiency the expected value of the jet efficiency, given by Eqn. (2.7) from Tchekhovskoy et al. (2010), which uniquely determines the jet efficiency for any MAD disc if one knows the BH spin and magnetic flux threading the BH horizon.

The average wind efficiencies for the slim disc, given by this procedure, are shown for each simulation performed by Ricarte et al. (2023) as points in the left-hand panel of Fig. 2.6. For $a = 0$, the efficiency clearly depends on magnetic flux in a monotonic way. We find that it can be described with the following fitting function (compare green line and green data points in the figure):

$$\epsilon_{\rm wind,slim}(\phi, a = 0) = 0.065\left[1 + \left(\frac{\phi}{50}\right)^2\right]. \tag{2.49}$$

For non-zero values of BH spin, the wind efficiencies from the simulations (the individual data points) seem to have a much larger scatter, and do not follow an obvious monotonic relation. For simplicity, we have assumed that the wind efficiency

can be parameterized in the following way:

$$\epsilon_{\rm wind,slim}(\phi, a) = 0.065\left[1 + \left(\frac{\phi}{50}\right)^2\right] f(a), \tag{2.50}$$

where $f(a)$ is a function that depends only on spin. In other words, we have assumed that the dependencies on magnetic flux ϕ and BH spin a are decoupled (which does not necessarily have to be the case). Given this assumption, we find the average value of $f(a)$ for different values of spin a by dividing $\epsilon_{\rm wind}(\phi, a)$ with the fitting function $\epsilon_{\rm wind,slim}(\phi, a = 0)$ (given by Eqn. 2.49) for each individual simulation, and then taking an average over multiple simulations (and therefore multiple values of ϕ). This yields the functional form $f(a)$, which we show in the right-hand panel of Fig. 2.6. We also show a simple fit to the obtained values of the function, given by

$$f(a) = \max(0, 1 + \Omega_{\rm H} - 8\Omega_{\rm H}^2), \tag{2.51}$$

where we have opted to parametrize the fit using the (dimensionless) angular velocity of the BH horizon, $\Omega_{\rm H}$, rather than the BH spin itself, since the former is a more physically meaningful quantity when it comes to energy extraction from the BH.

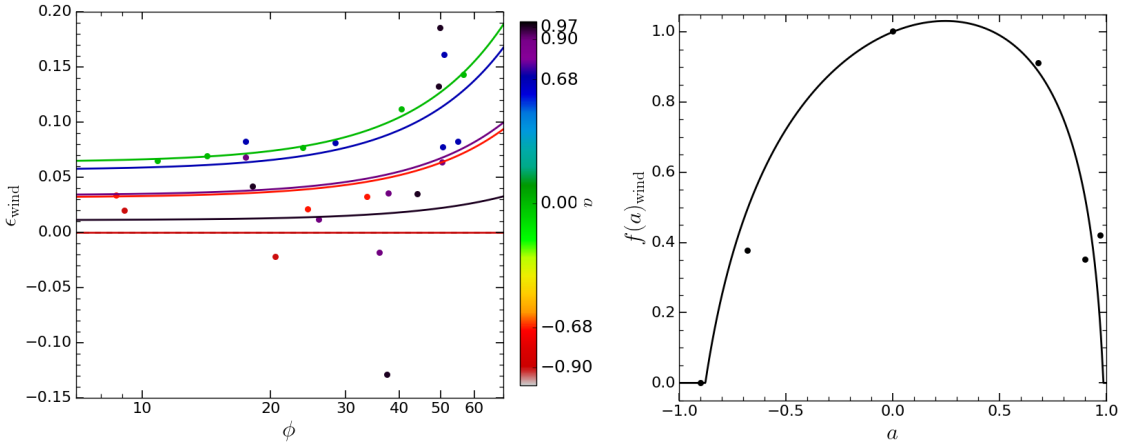

Figure 2.6: The slim disc wind efficiencies used in our model (left-hand panel), obtained using data from the simulations performed by Ricarte et al. (2023). The points show average values of the wind efficiency for each individual simulation performed by Ricarte et al. (2023), where the $x-$axis values are the average dimensionless magnetic fluxes ϕ for each of those simulations. The wind efficiencies are obtained as described in the text. The lines represent the fitting function given by Eqn. (2.50), which includes an explicit dependence on magnetic flux, which is most apparent for the zero spin case. The right-hand panel shows the remaining dependence on BH spin, $f(a)$, which we fit using Eqn. (2.51) (see text for how we obtain the individual values of that function).

CHAPTER 3

Idealized hydrodynamical tests of active galactic nuclei jets using smoothed particle hydrodynamics

3.1 Introduction

Our accretion and feedback model, presented in Chapter 2, has been implemented into SWIFT (Schaller et al. 2024), a modern galaxy formation code. The most important addition in our model, alongside BH spin, are AGN jets as a feedback mechanism. However, before including a jet feedback mode in large cosmological simulations, it is important to verify that the underlying hydrodynamical code can realistically simulate the effects of jets on the surrounding gas.

Such hydrodynamical tests can most simply be done by simulating an individual jet episode with a constant jet power, and comparing the behaviour of such a jet with theoretical predictions (see Komissarov & Falle 1998 as an early example). Performing this kind of test is especially important for cosmological simulations using SPH codes (SWIFT being one of those), since there has been virtually no effort to simulate individual AGN jets with SPH. We note that some previous SPH simulations have included AGN jets, but these simulations were more complex (e.g. self-consistent feedback in Barai et al. 2016 or jets as a feedback mechanism

in cosmological simulations as employed by Choi et al. 2015), and thus harder to compare with theoretical expectations. In recent years, SPH codes have been upgraded in various ways in order to better deal with problems such as fluid mixing and conduction across shocks, that plague traditional SPH schemes (Hopkins 2015, Menon et al. 2015, Wadsley et al. 2017, Rosswog 2020, Borrow et al. 2022). This is particularly important for jet simulations, since they involve extreme contrasts in fluid properties.

Theoretical studies of constant-power jets, propagating in a gaseous medium with a power-law density profile, predict that all jets start off with a ballistic phase (Falle 1991, Kaiser & Alexander 1997, Kaiser & Best 2007). During this phase they easily drill through the ambient medium. After the mass of the swept-up medium has exceeded that of the jet material, the jet transitions into a self-similar phase, which should always occur at large enough distances. In this phase, the jet material experiences strong shocks and begins to inflate hot lobes of gas (also referred to as 'cocoons', e.g. Komissarov & Falle 1998, although we use the former term hereafter for consistency). These lobes then provide collimation for the jets of unshocked material. The jet-inflated lobes in this regime expand in a self-similar fashion (with a constant aspect ratio), hence the name. This phase of jet evolution is especially suitable for hydrodynamical tests of jet behaviour since the dependence of jet and lobe properties (such as length) on time, jet power and background density should be very simple.

In this chapter, we describe results of simple hydrodynamical tests, in line with the description above, performed using SPHENIX, an SPH scheme implemented in SWIFT (Borrow et al. 2022). We use a jet power and opening angle, as well as properties of the ambient medium, that are close to observed values so that the properties of our simulated jets can be meaningfully compared to observations. We stress, however, that our main aim is not to make comparisons with observations, but rather with analytical predictions, for the purpose of validating the numerical scheme. The numerical resolution we achieve, of order $\sim$ 1 kpc (within the jet-inflated lobes), is on a par with many similar simulations of AGN jets that use grid-based codes (e.g. Yang et al. 2019, Smith andJustin Donohoe 2021,Wang &

Yang 2022).

3.2 Jet and lobe evolution in the self-similar regime

We compare our simulated jets with theoretical predictions for the self-similar regime of jet lobe evolution (e.g. Falle 1991, Kaiser & Alexander 1997, Komissarov & Falle (1998); see also Begelman & Cioffi 1989 and Bromberg et al. 2011 for alternative, but similar models). In the self-similar picture, the jet is launched from a conical region defined by a half-opening angle $\theta_{\rm j}$. The physical quantities that determine the evolution of the jet and its lobes are: 1) power $P_{\rm j}$, 2) launching velocity $v_{\rm j}$ (or equivalently, mass flux $Q_{\rm j} = 2P_{\rm j}/v_{\rm j}^2$), 3) background density ρ and 4) background pressure p (or equivalently, temperature T). Note that in our notation, the jet power and mass flux refer to the total, summed over both jets.

These quantities can be combined to yield two length scales, $L_1 < L_2$. The evolutionary phase of a jet, can be determined by comparing its current length, $L_{\rm j}$, with those length scales (Komissarov & Falle 1998). In the initial phase of ($L_{\rm j} \ll L_1$), the mass in the jet is large compared to the ambient medium being swept up by the jet. The jet is denser than the ambient medium and it drills through it without significantly being slowed down, due to its large inertia. The jet head moves with a velocity equal to the launching velocity, $v_{\rm j}$, and the jet length is thus given by $L_{\rm j} = v_{\rm j}t$. The jets have not yet reached the self-similar regime while the above condition is true. We will refer to jets that are in this evolutionary phase as 'ballistic'.

The length scale L_1 represents the scale at which the mass of the swept up medium becomes comparable to the mass launched into the jet. It is given by

$$L_1 = \frac{1}{\theta_{\rm j}}\sqrt{\frac{2}{\pi\rho}\sqrt{\frac{Q_{\rm j}^3}{2P_{\rm j}}}} = \frac{2}{\theta_{\rm j}}\sqrt{\frac{P_{\rm j}}{\pi\rho v_{\rm j}^3}}. \tag{3.1}$$

The second length scale, L_2 represents the scale at which the ambient pressure

becomes important. It is given by

$$L_2 = \left(\frac{P_{\rm j}^2 \rho}{p^3} \right)^{1/4}. \tag{3.2}$$

Note that these length-scales represent dimensional combinations, and thus do not necessarily include the correct numerical factors. Furthermore, previous work implies that the transition from one regime to another, which should occur once the jet has reached L_1 or L_2, can be fairly protracted (Komissarov & Falle 1998).

The majority of observed FR-II sources are expected to satisfy $L_1 \ll L_{\rm j} \ll L_2$ (Komissarov & Falle 1998). In this regime, both the mass flux and the ambient pressure are dynamically unimportant. The jet experiences strong shocks and it is effectively slowed down. The jet head velocity is thus expected to be much smaller than the launching velocity $v_{\rm j}$. The jet comes into equilibrium with its own lobe (previously shocked particles) through recollimation (reconfinement) shocks. The jet also launches a bow shock.

Once the mass flux and external pressure are excluded, one cannot form any length-scale from the remaining dynamical quantities, with the exception of time. As a result, the behaviour of the jet-inflated lobes is expected to be self-similar (Sedov 1959), and we thus refer to jets that satisfy $L_1 \ll L_{\rm j} \ll L_2$ as being in the 'self-similar' regime. For the rest of the analysis, we assume that the background medium follows a power law in density:

$$\rho(r) = \rho_0 \left(\frac{r}{r_0} \right)^{-\beta}. \tag{3.3}$$

Including time as a dynamical quantity, one can compute a length scale of the form

$$L = \left(\frac{P_{\rm j} t^3}{\rho_0 r_0^{\beta}} \right)^{1/(5-\beta)}. \tag{3.4}$$

(Falle 1991). The actual length of the jet (and the lobe) may differ from L by some numerical factor, which can depend on the dimensionless parameters that govern the jet evolution (half-opening angle $\theta_{\rm j}$ and adiabatic index γ). The actual jet length can be computed from energy conservation if one assumes self-similarity of the lobes

and a particular type of geometry. With a cylindrical geometry, the jet length is given by

$$L_{\rm j} = c_1 \left(\frac{P_{\rm j} t^3}{\rho_0 r_0^{\beta}} \right)^{1/(5-\beta)}, \tag{3.5}$$

where c_1 is

$$c_1 = \left\{ \frac{A^4}{18\pi} \frac{(\gamma_{\rm c}+1)(\gamma_{\rm l}-1)(5-\beta)^3}{9[\gamma_{\rm l}+(\gamma_{\rm l}-1)A^2/2]-4-\beta} \right\}^{1/(5-\beta)}. \tag{3.6}$$

Here, A is the aspect ratio of the lobe (its length divided by radius, also equal to $1/\theta_{\rm j}$ for cylindrical jets), and $\gamma_{\rm l}$ and $\gamma_{\rm c}$ are the adiabatic indices of the lobe and ambient gas, respectively (Kaiser & Best 2007).

3.3 Numerical implementation

We use the open-access[1] SWIFT hydrodynamics and galaxy formation code (Schaller et al. 2024), and the SPHENIX hydrodynamics scheme implemented therein (Borrow et al. 2022). SPHENIX is an SPH method (Monaghan 1992a). It includes artificial viscosity, which is necessary in order to capture shocks since traditional SPH is dissipationless. SPHENIX also includes artificial conductivity, which helps reduce unwanted surface tension otherwise present in SPH simulations (Agertz et al. 2007, Sijacki et al. 2012, Nelson et al. 2013), allowing for mixing between flows that are in pressure equilibrium but contrasting in temperature and/or density.

Both artificial viscosity and conductivity are crucial in our simulations: artificial viscosity because our jets experience strong shocks (in some cases with a Mach number, hereafter M, of $M \approx 100$), and artificial conductivity since the jet-inflated lobes feature extreme density and temperature contrasts, but are in approximate pressure equilibrium with their surroundings. An artificial viscosity limiter is included to prevent spurious viscosity in shear flows. An artificial conductivity limiter is also included, to prevent spurious energy transfer in all flows.

In our simulations we do not include radiative cooling, gravity, magnetic fields or cosmic rays, since such additional physics might cause deviations from the simple model of self-similar jet and lobe evolution. We have, however, performed runs

[1] https://swift.dur.ac.uk/

with gravity and radiative cooling as a consistency check. We found very small differences compared to purely hydrodynamical jets, which shows that the artificial conduction limiter in SPHENIX prevents spurious radiative losses, even with very poorly resolved jets. We do not include relativistic effects, since we do not include very large velocities where these effects occur (the reasoning for this choice is outlined in § 3.3.3). We therefore set the adiabatic index to $\gamma = 5/3$ for all gas in our simulations.

3.3.1 Jet launching scheme

AGN jets in an SPH code can be implemented through velocity kicks of gas particles. Given a jet power of interest, $P_{\rm j}$, the time interval at which particles need to be kicked is given by

$$\Delta t = \frac{2 \times \frac{1}{2} m_{\rm gas} v_{\rm j}^2}{P_{\rm j}}. \tag{3.7}$$

Here, $m_{\rm gas}$ is the mass of the gas particles in the simulation $v_{\rm j}$ is some arbitrary launching velocity, and the factor of 2 is present to ensure that two particles are always kicked (in opposite directions, ensuring conservation of momentum). The total number of kicking events can be calculated as

$$N_{\rm j} = \frac{T_{\rm j}}{\Delta t} = \frac{T_{\rm j} P_{\rm j}}{m_{\rm gas} v_{\rm j}^2}, \tag{3.8}$$

where $T_{\rm j}$ is the lifetime of the jet episode. The larger $N_{\rm j}$, the better the jet will be resolved (as one might expect, and as will be clear from our results).

$N_{\rm j}$ can be increased by decreasing the particle mass or launching velocity, or by increasing the total energy launched into the jet (by increasing either the jet power or jet duration). When attempting to simulate the self-similar regime of jet evolution, one also has to keep in mind that the length scale L_1 (Eqn. 3.1) needs to be small, while the length scale L_2 (Eqn. 3.2) conversely needs to be large. These represent additional constraints on the choice of parameters characterizing the jets and the ambient medium.

The most natural implementation of AGN jets in SPH would involve kicking particles from the smoothing kernel of the central black hole. The SWIFT hydro-

dynamical code, which we utilise here, includes black holes so this scheme is easy to implement (see Chapter 5, where we use such an implementation in the context of self-consistent accretion and feedback in idealized galaxy groups and clusters). We have attempted this scheme for the present study, and we find that it works in general. However, at very high resolutions (more than $10^4 - 10^5$ launching events per few dozen Myrs, the kind of resolution we are interested in when testing jet hydrodynamics), this scheme can become computationally expensive and unreliable. In particular, the black hole requires very small time steps between kicking events, smaller than the typical evolutionary time step of the particles kicked into the jet. This can result in particles being kicked more than once.

For simplicity, we instead populate the initial conditions with a reservoir of particles that are to be used for jet launching, therefore bypassing any issues that might arise in a setup using a BH. In general, the reservoir we use takes the shape of two cones (defined by some half-opening angle $\theta_{\rm j}$), placed along both directions of the z axis, up to some maximal radius (10 kpc in all our simulations). We obtain these cones by creating a uniform cube with a grid of particles, and then cut out the desired cones. These particles are not allowed to interact with any other particles until they have been kicked and have cleared the region associated with the reservoir. The particles are launched progressively from the outside-in, so that they can immediately interact with the ambient medium, instead of traveling through the frozen-in reservoir. The total number of particles in the reservoir exactly matches the number to be launched into the jets we are simulating. The density of this reservoir is $\approx 10^{-27}$ gcm^{-3}, which is ≈ 10 times less than the density of the ambient medium. In the case of ballistic jets with null opening angle (only a single simulation), we instead use a spherical reservoir with a radius of 5 kpc, from which particles are launched parallel to the $z-$axis. We have tested a cylindrical reservoir of similar size, but found the differences to be negligible.

3.3.2 Physical setup

The structure of realistic gaseous haloes, representing the intracluster medium, can be represented using a density profile that is constant in the centre, and falls off as

$r^{-\alpha}$ at large distances, with $\alpha \approx 2$ (Komatsu & Seljak 2001, Croston et al. 2008), at least out to roughly the virial radius (at larger distances the profile drops more sharply, Eckert et al. 2012). Many jet simulation studies incorporate profiles similar to this (e.g. English et al. 2016, Weinberger et al. 2017b). While it may be more realistic to launch jets into such a profile, we choose instead a constant density medium ($\alpha = 0$) for most of our simulations. We do this since the jet length should scale as $t^{0.6}$ in such a setup, whereas at large distances in a realistic profile ($\alpha = 2$), the jet length scales as t. This is due to the jet-inflated lobes not behaving self-similarly for $\alpha = 2$, whereas for $\alpha = 0$, they are firmly in the self-similar regime, provided an appropriate choice of parameters.

We launch most of our jets into the same background medium, with a constant density ρ_0 (the value we choose is discussed in the next subsection). In this case we choose periodic boxes that are slightly longer in each dimension ($\approx 20\%$) than the predicted sizes of the jets based on the theory outlined in § 3.2. We find that this works well in all cases, and the jets do not reach the edges of the box by the end of the simulation.

We have performed a few runs where the ambient medium instead features a power-law density profile, such that $\rho \propto r^{-\alpha}$. We restrict ourselves to $\alpha < 2$, since the self-similar solution from the previous section is applicable only in this regime. In these cases we use a Navarro et al. (1996a) (NFW) background gravitational potential, and we choose the gas pressure (and therefore the temperature) in such a way that the gaseous halo is held in hydrostatic equilibrium. For this purpose we choose NFW parameters representing a galaxy cluster with a halo mass $M_{\rm h} = 10^{15}$ $\mathrm{M}_\odot$ at redshift $z = 0$, virial radius $R_{\rm v} \approx 2$ Mpc and concentration parameter $c = 4$. Since it is impossible to implement a power-law density profile such that the power law is valid all the way to the centre of the halo, we use a cored β-profile

$$\rho(r) = \frac{\rho_{0,\beta}}{[1 + (r/r_{\rm c})^2]^{3\beta/2}}, \tag{3.9}$$

where we choose the value of β to match our desired value of the slope at large radii, $3\beta = \alpha$. We choose a small core, $r_{\rm c} = 10$ kpc, which matches the size of our

jet reservoir. The normalisation $\rho_{0,\beta}$ is then calculated so that the total mass of the gaseous halo is 15% of the total halo mass. This choice is not necessary in this application, since we are only interested in how our jets compare with theory (and not how realistic they are), but we make it for simplicity.

3.3.3 Simulations

In Table 6.1 we summarise the parameters used for all of our simulations. In the first row we specify the fiducial choice of parameters for our constant-density ambient medium simulations. This choice corresponds to: 1) $m_{\rm gas} = 1.81 \times 10^5$ M$_\odot$, 2) $P_{\rm j} = 10^{46}$ erg/s, 3) $v_{\rm j} = 15000$ km/s and 4) $\theta_{\rm j} = 10^\circ$. We vary all of these parameters, but we do not vary the ambient density, which we choose to be $\rho_0 = 1.2 \times 10^{-26}$ g/cm^3. We also do not vary the jet duration, which we set to $T_{\rm j} = 100$ Myr.

Our chosen ambient gas density is the typical central density of a galaxy cluster with a halo mass $M_{\rm h} = 10^{15}$ M$_\odot$, a virial radius 2 Mpc, and a baryonic mass ratio 0.15. The initial temperature of this gas is set to $T = 10^{7.2}$ K (and this is also the temperature of the gas kicked into the jets). This value is somewhat low for the cores of realistic clusters, but we choose it to ensure that our jets never reach the regime in which ambient pressure is important (Eqn. 3.2). In any case, our aim is not to produce perfectly realistic jets, but rather to check that SWIFT can correctly simulate jets.

Our fiducial mass resolution is 10 times better than the EAGLE simulation (Schaye et al. 2015). At this mass resolution, the typical smoothing length (corresponding to spatial resolution) is ≈ 1 kpc in the ambient medium and ≈ 7 kpc in the jet-inflated lobes, which are about 300 times less dense than the ambient medium. At our highest resolution level, the typical smoothing lengths are instead ≈ 0.3 and ≈ 2 kpc for the two cases. For comparison, the lobe is roughly 400 kpc long and 50 kpc in radius at the end of the simulation (see Fig. 3.4).

The jet power we use is relatively high compared to previous similar simulations (e.g. Weinberger et al. 2017b, Bourne & Sijacki 2017). However, observations imply that jet episodes with such powers are frequent in the most massive galaxy clusters (Kino & Kawakatu 2005, Hlavacek-Larrondo et al. 2012b). Our choice of half-

opening angle is somewhat large compared to most real jets (Pushkarev et al. 2009), but we choose such a value to ensure that jets are ballistic for as short a time as possible (Eqn. 3.1). In addition, observed subrelativistic jets have similarly large opening angles (Pushkarev et al. 2017).

The jet launching velocity, $v_{\rm j}$, is a very important parameter in our simulations, and it has both a physical and numerical role. On the physical side, the launching velocity determines when the jet reaches the self-similar phase of evolution, as well as whether it is in the relativistic regime. In addition, increasing the velocity leads to higher typical temperatures in the jet lobes, as well as lower densities. This latter fact is due to the kinetic energy per particle scaling as $\propto v_{\rm j}^2$, so the total mass and number of particles in the jets and lobes scale as $1/v_{\rm j}^2$, under the assumption that the energy within the jets and lobes is kept fixed. The same scaling ties into the role of the launching velocity as a numerical parameter. Less massive jets and lobes are represented with a smaller number of particles (given a constant jet power), so they are more poorly resolved.

We do not simulate relativistic or mildly relativistic jets with $v > 0.3c$ representing some of the stronger/younger Fanaroff-Riley (FR) II sources (Wardle & Aaron 1997, Jetha et al. 2006, O'Dea et al. 2009, Snios et al. 2018), which have been the focus of many recent simulation studies (Walg et al. 2013, Hardcastle & Krause 2013, Tchekhovskoy & Bromberg 2016, Matsumoto & Masada 2019, Perucho et al. 2022). This is because such jets would be poorly resolved in our simulations. Due to this restriction, we launch jets with subrelativistic velocities of order $0.1c$ at most, representing FRI sources or FRII sources that have either significantly decelerated or entrained significant amounts of ambient material on a kpc scale (Bicknell 1995). The differences between subrelativistic and relativistic jets, in terms of their properties such as the lengths or shapes of the lobes, are minimal (of order tens of percent), and they arise largely from the different adiabatic indices of the lobe material (4/3 versus 5/3).

The fiducial mass resolution we have chosen results in a total of $\approx 10^8$ particles in the simulation, while the jet power and launching velocity, in combination with the mass resolution and jet duration, yield $\approx$ 40000 particles launched per jet.

The actual number of particles in the jets and lobes may be larger due to ambient particles being swept up.

When varying any of the four parameters listed at the beginning of this subsection, we keep other parameters fixed. The variations we have done for our constant-density ambient medium case are given in the second row of Table 6.1. We have simulated jets with numerical resolutions corresponding to ten times worse than the EAGLE simulation ($m_{\rm gas} = 1.81 \times 10^7$ M$_\odot$), down to 3160 times better ($m_{\rm gas} = 5.73 \times 10^3$ M$_\odot$), differing by factors of 3.16 (logarithmic interval of 0.5). Our highest resolution simulation has a total of 2.8×10^9 particles, and 1.4×10^6 particles kicked into each jet. The lowest resolution one has only 450 particles per jet. We vary jet powers between 10^{45} erg/s and 10^{47} erg/s, launching velocities between 3750 km/s and 60000 km/s, and half-opening angles between 0° and 25°.

Finally, in the case of power-law gaseous atmospheres, we have performed three simulations, with $\alpha = 0.5$, $\alpha = 1$ and $\alpha = 1.5$. The parameters of these simulations are listed in the third and final row of Table 6.1. These power-law cases required a different set of parameters for two reasons. We found that the length scales L_1 and L_2 were larger and smaller, respectively, with our fiducial choice of jet-related parameters, than they were in the constant-density case. This means that the jets took a longer time to reach the self-similar phase, and would also take a shorter time to exit the same phase due to the external pressure becoming important.

Given these restrictions, we chose to modify our fiducial parameters in the following way. We launched the jets with: 1) a jet power of $P_{\rm j} = 10^{47}$ erg/s in order for the length scale L_2 to lie at comfortably large distances compared to the self-similar prediction (see Eqn. 3.2, although note that its meaning is somewhat moot in power-law atmospheres), 2) a jet velocity of $v_{\rm j} = 0.2c = 60000$ km/s, bringing L_1 down to $L_1 = 5$ kpc (given the new jet power), 3) a jet duration of $T_{\rm j} = 40$ Myr to prevent the jets from reaching large distances (wishing to avoid both L_2 and the virial radius). With these changes to the physical parameters, the number of particles launched into the jets is a quarter of that in our standard constant-density simulations. For this reason we have decreased the particle masses in the power-law simulations (i.e. increased the resolution) by a factor of four. This ensures that the

Table 3.1: List of all simulations and the parameters we use. In the first row we specify the parameters of our fiducial simulation with a constant-density ambient medium. In the second row we specify the parameters that are varied for this same case. In the final row we specify the parameters of the case with a power-law ambient density profile. The parameters are, in order: 1) $m_{\rm gas}$ - mass resolution, 2) $P_{\rm j}$ - jet power, 3) $v_{\rm j}$ - jet velocity, 4) $\theta_{\rm j}$ - jet half-opening angle, 5) ambient medium density ρ - constant value or power law slope and 6) $T_{\rm j}$ - jet duration.

$m_{\rm gas}$ [$\rm M_\odot$]	$P_{\rm j}$ [$\rm erg s^{-1}$]	$v_{\rm j}$ [$\rm km s^{-1}$]	$\theta_{\rm j}$ [°]	ρ [$\rm g cm^{-3}$]	$T_{\rm j}$ [Myr]
1.81×10^5	10^{46}	1.5×10^4	10	1.2×10^{-26}	100
$5.73 \times 10^3 - 1.81 \times 10^7$	$10^{45} - 10^{47}$	$3.75 \times 10^3 - 6 \times 10^4$	$0 - 25$	1.2×10^{-26}	100
4.53×10^4	10^{47}	6×10^4	10	$\propto r^{-\alpha}$, $\alpha = 0.5 - 1.5$	40

jets are resolved with the same number of particles.

3.3.4 Definition of jet lobe

All simulations of jets exhibit the so-called lobe, made up from hot, shocked gas that was previously part of the jet. Jets also invariably launch a bow shock that propagates through the ambient medium. The model of self-similar lobe evolution predicts that their aspect ratio should be constant, and it predicts the same for the ratio of energy in the lobes versus the energy added to the ambient medium (as well as for how much energy is in kinetic and thermal forms). In order to test these predictions, it is important to numerically determine which particles belong to what we might visually call the jet or the jet lobe, with remaining particles classified as making up the ambient medium.

Empirically, we find that the peak temperature $T_{\rm p}$ achieved by gas particles serves well to define the lobe. We use a threshold value $T_{\rm p,min}$, and all particles whose peak temperature was at some point above this value, i.e. $T_{\rm p} > T_{\rm p,min}$, are defined as constituting the lobe. This definition is motivated by the fact that particles that reach extremely high temperatures are exclusively located in the lobe, whereas the

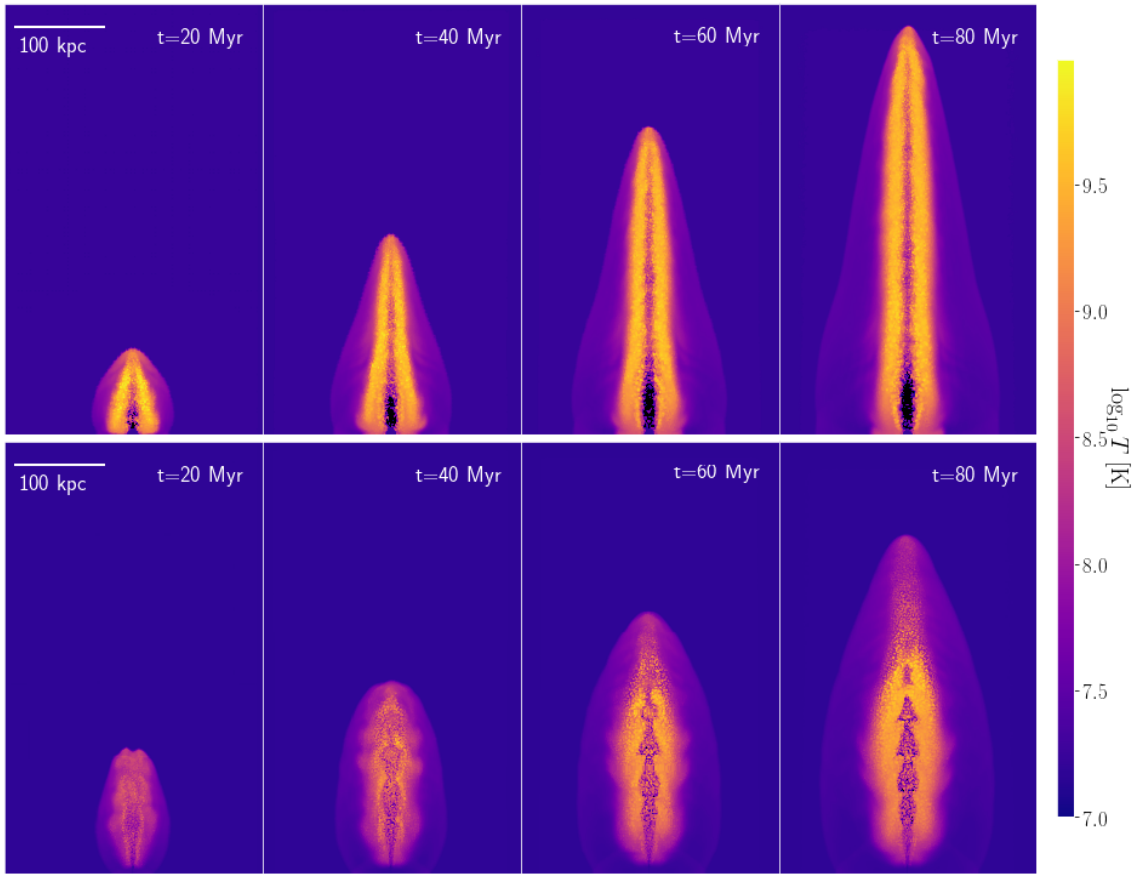

Figure 3.1: Visualisations of the gas temperature distribution for a ballistic jet (effective half-opening angle $\theta_j = 0°$, top) and a jet in the self-similar evolutionary phase (half-opening angle $\theta_j = 10°$, bottom) at different times. All other parameters correspond to our fiducial choice, given in the first row of Table 6.1. Colours represent the temperature of the gas, as given by the colour bar. The panels show slices 10 kpc in depth.

shocked ambient medium experiences temperature jumps of a factor of several at most.

The appropriate value of $T_{\rm p,min}$ varies from simulation to simulation, but it can easily be estimated (to better than an order of magnitude) by assuming that all of the kinetic energy launched into the gas becomes thermalised. From this condition, the characteristic temperature of the lobes is $T_{\rm lobe} \approx \mu m_{\rm p} v_{\rm j}^2 / 3k_{\rm B}$, with $\mu = 0.6$ the mean molecular weight, $m_{\rm p}$ the proton mass and $k_{\rm B}$ the Boltzmann constant. In reality the lobes are somewhat less hot since not all of the kinetic energy is thermalised. The appropriate value of $T_{\rm p,min}$ can thus be expected to be a factor of several times below $T_{\rm lobe}$. We find the particular value that we use by plotting the total mass in the lobe $M_{\rm lobe}$ versus $T_{\rm p,min}$, the defining peak temperature that determines how many particles will be assigned to the lobe. We find that this dependence exhibits a change in slope at some critical value of $T_{\rm p,min}$. Using a larger than the critical one results in fewer and fewer particles (that are part of the lobe) being assigned to the lobe, whereas using a lower one causes ambient medium gas to be assigned to the lobe (usually ambient gas particles near the jet head, where strong shocks are occurring). For our fiducial simulation, with a jet launching velocity of $v_{\rm j} = 15000$ km/s, we use $T_{\rm p,min} = 5 \times 10^8$ K. This value is ≈ 30 times larger than the initial temperature of the ambient medium, and ≈ 10 times smaller than the characteristic temperature of the lobe, which is in this case $T_{\rm lobe} \approx 5 \times 10^9$ K.

We also define unshocked, fast-moving, recently launched particles as constituting the lobe, which means that we include the jets into the lobes (for simplicity). Given a launching velocity $v_{\rm j}$, we thus define all particles with $|\mathbf{v}| > 0.5 v_{\rm j}$ as also being part of the lobe. Note that the factor 0.5 here is fairly unimportant; using any critical velocity value that is significantly above the sound speed of the ambient gas leads to almost all of the unshocked particles being included in the lobes, and none of the ambient medium. Particles not belonging to the jets or the lobes are classified as part of the ambient medium.

3.3.5 Measuring the energetics and jet/lobe lengths and radii

Given the above definition of the lobe, measuring the thermal and kinetic energy gains of both the lobes and the ambient medium is trivial. We calculate the kinetic energy gain of either component by calculating the total kinetic energy in the particles (all of the gas in the simulation is initially not moving), while the thermal energy gain is calculated relative to the initial temperature of all of the gas, which is $T_0 = 10^{7.2}$ K.

The length of the lobe is calculated by taking the mean distance from the origin of n farthest particles (ordered along the axis of launching), with n determined to be 3% of all of the particles launched into the jet. With this definition, n is both resolution and time-dependent. For the radius of the lobes, the procedure is similar, but we use cylindrical distances from the launching axis. Note that this choice yields the maximal radius of the lobe, not the average radius. For both the length and the radius of the lobe we use a mean of the values calculated for both of the jets.

3.4 Results: general properties of simulated jets

3.4.1 Ballistic jets

In this section we will discuss properties of jets launched into a constant-density ambient medium. Before focusing on self-similar jet and lobe evolution, it is worth addressing some properties of ballistic jets simulated with SWIFT. According to Eqn. (3.1), jets should remain ballistic at arbitrary distances in the $\theta_\mathrm{j} = 0^\circ$ case. The top panels of Fig. 3.1 show visualisations of jets from a simulation with a null half-opening angle, simulated at a mass resolution 10 times better than the EAGLE simulation ($m_\mathrm{gas} = 1.81 \times 10^5$ M$_\odot$). The jet power is $P_\mathrm{j} = 10^{46}$ erg/s, and the launching velocity $v_\mathrm{j} = 15000$ km/s (i.e. these parameters, other than the opening angle, match our fiducial choice listed in Table 6.1).

The figure shows a few visually distinct regions. The particles launched into the jets constitute a thin, cylindrical region (often called the jet spine) of unshocked, cold gas (with the temperature the same as the ambient medium). This gas experiences

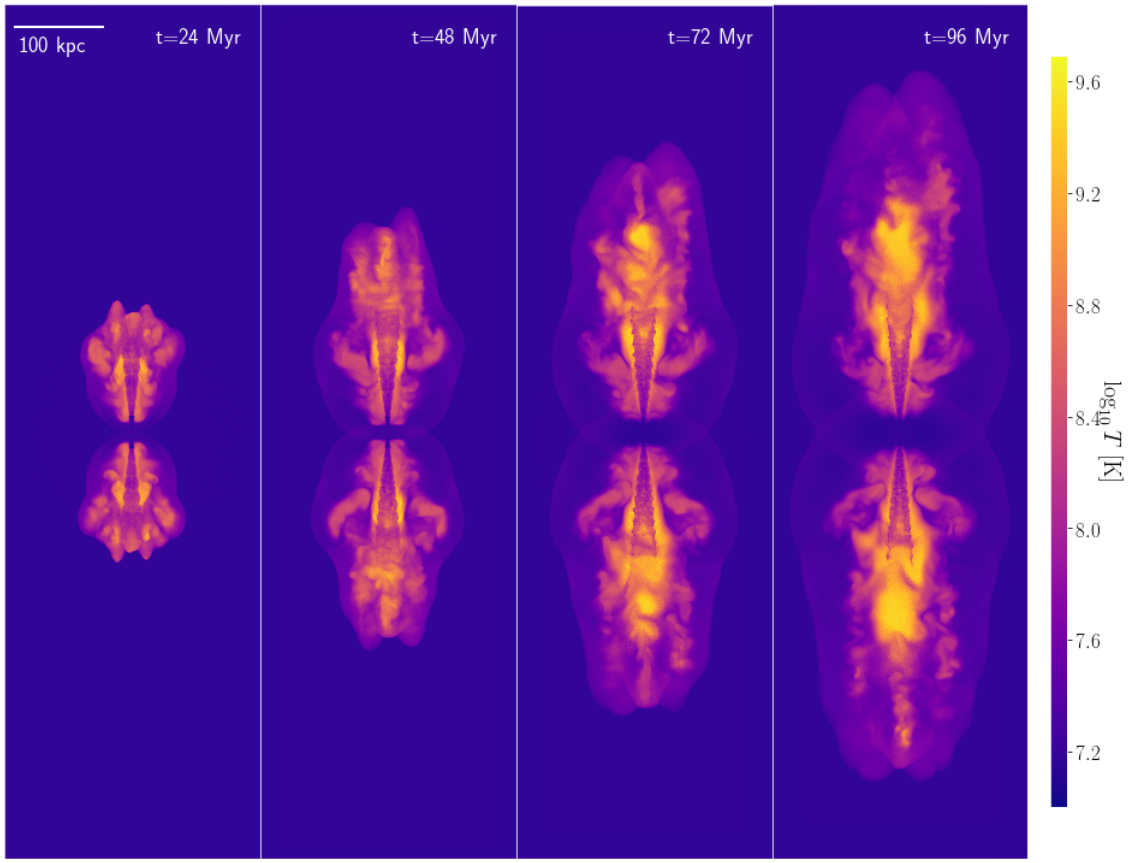

Figure 3.2: Visualisations of the gas temperature distribution in our highest resolution jet simulation, with particle mass $m_{\rm gas} = 5.73 \times 10^3$ M$_\odot$, at different times. All other parameters correspond to our fiducial choice, given in the first row of Table 6.1. Colours represent the temperature of the gas, as given by the colour bar. The panels are 10 kpc in depth.

some shocking all the way from the launching region to the jet head. The gas shocked in this way makes up the hot lobe that can be seen surrounding the jet itself. Finally, the action of the jet also launches a bow shock, which transitions from being strongly supersonic near the jet head to a sound wave in the perpendicular direction.

Visually inspecting the jet, we can surmise whether this jet is in the self-similar or ballistic phase. It is clear that the aspect ratio of the lobes (length vs. width) grows with time, whereas in the self-similar case it should remain constant. Furthermore, we can see that the jet increases in length by an approximately equal amount with each snapshot, indicating that the jet velocity is nearly constant (as it should be in the ballistic regime). More quantitatively, we find the power-law slope of the $L_{\rm j} - t$ dependence to be 0.9, very near the ballistic value of 1.

The typical velocity of the jet head is found to be $\approx$ 5500 km/s. However, a ballistic jet should drill through the medium at exactly the launching velocity, which is 15000 km/s in this case. Equally, one might wonder why is there significant shocking of the jet particles along the way from the launching region to the jet head, whereas we would expect all shocks to happen at the latter location (for ballistic jets). We have performed other simulations of ballistic jets, which we do not show here (since we focus on self-similar jets), where we find that this discrepancy is due to numerical resolution. In particular, we find that increasing the resolution leads to less shocking occurring inside the jet spine. The jet head velocity is consequently larger, and the jets thinner and denser. We find that simulated jets are close to being fully ballistic only at very high resolutions ($> 10^5$ particles per jet).

3.4.2 General properties of jets in the self-similar phase

In the bottom panels of Fig. 3.1 we show a jet from a simulation with an equivalent set of parameters as the previously discussed ballistic jet simulation, but with a half-opening angle of 10° rather than 0°. The jet power, $P_{\rm j} = 10^{46}$ erg/s and the launching velocity $v_{\rm j} = 15000$ km/s, yield the L_1 length-scale of 7.7 kpc, on order of our launching region size. This means that jets should reach the self-similar phase almost as soon as they are launched. The L_2 length scale is 970 kpc, so ambient pressure should not be important.

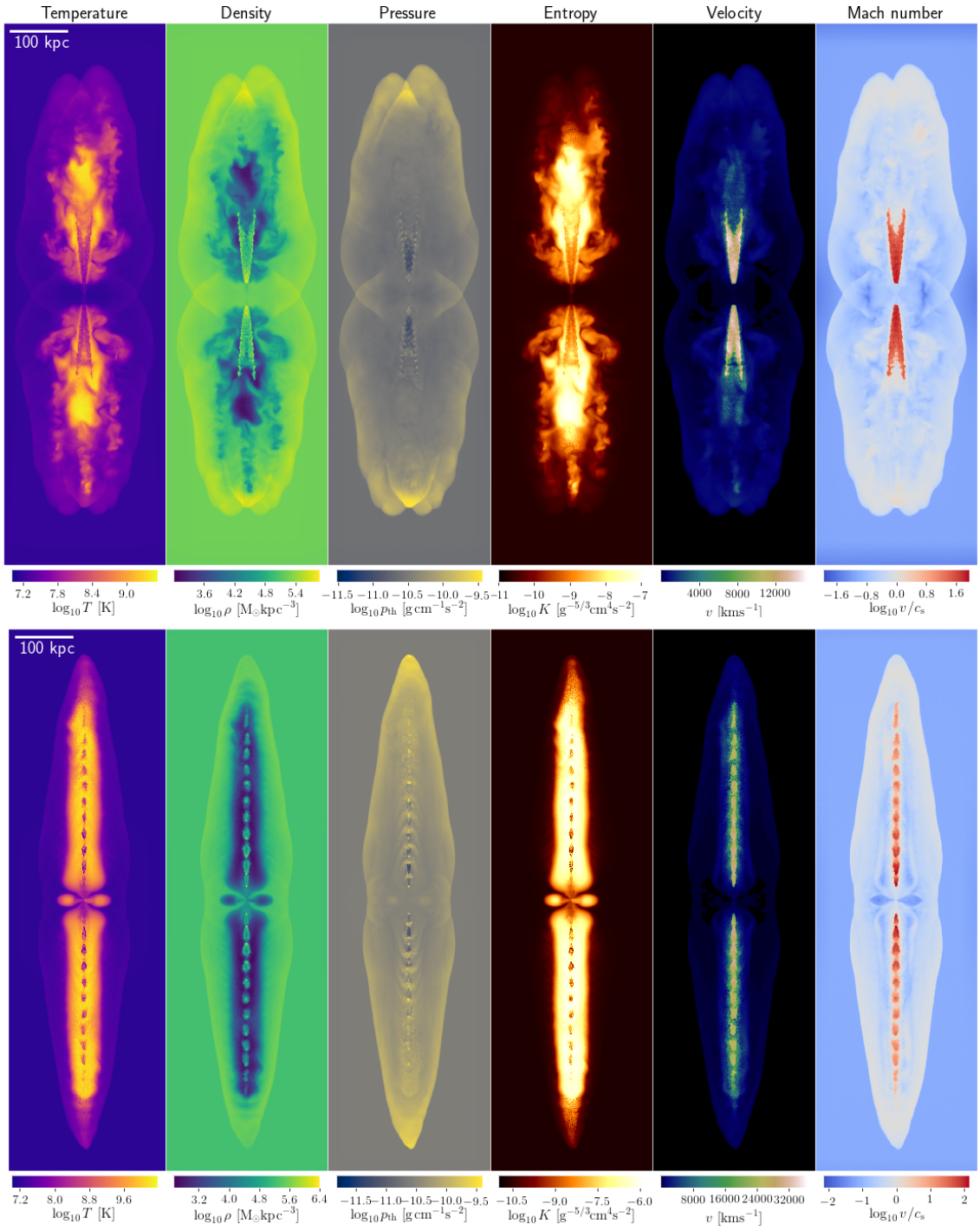

Figure 3.3: Top: properties of our highest resolution jet simulation after 96 Myr (with a mass resolution $m_{\rm gas} = 5.73 \times 10^3$ M$_\odot$, while other parameters correspond to our fiducial choice, given in the first row of Table 6.1). Bottom: properties of a simulation with a slightly lower resolution, $m_{\rm gas} = 1.81 \times 10^4$ M$_\odot$, a smaller opening angle $\theta_{\rm j} = 5°$ and a larger jet velocity $v_{\rm j} = 30000$ km/s, after 48 Myr. Each panel is 10 kpc in depth and shows different gas properties, as given by the titles and legends.

This jet is shorter and wider than the ballistic one, as one might intuitively expect. The central outflow of unshocked gas no longer forms a thin spine; this jet gas instead flows conically until it is recollimated at distances of $\approx$ 50 kpc (this is referred to as recollimation since all jets are initially collimated at small distances, e.g. Park et al. 2019, Chatterjee et al. 2019). The recollimation is driven by previously shocked jet gas, which constitutes a hot lobe surrounding the unshocked jet. The collimated gas then expands and collimates again in an oscillatory fashion; these spatially periodic recollimation shocks are expected theoretically (Falle 1991, Bamford & Komissarov 2018), have been found in other simulations (van Putten 1996, Mizuno et al. 2015, Hervet et al. 2017, Bodo & Tavecchio 2018, Gourgouliatos & Komissarov 2018, Smith & Donohoe 2019) and could explain multiple hotspots observed in some radio jets (Rees 1978, Dreher & Feigelson 1984, Hardcastle et al. 2003).

In Fig. 3.2 we show a visualisation of our highest-resolution jet simulation, with the same set of parameters but simulated at a resolution of $m_{\rm gas} = 5.73 \times 10^3$ M$_\odot$ (316 times better than EAGLE resolution). The jet shown exhibits clear signs of a conical outflow of particles, which is collimated at the point where significant shocking begins to occur (visible by a change in temperature). Unlike the lower-resolution simulation, we see no sign of multiple recollimation shocks. Based on analytical expectations (Eqn. 26 from Kaiser & Alexander 1997), the initial recollimation shock should occur at $\approx$ 60 kpc along the z axis for our jets. We find that the cone begins to lose coherence at roughly such a distance, albeit somewhat too far ($70 - 100$ kpc, difficult to pinpoint exactly since the outflow is shocked earlier in the centre of the cone than at the edges).

Due to instabilities, we find that the jet lobe does not exhibit a simple ellipsoidal shape. The lobe is also not very homogeneous in gas temperature (as well as other properties; see Fig. 3.3), and this is likely the reason why there are no multiple recollimation shocks (recollimation requires uniform pressure from all sides). For the same reasons, the bow shock created by the jet exhibits some irregularities. The deviation from a smooth ellipsoidal shape (which we do find at lower resolutions, see Fig. 3.6) could be explained in a few ways:

1. Usage of a fairly low launching velocity means that the jet is heavy, and thus mixes with the ambient medium less easily (Rossi et al. 2008, English et al. 2016, Donohoe & Smith 2016).

2. Only the largest-wavelength Kelvin-Helmholtz instabilities are resolved in this simulation. In other words, it is possible that at even higher resolutions, a jet lobe would again be recovered, but a highly turbulent one.

3. The recollimation shock is expected to occur at a large distance from the jet origin (60 kpc). A lobe is not expected to exist until the jet has reached that distance. A lobe-like feature does appear and become more prominent from snapshot 2 to 3, and 3 to 4 in Fig. 3.2. If the jet was allowed to become much larger than the distance to the recollimation shock, a clear lobe would likely be visible. This is supported by the equivalent lower-resolution jet also having a clear lobe only at later snapshots.

In the top panels of Fig. 3.3 we show several different gas properties in the high-resolution jet simulation after 96 Myr of evolution. The conical outflow is constituted by cold, dense and fast-moving gas, with a high Mach number ($M \approx 10 - 40$). This gas has a low entropy and is under-pressured compared to the jet lobe. This causes a collimation of the outflowing particles and subsequent shocking.

The jet lobe, constituted from previously shocked jet particles, is of high temperature and low density (by a factor of up to ≈ 300 relative to the ambient medium, although this varies greatly within the lobes), as well as in pressure equilibrium. Its high entropy indicates that this gas has experienced significant shock heating. The typical velocity in the jet lobe is of order a few $\times$ 1000 km/s, much lower than the launching velocity. Furthermore, although not visible on this plot, the velocity is not only in the z-direction. In particular, near the base of the jet, the lobe particles move in the direction opposite of the general jet direction, constituting the so-called backflow (Lind et al. 1989, Rossi et al. 2008, Cielo et al. 2014, Mukherjee et al. 2018).

The bow shock surrounding the jet lobes has a high density, indicating that it is constituted from particles swept up by the jet. It is mildly supersonic with Mach

number of order $M \approx 1.5$. Such Mach numbers have been found in deep X-ray observations of galaxy clusters, in the presence of weak shocks (Fabian et al. 2003, Forman et al. 2007, Snios et al. 2018), and are thought to be one of the main ways that jets can heat the intra-cluster medium in an isotropic fashion (Reynolds et al. 2001, Brüggen et al. 2007, Li et al. 2017, Weinberger et al. 2017b). Near the base of the jets, however, we find that the bow shock expands laterally at the sound speed. It is almost invisible on the entropy plot, indicating that it has experienced only mild shock heating, compared to both the lobe and the ambient medium near the jet head.

In the bottom panels of Fig. 3.3 we show a jet in the self-similar regime with a narrower opening angle ($\theta_{\rm j} = 5^\circ$) and higher launching velocity ($v_{\rm j} = 30000$ km/s). The jet power is the same, while the mass resolution is relatively fine at $m_{\rm gas} = 1.81 \times 10^4$ M$_\odot$. This would generally yield a high-resolution jet, but usage of a large launching velocity (larger by factor of two compared to our standard choice) effectively reduces the jet resolution by a factor of four. This jet exhibits an interesting streak of more than a dozen recollimation shocks, owing to the narrow opening angle and large launching velocity. The Mach number in this case reaches values up to $M \approx 100$. The large launching velocity results in very light and hot lobes with density/temperature contrasts of almost a factor of 1000, relative to the ambient medium.

3.4.3 Evolution of the jet-inflated lobe length and width

We now turn to comparing the length and radius of the lobes in our simulations to theoretical predictions of self-similar lobes discussed in § 3.2. Here we show results for our standard-resolution simulation (i.e. the one shown in the bottom panels of Fig. 3.1). We do this since for that simulation we have a relatively large number of snapshots (50), whereas we were only able to output four snapshots for the highest-resolution simulation (due to storage restrictions). We discuss the dependence of various properties on resolution in § 3.5.4.

Fig. 3.4 shows the time dependence of jet/lobe length and lobe radius (at its widest point), as well as the bow shock radius, in our standard-resolution simulation.

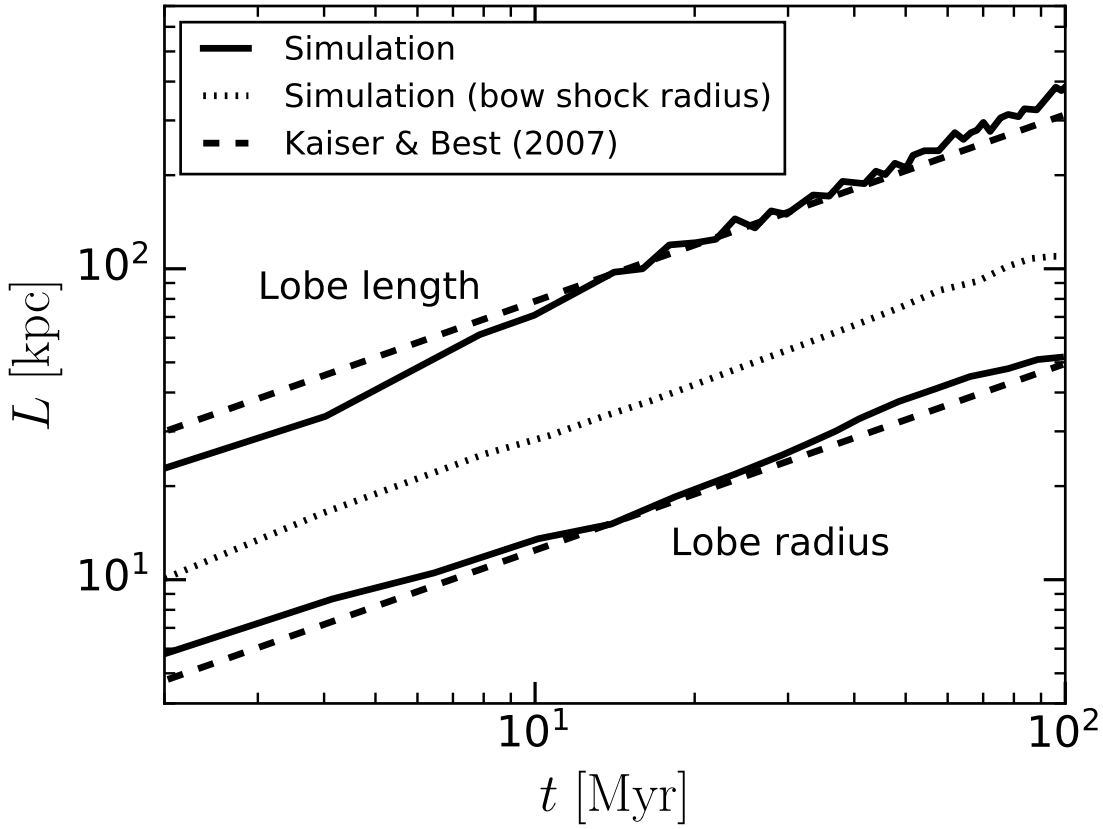

Figure 3.4: Time evolution of the jet lobe length and radius, as well as the bow shock radius (solid and dotted lines, as marked), in our standard simulation (first row of Table 6.1). These are compared to predictions from Kaiser & Best (2007) for the lobe (dashed lines; Eqn. 3.5).

We also show the prediction based on approximate theoretical models of jets and lobes in the self-similar regime (Eqn. 3.5, Kaiser & Best 2007). The agreement is clearly very good, especially at late times. This is true for both the lobe (and jet) length and the lobe radius, both of which have the same slope (0.6) in the time dependence. This means that the lobe has a constant aspect ratio, as predicted in the self-similar model, and its value is in agreement with the predictions. We find that the bow shock radius scales with time in the same way, which is also in agreement with the self-similar theory. We find that the lobe is slightly too short and too wide at $t < 5$ Myr, although this is likely related to lower resolution at these times, since only a small fraction of particles have been launched into the jets.

3.4.4 Jet, lobe and ambient medium energetics

The question of how much energy is in which component, and in what form, is an interesting one in the context of jets as a feedback mechanism that plays a role in the formation and evolution of galaxies. We again focus on the energetics of our standard-resolution self-similar simulation, rather than the high-resolution one, due to more snapshots being available. We have performed similar analyses for the higher-resolution simulations and we find that the energetics is well converged, down to the level of a few per cent. The procedure for calculating the energies in the jets and lobes (here we group the jets into the category of 'lobe' for the purpose of simplicity), as well as the ambient medium, is described in § 3.3.5.

In the top panel of Fig. 3.4.4 we show the energetics of our standard-resolution simulation. The top panel shows the kinetic and thermal energies of the jet-inflated lobes and the ambient medium. The sum of all of these energies exactly matches the total injected energy, showing that energy is conserved. During the initial phase of jet launching, the ambient medium and the lobe are approximately equal in total energy. At later times, the lobe carries about a third of the energy, whereas the remainder has been transferred to the ambient medium. At late times this ratio is constant, as one would expect for a jet in the self-similar phase (since the volume ratios of the lobe and the region defined by the bow shock remain constant, due to the constant shape of both components).

For the jet lobes we find that they are dominated by kinetic energy initially, but by the time they are turned off (at the end of the simulation), an approximately equal amount of energy is in the thermal component. The ambient medium initially has roughly equal amounts of added kinetic and thermal energy, but at later times about two thirds of the added energy is in the kinetic component. More quantitatively, at $t = 100$ Myr (the end of the simulation), the energy partition is as follows: 1) lobe kinetic - 20%, 2) lobe thermal - 14%, 3) ambient kinetic - 47% and 4) ambient thermal - 19%. Across different simulations we find that these fractions can vary, but none of the components becomes negligible.

In the bottom panel of Fig. 3.4.4 we show the energy density per unit length in the lobe, including the jet itself (normalised by the length of the jet), at the

end of the same simulation. Note that this is the energy density per unit length in slices perpendicular to the jet axis, and not just the energy density per unit length exactly along that axis. The kinetic energy density is roughly constant along the entire length, but shows signs of oscillations around the constant component. These oscillations are a result of the multiple recollimation shocks. Thermal energy is initially negligible, but reaches about the same density as the kinetic component at one third the jet length. The total energy density first rises, reaches a slight peak around half the jet length, and then falls - this is a result of the ellipsoidal shape. However, at the very end of the jet, both the thermal and kinetic energies reach a peak. This is likely a feature of the terminal shock.

3.4.5 Comparison with previous simulations

Here we will compare our results with previous hydrodynamical simulations of AGN jets, all of which were performed using grid-based codes. While there is an extensive literature of such simulations, most of these include and study the effects of more exotic physics that we do not include, such as magnetic fields (e.g. Hardcastle & Krause 2014, Tchekhovskoy & Bromberg 2016, Mukherjee et al. 2020), radiative cooling (e.g. Blondin et al. 1990, Stone et al. 1997, Guo et al. 2018) and cosmic rays (e.g. Guo & Mathews 2011, Ehlert et al. 2018, Yang et al. 2019). We thus do not compare with such studies. We also restrict our comparison to studies that launch jets into a constant-density ambient medium, since this is the focus of our study. We do not, however, restrict ourselves to comparisons with non-relativistic jet studies. We do this since the majority of the literature has included relativistic effects, and since differences between classical and relativistic jets (or more accurately, the lobes they inflate) should be minor (Kaiser & Best 2007).

The above restrictions leave only a few studies that are comparable with out study. We begin by comparing with the results of Falle (1991), who also presented the first analytical model of self-similar jet lobe expansion. They performed 3D simulations of classical jets launched into an ambient medium of fixed density. They did not use a finite (non-zero) opening angle (unlike our study), since they argue that this requires the jet launching region to be well resolved. Instead they used a

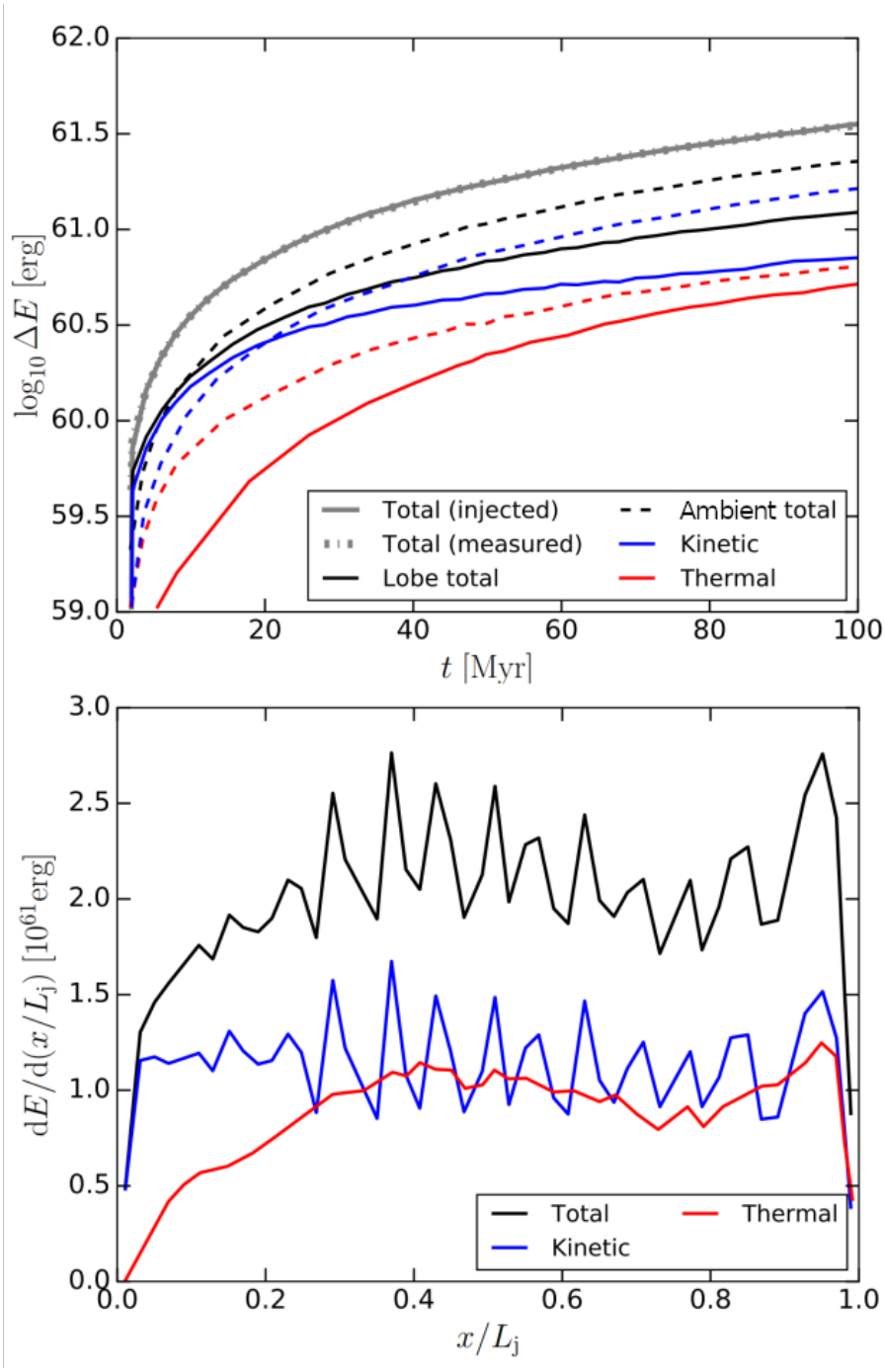

Figure 3.5: Energetics of our standard jet simulation (see the first row of Table 6.1 for a list of parameters), at $t = 100$ Myr. *Top:* Evolution of the total energies in the jet lobe and ambient medium. Blue lines represent kinetic energy, while red lines are the thermal energy. The sums for the lobe and ambient medium are given by the black lines. The grey lines represent the total injected energy and the total change in the energy of the lobes and the ambient medium. These two lines overlap, showing that energy is numerically conserved. *Bottom:* Kinetic, thermal and total energy densities per unit length along the jet axis, normalised by the total jet length.

zero opening angle and a relatively small internal Mach number, which should be similar to using a non-zero opening angle in combination with a large internal Mach number ($M \gtrsim 10$). We independently confirm this to be the case, although we do not show the results of those simulations here.

These two different set-ups lead to a similar outcome for the following reasons. In the finite-opening angle case, the outflowing jet gas has a conical geometry as a direct consequence of how it was set up. The gas is eventually recollimated once the pressure in the jet cone becomes lower than the pressure of the lobe gas. In the case of a zero-opening angle and small internal Mach number, the outflowing jet gas is instead hot enough that it expands on account of thermal pressure. It recollimates for the same reason as the finite-opening-angle case. We note, however, that the relation between an 'effective' opening angle (or aspect ratio of the lobes) and the finite Mach number is not obvious. The value Falle (1991) used is $M = 5$, which they find corresponds to $\theta_{\rm j} = 13^{\circ}$. They found that their jets inflate lobes that expand self-similarly, i.e. with a constant aspect ratio and whose length evolves with time as $L \propto t^{3/5}$. Both of these findings are in good agreement with our results (3.4). For comparison, our standard simulations have a finite opening angle of 10° and an internal Mach number of $M \approx 20$.

Komissarov & Falle (1998) performed simulations that are more directly comparable to ours, since they used finite opening angles ($\theta_{\rm j} = 5 - 20^{\circ}$) and very large internal Mach numbers. These simulations were also 3D, and included both the classical and relativistic variety of jets. They found that the latter are very similar to the former in qualitative behaviour, so we do not differentiate between the two for the purpose of this comparison. With their set-up, they also found jets whose lobes reach the self-similar regime at late times, with $L \propto t^{3/5}$. However, they found that this regime is not reached as soon as the jet is much larger in length (e.g. several times) than the transition length-scale L_1 that separates the ballistic and self-similar evolutionary period (Eqn. 3.1). Instead, the transition is complete once the *width* of the jet-inflated lobe is a few times larger than L_1. They also found that the transition is very prolonged, and there is no obvious break in the velocity, aspect ratio or jet length (i.e. the jet length does not suddenly change from scaling linearly

with time to a $\propto t^{3/5}$ scaling around L_1). Our findings are also in good agreement with these results. From Fig. 3.4 we see that there is no sudden transition at around L_1, which is ≈ 8 kpc in our case. Instead, the jet is too short but also too wide (and therefore too stumpy) compared to the self-similar prediction. By the time the width of the lobe is ≈ 15 kpc $= (2-3) \times L_1$, the jet has, however, reached the self-similar regime. Both the length and the radius of the lobe begin to agree with the self-similar prediction at the same time. This is in good agreement with the finding of Komissarov & Falle (1998), who argue that this transition is complete once the aspect ratio has increased enough to reach the value it should have in the self-similar regime.

Finally, we briefly compare with some of the newer work on hydrodynamical AGN jets by Krause et al. (2012). They used finite opening angles in a 2.5D simulation with a constant-density ambient medium. Their jets are very similar in appearance to those of Komissarov & Falle (1998), both of which show more mixing than our jets. It is hard to compare our results quantitatively (since Krause et al. 2012 do not show results on the evolution of the lobe length and radius), but we note that Krause et al. (2012) also find a distinct transition that occurs once the jets reach the L_1 length-scale.

3.5 Results: comparison of jets with varying parameters

In this section we compare the properties of jets simulated with different parameters. As in the previous section, all of these results concern our constant-density ambient medium case, with the exception of the results discussed in § 3.5.6.

The parameters we vary here are jet power, half-opening angle, launching velocity and mass resolution. The standard choice and ranges of variations are given in Table 6.1, and we also repeat the former here: $m_{\rm gas} = 1.81 \times 10^5$ M$_\odot$, $P_{\rm j} = 10^{46}$ erg/s, $\theta_{\rm j} = 10^\circ$ and $v_{\rm j} = 15000$ km/s. When varying any one of the parameters, we keep all other parameters fixed. For each variation, we have performed 5 simulations with different parameter choices (with the exception of mass resolution, where we have

performed 8 simulations in total, in order to probe the full range form very low to very high-resolution jets).

We varied the jet power by factors of $\sqrt{10} \approx 3.16$ between $P_{\rm j} = 10^{45}$ erg/s and $P_{\rm j} = 10^{47}$ erg/s, the half-opening angle in increments of 5° from $\theta_{\rm j} = 5°$ to $\theta_{\rm j} = 25°$, the jet launching velocity by factors of 2 from $v_{\rm j} = 3750$ km/s to $v_{\rm j} = 60000$ km/s, and finally the mass resolution by factors of $\sqrt{10} \approx 3.16$ from $m_{\rm gas} = 1.81 \times 10^7$ $\rm M_\odot$ to $m_{\rm gas} = 5.73 \times 10^3$ $\rm M_\odot$. Fig. 3.6 shows the visualisation of jets from all of these simulations after 100 Myr of evolution. In Fig. 3.7 we show the time evolution of jet/lobe lengths for all four cases of parameter variations.

3.5.1 Varying the jet power

The main effect of increasing the jet power, as is visible in the first row of Fig. 3.6, is the lengthening of the jets. The typical temperature of the jet-inflated lobes remains the same. This is because the launching velocity is kept constant ($v_{\rm j} = 15000$ km/s). At lower jet powers, we find a roughly ellipsoidal shape for jet lobes, and multiple recollimation shocks. At higher jet powers, instabilities destroy this ellipsoidal lobe shape. This is possibly a result of these higher-power jets being better resolved due to more particles being injected into the jets. The lobe disruption results in a much more complex structure, similar to our high-resolution simulation with standard jet power (Fig. 3.2). In our highest jet power simulation, the lobe (and therefore the bow shock) takes on a horned shape at the jet head, which is also similar to the high-resolution simulation shown in Fig. 3.2. This is a result of the transition length scale L_1 (that determines when the jet goes from the ballistic to the self-similar regime) being larger at higher jet powers (Eqn. 3.1). As a result, this jet is ballistic for a longer portion of its lifetime shown here.

From the top left panel of Fig. 3.7, we can see that the jet/lobe length evolution is self-similar for the three lower jet powers, and in fairly good agreement with theoretical predictions. At high jet powers, however, the slope of the time dependence is closer to 0.7 than the self-similar value of 0.6. This is possibly due to the already-mentioned instabilities causing some deviation from the self-similar model. Alternatively, the time dependence in these two highest power simulations could be

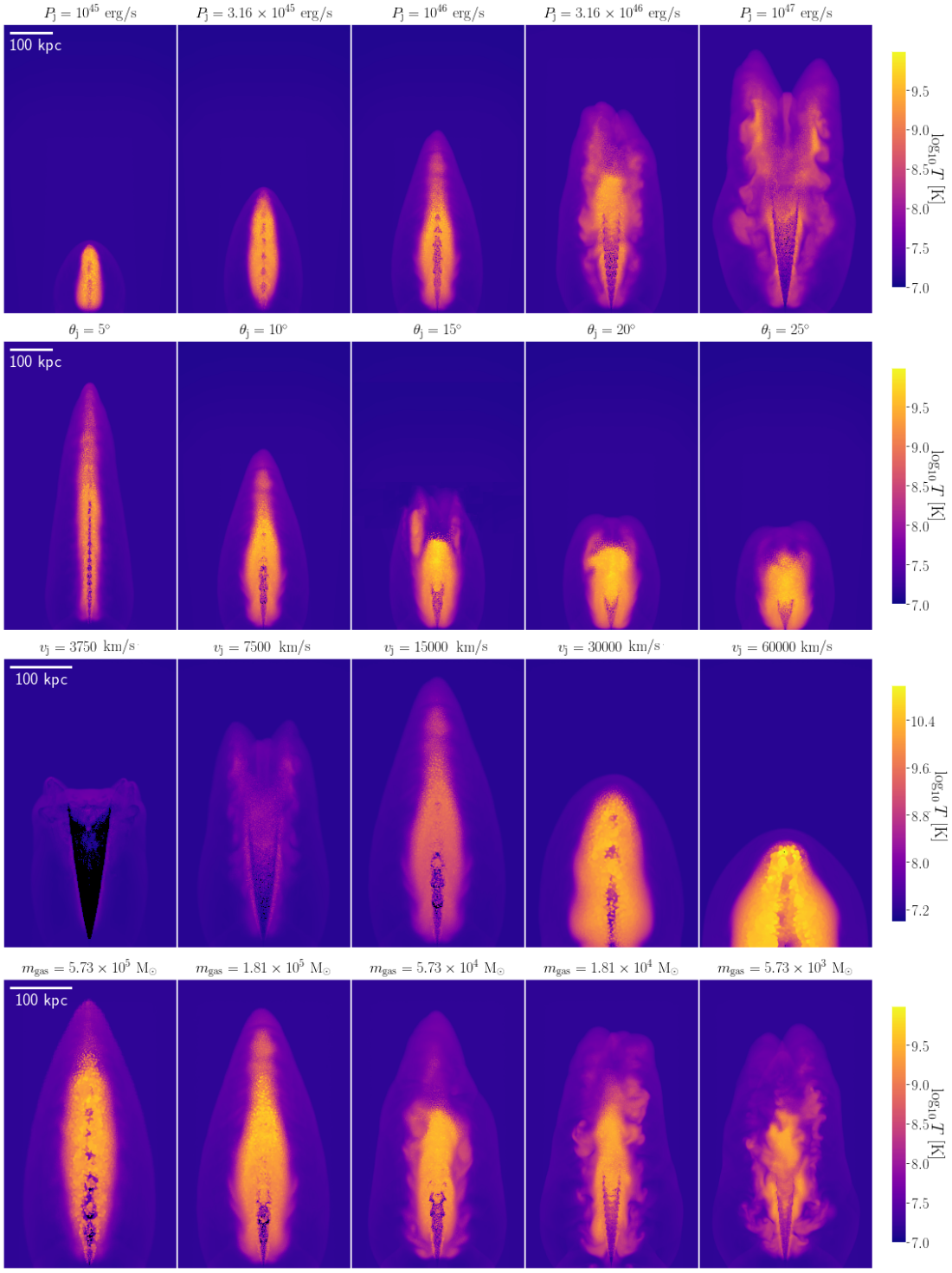

Figure 3.6: Comparison of jets simulated with different parameters (see Table 6.1 for the range of variations), after 100 Myr of evolution. The standard set of parameters is: $P_j = 10^{46}$ erg/s, $\theta_j = 10°$, $v_j = 15000$ km/s and $m_{gas} = 1.81 \times 10^5$ M$_\odot$. When varying one parameter, all others remain fixed. From top to bottom, each row contains variations of: jet power, half-opening angle, launching velocity and mass resolution. The colours show gas temperature, according to the colour bars. The panels are 10 kpc in depth.

interpreted as showing the gradual transition from a ballistic phase with $L_{\rm j} \propto t$ at early times to a self-similar phase with $L_{\rm j} \propto t^{0.6}$ at late times.

3.5.2 Varying the half-opening angle

From the second row of Fig. 3.6, we see that jets become shorter as their half-opening angle increases, also accompanied by an increase in the aspect ratio of the lobes. This is followed by the disappearance of multiple recollimation shocks. Instead, the outflow takes the shape of a simple cone with a single recollimation shock. The ballistic phase of the jet can be seen in the shocked jet gas near the bow shock. In the two lower-angle simulations, this gas takes the form of a thin strip, whereas at larger opening angles we see evidence of a horned feature. From the top right panel of Fig. 3.7 we can see that all jets, except that for $\theta_{\rm j} = 5^{\circ}$, agree well with the self-similar prediction of jet and lobe length evolution. This is because the $\theta_{\rm j} = 5^{\circ}$ jet is ballistic for a fairly long time.

3.5.3 Varying the launching velocity

The third row of Fig. 3.6 shows that the jet-inflated lobes change shape significantly, as well as becoming hotter, as we increase their launching velocity. The latter finding is expected, since there is more kinetic energy per particle available to be thermalised (due to constant total energy and a smaller number of particles). According to the self-similar model, changing the launching velocity of a jet should not result in any change in the jet/lobe length (see Eqn. 3.5). However, the launching velocity can affect when the evolution changes from ballistic to self-similar. We find that jets become shorter, relative to the $v_{\rm j} = 15000$ km/s case, as we either increase or decrease the launching velocity.

The shortening at higher $v_{\rm j}$ is unexpected since the ballistic phase should in this case be even shorter. This effect is possibly due to lower resolution from having a smaller number of particles in the jet (preventing a coherent central jet spine from traveling to larger distances). However, based on our results with varying mass resolution, down to very low resolutions of ≈ 500 particles per jet (see next

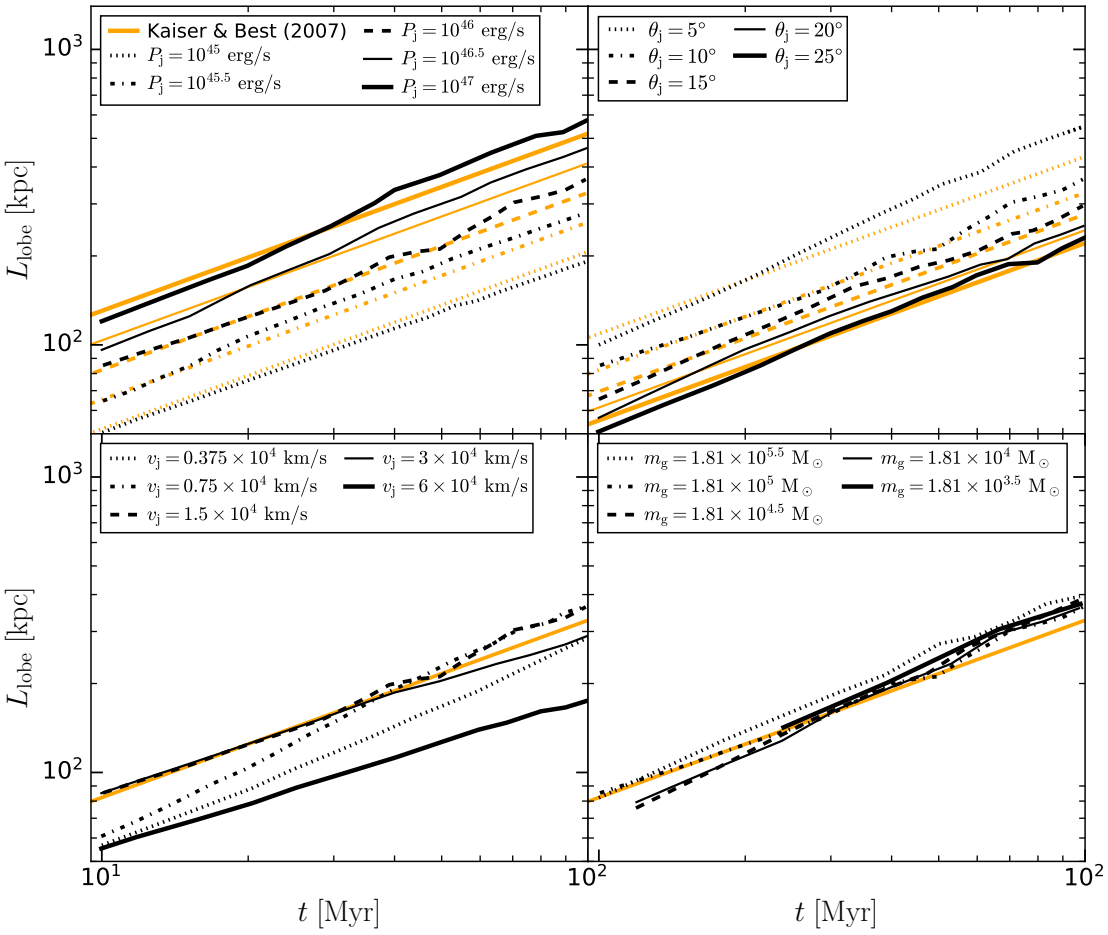

Figure 3.7: Jet and lobe length as a function of time for simulations with various parameters. The standard set of parameters is: $P_j = 10^{46}$ erg/s, $\theta_j = 10°$, $v_j = 15000$ km/s $m_{gas} = 1.81 \times 10^5$ M$_\odot$, and the range of variations is given in Table 6.1. Each panel represents a different variation of parameters, as visible in the legends (top left - jet power, top right - half-opening angle, bottom left - launching velocity, bottom right - mass resolution). Orange lines represent theoretical predictions from Kaiser & Best (2007). Where we show only one line, there should be no change of jet length with the parameter being varied.

subsection), these high-velocity jets should still reach the same size as our standard velocity case. According to the simulations by English et al. (2016) and Li et al. (2018), jet-inflated lobes in simulations with higher launching velocities should be lighter and wider at the base, due to a stronger backflow of gas near the terminal shock. We find that the two lobes are indeed wider at the base, to the point of the top and bottom lobes merging. This is possibly either due to a poorly-resolved backflow, or thermal expansion. Since the self-similar model of jet evolution takes the latter into account, but not the former, we conclude that these stubbier jets at very high velocities are likely due to a backflow, in agreement with previous simulations. We have performed other simulations with similarly large velocities, including 2D simulations with very high resolutions and near-relativistic velocities. We find the presence of strong backflows in all cases, causing the merging of the two lobes and a relatively stunted lobe.

We now move on to the lower-velocity cases. In the $v_\mathrm{j} = 7500$ km/s simulation, the jet is slightly shorter than the $v_\mathrm{j} = 15000$ km/s case, again due to instabilities being resolved better, which is itself a consequence of a larger number of particles being launched into the jets with lower velocities. However, at these velocities we are also approaching the ballistic limit, where the jet head velocity cannot be larger than the launching velocity. The ballistic nature is visible in the central jet outflow, which shows no sign of multiple recollimation shocks, but instead takes on a conical shape. Between this cone and the bow shock is a significant amount of shocked gas, indicating that this jet is not fully ballistic. The shocked gas, and therefore the bow shock, takes on a horned morphology. This can be traced to the fact that gas in the centre of the conical outflow is shocked at earlier times/smaller distances than that at the edges of the cone, resulting in a horned feature (if viewed as a slice; in 3D this feature is a ring). Similar features have been found in other simulations (Omma et al. 2004, Matsumoto & Masada 2019, Talbot et al. 2020). In the $v_\mathrm{j} = 3750$ km/s case, the jet is fully ballistic, which is visible by the conical outflow extending all the way to the bow shock. This jet is shorter because its launching velocity is smaller than the self-similar jet head velocity we expect in this case (≈ 5000 km/s). While this is a small difference, there is invariably some shocking affecting the ballistic jet,

causing its effective velocity to be less than 3750 km/s.

From the bottom left panel of Fig. 3.7 we see the evolution of jet lengths with time for all five cases. The $v_{\rm j} = 7500$ km/s jet length agrees very well with our fiducial choice $v_{\rm j} = 15000$ km/s, but only at late times (once it has reached the self-similar phase). The higher velocity jet with $v_{\rm j} = 30000$ km/s is similar to our fiducial case at early times, but slightly deviates from the theoretical prediction later on, possibly when a backflow begins to operate. Our highest velocity jet is in the self-similar regime at all times shown here, but with a lower normalisation, probably due to a backflow.

3.5.4 Varying the mass resolution

As is visible in the last row of Fig. 3.6, the mass resolution does not affect the lobe lengths and widths significantly, which is encouraging. If anything, the jet lengths decrease slightly with resolution, showing that high resolutions are not necessary in order for jets to be able to deposit their energy at large distances−a conclusion relevant for cosmological simulations. The jets are somewhat shorter at high resolutions since the Kelvin-Helmholtz instability is better resolved, and this instability increases the effective inertia of the lobes by mixing them with the ambient medium. We find that the lobes take the expected ellipsoidal shape at lower resolutions, whereas such a shape is only beginning to form at high resolutions. At the same time, due to the lack of a coherent lobe, there is only a single recollimation shock at high resolution, at the end of the conical outflow, whereas we see multiple such shocks at low resolutions. We posit that this is due to the lobe no longer being as uniform in pressure (due to instabilities), which prevents the outflowing jet gas from being uniformly collimated at regular intervals. We find that the jets and lobes have not fully converged in structure by our highest resolution level. At even higher resolutions, smaller-scale vortices caused by the Kelvin-Helmholtz instability would possibly help to recover a more ellipsoidal lobe.

At all resolutions, we can see that the main ellipsoidal lobe does not extend all the way to the bow shock, but rather out to roughly three quarters of the distance to it. The lobe is instead connected to the bow shock by a thin strip of shocked

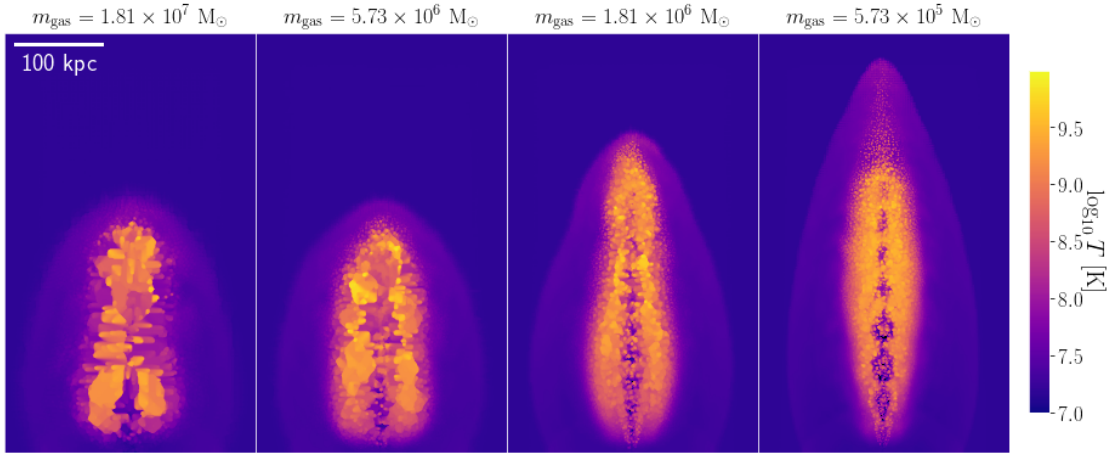

Figure 3.8: Comparison of jets simulated with varying numerical resolutions (see top of each panel, these are typical resolutions employed in cosmological simulations of galaxy clusters or large-volume cosmological simulations). The number of particles in each jet varies from ≈ 450 to ≈ 14000. Other jet parameters used are the same as the fiducal case, see Table 6.1. The panels show the jets after 100 Myr of evolution. The colours show gas temperature, according to the colour bar. The panels are 10 kpc in depth.

jet particles. These are most easily visible in the three lower resolution snapshots, and especially at $m_{\rm gas} = 1.81 \times 10^5$ M$_\odot$. These particles are among the first that were launched into the jet, and they are the relic from its ballistic phase, with the self-similar lobe being built up in its wake. At higher resolutions, these particles are not easily visible because they were likely mixed with the ambient medium. From the bottom right panel of Fig. 3.7, we can see that despite the qualitative differences in jet morphology, the evolution of jet lengths is in good agreement with the self-similar theory at all resolution levels. Our simulated jets show a slightly steeper evolution with time than expected from self-similar models, more consistent with $L_{\rm j} \propto t^{0.7}$ than $L_{\rm j} \propto t^{0.6}$.

3.5.5 Varying the mass resolution - implications for cosmological simulations

In the bottom row of of Fig. 3.6 we showed how our jets vary visually across 5 resolution levels, separated by factors of 3.16. However, the lowest-resolution case shown ($m_{\rm gas} = 5.73 \times 10^5$ M$_\odot$) is itself better than the EAGLE cosmological simulation (Schaye et al. 2015) by a factor of 3.16, and it has a relatively high number

of particles per jet, ≈ 14000. As a result, the comparisons shown in those figures, while interesting, are not necessarily relevant for cosmological simulations.

In order to probe more poorly-resolved jets, such as those likely to occur in large-scale cosmological simulations, we extend our analysis down to even lower resolutions. In Fig. 3.8 we show the equivalent visualisations of jets as in the bottom row of Fig. 3.6, but for resolutions down to ten times worse than EAGLE, i.e. $m_{\rm gas} = 1.81 \times 10^7$ M$_\odot$. The highest-resolution simulation shown is the one with $m_{\rm gas} = 5.73 \times 10^5$ M$_\odot$. As we can see, reducing numerical resolution results in a shortening of the jets and lobes they inflate. This is likely due to spherical averaging from SPH effects, as the total number of the jet particles approaches the number of particles expected in a single SPH smoothing kernel (≈ 50). Despite the shortening, the jet (lobe) length is still within 15% of the self-similar prediction. This is true even for the lowest-resolution case shown here, which has only ≈ 450 particles launched per jet. We have simulated cases down to 100 particles - these jets appear very spherical due to SPH averaging, with their jet and lobe components blended together. They are also significantly (factor of ≈ 2) shorter than the self-similar prediction.

Our worst-resolution simulation, with $m_{\rm gas} = 1.81 \times 10^7$ M$_\odot$, matches the resolution of some simulations of galaxy clusters (e.g. Dubois et al. 2010, Martizzi et al. 2014, Richardson et al. 2016, Hahn et al. 2017) and of cosmological simulations that are large enough in volume to contain many galaxy clusters (e.g. Bocquet et al. 2016, Kaviraj et al. 2017, Pillepich et al. 2018). This means that jet episodes with our fiducial power ($P_{\rm j} = 10^{46}$ erg/s) and duration ($T_{\rm j} = 100$ Myr) are likely to be well-converged in such simulations, at least in terms of basic properties.

State-of-the-art zoom-in simulations of galaxy clusters often have resolutions significantly better than $m_{\rm gas} \approx 10^7$ M$_\odot$ (e.g. $m_{\rm gas} \approx 10^6$ M$_\odot$ in Barnes et al. 2017, Bahé et al. 2017b, or $m_{\rm gas} \approx 10^5$ M$_\odot$ for a $M_{\rm h} = 10^{14}$ M$_\odot$ halo in Tremmel et al. 2019), so even weaker jet episodes are likely to be resolved at a basic level in these simulations ($P_{\rm j} = 10^{44}$ erg/s in a galaxy cluster with $M_{\rm h} = 10^{15}$ M$_\odot$ or $P_{\rm j} = 10^{43}$ erg/s in one with $M_{\rm h} = 10^{14}$ M$_\odot$). Modern cosmological simulations with box sizes of $L \approx 100$ Mpc have a resolution of $m_{\rm gas} \approx 10^6$ M$_\odot$ (Vogelsberger et al. 2014, Schaye et al. 2015, Pillepich et al. 2018), and thus our numerical scheme can correctly model

jets in such simulations at least down to systems with $M_{\rm h} = 10^{14}$ M$_\odot$, and possibly $M_{\rm h} = 10^{13}$ M$_\odot$.

Small zoom-in cosmological simulations often aim to reproduce individual Milky-Way type systems (Kim et al. 2014, Hopkins et al. 2014, Sawala et al. 2015, Fattahi et al. 2016,Grand et al. 2016), or host multiple such systems in group environments within a $L = 25$ Mpc box (Crain et al. 2015, Tremmel et al. 2017, Dubois et al. 2021). There is some evidence that jet feedback could be important even in such lower-mass systems (Kaviraj et al. 2015, Singh et al. 2015, Olguín-Iglesias et al. 2020). These simulations do not host any galaxy clusters, and can thus be simulated at much higher resolutions of $m_{\rm gas} \approx 10^3 - 10^5$ M$_\odot$, depending on the type of simulation. While this is very low, the halo masses in these systems are lower by similar factors (relative to a resolution of $m_{\rm gas} \approx 10^6 - 10^7$ M$_\odot$). The black holes hosted by these systems are less massive by even larger factors, due to the approximate $M_{\rm BH} \propto M_{\rm h}^{1.5}$ scaling (Croton et al. 2006, Bandara et al. 2009). In combination with shorter jet episodes of $1 - 10$ Myr (Guo & Mathews 2012, Garofalo et al. 2018, Davis et al. 2022), instead of few 10s or up to 100 Myr (Konar et al. 2006, Machalski et al. 2007, Mahatma et al. 2020), it is possible that jet episodes in these systems could be less energetic by factors of up to 10^6. It is unclear if simulations with $m_{\rm gas} \approx 10^3 - 10^5$ M$_\odot$ can correctly include such jet episodes, in the context of our numerical scheme.

As an example, we take a jet episode with $P_{\rm j} = 10^{42}$ erg/s, lasting 5 Myr. This jet power and duration correspond to the medians for jets in radio AGN (Mezcua et al. 2019, Davis et al. 2022), and the total energy matches the episode that likely recently occurred in the Milky Way (Guo & Mathews 2012, Predehl et al. 2020). Such an episode is 2×10^5 times less energetic than the standard one we simulate. Assuming the same launching velocity of $v_{\rm j} = 15000$ km/s, the mass resolution required to resolve each of these jets with 450 particles (the resolution we have shown to be sufficient) would be $m_{\rm gas} \approx 10^2$ M$_\odot$. This is about an order of magnitude smaller than achievable with the highest-resolution cosmological simulations performed thus far (Hopkins et al. 2018). A convenient workaround, but still a physically relevant one, is to launch jets in lower-mass systems with lower velocities. As an example, $v_{\rm j} = 1500$ km/s in a Milky-Way type system would produce a jet that is similarly

underdense and hot compared to its ambient medium as in our simulations (factor of ≈ 100), due to a lower sound speed in the gas halo of the Milky Way ($c_{\rm s} \approx 150$ km/s with $T_{\rm vir} = 10^6$ K). This would imply that our example jet episode with $P_{\rm j} = 10^{42}$ erg/s and $T_{\rm j} = 5$ Myr could realistically be simulated with $m_{\rm gas} \approx 10^4$ M$_\odot$ or lower. This is in reach for modern cosmological simulations.

Overall, for our standard case, we find jets of very similar lengths and shapes (and therefore energetics, as the two are closely connected in self-similar models of jet lobes) across a very large range of numerical resolution: from $m_{\rm gas} = 1.81 \times 10^7$ M$_\odot$ down to $m_{\rm gas} = 5.73 \times 10^3$ M$_\odot$, a factor of 3160 difference. The implications of these findings, as discussed above, is that jets are likely to be correctly simulated at a basic level in SPH codes in all systems where they may be relevant. A caveat to this is that the highest resolutions achievable may need to be employed. Otherwise, low-power jet episodes will be poorly resolved. However, this is not necessarily a large issue, since it is likely that stronger episodes are more relevant in terms of feedback on galaxy formation.

An additional caveat is that one may need to carefully vary the jet launching velocity from system to system to ensure that the jets are sufficiently resolved, but also that sufficiently strong shocks occur in these systems (as well as sufficiently large density and temperature contrasts). For this reason, constant-velocity schemes with jet launching velocities of $\approx 10^4$ km/s (e.g. Dubois et al. 2012) will likely lead to very poorly resolved jets in any system with a dark matter halo mass below $M_{\rm h} \approx 10^{14}$ M$_\odot$, at resolutions comparable to EAGLE ($m_{\rm gas} \approx 10^6$ M$_\odot$). We instead suggest that scalings such as $v_{\rm j} = AM_{\rm h}^{\gamma}$ or $v_{\rm j} = AM_{\rm BH}^{\gamma}$ may be more appropriate. The normalization and slope can be chosen in such a way that the ratio between typical temperature of shocked jet gas (i.e. the lobe temperature) and that of the ambient medium is roughly constant regardless of the mass of the system (and of order e.g. 100, corresponding to jets that are supersonic by a factor of 10).

3.5.6 Power-law ambient medium density profiles

Here we will discuss some results of simulations where jets were launched into gaseous atmospheres with power-law density profiles ($\rho \propto r^{-\alpha}$), rather than into a constant-

density ambient medium. The set-up for these simulations is described towards the end of § 6.2.2. We test cases with $\alpha = 0.5$, $\alpha = 1$ and $\alpha = 1.5$, all of which should, in principle, feature the self-similar phase of jet evolution (if various parameters are chosen correctly). Given the β profile we have chosen (Eqn. 3.9), outside the small core, the density profile is $\rho(r) = \rho_{0,\beta} r^{-\alpha}$. The normalization $\rho_{0,\beta}$ depends on α in our set-up, since we have chosen to keep the mass of the gaseous halo constant within the virial radius of the external NFW potential. This means that an increase in α is also followed by an increase in $\rho_{0,\beta}$. An alternative would have been to keep the normalization constant, but to instead track the evolution of the jets over larger distances. We chose against this, and instead chose to keep the jets confined within the extent of gaseous haloes of the same size. We did this in order to be able to compare the jets at a similar size scale.

In Fig. 3.9 we show a visual comparison of all three power-law simulations we have done, at different times up to $t = 40$ Myr. All three simulations feature very similar jets and jet-inflated lobes. However, there are differences between these simulations and the constant-density ones featured up to this point. Among these is that the jet-inflated lobes appear to have a larger aspect ratio (i.e. they are thinner), despite having the same half-opening angle $\theta_{\rm j} = 10^{\circ}$. In addition, the unshocked, colder jet gas appears to extend all the way to the jet head in all three cases. This is a feature also shared by ballistic jets (see top row of Fig. 3.1). However, these jets also clearly feature multiple recollimation shocks, which only appear in the self-similar regime. Inspecting the unshocked jet gas more closely, one can see that the recollimation shocks appear at distances closer to the origin, while at large distances (close to the jet head), they blend into a single stream (spine) of unshocked gas, appearing very similar to the unshocked jet gas in ballistic jets (see top panels of Fig. 3.1).

In Fig. 3.10 we show the time evolution of the lobe lengths and radii for the three simulations compared to predictions from Kaiser & Best (2007). In all cases, the lobes start off as being shorter and wider than predicted by the self-similar theory. As explained in § 3.4.5, this is potentially a result of the rather long transition from the initial ballistic phase to the self-similar phase. It could also be a result of the

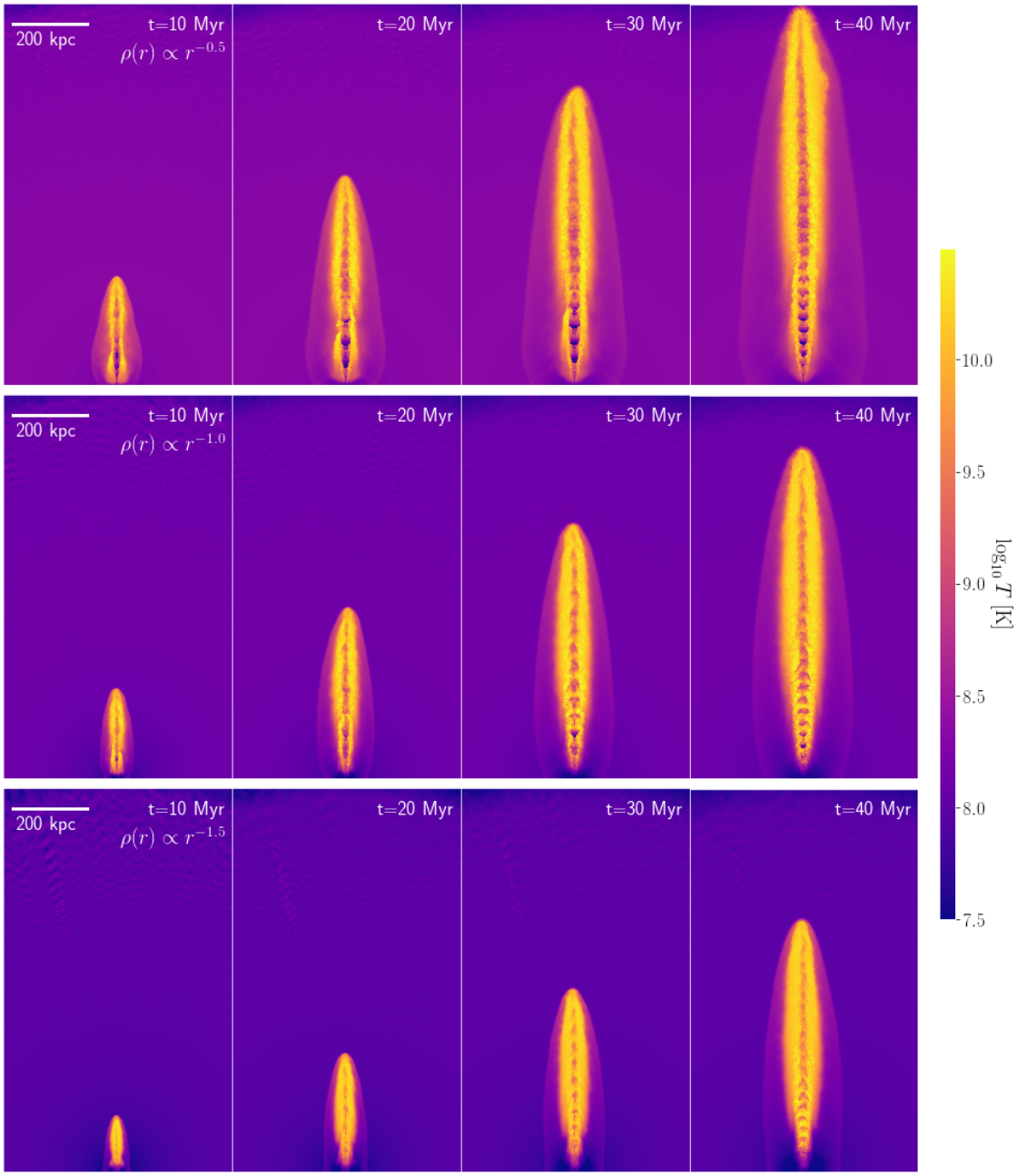

Figure 3.9: Comparison of the evolution of jets launched into power-law ambient density profiles (see top-right-hand corner of the first panel in each row). Other jet-related parameters used are listed in the last row of Table 6.1. The colours show gas temperature, according to the colour bar. The panels are 25 kpc in depth.

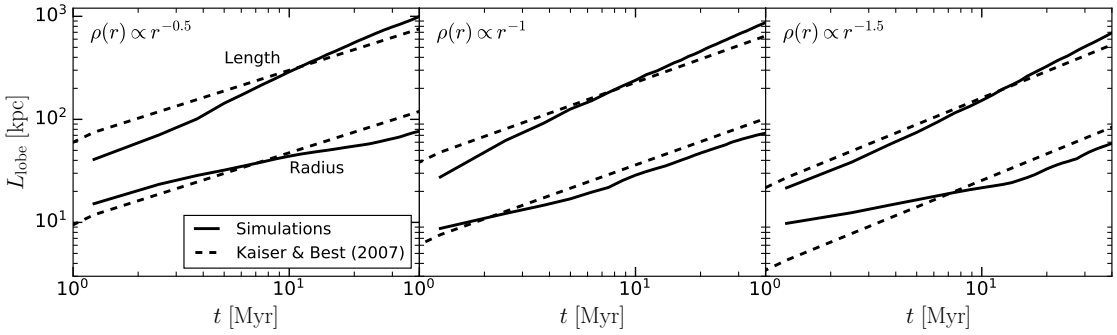

Figure 3.10: Comparison of jet-inflated lobe lengths and radii in simulations with power-law ambient density profiles (see top-left corner of each panel). Other jet-related parameters used are listed in the last row of Table 6.1. The solid lines show measured lengths and radii from the simulations, while the dashed lines give equivalent predictions for self-similar jet-inflated lobe expansion from Kaiser & Best (2007).

initial phase of the jet evolution being relatively poorly resolved (simply due to a small number of particles having been launched into the jets), which tends to make the poorly-resolved lobes more spherical due to SPH averaging effects (see Fig. 3.8).

At late times, in all three cases the lobes transition to behaviour that is in better agreement with the theoretical predictions. However, the lobes appear to be somewhat too long at late times, while also too thin (both disagreements are at a level of $20 - 30\%$). These findings confirm the visual appearance of the jets shown in Fig. 3.9. We posit here that this may be a result of the self-similar theoretical predictions relying on assumptions that may not hold in these simulations. One of these is that the lobe is cylindrical, whereas we find a more ellipsoidal shape. The second assumption is that the lobes have a constant pressure throughout. However, the lobes are more likely to be in pressure equilibrium with the ambient medium locally (i.e. at a given radius). The pressure profile of the ambient medium varies significantly with radius, which means that the lobe has a higher pressure at smaller radii than near the jet head. This could help the jet propagate or the lobes to expand more easily in the radial direction rather than laterally. It could also explain why the recollimation shocks (which occur by means of the lobe pressure acting on the unshocked jet gas) are stronger at smaller radii.

3.6 Summary and conclusions

In this chapter we presented results of simple hydrodynamical tests of jets using the SPHENIX SPH scheme implemented in the SWIFT code. These simulations featured only hydrodynamics and no other physics. The jets were launched with a constant power and launching velocity, and with finite opening angles, by kicking particles from initially placed reservoirs. These jets propagate through ambient media with constant gas densities as well as power-law density profiles. We find that jets initially evolve ballistically, during which time they drill through the medium with ease, while also launching a bow shock. Once the mass of the swept up ambient medium becomes comparable to that injected into the jet, the jets transition to a self-similar regime, and start inflating lobes of hot and diffuse gas. This transition is fairly prolonged, and evidence of the ballistic phase can be seen in the jet morphology even at late times.

The existence of these two phases is in agreement with theoretical predictions. We also find that the jet and lobe lengths and lobe radii are in agreement with self-similar predictions. In the self-similar phase, the aspect ratio of the lobes is constant, as is the fraction of initially injected energy contained in the lobes (including the unshocked jets) versus that in the ambient medium. This is also true for the kinetic and thermal components of both the lobes and ambient medium. We find that energy is effectively transferred from the jets to the ambient gas, although it is not immediately and fully thermalised while the jet is active. The fraction of energy in the thermal and kinetic components, of both the lobe and ambient medium, vary from simulation to simulation depending on the parameters, but none of them are ever negligible.

By performing a parameter study, we find that increasing the jet power results in longer jets, but also better resolution in the jets due to more particles being launched (at a fixed launching velocity). Increasing the half-opening angle results in shorter jets. Varying the jet launching velocity changes both the physical properties of jets (i.e. the temperature and mass of the lobes), as well as the degree to which the jet and lobe are resolved. By varying numerical resolution through the mass of gas particles, we find that our high-resolution ($m_{\rm gas} \approx 10^4$ M$_\odot$) jet lobes deviate

somewhat from the picture expected theoretically. In this case, Kelvin-Helmholtz instabilities prevent the formation of a classical ellipsoidal lobe. For the same reason, the jet spine takes the shape of a conical outflow, and not a series of multiple recollimation shocks, as expected and as found in the lower-resolution cases.

The self-similar regime is also reached in our simulations of jets launched into power-law density profiles of the ambient medium ($\rho \propto r^{-\alpha}$, with $\alpha < 2$). However, the lobes inflated by these jets appear to be up to $20 - 30\%$ too long and too thin compared to self-similar predictions. This may be a result of some of the theoretical assumptions breaking down in the power-law case (e.g. pressure equilibrium throughout the lobes), rather than our simulations being inaccurate.

We find that high-resolution simulations are not necessary in order for the jets to deposit their energy where they should. On the contrary, we find that very poor resolution (≈ 500 particles launched per jet) is sufficient for an accuracy of 15% (for the lengths and radii of the jet-inflated lobes). We find that the level at which jets are resolved depends not only on numerical resolution directly (through the gas particle mass), but also indirectly on physical parameters such as jet power and launching velocity. This means that different jet episodes will be resolved at different levels depending on the details of the launching scheme and on the energetics of a particular jet episode. We find that resolving a jet with ≈ 500 particles is sufficient to reproduce basic properties such as jet lengths and energetics. The implication of this finding is that jet launching velocities of $\approx 10^4$ km/s are appropriate for typical modern cosmological simulations of galaxy clusters. However, we suggest that the jet launching velocity be varied from system to system in order to achieve a balance between resolution and sufficiently strong shock heating of the ambient medium (e.g. through a scaling with the halo mass $v_{\rm j} \propto M_{\rm h}^{\gamma}$, or with the black hole mass $v_{\rm j} \propto M_{\rm BH}^{\gamma}$).

CHAPTER 4

Idealized simulations of the jet-intracluster medium interaction

4.1 Introduction

In the previous Chapter, we presented results of fairly simple simulations, where the focus was on validating the numerical scheme. For this reason, hydrodynamics was the only form of physics included. These simulations were relevant for the active phase of AGN jet evolution, since in that phase, hydrodynamics is indeed the dominant physics at work, at least for powerful sources. However, in a more realistic scenario, gravity becomes important at certain time-scales. Furthermore, we are generally interested in the evolution of the remnant bubbles that form after the AGN jet is turned off, and how it interacts with the ambient medium.

Early idealized simulations of single-episode AGN jet feedback often circumvented the highly-uncertain jet physics, and instead manually placed bubbles of hot gas into the ICM (Churazov et al. 2001, Brüggen et al. 2002, Reynolds et al. 2006, Pavlovski et al. 2008, Sternberg & Soker 2008). The bubbles were then studied as they interacted with and rose through the ICM, on account of buoyancy. Drag and mixing with the ambient medium (entrainment) are both likely to be important in the evolution of jet-inflated bubbles (Pope et al. 2010). Observations with ALMA

have also found that X-ray cavities/radio bubbles are often enveloped by cool ICM gas (e.g. Russell et al. 2017), or accompanied by cool gas filaments trailing them (e.g. Russell et al. 2016, Vantyghem et al. 2018, Olivares et al. 2019, Russell et al. 2019). Observations in other wavelengths also find such filaments (e.g. Wilman et al. 2009, Salomé et al. 2011, Tremblay et al. 2015, Gendron-Marsolais et al. 2017, Maccagni et al. 2021, Gatuzz et al. 2021). Jet activity is associated with metal outflows (Sanders et al. 2005, Kirkpatrick et al. 2009, Doria et al. 2012); it is likely that the uplift associated with these filaments is responsible for the metal redistribution. These filaments have been successfully reproduced in simulations (Revaz et al. 2008, Li & Bryan 2014b, Brighenti et al. 2015, Qiu et al. 2019).

According to the analytical model by Pope et al. (2010), the observed filaments trailing the bubbles form on account of two different processes. The first of these is the so-called Darwin drift (Darwin 1953), which constitutes the main body of the filaments. These filaments form and rise on account of displacement by the bubbles: the bubbles push aside some of the ambient medium, which is then pulled back into the region left empty by the moving bubbles. The second process leading to the filaments is the wake, which is associated with trapping of some amount of the ambient medium in an indentation at the bottom of a bubble, as the bubble begins to rise due to buoyancy. One of the goals of this Chapter is to study these secondary processes which occur in tandem with bubble evolution. This includes drag and entrainment, but our main focus is on the drift and wake. To date, no simulation of jet-inflated bubbles in a realistic ICM setup have been performed with the aim of measuring the masses and volumes of the drift and wake, and comparing those with theoretical expectations and experiments. We expect the drift and wake to be energetically significant (due to their masses and volumes being comparable to that of the bubbles), at least at late times in the simulation, once the bubbles have moved significantly.

4.2 Simulations

As in Chapter 3, we use the SWIFT code and the SPHENIX SPH scheme. In this section we discuss the details of the physical setup which we use in these simulations, as well as the different simulations we perform, with varying parameters.

4.2.1 Physical setup

We launch our jets into a spherically symmetric gas distribution, which represents the intracluster medium of a dark matter halo with a virial mass of $M_{\rm vir} = 10^{14}$ M$_\odot$. We do not include dark matter explicitly, and instead model its effects through an external NFW potential. We assume a concentration parameter of $c = 5.6$, leading to a virial radius of $R_{\rm vir} \approx 950$ kpc. We model the gas distribution with the beta profile, which has the following form:

$$\rho(r) = \frac{\rho_0}{[1 + (r/r_{\rm c})^2]^{3\beta/2}} \tag{4.1}$$

Here, ρ_0 is a normalisation constant, $r_{\rm c}$ the core radius, and β the parameter which determines the slope at large distances. We use $\beta = 0.5$, yielding a slope of -1.5 at large distances, which is appropriate for a $M_{\rm h} = 10^{14}$ M$_\odot$ halo (Voit et al. 2002). The core radius is set to 25 kpc, which is also appropriate for such haloes. ρ_0 is calculated from the condition that the total gas mass within $R_{\rm vir}$ is 8 per cent of the total dark matter mass (Pratt et al. 2009, Sun et al. 2009, Lin et al. 2012). The actual gas profile extends out to $4R_{\rm v}$. In order to reduce the time required to computationally evolve the system, we reduce the gas masses progressively as $m_{\rm gas} \propto r^2$ beyond the virial radius. The gas is assumed to be in hydrostatic equilibrium, with the external NFW potential being used to calculate the pressure profile from this assumption. We then calculate the temperature profile from the equation of state, assuming the gas is ideal.

As a default, we do not include additional physics such as self-gravity and radiative cooling. We have attempted simulations with both included, as well as realistic rotation in the gaseous halo, but we find that none of these have a significant impact on our simulations, at least for 2 Gyr (the simulation time).

4.2.2 Jet launching

We launch jets from an initially conical setup, as was done in Chapter **??**; we place two particle reservoirs of conical shapes in opposite directions along the z-axis in the centre of the gaseous halo. Each cone is 5 kpc long and is defined by its half-opening angle $\theta_{\rm j}$, the same as the launching angle of the jet. The reservoir particles are launched from the cones with a velocity of $v_{\rm j}$, with the velocity vector pointing radially from the centre. The temperature of the reservoir is the same as the rest of the gas in the centre of the halo ($\approx 10^7$ K). The jets are active for $T_{\rm j} = 50$ Myr with a (total, summed over both jets) power of $P_{\rm j}$. The particles are kicked at intervals of $(1/2)m_{\rm gas}v_{\rm j}^2/P_{\rm j}$.

4.2.3 Seeding of particle positions

In our simulations we find that jet-inflated bubbles feature instabilities at late times, which grow from random perturbations. As a result, the initial positions of particles in the conical reservoirs can have an impact on the morphology of the bubbles. We have attempted various choices, including: i) random placement within the cones, ii) a uniform, face-centred cubic lattice of particles, out of which cones are cut out, and iii) a hydrodynamical or gravitational glass of particles, out of which, again, we cut out the cones. We find that instabilities and asymmetries arise in all three cases, even with a perfectly symmetric uniform initial setup. In the simulations presented in this chapter, the default choice was to use a hydrodynamical glass.

We have attempted the same three choices when seeding the particles in the gaseous halo, which represents the bulk of the particles being evolved. An additional complication is that with the gaseous halo, we construct the desired spherically symmetric density distribution by radially rescaling the positions of an initially homogenous (constant-density) cube. We find that drawing particle positions randomly results in overdensities and underdensities which can take more than a few Gyr to homogenize. Similarly, using a uniform cubic face-centred lattice results in radial spokes of overdensities and underdensities, which arise from the uniform setup being radially rescaled and deformed. Our choice is, again, to use a hydrodynamical

glass. Even with this choice, there are some perturbations which arise in the gaseous halo, but they are much smaller than in the other two cases.

4.2.4 Parameter choices and variations

Our standard choice for the physical, jet-related parameters is: jet duration $T_{\rm j} = 50$ Myr, jet power $P_{\rm j} = 3.16 \times 10^{45}$ erg/s, launching velocity $v_{\rm j} = 20000$ km/s and half-opening angle $\theta_{\rm j} = 15^{\circ}$. These choices are a result of much trial and error, and we make them as they result in a self-similar jet at early times (which has a lobe which smoothly transitions into a bubble, as opposed to ballistic jets). In addition, the bubbles form at distances of several hundred kiloparsecs, allowing the study of the interplay with the bubbles and the ambient medium as they rise out to the virial radius and beyond. Finally, the subrelativistic velocity allows a fairly good resolution to be achieved in the bubbles (see discussion below). We do vary all of the parameters, with the exception of the jet duration, in order to study their impact on the properties of the bubbles, as well as on their interaction with the ambient medium.

The main simulation we will discuss in this chapter was performed with a numerical resolution of $m_{\rm gas} = 10^4$ M$_{\odot}$. The total number of particles in this simulation is $\approx 1.4 \times 10^9$. In the centre of the halo, the typical smoothing length (and thus spatial resolution) is 0.2 kpc. The number of particles injected into each jet in this simulation (given the standard, jet-related parameters discussed above) is 1.35×10^5, which is sufficient to achieve convergent properties of self-similar jets (Huško & Lacey in prep.). In this simulation, the jets and subsequent bubbles entrain significant amounts of material (as we will discuss in the results), so the number of particles in each bubble at late times is $\approx 10^6$. If one were to compare this resolution to a grid-based code, very crudely this corresponds to a grid of $30 \times 30 \times 30$ cells across the bubble. We have also performed simulations with resolutions of up to $m_{\rm gas} = 10^7$ M$_{\odot}$, in order to see if our simulations numerically converge. Finally, we also performed simulations where we vary the hydrodynamical scheme used to evolve the bubbles. We compare SPHENIX with a 'minimal SPH' scheme (Monaghan 1992b), without any artifical viscosity or conductivity, and with anarchy-pu,

the scheme used in the EAGLE simulations (Schaye et al. 2015, Schaller et al. 2015).

4.3 General characteristics of jet-inflated bubbles

In this section, we will discuss general features of bubbles which appear in all of our simulations. Some of the details differ from one simulation to another, but in this case we choose to analyze one simulation in detail: our highest resolution simulation (with $m_{\rm gas} = 10^4$ M$_\odot$).

4.3.1 Jet launching and lobe inflation

The origins of AGN bubbles can be traced to the jets which inflate them, and more directly to the lobes. These lobes are the precursors of the bubbles, which exist in the phase while the jets are still active. In Fig. 4.1, in the top panels we show slices of the temperature distribution of gas in the central regions of the gaseous halo, during this initial phase (we show the slices up to 75 Myr, but the jets are active for 50 Myr). In the bottom panels we show various properties of the gas in slices at $t = 50$ Myr.

Three distinct features are visible in these plots. The jet spine (or more simply, the jet itself) is made up of the relatively cold and dense outflowing gas which has been launched as part of the jet launching process, but has not yet been shocked (visible through its high velocity and Mach number). Surrounding the jet itself are lobes of very hot ($T \approx 10^9$ K) and high-entropy gas, which is made up from previously shocked jet gas. Finally, the launching of the jet also results in a bow shock, which transitions from supersonic velocities near the jet head to expansion at the sound speed (i.e. a sound wave) far away from the jet head.

Our jets show features which match the theory of self-similar jets (e.g. Kaiser & Alexander 1997, Komissarov & Falle 1998). The self-similar regime occurs when the swept-up mass of the ambient medium exceeds that of the material launched directly into the jets. The jet transitions from being ballistic to experiencing significant shocking, since it has to impart significant amounts of its own momentum to the ambient medium in order to sweep it up. The main parameter which controls where

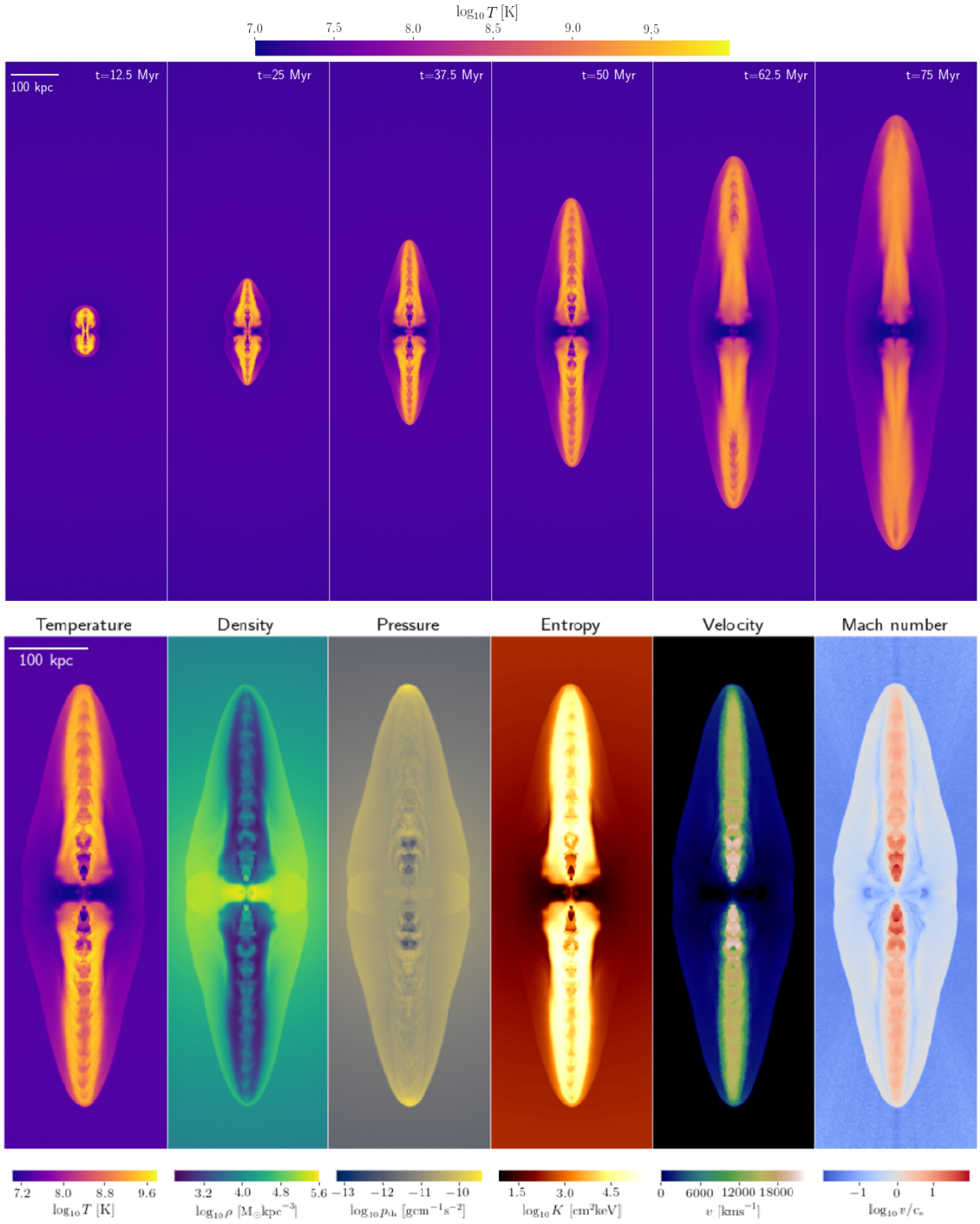

Figure 4.1: Visualizations of jet launching in our highest resolution simulation ($m_{\rm gas} = 10^4$ M$_\odot$), through temperature maps at different times (top) and maps of various properties (as labeled), at $t = 50$ Myr (bottom). The panels measure 400×120 kpc^2, in slices with a depth of 15 kpc. The jets are active for 40 Myr with a (total) power of 3.16×10^{45} erg/s. Jet particles are kicked conically within half-opening angles of 15°, and with launching velocities of 20000 km/s. The total gas mass, its distribution and the external potential correspond to a dark matter halo with a virial mass of 10^{14} M$_\odot$.

a jet transitions from the ballistic to the self-similar regime is the jet launching velocity, $v_{\rm j}$ (Kaiser & Best 2007). Higher values lead to the transition occurring at smaller distances. Our choice ($v_{\rm j} = 20000$ km/s) leads to a transition at ≈ 2 kpc, so our jets should be firmly self-similar. This self-similarity is visible from the ribbed structure of the jet spine, which indicates that the outflowing gas is experiencing multiple recollimation shocks (van Putten 1996, Bodo & Tavecchio 2018, Gourgouliatos & Komissarov 2018, Smith & Donohoe 2019), which are only present if the jet is not ballistic (Falle 1991, Bamford & Komissarov 2018). The shocked jet material begins to create a cocoon (lobe) around and ahead of the unshocked jet gas; this is again a feature which occurs only with non-ballistic jets. The inflated lobe expands in a manner similar to a Sedov-Taylor blast wave (Sedov 1959, although with different exponents in the time evolution of relevant quantities, due to differences in dimensionality of the problems).

In the self-similar regime, the shape of the lobes should stay constant with time. From the first few snapshots in Fig. 4.1 we see that the lobes are initially wider at the base than near the head jet. This has to do with the jets exiting the ambient gas density core (at $r = 25$ kpc) and entering a much different regime, where the slope of the profile is -1.5. As the jets leave the core, they experience less resistance and propagate more freely. In the last two snapshots (after the jets have been turned off), we can see the last of the jet gas being shocked. There are also signs of buoyancy beginning to affect the lobes: this is visible as the slight 'break' in the lobes at around half their lengths. The ambient gas begins to compress and displace the shocked jet gas, initially from the sides, under the action of hydrostatic pressure.

4.3.2 Bubble inflation

In Fig. 4.2 we show the evolution of the shocked jet gas as it transitions from lobes to bubbles. These visualizations are on much larger scales in both time (from twice the jet launching duration, $t = 100$ Myr, to $t = 1600$ Myr, separated by factors of 2) and physical size (up to 1500 kpc, which is ≈ 1.5 times the virial radius). The top half of the simulation is shown in terms of volume renderings of the temperature, whereas the bottom half is displayed through temperature slices. We can see that,

over time, the hot gas takes the form of a typical mushroom cloud. It also expands and cools on account of adiabatic expansion, but also possibly due to mixing with the ambient medium. In the first snapshot, the hot gas has a jet-like shape, with the jets having been turned off 50 Myr prior. By the second snapshot, the gas near the jet head has formed a nearly spherical bubble. However, some of the hot gas is still buoyantly rising and joining with the rest of the gas (with that process finishing by the third snapshot).

In the other snapshots, the hot gas is mostly in the form of nearly-spherical bubbles, but some of that gas is trailing behind the main body of the bubbles. From the slices, we can see that this trailing gas takes the form of shedding vortexes. Some asymmetry is visible both around the z-axis and between the top and bottom bubbles. We have attempted to construct the initial conditions in many ways, including: random seeding, uniform face-centred cubic lattice and hydrodynamic glass (our fiducial choice). We find that asymmetries are unavoidable regardless of the initial conditions, even with no seeded perturbations. It is possible that the process by which we stretch our original box to construct a desired density profile introduces perturbations and eliminates perfect symmetry (Diehl et al. 2015).

Another feature clearly visible from the slices are filaments of colder gas trailing the bubbles, and connecting them with the centre of the gaseous halo. These filaments are not unexpected (Pope et al. 2010). We leave the detailed discussion of their properties for § 4.4.

4.3.3 Bubble and ICM energetics

We now turn to the question of how much energy is in which form, and in which component (the bubbles/lobes or the ambient gas). For this purpose, it is important to have a consistent way of determining which particles constitute the bubbles, and which ones belong to the ambient medium. We find that, empirically, the bubble gas, at some given location, is the only gas in the simulation whose density is significantly lower than the expected density at that location, while at the same time being significantly hotter. As a result, we define the bubbles as all gas particles whose density ρ and temperature T satisfy $\rho < 0.75\rho_0(r)$ and $T > 1.25T_0(r)$, where $\rho_0(r)$

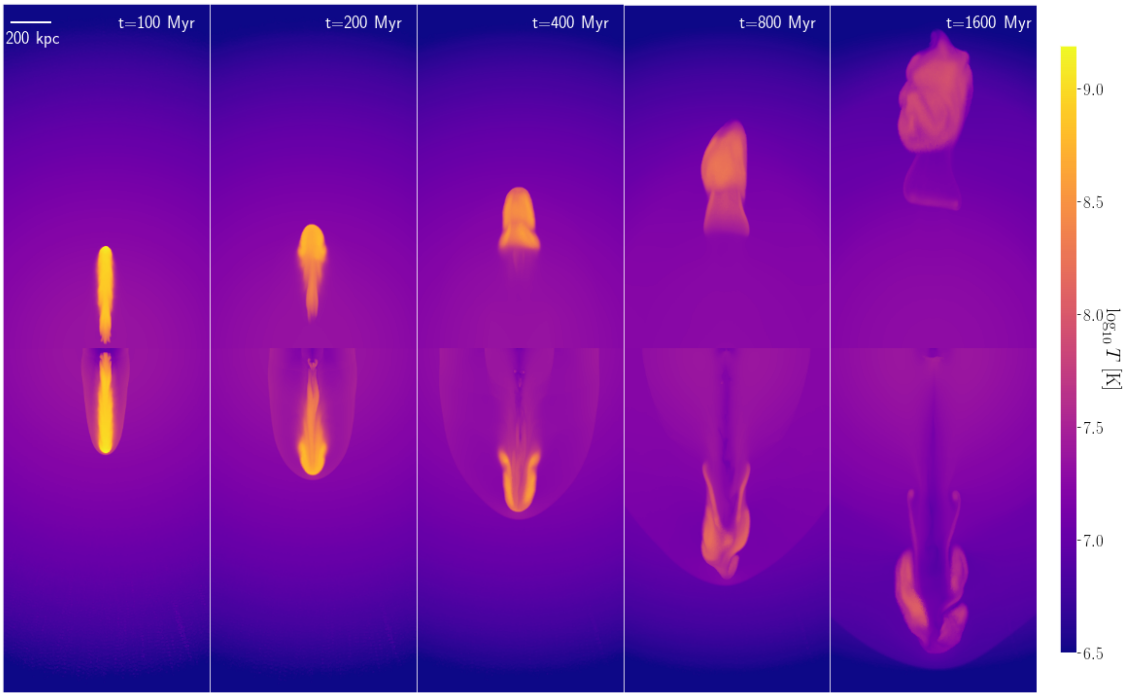

Figure 4.2: Bubble inflation and propagation in our highest resolution simulation ($m_{\rm gas} = 10^4$ M$_\odot$), at different times. The top half of the simulation is shown through volume renderings of the temperature, in order to highlight the 3D structure of the bubbles. The bottom half shows slices 30 kpc in depth. The panels measure 1200×360 kpc^2. See caption of Fig. 4.1 for details of the jet launching and external medium.

and $T_0(r)$ are the initial density and temperature profiles, and r is the distance to the centre of the halo of a gas particle being inspected.

The definition above is somewhat arbitrary, but we find that the particular choices of the numerical factors aren't too important. As long as they are sufficiently different from 1, other gas which may deviate from its initial density/temperature is not included in this definition. At the same time, most of the gas in the bubbles is much less dense than $\rho_0(r)$ and much hotter than $T_0(r)$. As a result, the choice of the numerical factors does not affect the bubble mass for the vast majority of their evolution. Instead, it determines how quickly the bubble gas which is being mixed with the ambient medium becomes redefined as constituting the ambient medium. For simplicity we also include the jets, while they are active, as part of the bubbles (which are actually the lobes while the jets are active). We do this by including into the bubbles any gas which has a velocity larger than $0.25v_{\rm j}$ (gas which has not yet fully been shocked since it was launched into the jets).

We calculate the energies in kinetic, thermal and gravitational potential form for both the jets/bubbles and the ambient medium. We calculate all of these energies as the total energies of the gas relative to that which the particles constituting it had in the initial conditions. These findings are summarized in Fig. 4.3. We find that during the jet launching phase, most of the energy is efficiently being transferred to the ambient gas (through the bow shock). The fractions of total energy in the bubbles versus the ambient gas are 40 and 60 per cent of the injected, respectively, and they are constant with time. The bubbles have around 60 per cent in the kinetic component and 40 per cent in the thermal component, with the latter dropping slightly with time, likely because the jet is escaping the core and experiencing less shocking while it is being launched. The ambient gas has 70 per cent in thermal form and 30 per cent in kinetic, indicating that the bow shock efficiently thermalizes. These roughly constant fractions confirm that the jets are self-similar.

As soon as the jets have turned off, the energy in the jets/bubbles begins to drop. This is especially true for the kinetic component, due to almost all of the gas soon being shocked. Despite this thermalization, the thermal component reaches a peak at around $t = 50$ Myr, when the jets are turned off, and also begins to drop

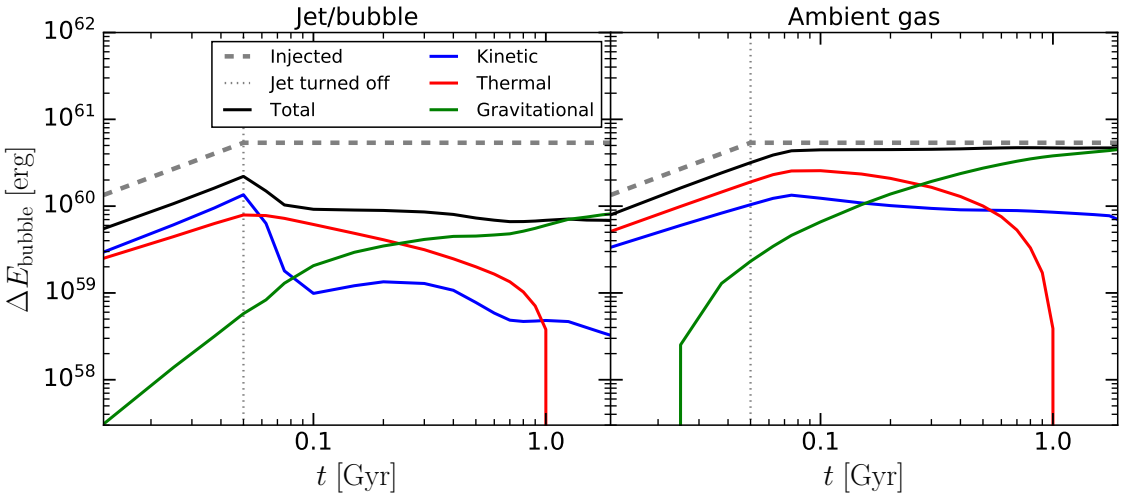

Figure 4.3: Jet/bubble and ambient medium energetics in our highest resolution simulation ($m_{\rm gas} = 10^4$ M$_\odot$), at different times. We define all jet particles as the bubble, even before the bubble has formed. See caption of Fig. 4.1 for details of the jet launching and external medium.

after that. This is likely due to the lobes of hot gas transferring their energy to the ambient medium as they are expanding adiabatically. At late times, the relative thermal energy of the bubbles becomes negative. This is possible since the bubbles have reached the outer regions of the halo, where the ambient temperatures are lower than that in the centre of the halo, and since the typical ratio between bubble and ambient medium temperature drops with time.

It is also evident from the plot that the bubbles have a roughly constant total energy soon after the jets are turned off, at $10 - 15$ per cent of the total injected energy. In other words, the bubbles also have to gain energy through some other process. This process is buoyancy, the effects of which can be seen in the gravitational potential energy of the bubbles beginning to dominate after $t = 300$ Myr. This is supported by visualizations, which show buoyancy clearly beginning to have a strong impact by this time (see Fig. 4.2). It is also consistent with the bubbles having a roughly constant kinetic energy (due to a constant net upward velocity, which would otherwise fall due to processes such as bow shock launching or drag).

The ambient medium shares some similarities with the bubbles, in terms of energy components, after the jets are turned off. The thermal energy quickly reaches a peak and begins to drop. This is possible despite bow shock thermalization, since the bow shock is also transferring particles to outer regions of the halo (where the

temperatures are lower). The filaments visible in Fig. 4.2 also play a role, since they are made up from low-entropy gas being uplifted from more central regions of the halo. As they rise, they reduce their temperature in order to come into pressure equilibrium (see next section). They have a significant upward velocity, which is visible in the kinetic component of the ambient energy dropping only mildly. At late times, the ambient medium energy is dominated by the gravitational potential energy. This indicates that the main consequence of jet feedback is the displacement of particles to larger radii.

4.3.4 Effects of jet-inflated bubbles on gas profiles

Additional insight on the action of jet-inflated bubbles can be gleaned from inspecting their effects on the radial dependence of gas properties, such as density, temperature, thermal pressure or entropy. In Fig. 4.4 we show these dependencies at several different times. With the exception of $t = 100$ Myr, the gas profiles very closely follow the initial ones at $r > 30$ kpc. Within this region, there are significant differences at late times. The core of the new equilibrium profile, after the passage of the jets (bubbles) is around two times less dense, 70 per cent hotter and has a 30 per cent lower thermal pressure and 2.5 times higher entropy. These changes in the core are likely due to a combination of both heating and transfer of gas to larger distances (through either the bow shock or filaments).

In addition to the global changes in the profiles, the effects of the jets are visible as local features. At $t = 100$ Myr we can see signs of a high-density, high-temperature, and over-pressured region at $r = 100 - 200$ kpc. Behind this region, between 20 and 80 kpc, we find low-density, low-temperature and under-pressured gas. This configuration is typical of shock waves, so we interpret this as the bow shock. The bubbles are not visible on these plots due to spherical averaging. At later times, spherical averaging makes even the bow shocks hard to discern.

Our results here indicate that the jets/bubbles have transported significant amounts of material from the inner portions of the gaseous halo out to larger distances (beyond the virial radius at late times). We will now look at similar profile plots, but at one time ($t = 400$ Myr), and showing the profiles along the jet/bubble axis, as well

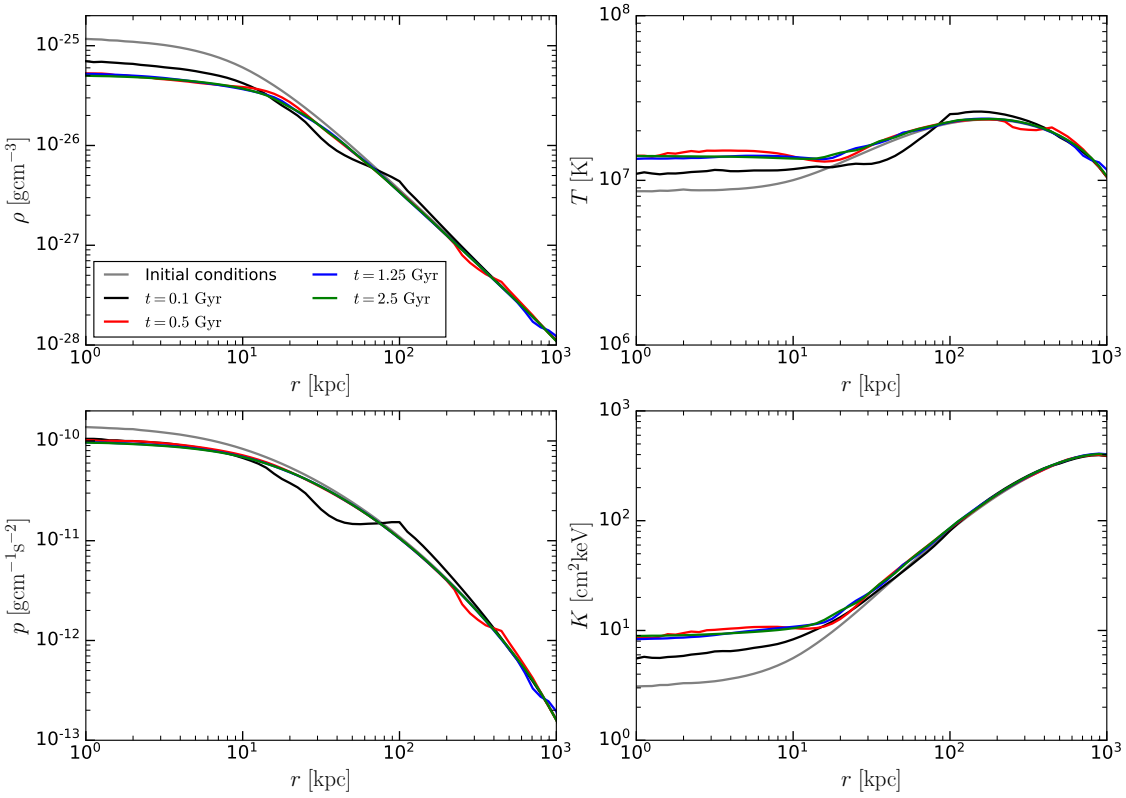

Figure 4.4: Impact of the jets and bubbles on the radial profiles of gas (top left), temperature (top right), pressure (bottom left) and entropy (bottom right). These results are for our highest resolution simulation ($m_{\rm gas} = 10^4$ M$_\odot$), at different times as per the legend. See caption of Fig. 4.1 for details of the jet launching and external medium.

as in other directions. First we calculate profiles within 10 degree cones around the z-axis, ensuring that at any given radius, only one feature is present in the profile. We then calculate profiles using all gas particles outside 30 degree cones around the z-axis. This profile serves as a basis against which we can compare the first one, although it does also include the laterally expanding bow shock.

In Fig. 4.5 we show the profiles calculated in the above manner, with an average profile (using all gas particles) also shown. Along the jet-launching axis, we can see the bow shocks at largest distances ($r = 500$ kpc) as high-density, high-temperature, over-pressured gas. Immediately within the bow shocks are even hotter, jet-inflated bubbles which have a very low density and a very high entropy. They are close to pressure equilibrium with the ambient gas. At distances even smaller than the bubbles ($r < 100$ kpc), we find low-entropy, low-temperature and high-density gas which extends from the centre of the bubbles smoothly down to the centre of the gaseous halo. These are the filaments which we discuss in the next section.

Turning now to the profiles outside the cones near the z-axis, we find the bow shocks, as well as low-density and low-temperature gas immediately following the bow shocks. This is a result of the bow shocks sweeping up gas, so the profiles take some time to settle down to a new equilibrium. We find that this profile is very similar to the average profile (using the whole halo). Note that these features are visible at radii smaller than $r = 500$ kpc, the distance to the bow shock along the z-axis, due to its ellipsoidal shape.

4.4 The uplift of ambient gas behind jet-inflated bubbles

As we have seen from some of the results presented in the previous section, at late times in the simulations, we find that the ambient gas behind the bubbles has a lower entropy, higher density and lower temperature than the ambient gas surrounding it. In fact, this gas even has a lower temperature than its starting temperature in the initial conditions. In this section we will consider some general properties of the bubbles and ambient gas, focusing mostly on the latter, and including the drift and

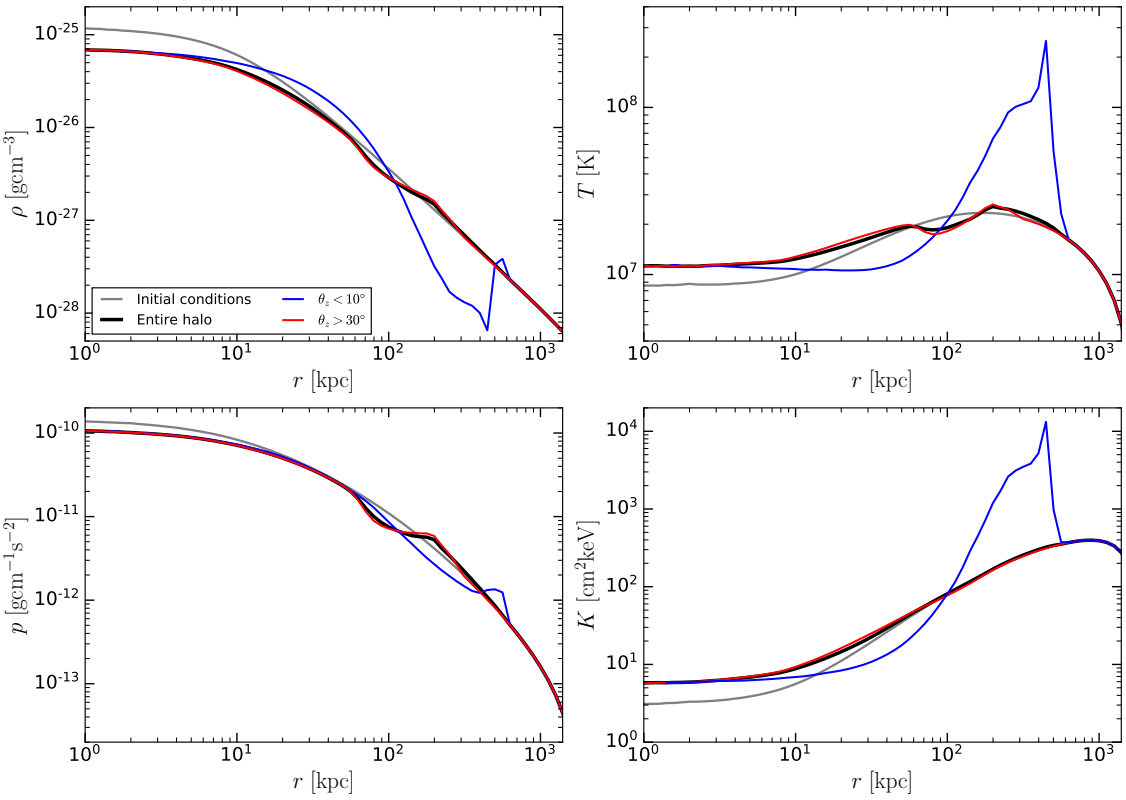

Figure 4.5: Impact of the jets and bubbles on the radial profiles of gas (top left), temperature (top right), pressure (bottom left) and entropy (bottom right). These results are for our highest resolution simulation ($m_{\rm gas} = 10^4$ M$_\odot$), at $t = 800$ Myr. We show the profiles using all particles (black), using particles only within 10 degrees of the jet-launching axis (blue), and outside 30 degrees of the jet launching axis. See caption of Fig. 4.1 for details of the jet launching and external medium.

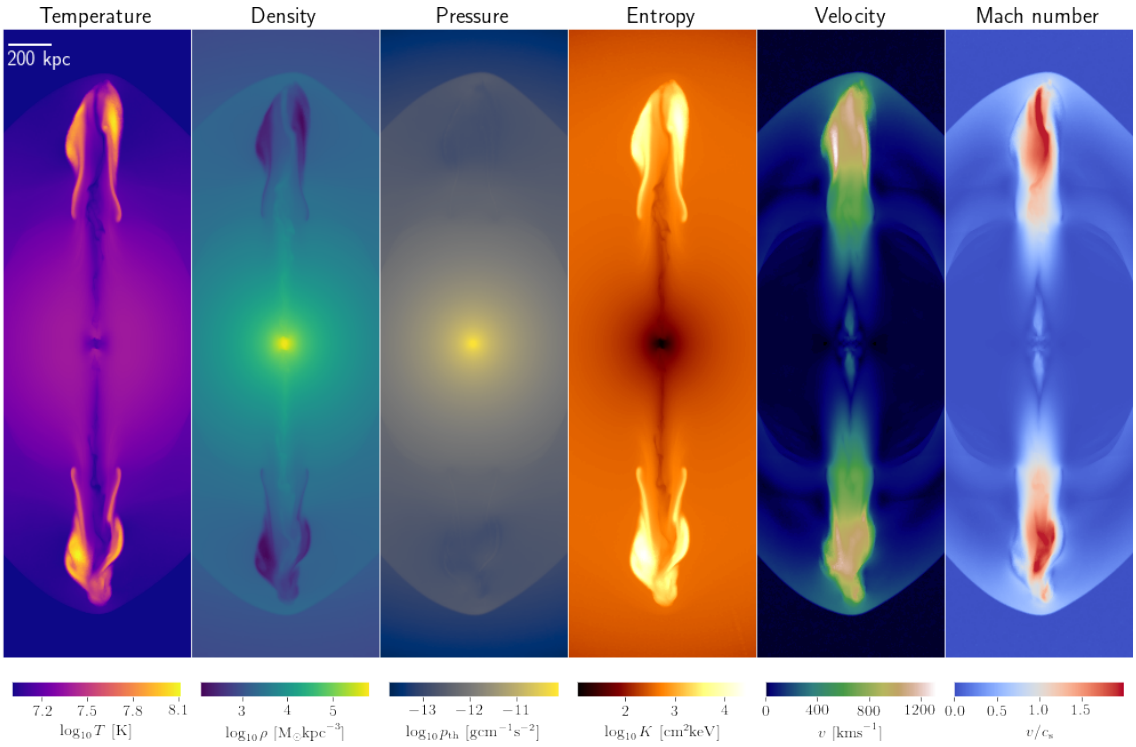

Figure 4.6: Slices through the gas (30 kpc depth) showing the structure of the jet bubbles and their surroundings, at a resolution level of $m_{\rm gas} = 10^4$ M$_\odot$, and 800 Myr after the start of the simulation. The panels measure 1200×360 kpc^2. Each panel shows a different property, as in the panel titles. See caption of Fig. 4.1 for details of the jet launching and ambient medium.

wake which form behind the bubbles.

4.4.1 General properties of gas at late times

In Fig. 4.6 we show visualizations of various gas properties in our highest-resolution simulation at $t = 800$ Myr. These panels show slices of 30 kpc in depth, so projection effects do not hide any features in these plots. Most obviously, we can see the jet-inflated bubbles of hot, low-density and high-entropy gas. The typical temperature of the bubble gas has fallen to no more than $\approx 10^8$ K by this point, and the density ratio relative to the ambient medium is of order a factor of 10. The bubbles are in almost perfect pressure equilibrium with their surroundings. They are moving with velocities of order 1000 km/s, or less, which is similar to the sound speed of the medium. In Fig. 4.6 we can also see the bow shocks moving ahead of the bubbles. The gas being shocked has virial temperatures ($\approx 10^{7.5}$ K), is over-dense and over-pressured. It is moving at the sound speed, with a Mach number of ≈ 1 or slightly

above.

In the central regions of the gaseous halo, within 600 kpc, we find what looks like a core of high temperature and high density gas which is overpressured relative to the rest of the ambient gas. This gas makes up the new equilibrium gas profile being established just inside the propagating bubbles and bow shock fronts. This can also be seen on the velocity plots, as this gas has a net zero velocity. Gas just outside this core has a net radial velocity inwards. This is gas that was swept outwards by the bow shocks, but is now falling and settling down to a new equilibrium.

The last feature visible in Fig. 4.6, which we have not yet discussed, are the two filaments of cold (10^7 K), somewhat dense and low-entropy gas connecting each bubble to the centre of the halo. These filaments are a result of uplift of ambient, low-entropy gas from central parts of the gaseous halo (Pope et al. 2010), in the form of the drift (Darwin 1953, Dabiri 2006) and the wake (Yang 2003, Crowe 2005). The drift should correspond to the main body of the filaments, while the wake should be cold gas in an indentation in the bubbles. We do indeed find cold, ambient gas in the centre of the bubbles. In fact, this gas is among the fastest moving in the simulation, to the point that it is puncturing/deforming the bubble. Visually, however, it is hard to distinguish the drift and the wake.

4.4.2 The masses and volumes of the drift and wake

From the discussion in § 4.3.3, it is apparent that the filaments, made up from the drift and the wake, are energetically important. They are also sufficiently massive to be visually distinct in plots of profiles of various gas properties. Here we will look at the masses and volumes associated with these filaments, separately for the drift and the wake. This will also be important for some of our subsequent analysis.

As we have mentioned, the drift and the wake are difficult to distinguish. In a simple theoretical picture, the wake should be any ambient gas within a sphere with the smallest surface area that also encloses the bubbles. We will use a similar definition, but a more general one (applicable for any convex bubble shape). We define the wake as any gas belonging to the ambient medium that resides in the convex hull of the bubble, i.e. any ambient gas within a minimal-surface area which

encloses all bubble particles. For this purpose, we use particles originally launched into the jet as tracer particles of the bubble.

The definition of the drift is somewhat more difficult. Visually, from Fig. 4.6, it is clear that it is low-temperature, high-density and low-entropy gas behind the bubbles. We thus classify a gas particle as part of the drift if it is an ambient particle in a cylindrical region through which the bubbles have traveled, which has an entropy 20 per cent lower than the initial entropy profile at its location. We find that the exact threshold is relatively unimportant, as long as it is above 10 per cent.

In Fig. 4.7 we show the masses and volumes of the drift and wake as functions of time, and the same for the bubbles as a basis of comparison. The bubbles experience significant entrainment in the first 100 Myr, which results in an increase in the bubble mass from $M_{\rm b} \approx 10^9$ $\rm M_\odot$ to $M_{\rm b} \approx 1.5 \times 10^{10}$ $\rm M_\odot$ (the initially injected mass is $M_{\rm b} = 1.35 \times 10^9$ $\rm M_\odot$). After this initial entrainment, the bubble mass remains approximately constant. The drift begins to appear after 100 Myr, and it also reaches a constant mass, of around $M_{\rm d} \approx 10^{11}$ $\rm M_\odot$. The wake appears after 500 Myr (this is when an indentation in the bubble begins to form, see Fig. 4.2), and its mass saturates at $M_{\rm w} \approx 10^{10}$ $\rm M_\odot$. From the plot showing the volumes of each component, we can see that all of them increase with time, and in a similar way. The bubble volume increases due to adiabatic expansion. The drift volume increases since its volume should be proportional to that of the bubbles (see next subsection). The wake volume increases since it is coincident with the cavity in the bubbles; if the bubbles expand, the cavity will as well.

4.4.3 Direct comparison with a theoretical model

We will now compare the masses and volumes of the drift and wake with the model presented in Pope et al. (2010). At a minimum, their model posits that bubbles inflated by jets rise through the ICM on account of buoyancy, while also expanding adiabatically (but in pressure equilibrium with the ICM). As we have found, these assumptions are justified. Pope et al. (2010) also include the effects of drag and mixing with the ambient medium (entrainment). The drag is not directly measurable from our simulations (since there are many other processes at play), but the

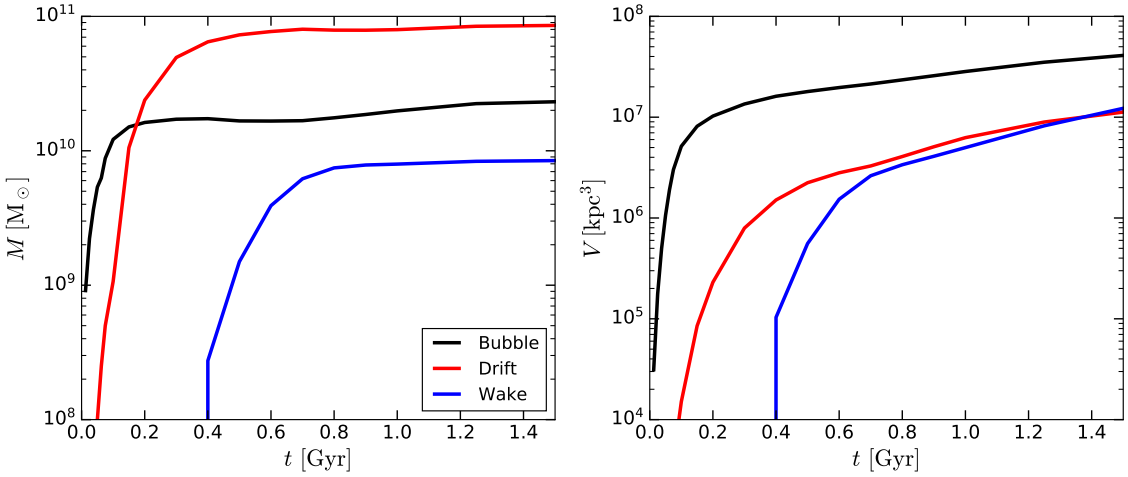

Figure 4.7: Bubble, drift and wake masses and volumes (see main text for definitions and methods of measurement) in our highest resolution simulation, as functions of time. See caption of Fig. 4.1 for details of the jet launching and the ambient medium.

entrainment is, as we will show.

The volume of the drift can be related to that of the bubble by a numerical coefficient: $V_\mathrm{d} = kV_\mathrm{b}$. This relation can be shown to be true quite generally, in simple models of a sphere passing through a medium with a constant velocity (Darwin 1953, Benjamin 1986, Dabiri 2006), although k depends on the shape of the bubble. The effects of the wake can be quantified as additional mass added to the bubble: $M_\mathrm{w} = qM_\mathrm{dis,0}$, where $q < 1$ is a numerical coefficient and $M_\mathrm{dis,0}$ is the mass initially displaced by the bubble. According to the entrainment hypothesis (Morton et al. 1956), the rate at which ambient material enters the bubble is given by $\dot{M}_\mathrm{b} = \alpha\rho_\mathrm{amb}v_\mathrm{b}S_\mathrm{b}$, where ρ_amb is the ambient density, v_b the bubble velocity, S_b the surface area of the bubble and α is a numerical coefficient which depends on the type of mixing. We refer the reader to Pope et al. (2010) for a more comprehensive discussion of all three of these effects.

The values of the numerical coefficients described above have been well determined at least for spherical bubbles. In this case, we expect $q = 0.24$ (Yang 2003, Crowe 2005) and $k = 0.5$ (Darwin 1953). α should be around 0.05 where mixing is due to turbulence in a momentum-driven (jet-like) flow (Turner 1986). Jets in the presence of buoyancy have $\alpha = 0.065 - 0.08$, while buoyantly-rising plumes should have $\alpha = 0.1 - 0.16$ (see Carazzo et al. 2006) for a review. Magnetic fields and viscosity can reduce the value of α; the former is not included in our simulations,

but the latter is (see Borrow et al. 2020 for a discussion of artificial viscosity in SPHENIX).

The values of k, q and α are unlikely to be truly constant, since our simulation includes many processes and a relatively complex setup. An additional problem is that the shapes of our bubbles change continuously throughout the simulation. In addition, usual derivations/measurements of k for the drift are done with no buoyancy. It is unknown what is the interplay between the three effects, and if there is any at all.

Despite the expected difficulties, we will attempt to measure these coefficients. We do so in the following way.

- Drift: $k = V_\mathrm{d}/V_\mathrm{b}$. See previous subsection for the definition of the drift and beginning of § 4.3.3 for the definition of the bubbles.

- Wake: $q = M_\mathrm{w}/M_\mathrm{dis,0}$. See previous subsection for the definition of the wake. The initially displaced mass $M_\mathrm{dis,0}$ can be calculated as the product of the ambient density and bubble volume, $\rho_\mathrm{amb}V_\mathrm{b}$. While there is an arbitrary choice in when this product is taken (since the bubble is not initially placed, but rather forms from a particle distribution which was launched with some velocity), we find that the product is roughly constant with time.

- Entrainment: $\alpha = \dot{M}_\mathrm{b}/S_\mathrm{b}\rho_\mathrm{amb}v_\mathrm{b}$. We measure $\dot{M}_\mathrm{b}$ directly as the differential in the sum of all bubble particle masses. The surface area of the bubble S_b is given by the convex hull which describes the bubble particle distribution, while v_b is the average z-direction velocity of the bubble particles.

In Fig. 4.8 we show the time variation of the three coefficients in our highest-resolution simulation. The earliest of the three effects which appears in the simulation is entrainment. While the jet is active ($t < 50$ Myr), the entrainment coefficient has a value of $\alpha = 0.04 - 0.05$, which is consistent with a momentum-driven flow (Turner 1986, Dellino et al. 2014), despite the fact that buoyancy is present in this phase, and that we might expect $\alpha \approx 0.07$ (Carazzo et al. 2006). This is perhaps due to buoyancy beginning to operate on longer time-scales (several hundred Myr rather than 50 Myr). After the jet is turned off, the entrainment increases to a peak

of $\alpha = 0.19$, and quickly drops to very small values by $t = 300$ Myr. The peak value is similar to that expected for a buoyantly-rising plume ($\alpha = 0.16$; Carazzo et al. 2006, Suzuki & Koyaguchi 2010). At late times, the entrainment is very small, usually $\alpha < 0.01$. This is potentially due to a lack of resolved small-scale turbulence during the buoyancy-driven phase, or due to the artificial viscosity in SWIFT.

The drift coefficient grows to $k = 0.1$ within 300 Myr, and has an approximately constant value ($k = 0.1 - 0.13$) for the rest of the simulation. This is much lower than expected for spherical bubbles in a constant-density medium ($k = 0.5$; *Darwin* 1953). The value we have measured matches the thin nature of the filaments, as is visible in e.g. Fig. 4.6. The drift in a constant-density medium has a much wider base (see Fig. 1 in Pope et al. 2010 for a schematic), but this is likely impossible in a gravitationally supported gaseous atmosphere. It is likely that hydrostatic pressure compresses the drift filament, such that it is thinner at the base than near the bubbles.

The wake coefficient grows to an approximately constant value of $q = 0.15 - 0.17$ by $t = 800$ Myr. This value is lower than expected for a spherical bubble ($q = 0.24$; Yang 2003, Crowe 2005), for a few possible reasons: i) the bubbles form from gas which is initially moving, ii) the bubbles are typically somewhat elongated, iii) the gravitational field weakens as the bubble rises.

Inferring drift, wake and entrainment from a theoretical model

Pope et al. (2010) present a model which includes buoyancy, adiabatic expansion, drag, drift, wake and entrainment. They quantified these effects through the numerical coefficients described thus far and developed a system of differential equations which can be used to predict the evolution of a rising spherical bubble. The drift and wake serve as additional terms in the inertia of the bubbles, whereas entrainment enters the equations as a mass flux term. Along with buoyancy, the only force directly acting on the bubbles is drag, which is modeled using the usual formula: $F_{\rm D} = (1/2) C_{\rm D} \rho_{\rm amb} A_{\rm b} v_{\rm b}^2$, where $C_{\rm D}$ is the drag coefficient (dependant on the shape of the bubble and the Reynolds number), $v_{\rm b}$ the bubble velocity, $A_{\rm b}$ its cross-section and $\rho_{\rm amb}$ the ambient density.

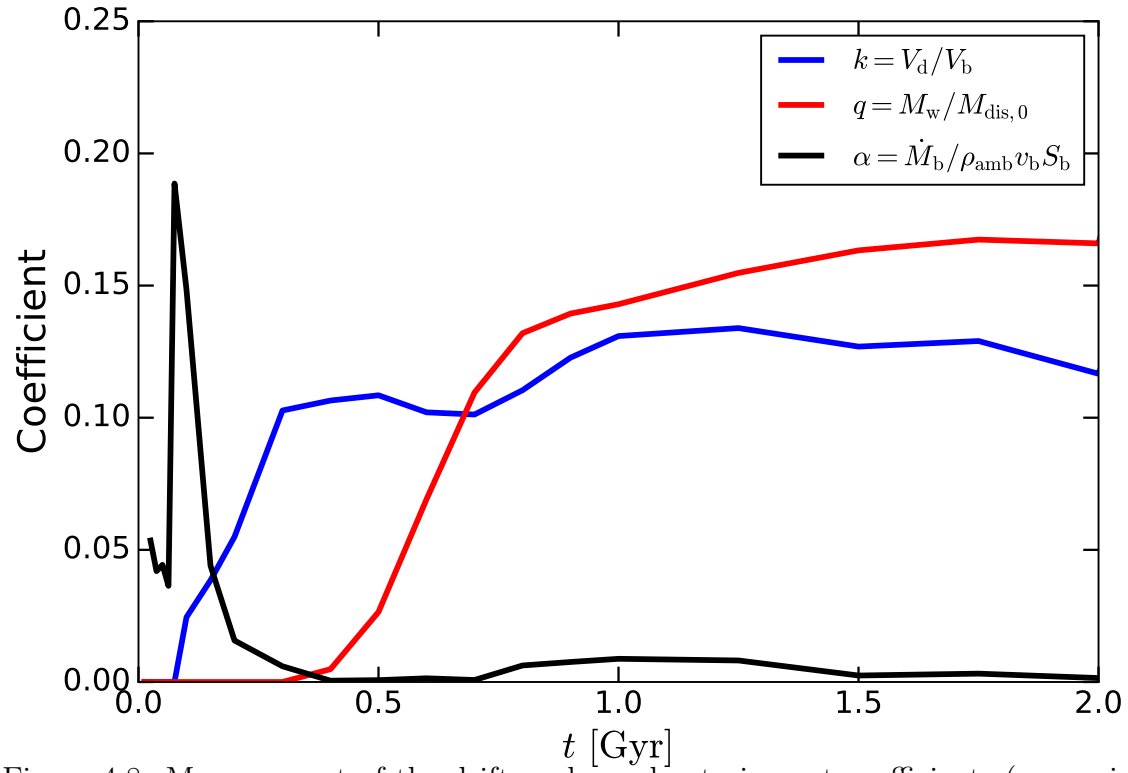

Figure 4.8: Measurement of the drift, wake and entrainment coefficients (see main text for definitions and methods of measurement) in our highest resolution simulation, as functions of time. See text or caption of Fig. 4.1 for details of the jet launching and ambient medium.

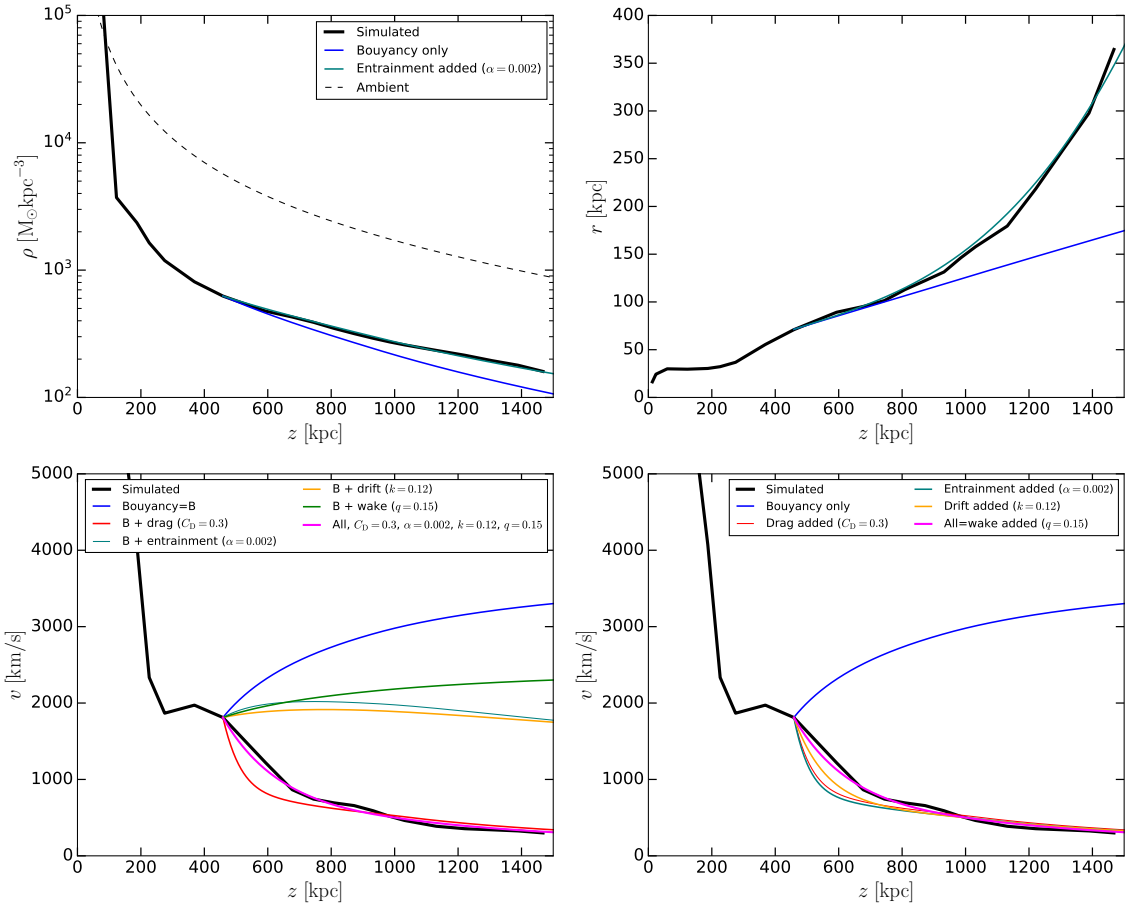

Figure 4.9: Bubble properties measured from our highest resolution simulation (see main text for methodology), as functions of bubble position (black lines). The panels show density (top left), radius (top right), and velocity (bottom). These are compared with predicted values from the theoretical model by Pope et al. (2010). The initial conditions for this model are our measured values at 100 Myr. In the bottom left panel, different lines represent model predictions with different effects included; the blue line represents buoyancy and adiabatic expansion, while all other lines, with the exception of magenta, model one additional effect (as per the legend). In the bottom right panel, lines of those same colours represent each effect included successively. Magenta lines represent model predictions with all effects included. Numerical coefficients for each effect are given in the legends. In the top two panels we do not show model predictions with drag, entrainment, drift or the wake, as they do not influence bubble densities or radii. See caption of Fig. 4.1 for details of the jet launching and ambient medium.

Without the effects of drag, the wake, drift or entrainment, the adiabatic expansion of the bubbles leads to a slower drop in density than that of the ambient gas (which falls as $1/r^{1.5}$ in our case), meaning that the bubble will stop accelerating at some distance where its density becomes equal to that of the ambient gas. The inclusion of drag should lead to the bubble rising at a terminal velocity (which can weakly depend on radius, since the gravitational acceleration does as well). Including drift, wake or entrainment will make the bubbles harder to either accelerate or decelerate (depending on whether buoyancy or drag dominates).

The system of equations developed by Pope et al. (2010) has three dependant variables: the density $\rho_{\rm b}$, radius $r_{\rm b}$ and velocity $v_{\rm b}$ of the bubble. The independant variable is the radial distance (height) of the bubble z. Their system of equations requires one to assume some values for the coefficients $C_{\rm D}$, k, q, and α. The initial conditions are bubble density, velocity and radius at some distance/height. We choose the initial conditions for their system of equations from our own simulations at 100 Myr.

We measure the bubble properties (density, velocity, radius and height) at every snapshot in the following way. We use the particles originally launched into the jet as tracer particles, since we find that they trace the bubble shape very well. These particles are not the only ones that constitute the bubbles (due to entrainment, especially at higher resolutions), but provided that mixing is strong enough, the properties of these particles should trace those of the overall bubble on average. We first calculate their centre of mass (a point along the z-axis). We define the height of the bubble as the distance of the centre of mass from the origin (including both bubbles). The radius is defined as the average cylindrical radius of the 20 particles farthest from the z-axis. The bubble velocitities and densities are calculated as the mean values using all particles classified as making up the bubbles (using the same definition of the bubbles as in § 4.3.3).

In Fig. 4.9 we show these properties of the bubbles in our highest-resolution simulation as a function of bubble height. The drag, drift and wake do not play a role in the evolution of bubble densities and radii in this model, which are shown in the top two panels. For this reason, we can use our simulated bubble densities and

radii to infer how much entrainment is ocurring (regardless of the bubble velocities). The decrease in the bubble density with height is consistent with entrainment being present at these late times, although with a very small value of the entrainment coefficient α. The evolution is consistent with the entrainment coefficient being equal to $\alpha = 0.002$, with no entrainment leading to somewhat lower densities. The evolution of bubble radii is consistent with the same value of α. This value is similar to that which we directly measured (Fig. 4.7).

In the bottom left panel of Fig. 4.9, we show the bubble velocity as a function of bubble height. The bubble velocity drops sharply by 250 kpc, as the outflowing jet material is strongly shocked. It reaches a small local minimum, and then begins to rise on account of buoyancy. It reaches a local maximum velocity of 2000 km/s at 400 kpc, and then drops slowly, beginning to asymptote to a value of 150 km/s at large distances. We compare this velocity evolution with that inferred by the Pope et al. (2010) model by including the relevant effects one by one. As already mentioned, the initial conditions used for the model are the measured values shown on these plots, at 100 Myr (bubble length of 450 kpc). We choose this time as this is the first snapshot after which all of the jet gas has been shocked.

Including only buoyancy and adiabatic expansion in this comparison leads to an increase in the velocity (but also a saturation, which is not shown in this plot, due to adiabatic expansion leading to the bubble becoming comparable in density to the ambient medium). Adding drag (with $C_{\rm D} = 0.3$, typical for bullet-shaped objects at large Reynolds numbers, matching the morphology of our jets early on and bubbles later on) changes the picture considerably. The bubble with drag decelerates more quickly than measured, but reaches velocities which agree with the measured ones later on. Modeling either drift or wake (in the place of drag) with coefficents of $k = 0.12$ and $q - 0.15$ matching those that we measured (Fig. 4.8), leads to a peak and decline with drift and a saturation with the wake. Including only entrainment alongside buoyancy and adiabatic expansion leads to a similar peak and decline as with the drift. Once all processes are included at the same time, the simulated and predicted data become comparable. The velocity drop is perhaps a bit too steep at early times, which is possibly from too high a drag coefficient, overestimating that

for very thin jets at early times.

In the bottom right panel of Fig. 4.9 we show the same simulated values as in the bottom left panel, but the lines showing predicted evolution now include each effect successively. We start off from only buoyancy and adiabatic expansion, and add drag, entrainment, drift and the wake, in that order. Including entrainment on top of drag leads to a slightly quicker decline in the velocity, as compared to only drag. Adding drift causes a slower decline in the velocity. Similarly, adding the wake on top of that makes the velocity drop even more slowly, yielding the final prediction, which agrees well with our measured evolution of jet velocity. The last two changes may appear somewhat counterintuitive: why would adding the drift or the wake make the bubbles decelerate less quickly, considering the fact that they individually decelerate the bubbles in isolation? The reason they delay the deceleration is due to the drift and the wake being modeled as added mass (inertia) of the bubbles. This means that the bubbles are harder to both accelerate or decelerate. In a situation where deceleration dominates (due to drag overcoming buoyancy), the bubbles will be decelerated more slowly, as the drift and the wake must also decelerate in tandem.

4.5 Jet-inflated bubbles with varying parameters

In the previous sections we focused on general features of jet-inflated bubbles, as well as features of the ambient medium which arise on account of these bubbles. These analyses were done for our highest resolution simulation ($m_{\rm gas} = 10^4$ M$_\odot$), which has a jet power $P_{\rm j} = 3.16 \times 10^{45}$ erg/s, launching velocity $v_{\rm j} = 2 \times 10^4$ km/s and opening angle $\theta_{\rm j} = 15^\circ$. Here we will broaden our analysis by varying all of these parameters. In addition, we vary the hydrodynamical scheme used in the simulations. The standard resolution at which we vary other parameters is $m_{\rm gas} = 10^5$ M$_\odot$, and our standard hydrodynamical scheme is SPHENIX. The standard set of physical parameters is the same as listed above for the high-resolution simulation. We keep the jet duration the same in all cases ($t = 50$ Myr), and we also keep the gaseous profile unchanged.

We analyse these different simulations through visual renders of the bubbles

in terms of temperature, which are shown in Fig. 4.5 for variations of jet-related parameters and (jet power, jet power and velocity, velocity, half-opening angle), as well as in Fig. 4.5 for variations of numerical resolution and hydrodynamical scheme. We have also studied these different simulations in terms of energetics, but we find that it is overall similar, and that any differences among the different simulations agree with qualitative differences in the visualizations.

4.5.1 Varying the jet power

We vary jet powers by factors of $\sqrt{10} \approx 3.16$, with one lower-power and two higher-power simulation relative to the fiducial one (which has $P_{\rm j} = 3.16 \times 10^{45}$ erg/s). In the first row of Fig. 4.5 panels we show visualizations of the jets/bubbles in these simulations after 200 Myr of evolution. The impact of this variation is relatively drastic (compared to the differences for self-similar jets, where the jet power changes the jet lengths weakly, $L_{\rm j} \propto P_{\rm j}^{0.2-0.33}$, Kaiser & Best 2007). The bubble reaches a smaller distance in the lowest-power case than the fiducial case (shown in the second snapshot), and it does not escape the halo. It is also more spherical, because the jet which created it was shorter and thus traveled for a shorter time in the near-isothermal portion of the gaseous halo ($\rho \propto r^{-1.5}$), compared to the constant-density core. The case with $P_{\rm j} = 10^{46}$ erg/s (in the third snapshot), on the other hand, features a jet which has traveled to $r \approx 1500$ kpc by $t = 200$ Myr, which is already well outside the virial radius.

These drastic differences in the three lower-power cases are possibly related to the fact that the mass resolution and launching velocity are the same, so lower jet powers (and total energies) lead to a smaller number of gas particles being launched, and therefore a worse-resolved jet. More likely these differences arise due to lower total jet/bubble masses and momenta, which means that they are more quickly decelerated by the action of the various processes at play (drag, drift, wake, entrainment). In addition, buoyancy, the only force accelerating the bubble, decreases with the reduction in bubble volume, which accompanies the reduction in jet power. In the last snapshot in the first row of Fig. 4.5 we show our highest-power simulation. Surprisingly, the bubble is being formed from a jet which has traveled

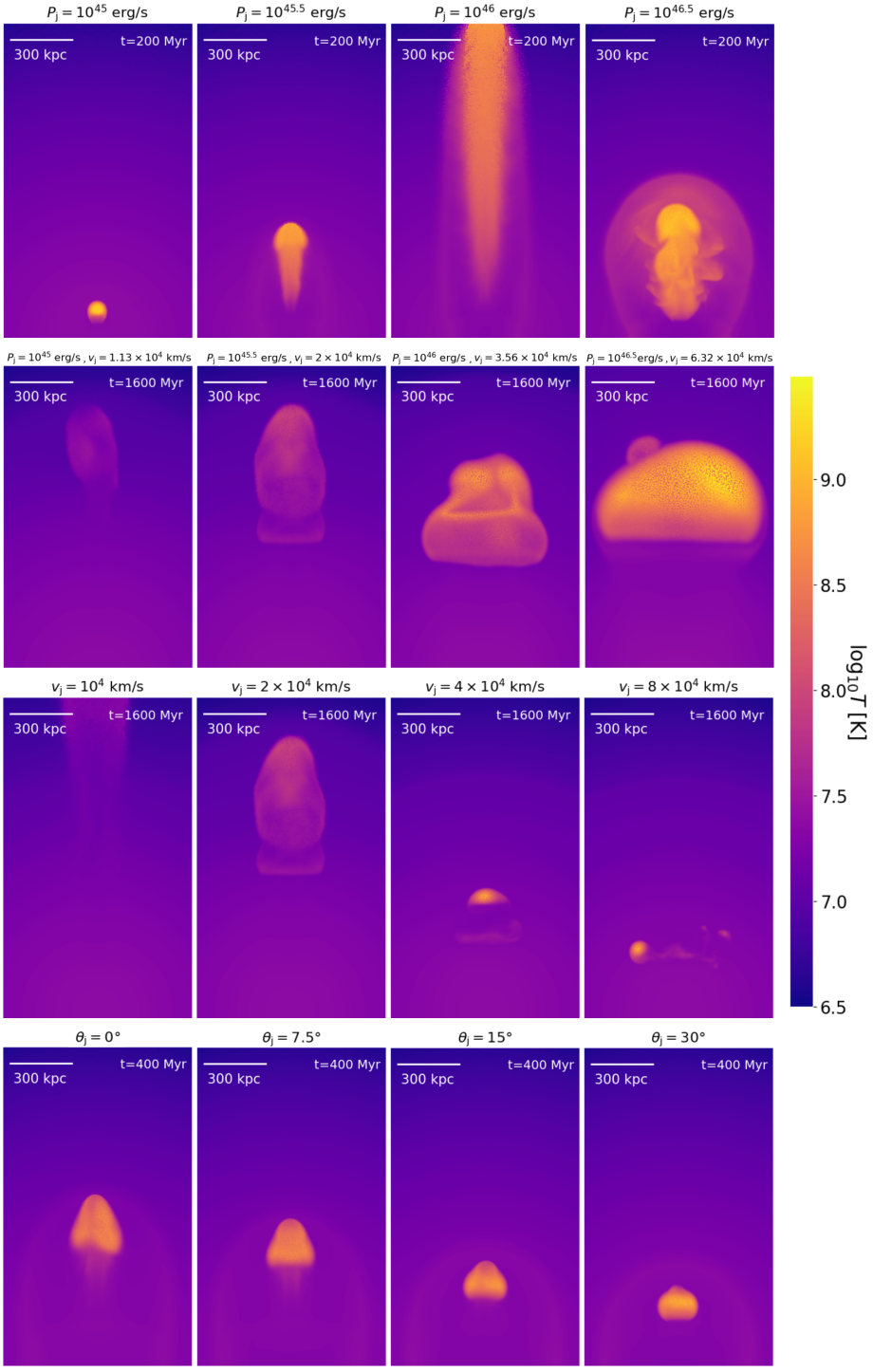

Figure 4.10: Renderings of the gas temperature in simulations with varying physical parameters (first row - jet power, second row - jet power and launching velocity, third row - launching velocity, fourth row - half-opening angle). The standard set of parameters is $P_{\rm j} = 3.16 \times 10^{45}$ erg/s, $v_{\rm j} = 2 \times 10^4$ km/s and $\theta_{\rm j} = 15°$. In each case of a varying parameter(s), we show the visualizations at a specific time of interest for that variation (top right corner in each panel). The relevant parameter(s) being varied in each simulation is shown above each panel. The jet duration is 50 Myr, and the numerical resolution $m_{\rm gas} = 10^5$ M$_\odot$.

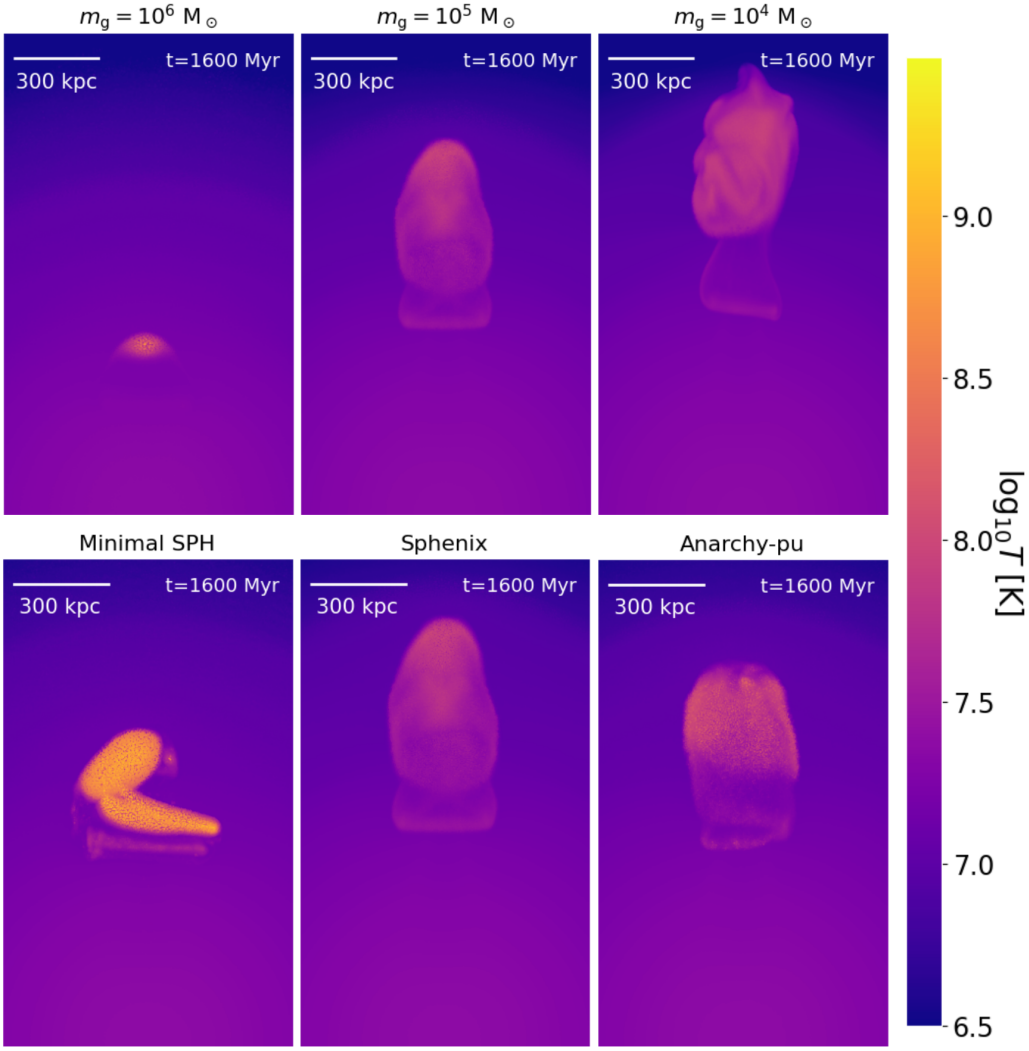

Figure 4.11: Renderings of the gas temperature in simulations with varying numerical resolution (top row) and hydrodynamical scheme (bottom row). The jet-related parameters used in these simulations are $P_\mathrm{j} = 3.16 \times 10^{45}$ erg/s, $v_\mathrm{j} = 2 \times 10^4$ km/s and $\theta_\mathrm{j} = 15°$, $T_\mathrm{j} = 50$ Myr. The numerical resolution or scheme being used in each simulation is shown above each panel.

a smaller distance than the case with a jet power 3.16 times lower. This is likely due to instabilities, which promote the mixing between the hot gas and the ambient medium.

4.5.2 Varying both the jet power and launching velocity

We now vary the jet powers in the same way as in the previous case, but we also vary launching velocities by factors of $10^{1/4} \approx \sqrt{3.16} \approx 1.78$, relative to the fiducial choice of $v_{\rm j} = 2 \times 10^4$ km/s. This ensures that the mass of the jets/bubbles remains the same regardless of jet power, and in turn also the numerical resolution (number of particles) in the jets/bubbles. From the second row in Fig. 4.5, showing the bubbles at $t = 1600$ Myr, we can see that the differences in bubbles are less drastic than if only jet power was varied. Somewhat surprisingly, the bubbles reach smaller and smaller distances as the jet power and launching velocity are increased. This is likely due to a backflow which widens the jet lobes at higher launching velocities (English et al. 2016, Li et al. 2018, Huško & Lacey in prep), which is visible in the wider bubbles shown in the snapshots.

4.5.3 Varying the jet launching velocity

We now discuss cases with varying jet launching velocities, by factors of two relative to our fiducial value of $v_{\rm j} = 2 \times 10^4$ km/s. The visualizations of these simulations are shown in the third row of Fig. 4.5. As is visible, the jet launching velocity can impact the bubbles significantly. Lower launching velocities lead to more elongated, less spherical bubbles which traverse larger distances. This is likely due to a larger momentum in the jets with lower velocities (the total jet momentum is $p_{\rm j} = 2E_{\rm j}/v_{\rm j}$). With the highest launching velocity, the bubble has broken up at a small distance. This is potentially due to lower resolution of the bubble (the number of particles in the bubble scales as $N \propto 1/v_{\rm j}^2$), the backflow at higher launching velocities, or different stability properties of the bubble at smaller distances.

4.5.4 Varying the jet half-opening angle

We now discuss cases with varying half-opening angles. Our fiducial choice is $\theta_{\rm j} = 15°$, and we compare with simulations where it is a factor of two lower and higher, as well as with a case with $\theta_{\rm j} = 0°$. The visualizations of these simulations are shown in the bottom panels of Fig. 4.5, at $t = 400$ Myr. The bubbles are wider and reach smaller distances with larger opening angles. However, the differences are not drastic. This is likely due to the change in behaviour once the jets leave the core of the gaseous halo. At that point, they begin to expand more freely near the jet head, and the opening angle becomes less significant.

4.5.5 Impact of numerical resolution

It is important to verify that the simulations converge to the same results if numerical resolution is varied. We compare out standard resolution of $m_{\rm gas} = 10^5$ M$_\odot$ with simulations which are a factor of 10 higher (our highest-resolution simulation, the one which we discussed in § 4.4 and § 4.3) and a factor of 10 lower in mass. The visualizations of the different simulations are shown in the top panels of Fig. 4.5. The low-resolution bubble appears shorter and has traveled a smaller distance than the two higher-resolution ones, which are very similar in shapes and positions. The low-resolution jet is likely too spherical due to spherical averaging in SPH. The agreement at higher resolutions is encouraging.

4.5.6 Impact of hydrodynamical scheme

The hydrodynamical scheme we used for all of the simulations presented so far was SPHENIX (Borrow et al. 2020). It includes an artificial viscosity limiter, since artificial viscosity is a known problem for SPH. It also has artificial conductivity, which is meant to reproduce diffusion of energy through unresolved mixing. Here we compare SPHENIX to a 'minimal SPH' scheme in SWIFT, which mimics traditional SPH schemes without artifical viscosisty limiters or artificial conduction (Monaghan 1992b). We also compare to anarchy-pu, the scheme used for the EAGLE simulations (Schaye et al. 2015, Schaller et al. 2015).

The bottom panels of Fig. 4.5 show the bubbles simulated with each of these schemes. The bubble in minimal SPH is more spherical and hotter than the ones in SPHENIX and anarchy-pu, as well as in the process of breaking up. The other two bubbles are fairly similar. The minimal SPH bubble also shows 'droplets' in its wake, which is likely parts of the bubble detaching due to artificial surface tension (Agertz et al. 2007, Sijacki et al. 2012, Nelson et al. 2013), likely from a lack of an artifical viscosity limiter. It is hotter probably due to a lack artificial conduction. The anarchy-pu bubble is not hotter than the SPHENIX one, indicating similar conduction. However, it does feature a somewhat more grainy and less smooth surface, possibly due to a somewhat smaller conduction or viscosity limiter.

4.6 Conclusions

We performed simulations of bubbles that form in the aftermath of constant-power, individual jet episodes launched by active galactic nuclei. The jets are launched into a gravitationally-supported gaseous halo representing the intracluster medium of a low-mass galaxy cluster. We studied the evolution of the jet-inflated bubbles and their interaction with the ambient medium as they rise through it.

After the jets are turned off, buoyancy begins to act on the shocked jet gas from the sides. The shocked jet gas transitions from a jet-like shape to a spherical bubble, and eventually develops an indentation at its bottom from ambient gas which is acting on it. As the bubbles rise, they draw out filaments of low-entropy gas from the central regions of the gaseous halo (the drift), as well as trapping a portion of the ambient medium at their bottom (the wake), which rises alongside the bubbles. Entrainment of the ambient medium is important only during the early phase (when the bubbles are forming), where the amount of it is consistent with being caused first by the momentum-driven launching of the jets, and then Rayleigh-Taylor instabilities.

Most of the injected jet energy is transferred to the ambient medium through bow shocks. Later on, as the wake and drift begin to rise, almost all of the injected energy is in the change of the gravitational potential energy (for both the bubbles

and the ambient medium). This is consistent with radial profiles of gas-related quantities such as density, which indicate that the drawing out of the drift and wake has reduced the central density of the gaseous halo by a factor of two, while the central temperature is raised by 40 per cent. These findings indicate that it is possible, in a realistic scenario, that jet feedback proceeds not only through heating of the ambient medium, but also through a reduction of the central density.

By varying the jet power and jet velocity, as well as both at the same time, we find that the dominant changes in late-time behaviour of the bubbles do not come from extra energy, but rather extra momentum of the jets. Bubbles with more momentum can travel much farther in the ambient medium, to the point of escaping it. By varying the half-opening angle of the jets, we find more spherical bubbles that travel shorter distances at larger opening angles, as expected. By varying numerical resolution, we find that our simulations are well converged. Comparing our standard bubbles with those simulated using minimal SPH, we find that minimal SPH features too much artificial viscosity and not enough diffusion. The anarchy-pu scheme, which was used for the EAGLE simulations, matches our bubbles closely.

CHAPTER 5

Spin-driven jet feedback in idealised simulations of galaxy groups and clusters

5.1 Introduction

In Chapters 3 and 4 we presented results of idealised hydrodynamical studies where no black holes were used, and where jet episodes were implemented 'manually' by means of particle kicks from initially placed reservoirs, with a constant jet power. However, our ultimate aim is to implement realistic jet feedback in cosmological simulations of galaxy formation. We will thus generalize our approach, and test the model for black hole spin evolution and jet feedback presented in Chapter 2.

We decide to perform our tests of more realistic jet feedback in simulations of idealized galaxy clusters (similar as in Chapters 3 and 4), since there is abundant evidence of jet activity in these clusters, and their effects are understood to at least some degree (Fabian 2012). While evidence of jet activity in group-size systems is harder to detect, it appears that similar feedback is going on in such systems as well (Bîrzan et al. 2004, Eckert et al. 2021), so we will also simulate them. The main difference, compared to Chapters 3 and 4, is that we include more physics in the tests presented in this Chapter, such as radiative gas cooling, star formation,

and black hole accretion and feedback. Since we implement accretion based on gas properties, the feedback in the results presented in this chapter is self-consistent, rather than representing a controlled experiment with a single burst of activity.

Previous such simulations have already been performed. These simulations almost exclusively use adaptive mesh refinement (AMR), with spatial resolutions typically reaching $200-500$ pc (e.g. Gaspari et al. 2011, Li et al. 2015, Beckmann et al. 2019) in the centres of the simulated systems. The jet velocities used are of order 10^4 $\mathrm{km s^{-1}}$ (e.g. Gaspari et al. 2011, Yang & Reynolds 2016, Meece et al. 2017), and the jet efficiencies ϵ_j are typically low, in the range $\epsilon_\mathrm{j} = 10^{-4} - 10^{-2}$ (e.g. Gaspari et al. 2012, Yang & Reynolds 2016, Martizzi et al. 2019). The jets are usually launched in a fixed direction, but some studies have included precession imposed by hand (e.g. Li et al. 2017, Meece et al. 2017). The jet powers achieved in these simulations are in the range $P_\mathrm{j} = 10^{45} - 10^{46}$ $\mathrm{erg s^{-1}}$ (e.g. Yang & Reynolds 2016, Li et al. 2017, Martin et al. 2019). The cold gas masses found in these simulations are often fairly large, $M_\mathrm{cold} = 10^{10} - 10^{11}$ $\mathrm{M_\odot}$ or larger (e.g. Li & Bryan 2014a), probably due to low jet efficiencies. The only previous study of jet feedback with spin evolution, in a similar context, is that of Beckmann et al. (2019).

5.2 Numerical implementation and physical set-up

5.2.1 Black hole feedback model

In Chapter 2 we presented our full hybrid model, which has three accretion disk types, with different formulas for wind, radiative and jet efficiencies for each of them. In this Chapter, our aim is to test self-consistent jet feedback in a fairly controlled manner. We also choose to do it in idealized galaxy clusters at low redshifts. This means that the black holes we simulate are unlikely to have Eddington ratios larger than $f_\mathrm{Edd} \approx 0.01$ (supported by observations very rarely finding quasars in BCGs). For these reasons, we will test only our thick disc accretion and feedback regime. In addition to not implementing the winds in the thick disc regime, we also choose to not implement the suppression of the accretion rate due to these winds.

However, relative to the model presented in Chapter 2, we modify the spinup/spindown

rate of black holes slightly. The reason is that jet launching, as inferred from thick discs from GRMHD simulations, will cause the black holes to be spun down from a finite spin to nearly $a \approx 0$ in a finite (and potentially short) time. At low spins, however, the jet efficiency is very low, and black holes begin to grow uncontrollably due to lack of effective feedback. This is not a realistic situation, as in reality, the black holes would simply tip over into the thin disc regime at $f_{\rm Edd} > 0.01$, where spinup is again very efficient. Furthermore, black hole mergers may provide additional spin evolution in a more realistic context.

Given the above issue with implementing GRMHD spinup/spindown formulas for the sole thick disc accretion/feedback regime, we instead use an analytical prescription, motivated by Moderski & Sikora (1996) and Benson & Babul (2009). We write the spinup/spindown rate as

$$s_{\rm thick} = \left(\frac{{\rm d}a}{{\rm d}M_{\rm BH,0}/M_{\rm BH}} \right)_{\rm thick} = \ell_{\rm in} - 2ae_{\rm in} - s_{\rm jet}, \tag{5.1}$$

where $\ell_{\rm in} = cL_{\rm in}/GM_{\rm BH}$ is the dimensionless specific angular momentum at the event horizon. We assume that $\ell_{\rm in}$ is equal to 45 per cent of the value at the ISCO (consistent with the model in Benson & Babul 2009, and also with results from GRMHD simulations).

The change in mass of the SMBH can be related to the mass funneled towards it from large distances through ${\rm d}M_{\rm BH} = (1 - \epsilon_{\rm jet}){\rm d}M_{\rm BH,0}$, where we have assumed jets to be the only mechanism of energy extraction or mass loss from the accreting gas and the BH (i.e. no radiative or wind losses). We assume $e_{\rm in}$ at the event horizon to be $e_{\rm in} = 1$ (see Benson & Babul 2009 for the effects of varying the choice of $e_{\rm in}$). This corresponds to the assumption that the radiative efficiency $\epsilon_{\rm rad}$ is negligible in the thick disc (see e.g. Mahadevan 1997 or Yuan & Narayan 2014), and also that the transport of energy outwards through viscous or magnetic forces is negligible.

The first two terms in Eqn. (5.1) appear due to accretion, while the third one is present due to jet spindown. In this chapter we assume the form from Benson & Babul (2009):

$$s_{\rm jet} = \epsilon_{\rm jet}(a) \frac{\sqrt{1-a^2}}{a} \left[\left(\sqrt{1-a^2} + 1 \right)^2 + a^2 \right]. \tag{5.2}$$

Here we have ignored the effects of disc winds (unlike Benson & Babul 2009), which would generally appear as an additional efficiency term along with $\epsilon_{\rm jet}$. The derivation of equation (5.2) assumes that the launching of the jet and accretion onto the BH are decoupled processes, i.e. the mass-energy of the gas in the accretion disc does not directly contribute to the jet, and it is instead powered entirely by the rotational energy of the SMBH.

A further assumption in the derivation of equation (5.2) is that the change of rotational energy of the SMBH, $\dot{E}_{\rm rot}$, exactly matches the jet power (in magnitude). This is equivalent to assuming that the irreducible mass-energy of the SMBH, $E_{\rm irr}$ (which is related to the rotational energy through $E_{\rm rot} + E_{\rm irr} = c^2 M_{\rm BH}$), remains constant as the jet is launched. While the irreducible mass-energy cannot be reduced in the jet launching process, it is possible that the irreducible mass-energy grows as the jet is launched, with the rotational mass-energy being decreased at a rate even greater (in magnitude) than $-P_{\rm j}$. Thus, equation (5.2) represents a *minimum* spin-down rate due to jet launching. GRMHD simulations show stronger spindown than this, but our current formulation has the advantage (for this particular application!) that the equilibrium spin value is $a_{\rm eq} \approx 0.25$, rather than $a_{\rm eq} \approx 0$, so the amount of feedback that our black holes can do (if they are only allowed to be in the thick disc regime) is allowed to be much higher.

5.2.2 Numerical code and subgrid physics

As in the previous chapters, we use the numerical code SWIFT. We have included our full BH and AGN feedback model into it, as well as options that allow the use of simpler versions of it, such as that of interest in this Chapter (i.e. solely accretion in the thick disc regime with jet feedback). We again use the SPHENIX hydrodynamical scheme.

In our simulations, we represent the gravity of the dark matter halo using an external potential. The stellar component is represented by a live population of gravitationally interacting particles, while the gaseous component is represented with SPH particles. The smoothing lengths are set to 1.2348 times the local inter-particle seperation, corresponding to a target neighbour number of 58. The minimal

smoothing lengths are set to 0.01 times the gravitational softening length (the values of which are discussed in §5.2.7).

The gas is allowed to cool radiatively based on the cooling function from Ploeckinger & Schaye (2020), although it is not allowed to cool down to the molecular phase. Instead, we use an entropy floor (see Nobels et al. 2022 for details). Star formation is modeled based on the Kennicutt-Schmidt law (Kennicutt 1998) using the gas pressure (Schaye & Dalla Vecchia 2008). We do not include any stellar feedback, magnetic fields or other physics.

5.2.3 Black hole accretion

In the centre of the halo we place a SMBH and fix its position, not allowing it to wander around based on gravitational interactions with the surrounding gas, nor to reposition to the potential minimum (Bahé et al. 2022). We model the accretion rate using the Bondi-Hoyle-Lyttleton prescription (Hoyle & Lyttleton 1941, Bondi 1952b):

$$\dot{M}_{\rm BHL} = 4\pi \frac{G^2 M_{\rm BH}^2 \rho}{(c_{\rm s}^2 + v^2)^{3/2}}, \tag{5.3}$$

where ρ, $c_{\rm s}$ and v are the kernel-weighted density, isothermal sound speed and velocity (relative to the SMBH) of the gas, respectively, all of which are calculated from the smoothing kernel of the SMBH. We assume that $\dot{M}_{\rm BH,acc,0}$, the large-scale accretion rate of the SMBH, is equal to the Bondi rate. Here we use the subscript '0' to differentiate the large-scale accretion rate and the mass growth rate $\dot{M}_{\rm BH}$; the two differ since the radiative and/or jet efficiencies are non-zero.

Some observations (e.g. Nemmen & Tchekhovskoy 2015) indicate that a fraction (possibly a very large fraction) of the material infalling from the Bondi radius does not reach the black hole. Instead, it could be blown away in a kinetic wind (Blandford & Begelman 1999, Yuan & Narayan 2014), effectively reducing the feedback efficiency. Most simulations with a similar set-up as ours have used low efficiencies, since such efficiencies appear to be in line with observations. For simplicity, and since we are presenting the first application of a model with self-consistent, spin-driven jet feedback hosted by a thick accretion disk, we do not reduce the Bondi

accretion rate by any such factor. For a similar reason, we do not suppress the Bondi rate due to the turbulence and vorticity of the gas (e.g. Krumholz et al. 2005, Krumholz et al. 2006). Our results should thus be treated as an upper limit to the possible impact of jets. Given we do not suppress the accretion rate, the Eddington ratio defined in terms of the net accretion rate onto the BH, $f_{\rm Edd}$, is the same as the one defined using the large-scale one, $f_{\rm Edd,0}$, in this chapter. Note that here we also use the definition of the Eddingtion ratio in which the radiative efficiency is constant ($\epsilon_{\rm rad} = 0.1$), rather than the spin-dependent Novikov & Thorne (1973) one as in Chapter 2.

5.2.4 The numerical algorithm for spin evolution

In the previous section we discussed the theory behind our model for spin evolution. Here we will lay out how we implement the model, and and how this can be generalized to other hydrodynamical simulations (e.g. EAGLE, Schaye et al. 2015), and in general in any hydrodynamical code (e.g. SWIFT, Schaller 2018). Using the same SPH particles that are used to calculate the Bondi accretion rate onto the SMBH, we measure the angular momentum direction of the gas, $\hat{\mathbf{J}}_{\rm d}$, in SMBH smoothing kernel. We assume this to be the direction of the angular momentum of the subgrid accretion disc at large distances, outside the influence of LT torques (i.e. outside the warp radius).

At the beginning of every time step of length Δt, given a mass reservoir $\Delta M_0 = \dot{M}_{\rm BH,acc,0}\Delta t$ to be consumed and disc angular momentum direction $\hat{\mathbf{J}}_{\rm d}$, our algorithm for evolving SMBH-related quantities is as follows:

1. Calculate the warp radius $R_{\rm warp}$, mass $M_{\rm warp}$ and angular momentum $J_{\rm warp}$.

2. Decide whether accretion is prograde or retrograde, based on the angle between the current SMBH angular momentum direction $\hat{\mathbf{J}}_{\rm BH}$ and that of the disc $\hat{\mathbf{J}}_{\rm d}$, as well as the ratio of warp and SMBH angular momenta. If prograde, we set $a = +|a|$, and if retrograde $a = -|a|$.

3. Calculate the jet feedback efficiency $\epsilon_{\rm j}$.

4. Increase the SMBH mass by $(1-\epsilon_{\rm j})\Delta M_0$ and evolve the SMBH spin. The direction of the angular momentum of the SMBH is modified such that it matches that of $\mathbf{J}_{\rm BH} + N_{\rm warp} J_{\rm warp} \hat{\mathbf{J}}_{\rm d}$, where $\mathbf{J}_{\rm BH}$ is the old SMBH angular momentum vector, and $N_{\rm warp}$ is defined below. The jet feedback energy reservoir is incremented by $\epsilon_{\rm j} c^2 \Delta M_0$.

Note that step i) can precede step ii) since warp-related quantities do not depend on the sign of a. In the above algorithm, $N_{\rm warp} = \Delta M_0 / M_{\rm warp}$ represents the number of individual accretion events assumed to occur over a single time step. This can also be viewed as the SMBH acquiring angular momentum through LT torques from the warped disk with an effective specific angular momentum of $L_{\rm warp} = J_{\rm warp}/M_{\rm warp}$, so the total angular momentum acquired through LT torques by the SMBH is $\Delta J = L_{\rm warp}\Delta M_0 = (J_{\rm warp}/M_{\rm warp})\Delta M_0 = N_{\rm warp} J_{\rm warp}$. Note that typically, $N_{\rm warp} \gg 1$, due to small warp radii of the thick disc, and thus also small warp masses. Numerically, it is not feasible to evolve the system one warp increment at a time (nor is there any gain in doing so). Finally, the above algorithm is only applicable if the black hole spin and its direction change very little over a single time step. We ensure this by adding a SMBH time-step whose duration is chosen such that $\Delta J \approx 0.01 J_{\rm BH}$, or less.

In the Appendix 5.A we show that the timescale for alignment of the SMBH spin vector with that on large scales using this scheme is similar to the alignment timescale in an approach where LT torques are explicitly included in the equation for angular momentum evolution. This demonstration was done for the thin, radiatively-efficient disc (Shakura & Sunyaev 1973), rather than the thick disc, since the relevant LT torque terms in the angular momentum evolution equation are valid only for the thin disc. We found that the timescale in our warp increment approach is $\approx 10\%$ longer, but it depends on SMBH mass and accretion rate in the same way as the one in the differential equation approach.

5.2.5 Jet launching

Here we describe the numerical scheme for the kicking of jet particles used in this Chapter. The scheme is slightly different than that described in Chapter 2 since the

research presented in this Chapter was done earlier, while Chapter 2 presents our fully developed and most up-to-date version of the model.

The jet power is calculated from the current spin and mass accretion rate as $P_{\rm j} = \epsilon_{\rm j} \dot{M}_{\rm BH,acc,0} c^2$, using the spin-dependent efficiency of the thick disc presented in § 2.4. With every time step Δt, the jet energy reservoir is increased by $P_{\rm j} \Delta t$. When this reservoir exceeds $2 \times (1/2) m_{\rm g} v_{\rm j}^2$, where $m_{\rm g}$ is the particle mass and $v_{\rm j}$ the launching velocity, two particles are kicked from the SMBH smoothing kernel,[1] and the jet reservoir is decremented by $2 \times (1/2) m_{\rm g} v_{\rm j}^2$. The two particles kicked in each jet event are the farthest from the SMBH (within the smoothing kernel) in our standard scenario, with one on each side of the SMBH (relative to its angular momentum vector). We choose the farthest particles as our fiducial prescription since we found that other choices can lead to rapid evacuation of the region around the SMBH. The velocity vectors are chosen at random within cones with half-opening angles, relative to the spin axis, equal to some value $\theta_{\rm j}$ (our standard choice being 10°). We compute jet powers using actual jet kicking events (with adaptive time bins, each with a target number of 20 kicking events), instead of defining it as the rate at which the the jet energy reservoir is increased due to accretion.

The jet launching velocity, $v_{\rm j}$, is a free parameter in our model, and probably the most important one (see Chapters 3 and 4). Choosing values that are too low leads to high-momentum (ballistic) jets that drill through the gaseous halo, without experiencing significant shocks, inflating bubbles or heating the gaseous halo. Real AGN jets are highly relativistic and low-density, thus reaching the self-similar stage very quickly, or equivalently at very small distances (see e.g. Kaiser & Best 2007 for the physics of jets in the self-similar regime). On the other hand, using very large values of the jet launching velocity (close to relativistic) leads to poorly resolved jets. Note that the evolution of the shapes of the self-similar lobes inflated by jets in the self-similar regime, as well as their energetics, should not vary at all with velocity (Kaiser & Best 2007). Furthermore, non-relativistic jets that inflate self-similar lobes are very similar to self-similar lobes produced by relativistic jets of

[1]Note that energy is not exactly conserved with this scheme. However, since our launching velocities are always much larger than the initial ones, this effect is negligible.

the same jet power, with differences of order 10%. Through trial and error we have found that values of $v_{\rm j} \approx 10-30c_{\rm s}$, where $c_{\rm s}$ is the sound speed of the ICM, represent a reasonable compromise.

The choice of an appropriate velocity can ensure that the jet-inflated lobes in our simulations reach the self-similar regime. This in turn means that they exhibit similar hydrodynamics as in the case where they are inflated by fully relativistic jets. However, it is important to note that such jet-inflated lobes do not capture all aspects of observed radio lobes. This is because we do not model physics that may be important for this particular problem. Magnetic fields could be dynamically important in real jets and lobes since they can contribute some fraction of pressure to the lobes (e.g. Konar et al. 2009), and they can affect the stability of the jets (Nakamura et al. 2001, Tchekhovskoy & Bromberg 2016). The inclusion of cosmic rays (CRs) may also be important, especially if jet-inflated lobes are dominated by CRs. This is because such lobes may not easily exchange energy with the ambient medium, depending on the properties of CR transport (see e.g. Ruszkowski et al. 2017). However, CR physics is still not fully understood, nor is it clear whether CRs are dynamically dominant in real jet-inflated lobes (although they are likely dynamically significant, see e.g. Beckmann et al. 2022). Even in the case that magnetic fields and CRs are important for the evolution of jets and lobes, our kinetic jet feedback without magnetic fields and CRs may still quench cooling flows in a manner similar as observed. This is because a large fraction (of order 50% or more) of the energy launched into the jets is quickly transferred to the ICM through bow shocks (e.g. Bourne & Sijacki 2017, Weinberger et al. 2017a, Huško & Lacey 2022). These bow shocks are launched by the lobes displacing the ICM and this process should be insensitive to the makeup of the lobes.

5.2.6 Dark matter, stars and gas

The initial conditions for our set-up are discussed in detail in Nobels et al. (2022). Here we present a summary of the main features of the set-up. The dark matter component is represented with an external Navarro et al. (1996b) potential, and its concentration parameter depends on the mass of the system (see § 5.2.7). We

include a stellar component in the form of a spherically symmetric Hernquist profile (Hernquist 1990). The velocity dispersion of the stellar halo is determined from the Jeans equation (Jeans 1915), with the choice of no net rotation.

The main component in our simulations, other than the SMBH, is the gaseous halo, which represents the circumgalactic/intracluster medium (CGM/ICM hereafter). The sound speed of this gas, $c_{\rm s}$, is set equal to the circular velocity, $v_{\rm c}$, which determines the temperature profile of the halo. Along with the equation of hydrostatic equilibrium, this condition sets the shapes of the pressure and density profiles. We assume that the gas is ideal, with an adiabatic index $\gamma = 5/3$. The normalisation of the density profile is determined from the total gas fraction within the R_{500} radius, which is calibrated using the results from the BAHAMAS simulations (McCarthy et al. 2017), and which reproduce the observed gas fractions.

In the central regions of the gas halo, the temperature profile is modified such that it can represent a typical profile found in cool-core clusters. This modification is controlled by a free parameter: the minimal central temperature of the gas, T_0. The gas is given a constant fraction of the (radially varying) circular velocity $v_{\rm c}$ in the positive $z-$axis direction, such that the dimensionless spin parameter of the halo, $\lambda_{\rm g} = J_{\rm g}/(\sqrt{2}M_{\rm g}V_{200}R_{200})$ (Bullock et al. 2001), is equal to the mean value $\lambda = 0.05$ for dark matter haloes found in cosmological simulations. Here, R_{200} and V_{200} are the virial radius and the circular velocity at the virial radius of the dark matter halo, respectively, and $M_{\rm g}$ and $J_{\rm g}$ the total mass and angular momentum, respectively, of the gaseous halo within R_{200}. The metallicity of the gas is set to $0.3Z_{\odot}$ (with $Z_{\odot} = 0.0134$). In the central regions of our gaseous halo, within a radius of $R_{\rm res}$, we use a gas particle mass resolution of $m_{\rm gas,0}$. The same mass is used to represent the stellar Hernquist component. Beyond $R_{\rm res}$ the mass resolution of the gas increases as $m_{\rm g} = m_{\rm gas,0}(r/R_{\rm res})^2$. Using a variable resolution allows for, effectively, higher-resolution simulations to be run. In order to properly resolve the cooling flow and jet feedback, we use a large value of $R_{\rm res} = 500$ kpc.

5.2.7 Simulations

We focus on three different systems: the 10^{13} $M_\odot$, 10^{14} $M_\odot$ and 10^{15} $M_\odot$ haloes, where the halo masses are defined as the masses within the virial radius R_{200}, the radius within which the mean density is 200 times larger than the critical density (assuming $z = 0$). The virial radii of the three haloes are 442.7 kpc, 953.8 kpc, 2054.8 kpc, respectively. In terms of virial overdensities computed using mean densities that are 500 times the critical density, the halo masses, M_{500}, are 7.79×10^{12} $M_\odot$, 7.52×10^{13} $M_\odot$ and 7.16×10^{14} $M_\odot$, while the virial radii, R_{500}, are 305.8 kpc, 651.2 kpc and 1358.8 kpc. The concentration parameters of these haloes are 7.2, 5.6 and 4.0. The stellar masses of the galaxies placed in their centres are 10^{11} $M_\odot$, 2.5×10^{11} $M_\odot$ and 6×10^{11} $M_\odot$, and the black hole masses are 2.5×10^8 $M_\odot$, 10^9 $M_\odot$ and 5×10^9 $M_\odot$, respectively. These systems represent galaxy groups and clusters. The simulations are run for 8 Gyr in the 10^{13} $M_\odot$ and 10^{14} $M_\odot$ cases, while the largest system is run for 16 Gyr due to its longer cooling times. The parameter values used for the simulations presented in this Chapter are summarised in Table 6.1.[2]

For each of our three halo masses, we perform a few parameter variations. We simulate each halo at three different mass resolutions, differing by factors of 8 (corresponding to changes in the gravitational softening length, $\epsilon_{\rm g}$, by factors of 2). In the two lower halo mass cases, our highest-resolution simulations have a central particle mass resolution of $m_{\rm gas,0} = 10^5$ $M_\odot$ and gravitational softening length $\epsilon_{\rm g} = 300$ pc. The highest-resolution simulation for our most massive halo is 8 times worse in terms of mass resolution, since it is computationally more expensive. The typical smoothing length of the SMBH in our simulations, as well as the highest-density gas, is $2-3$ times lower than the softening length during strong cooling flows, and around 10 times higher than that outside the cooling flows. In our highest-resolution simulation, this corresponds to 100 pc and 1 kpc, respectively. These differences arise due to the presence of cold gas or lack thereof.

We vary the initial SMBH spin for each of the three halo masses. Our fiducial spins (directed along the $z-$axis) are 0.2 in the two lower-mass systems and 0.4

[2]The initial conditions can be found online; see the SWIFT repository.

for the most massive galaxy cluster, corresponding to jet efficiencies of $\approx 3\%$ and $\approx 12\%$, respectively. Even though we use relatively low values of spin, the jet efficiencies are larger than typically assumed in similar simulations (of order 10^{-3}, e.g. Gaspari et al. 2012, Yang & Reynolds 2016, Martizzi et al. 2019). This is a result of our assumption that the accretion efficiency is 100%, i.e. that there are no disc winds and that all of the matter accreting from the Bondi radius reaches and accretes onto the SMBH. Note that the initial SMBH spin does not only change the efficiency; lower values of spin make the SMBH more susceptible to perturbations in the angular momentum of accreting gas, so the SMBH spin vector will precess more or become reoriented more rapidly.

For each halo we vary the central temperature of the initial gas distribution, T_0. This parameter controls whether the halo being simulated starts off as an analogue of a cool-core cluster (low T_0, e.g. 4 times lower than the virial temperature of the halo), a non-cool-core cluster (high T_0, near the virial temperature of the halo), or something in between. For this reason, the choice of the initial central temperature can have a very strong impact on the evolution of the system, as shown by Nobels et al. (2022).

For the highest-mass halo, we have also performed variations of many other parameters. This includes jet-related parameters such as the launching velocity. We also test cases where the axis along which the jets are launched is fixed to be the $z-$axis; in this situation the jet efficiency is also fixed in time, and we vary this constant efficiency. We found that varying the half-opening angle of the jet does not affect our results (see Appendix 5.B).

We also varied parameters related to the ICM. This includes its total angular momentum, the inclination of the ICM angular momentum vector relative to the initial spin vector of the SMBH, and the metallicity distribution of the ICM. We varied several other unrelated parameters. We found that these variations did not affect the feedback cycle significantly, at least in our most massive halo. We discuss these variations in more detail in Appendix 5.B.

Finally, we varied the scheme with which particles are kicked from the SMBH smoothing kernel. Our standard choice, where we kick particles in the SMBH

Table 5.1: List of all simulations. In the first three rows we specify the parameters of our fiducial simulations for each of the three halo masses we have simulated. We then specify the ranges of variations of all other parameters in the next three rows. The parameters are, in order: 1) M_{200} - halo mass, 2) $m_{\rm gas,0}$ - central gas resolution in terms of particle mass, 3) T_0 - central gas temperature, 4) a_0 - magnitude of initial SMBH spin, 5) $\epsilon_{\rm j}$ - jet efficiency; constant value or $\epsilon_{\rm j}(a)$, the spin-dependent efficiency given by equation (2.7), 6) $v_{\rm j}$ - jet launching velocity, 7) Scheme - which particles within the SMBH smoothing kernel are kicked from the SMBH, F: farthest, C: closest, S: closest to the axis of the spin vector (in terms of angular distance), L: lowest density.

M_{200} [$\rm M_\odot$]	$m_{\rm gas,0}$ [$\rm M_\odot$]	T_0 [K]	a_0
10^{13}	10^5	$10^{5.75}$	0.2
10^{14}	8×10^5	$10^{6.75}$	0.2
10^{15}	6.4×10^6	$10^{7.75}$	0.4
10^{13}	$10^5-6.4\times10^6$	$10^{5.25}-10^{6.25}$	$0.1-0.4$
10^{14}	$10^5-6.4\times10^6$	$10^{6.25}-10^{7}$	$0.1-0.4$
10^{15}	$8\times10^5-5.12\times10^7$	$10^{7.25}-10^{8}$	$0.2-0.8$

$\epsilon_{\rm j}$	$v_{\rm j}$ [$\rm kms^{-1}$]	Scheme
$\epsilon_{\rm j}(a)$	5×10^3	F
$\epsilon_{\rm j}(a)$	10^4	F
$\epsilon_{\rm j}(a)$	3×10^4	F
$\epsilon_{\rm j}(a)$	5×10^3	F
$\epsilon_{\rm j}(a)$	10^4	F
$\epsilon_{\rm j}(a), 0.01-1$	$1.5-6\times10^4$	F, C, L, S

smoothing kernel that are farthest from it, is compared with that where we kick the closest particles, the ones closest to the spin axis in terms of angular distance, and the ones of lowest density.

5.3 Results: The quenching of galaxies across the mass scale

5.3.1 Galaxy group

In our lowest-mass system, representing an idealised galaxy group with a halo mass of $M_{200} = 10^{13}$ M$_\odot$, we find that regardless of the initial SMBH spin, mass resolution or initial central gas temperature, the evolution of the system is similar. Initial cooling due to the presence of a cool core leads to a strong jet episode, which subsequently turns off any significant cooling during the next 8 Gyr of evolution. Our results are similar to those found by Nobels et al. (2022) for the same initial conditions using thermal AGN feedback instead of jets. We find that the Eddington-normalised accretion rate $\dot{m}$ reaches peak values of ≈ 0.01 during the initial cooling flow, but only for the low initial spin case ($a_0 = 0.1$) and low initial central gas temperature case ($T_0 = 10^{5.25}$ K). This lasts only for several Myr, after which the accretion rate falls well below that value. In other cases, the accretion rate is always well below 0.01, indicating that the jet-efficient, thick disc regime is applicable in these simulations.

Fig. 5.1 shows the temperature of the gas in our highest-resolution simulation with our fiducial jet launching parameters. We see ellipsoidal lobes being inflated in the first two snapshots. In the third snapshot we see a weak jet, resembling an FRI source (Fanaroff & Riley 1974). This jet is weakly precessing due to the chaotic nature of the angular momentum of accreting gas and since redirecting the spin vector by a few degrees requires very little accretion. The spin value of the SMBH stays very similar to the initial one. The last snapshot shows the system at late times. By this point, the jet power has reduced even more, but it is still non-zero. The system is kept in a steady state by these very weak jets.

In order to quantify jet feedback, we focus on the time dependence of jet powers and star formation rates (cold gas masses follow the SFR very closely). Fig. 5.2 shows the jet powers and star formation rates in our $M_{200} = 10^{13}$ M$_\odot$ simulations, with varying numerical resolution, initial SMBH spin and initial central temperature.

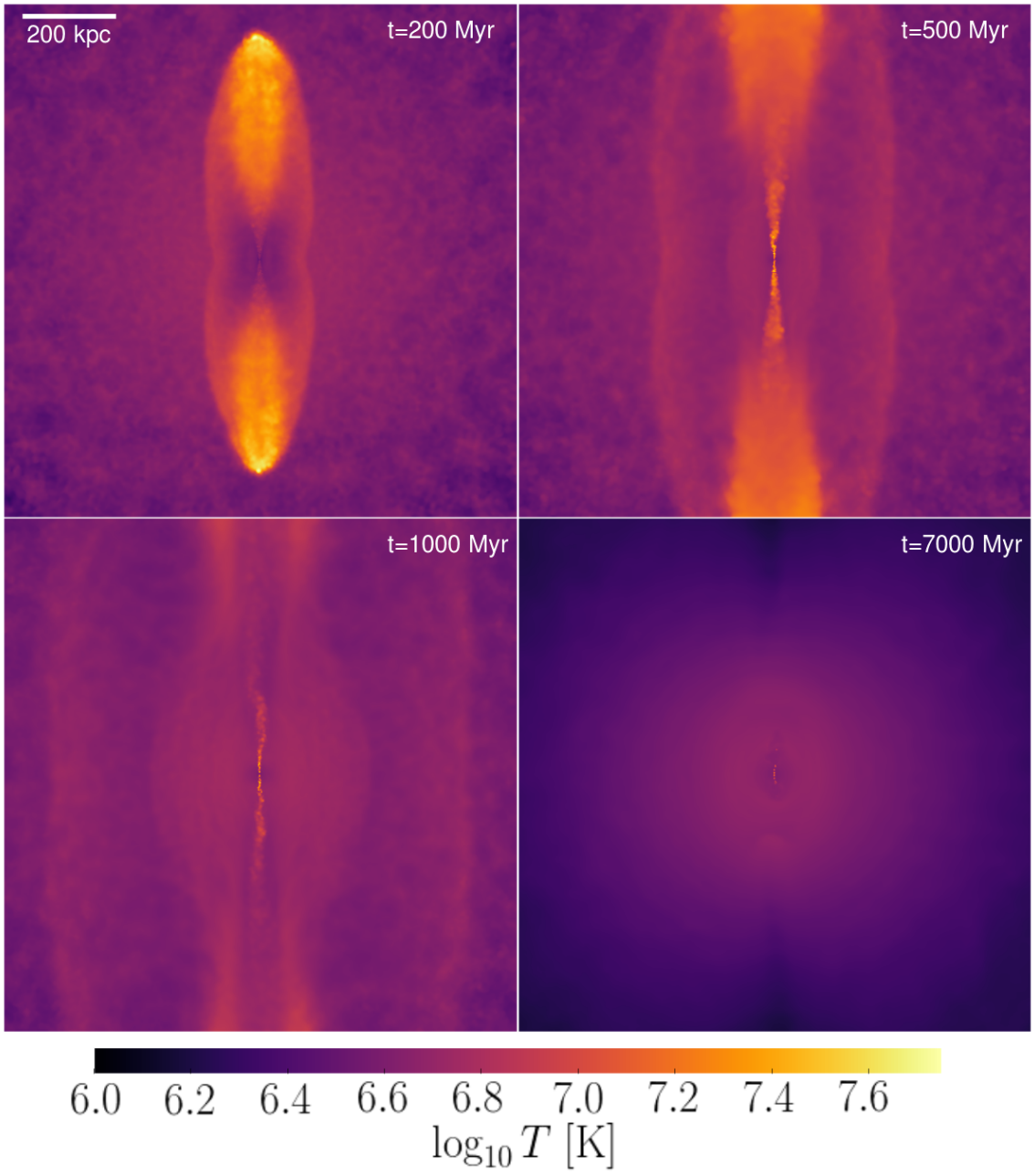

Figure 5.1: Gas temperature projections (mass-weighted mean) in our fiducial simulation (see Table 6.1 for details) of the galaxy group halo ($M_{200} = 10^{13}$ $M_\odot$) at different times. The images show a region 1 Mpc across and 200 kpc in depth. They show initially strong jets that inflate lobes and launch bow shocks, a weaker, precessing jets at intermediate times, and a very weak jet at late times.

These are all very similar, in that there is an initial jet and SFR episode, with the SFR being fully quenched by $t = 0.5$ Gyr. The jet power gradually reduces after reaching a peak within the first 0.5 Gyr. The powering down of the jets is completed by 2 Gyr in all cases. For the remainder of the simulations, the jet powers remain close to their average values, indicating that the system has reached a quenched steady state.

From the left-hand panel, we see that jet powers converge onto the same time dependence across different resolution levels. During the initial jet episode, the three simulations have a very similar jet power. The highest-resolution simulation features a more protracted decrease from the peak, possibly because the jets in that simulation can travel to farther distances and thus heat local gas less effectively. The highest-resolution simulation is also the most variable, as expected due to the finer sampling of energy injection. Star formation is present only during the peak of the initial episode and only in the two higher-resolution runs, and it increases with resolution. After the initial jet episode, the lowest resolution run is so noisy that it features only a few jet kicking events around $t = 3$ Gyr. The two higher-resolution runs appear converged onto a fairly constant jet power after 2 Gyr, with a value of $P_{\rm jet} \approx 10^{41}$ ergs^{-1}. The lower-resolution simulation is less variable in this period due to courser sampling.

From the middle panel, we see that the details of the quenching are very similar regardless of initial SMBH spin (which is, in this case, a proxy for jet efficiency, since spin varies very little during the simulations, and jet efficiency varies as $\epsilon_{\rm j} \propto a^2$ at small spin values, see § **??**). The main difference is that the highest spin case appears less variable during the initial jet episode. This is likely due to the SMBH being able to react more quickly to gas cooling, by launching a pair of particles earlier and thus preventing buildup of too much cold gas.

From the right-hand panel we see that haloes with lower initial central temperatures show more energy injection from jets, as well as more star formation, as expected due to higher rates of gas cooling. Star formation is quenched successfully in all three cases. By $t = 3$ Gyr, all simulations converge onto the same jet power as in the previous cases, including the one where the central temperature is close to

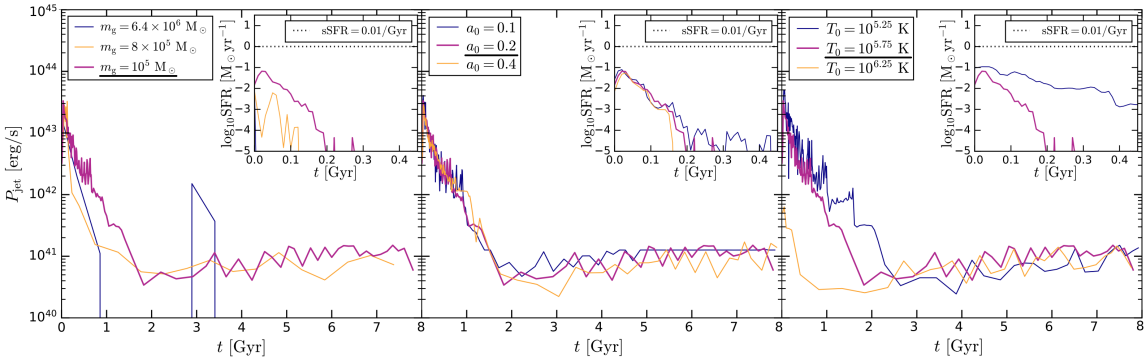

Figure 5.2: Jet power and star formation rate in the $M_{200} = 10^{13}$ M$_\odot$ simulations with varying resolution (left), initial SMBH spin (middle) and initial central temperatures (right). The details of the fiducial case, relative to which these variations are made, are given in Table 6.1 (purple line in each panel, underlined parameter in each panel legend). The dotted black lines represent the upper limit of the specific star formation rate required to classify a galaxy as quenched.

the virial temperature. This likely indicates that all of the gas that differs between the initial profiles is effectively heated or ejected from the central regions of the halo. Since the spin remains constant ($a = 0.2$), a constant jet power implies that the accretion rate is the same between the different simulations. This accretion rate corresponds to Bondi growth directly from the hot halo. These simulations indicate that 'hot accretion' is sufficient to keep the galaxies quenched, at least in systems with $M_{200} = 10^{13}$ M$_\odot$.

5.3.2 Low-mass galaxy cluster

In the low-mass galaxy cluster case, with a halo mass of $M_{200} = 10^{14}$ M$_\odot$ halo, we find that hot halo accretion is not sufficient to keep the central galaxy quenched after the first jet episode. Instead, the galaxy experiences multiple episodes of jet activity and star formation; in each episode, the jets are fed by cold gas. We find that the accretion rate $\dot{m}$ never exceeds values of 0.03, indicating that our jet feedback model is applicable in these simulations.

Fig. 5.3 shows visualisations of jets in the low-mass galaxy cluster at various times, in our highest-resolution simulation ($m_g = 10^5$ M$_\odot$), with our fiducial jet parameters. Since we use the same gas mass resolution as for the galaxy group simulations, and the typical jet powers are significantly larger, the jets appear better

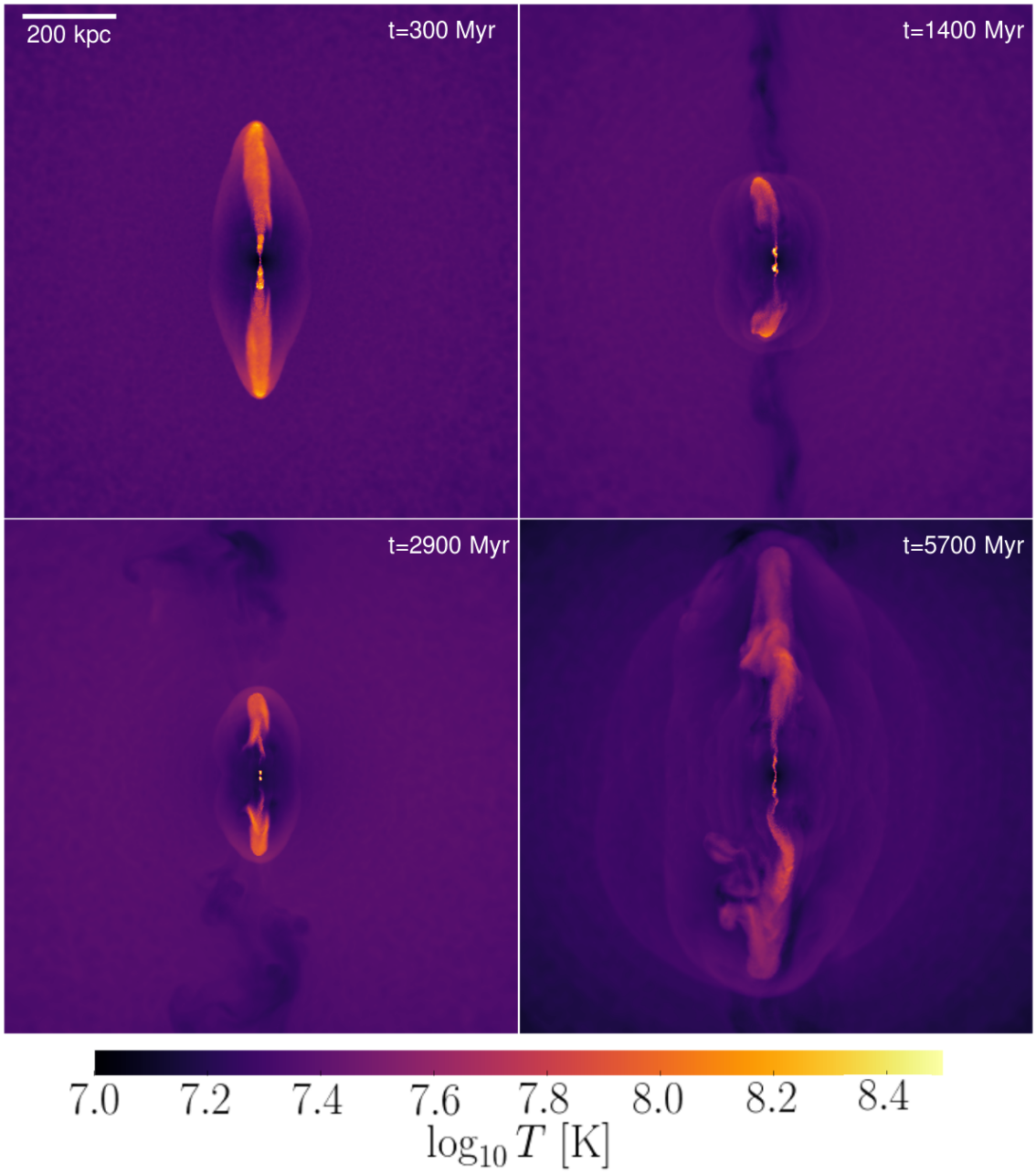

Figure 5.3: Gas temperature projections (mass-weighted mean) in our fiducial simulation (see Table 6.1 for details) of the low-mass galaxy cluster ($M_{200} = 10^{14}$ $M_\odot$) at different times. The images show a region 1 Mpc across and 200 kpc in depth. They show the variety of jet morphologies featured during and between multiple cooling flows. The video version of this plot is available to view at https://youtu.be/Edf2hS7HU70.

resolved. These snapshots highlight the different jet morphologies seen throughout this simulation. In the first snapshot we show the initial jet episode. We see two ellipsoidal lobes, as well as bow shocks propagating through the halo. The hottest gas is near the jet head, as well as near the jet base. This indicates that the jets have features akin to both FRI and FRII jets (Fanaroff & Riley 1974).

In the second snapshot we show the aftermath of a second, weaker episode that occurs ≈ 1 Gyr after the first one. The third snapshot shows an episode of a similar power after a third episode. In both the second and third snapshot, there are signs of low-temperature gas ahead of the bubbles inflated by these weaker jet episodes. This low-temperature gas is a result of uplift of low-entropy gas caused by the first, strong jet episode. We discuss this gas uplift in § 5.4.1. The last snapshot shows the complex morphology caused by a precessing jet that is also varying in power during its episode, causing multiple distinct bow shocks. These jets and bow shocks are also interacting with the infalling low-entropy gas that was previously uplifted, further complicating the picture.

Fig. 5.4 shows the time dependence of jet powers and star formation rates in our low-mass galaxy cluster simulations with varying parameters (the same ones as for the galaxy group case, shown in Fig. 5.2). We also include plots of total injected energy, cold gas mass (cold gas here meaning gas with $T < 2 \times 10^4$ K) and magnitude of SMBH spin. In all cases, jet feedback leads to successful quenching.

In the top panels we show the results of varying the numerical resolution. Overall, increasing the resolution leads to more energy injection from jets, as well as more variability in the jet power. The amounts of cold gas do not increase with resolution, while the SFR increases only from the lowest to the intermediate-mass case. In the two lower-resolution cases, the peaks in the SFRs are well correlated with peaks in the jet power, indicating that the cool gas feeding the jets is also star-forming. In the highest-resolution case, the cold gas mass and SFR is less variable, possibly due to the jets affecting the cold gas to a lesser degree at higher resolutions. The cold gas masses that we find, of order $10^7 - 10^8$ $M_\odot$, are consistent with observations of massive elliptical galaxies (Georgakakis et al. 2001, O'Sullivan et al. 2015).

In the middle panels we see how the feedback depends on the initial SMBH spin.

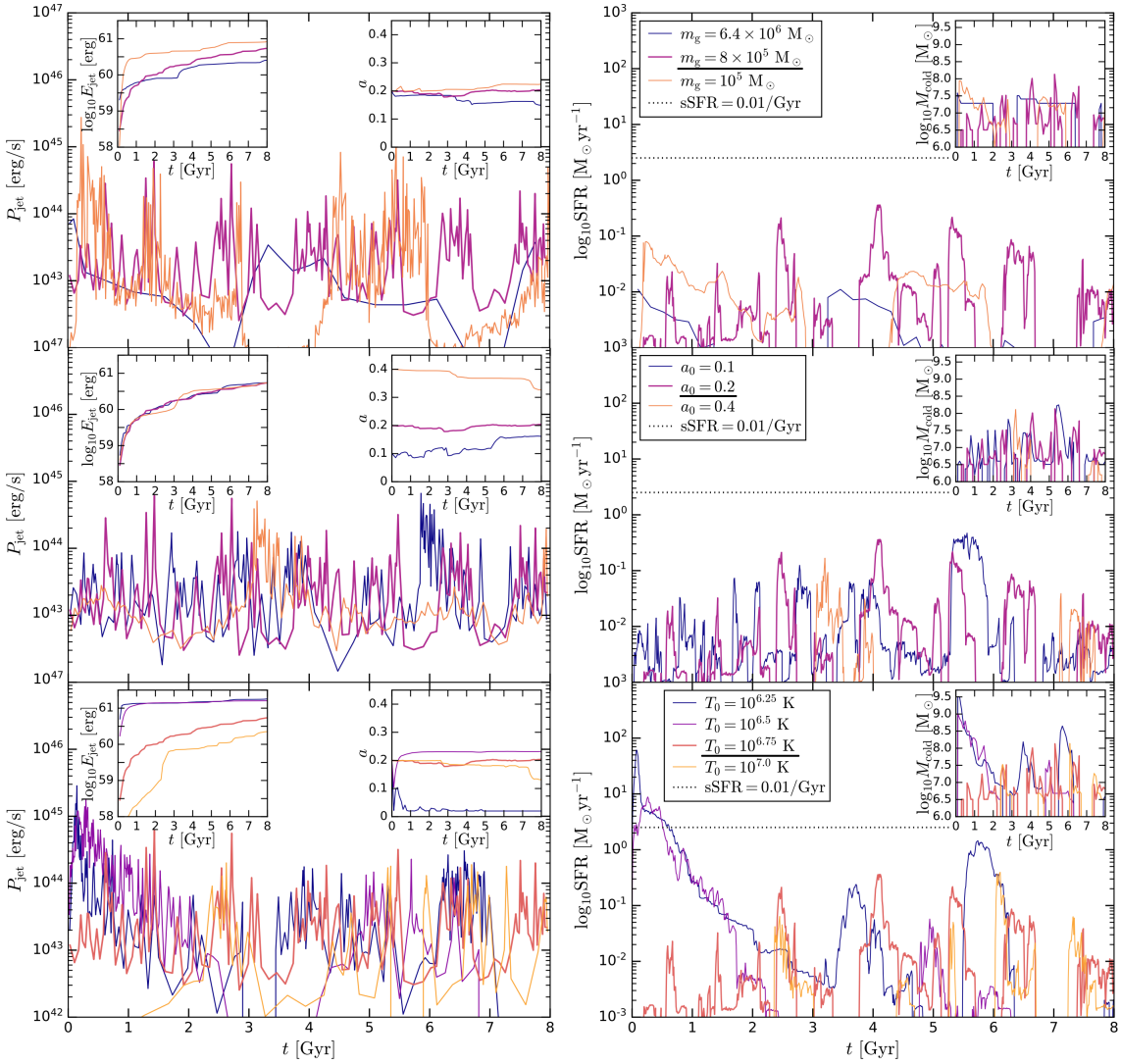

Figure 5.4: Time dependence of the quenching/feedback process in the low-mass galaxy cluster simulations ($M_{200} = 10^{14}$ M$_\odot$) with varying mass resolution (top row), initial SMBH spin (middle row) and initial central temperatures (bottom row). The left-hand panels show the jet power, while the right-hand panels show the star formation rate. Insets in the left-hand panels show the injected jet energy and magnitude of SMBH spin. The insets in the right-hand panels show the cold gas mass. The details of the fiducial case, relative to which these variations are made, are given in Table 6.1 (purple and orange lines in the top/middle and bottom panels, respectively; underlined parameter in each panel legend). The dotted black lines represent the upper limit of the specific star formation rate required to classify a galaxy as quenched.

Unlike in the low-mass simulations, the spin changes somewhat. The medium-spin simulation shows no spin evolution, while in the low-spin simulation, the SMBH is spun up from $a = 0.1$ to $a = 0.15$. The higher-spin simulation features spindown, from $a = 0.4$ to $a = 0.32$ by $t = 8$ Gyr. This spindown is a result of jet activity; in the thick disc regime, jet launching causes a decrease in spin for SMBHs with spins above ≈ 0.25. Although we do not show these results here, we find that the direction of the spin vectors is very well aligned with the $z-$axis, with only the low-spin case showing a small deviation (10°) from the initial direction.

The simulations with $a_0 = 0.1$ and $a_0 = 0.2$ both feature fairly variable jet powers. The peaks of jet activity are very well correlated with peaks in the SFR and cold gas mass. The galaxies are quenched at all times, with cold gas masses reaching values of up to 10^8 $M_\odot$. Outside the strongest SFR/jet episodes, we find small cold gas reservoirs with $M_{\rm cold} < 10^7$ $M_\odot$ throughout most of the simulation. The jet powers are always above 10^{42} ergs^{-1}, which represents the minimum jet power from hot halo accretion. The case with $a_0 = 0.4$ is less variable than the other two. The jet power exhibits two peaks (at $t = 3$ Gyr, and at the very end of the simulation), which coincide with periods when cold gas mass is present, and when stars are being formed. The cold gas masses and SFRs are lower than in the cases with lower initial SMBH spin. This is probably a result of the jet being able to react to an accumulation of cold gas more rapidly (due to higher jet efficiencies), thus promptly shutting off a cooling flow. At the same time, the hot halo accretion launches stronger jets (i.e. the minimum in the jet power is higher, nearer to 10^{43} ergs^{-1}, rather than 10^{42} ergs^{-1}), which results in less cooling during eventual cooling episodes. During the very beginning of the simulation, this is likely what prevented any gas from cooling quickly and launching an initial jet episode. Despite the qualitative differences discussed so far, the total injected energy is very similar in all three cases.

In the bottom panels we show results of varying the initial central temperature. A case with higher initial temperature than fiducial, close to the virial temperature, takes a longer time to show any jet/star formation activity, but even in this case there are jet/star formation cycles. As expected, lower initial central temperatures lead to more cold gas (exceeding 10^9 $M_\odot$), more star formation and stronger jet activity. In

the two lowest-temperature cases, the simulations feature strong initial jet episodes, similar to the lower mass halo. The jet powers peak at 10^{45} ergs^{-1}, and the SFRs reach 100 M$_{\odot}$yr^{-1} in the lowest-temperature case. Unlike the galaxy group case, both of these simulations also feature further jet and star formation episodes later on. However, in the later episodes the jet powers are weaker, and the SFRs are low enough to consider the galaxies quenched. Both simulations feature significant spin evolution. There is significant initial SMBH spindown, with the lowest-temperature case settling down to a very low spin of $a = 0.03$ and misaligned relative to the $z-$axis (not shown here). The somewhat higher temperature case features spinup back to around $a = 0.2$ during the initial jet episode, and the angle between the spin vector and $z-$axis is small throughout the simulation. This is expected since large amounts of cooling generally result in a cold circumnuclear disc. In the lowest-temperature case, it is possible that this did not occur, and the SMBH was spun down into an effectively random direction, because there was sufficient cooling in the very centre of the gaseous halo (where the angular momentum of the gas is lower).

Our results for the low-mass galaxy cluster are overall similar to Nobels et al. (2022) for the same system using thermal feedback. However, we find that the jets quench cooling more effectively, leading to less star formation. The quenching is also less protracted. Furthermore, the jets are able to quench haloes with lower initial central gas temperatures. Finally, we find that our cooling and jet episodes are largely non-periodic, while Nobels et al. (2022) find periodicity. This difference is likely a result of varying efficiency in the jet case.

Beckmann et al. (2019) performed simulations similar to ours (including AGN jet feedback and SMBH spin evolution) and focused on a set-up of an idealised Perseus-like galaxy cluster (which they assumed to have a halo mass of 3.4×10^14 M$_{\odot}$, this may be more comparable to our high-mass galaxy cluster simulations$-$see next subsection). They found much higher cold gas masses and star formation rates than we do ($M_{\rm cold} = 10^{10} - 10^{11}$ and SFR $= 0 - 1000$ M$_{\odot}$yr^{-1}, respectively). Such a lack of strong quenching is not necessarily surprising since the Perseus cluster is a cool-core cluster (Schmidt et al. 2002), as well as having a central SMBH which is relatively undermassive for its host halo, by an order of magnitude (Sani et al.

2018).

The recurrence time between SFR episodes found by Beckmann et al. (2019) is of order $0.1 - 0.2$ Gyr instead of $1 - 2$ Gyr as in our case (even when we compare their simulations with our cool-core simulations). This suggests that their jets heat the ICM more locally instead of traveling to the outer reaches of the halo−this interpretation is in line with the distances reached by the jets in the two sets of simulations (tens of kpc in their case versus hundreds of kpc in ours). This means that the closest gas that has not been effectively heated lies at smaller radii in their case than in ours. Such gas has shorter cooling times, leading to a shorter recurrence interval between cooling flows. The difference in the distances reached by the jets may be due to numerical resolution. Beckmann et al. (2019) resolve the ICM with a cell mass of $m_{\rm gas} = 3.5 \times 10^9$ $\rm M_\odot$ (more than a factor of 10^3 poorer resolution than in our case). They resolve their jets to a much better degree (up to ≈ 100 pc, which is in turn much better than our resolution in the jets, of order 1 kpc), but this is progressively derefined as the gas launched by the jets ages (with an exponential decay time of 10 Myr). On the order of several tens of Myr, the jets probably quickly deposit their energy into the local ICM as they become poorly resolved, thus only being able to reach distances of tens of kpc.

5.3.3 High-mass galaxy cluster

We now turn to our most massive test case, an idealised high-mass galaxy cluster with a halo mass of $M_{200} = 10^{15}$ $\rm M_\odot$. We find multiple episodes of gas cooling and jet activity in this system, similar to the low-mass galaxy cluster. However, in this case, even with our fiducial initial central temperature, the cooling flows are strong enough to induce significant SMBH growth, and therefore also changes in SMBH spin (both its magnitude and direction).

We find that the accretion rate $\dot{m}$ occasionally exceeds 0.03, i.e. at those times our thick disc and jet model is unrealistic. Instead, the SMBH should enter the radiatively-efficient thin disc regime (Shakura & Sunyaev 1973). We find that these periods are relatively short (< 5 Myr in every case). However, in a realistic simulation where the SMBH switches between the regimes depending on the accretion

rate, it is possible that these periods of high accretion rates may be longer. This is because once the SMBH enters the radiatively-efficient regime, it is likely that the thermal feedback associated with radiation is less effective at quenching the cooling flow, which would further exacerbate an ongoing increase in accretion rate. We leave a study of the interplay between thermal and jet feedback in such a scenario for a future study.

Fig. 5.5 shows the gas temperature at various times in our highest-resolution simulation of the high-mass galaxy cluster. In the first snapshot we see jets inflating a pair of bubbles, very close to the $z-$axis. In the second snapshot, the spin vector is still aligned with the z direction, and we see a highly precessing active jet, as well as lobes/bubbles from a previous pair of episodes (which are blending into a single one in the top half). In the third snapshot, we see three pairs of bubbles, the outermost two of which are in the same direction, while the innermost pair appears perpendicular to those. None of these are in the z direction, with the spin axis of the SMBH having been changed. The last snapshot shows a strong jet being launched from the feeding off of a circumnuclear disc, which results in a long-lived jet with a well-defined direction, but also showing clear precession. These jets are 700 kpc long (each).

Fig. 5.6 shows a similar set of plots as Fig. 5.4, but for this most massive system. We also show plots of the misalignment angle between the SMBH spin vector and the $z-$axis, instead of the total injected energy. We see that the initial cooling flow takes a much longer time to develop (to the point of a non-zero cold gas mass reservoir/star formation), due to longer cooling times of the initial gas profile. In our fiducial case with an initial central temperature of $10^{7.75}$ K, this takes $3-4$ Gyr. Overall, we again find successful quenching of star formation, with multiple cycles of feedback. The peak jet powers approach 10^{47} ergs^{-1}, peak cold gas masses approach 10^{10} M$_{\odot}$, and peak SFRs reach values up to 100 M$_{\odot}$yr^{-1}. The peaks in SFRs are often large enough for the central galaxies to not be considered quenched. However, this is not a 'problem' per se, as many observations of central galaxies in clusters find similarly large cold gas mass reservoirs and SFRs (e.g. O'Dea et al. 2008), sometimes up to 10^{11} M$_{\odot}$ and 1000 M$_{\odot}$yr^{-1}, respectively (Edge 2001, McDonald

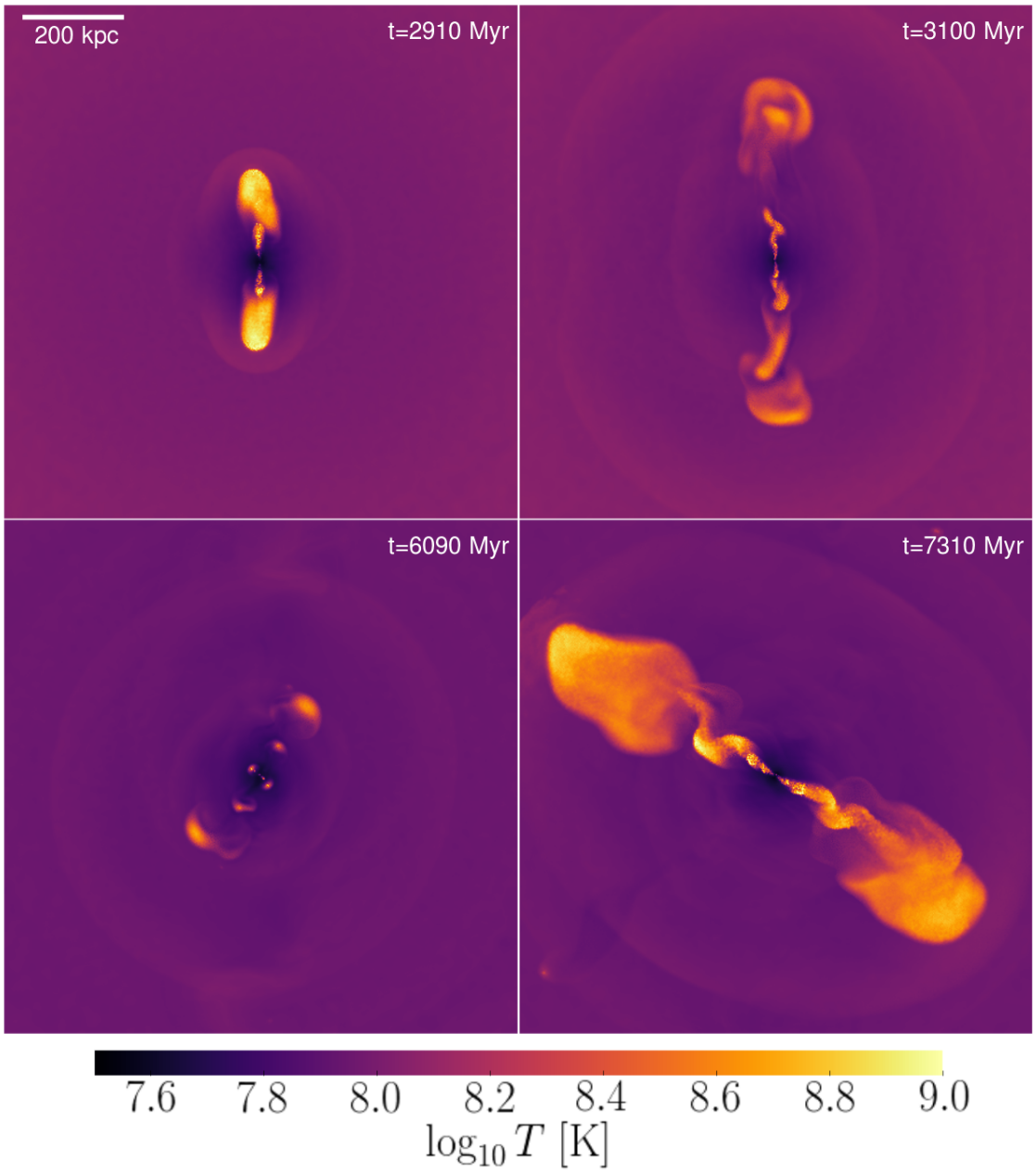

Figure 5.5: Gas temperature projections (mass-weighted mean) in our fiducial simulation (see Table 6.1 for details) of the high-mass galaxy cluster ($M_{200} = 10^{15}$ $M_\odot$) at different times. The images show a region 1.2 Mpc across and 400 kpc in depth. They show the variety of jet and bubble morphologies in this simulation, as well as jet reorientation. The video version of this plot is available to view at https://youtu.be/2herQHMnrZs.

et al. 2015, Castignani et al. 2020, O'Sullivan et al. 2021). These huge cooling flows are not found in the absence of jet feedback, but are instead correlated with it (Hlavacek-Larrondo et al. 2012a, McNamara et al. 2014, Russell et al. 2017).

In the top panels of Fig. 5.6 we show jet powers and SFRs with varying numerical resolution. All three simulations inject similar amounts of energy, but higher-resolution simulations show larger variability and clearly distinct episodes. Smaller jet/cooling episodes differ in timing and peak jet power/SFR, but all three simulations show a similar episode at $t \approx 8$ Gyr. The cold gas masses appear well converged with resolution, while the SFR grows by about an order of magnitude when resolution is increased from $m_{\rm g} = 5.12 \times 10^7$ M$_\odot$ to $m_{\rm g} = 6.4 \times 10^6$ M$_\odot$, but is converged down to $m_{\rm g} = 8 \times 10^5$ M$_\odot$. In all three cases the SMBH is spun down during the initial jet episode, and its spin varies throughout the simulation between values of 0 and 0.25. The spin vector becomes misaligned in all three cases, but there is no sign of less misalignment at higher resolutions. This indicates that the misalignment is not an effect of poor sampling of the gas distribution, but rather a physical effect. However, in our highest-resolution simulation, the cold gas reaches peak masses of 10^9 M$_\odot$, which means that it is resolved by about 1000 particles at most. This may not be enough to draw any strong conclusions about the morphology of the cold gas, and therefore about the evolution of the spin vector in terms of direction. It is possible that higher resolutions might result in fewer but longer-lived cooling episodes resulting in cold gaseous discs.

The middle panels of Fig. 5.6 show results of simulations with varying initial SMBH spin. We see that the the SMBH is spun down somewhat during the first cooling/jet cycle in all three cases, and the behaviour of spin is similar after the spindown. In the highest-spin case ($a_0 = 0.8$), the SMBH gets spun down to 0.6 during the initial cooling episode at $t = 3.5$ Gyr, and then it gets completely spun down in the second cooling episode at $t = 8 - 9$ Gyr. For the remainder of the simulation, in all three cases the spin takes on values between 0 and 0.2, with the latter maximal value near the equilibrium spin due to jet spindown. The case with largest initial SMBH spin initially shows a smaller angle between the spin vector and the $z-$axis, since it is harder to steer it off into a different direction. On the other

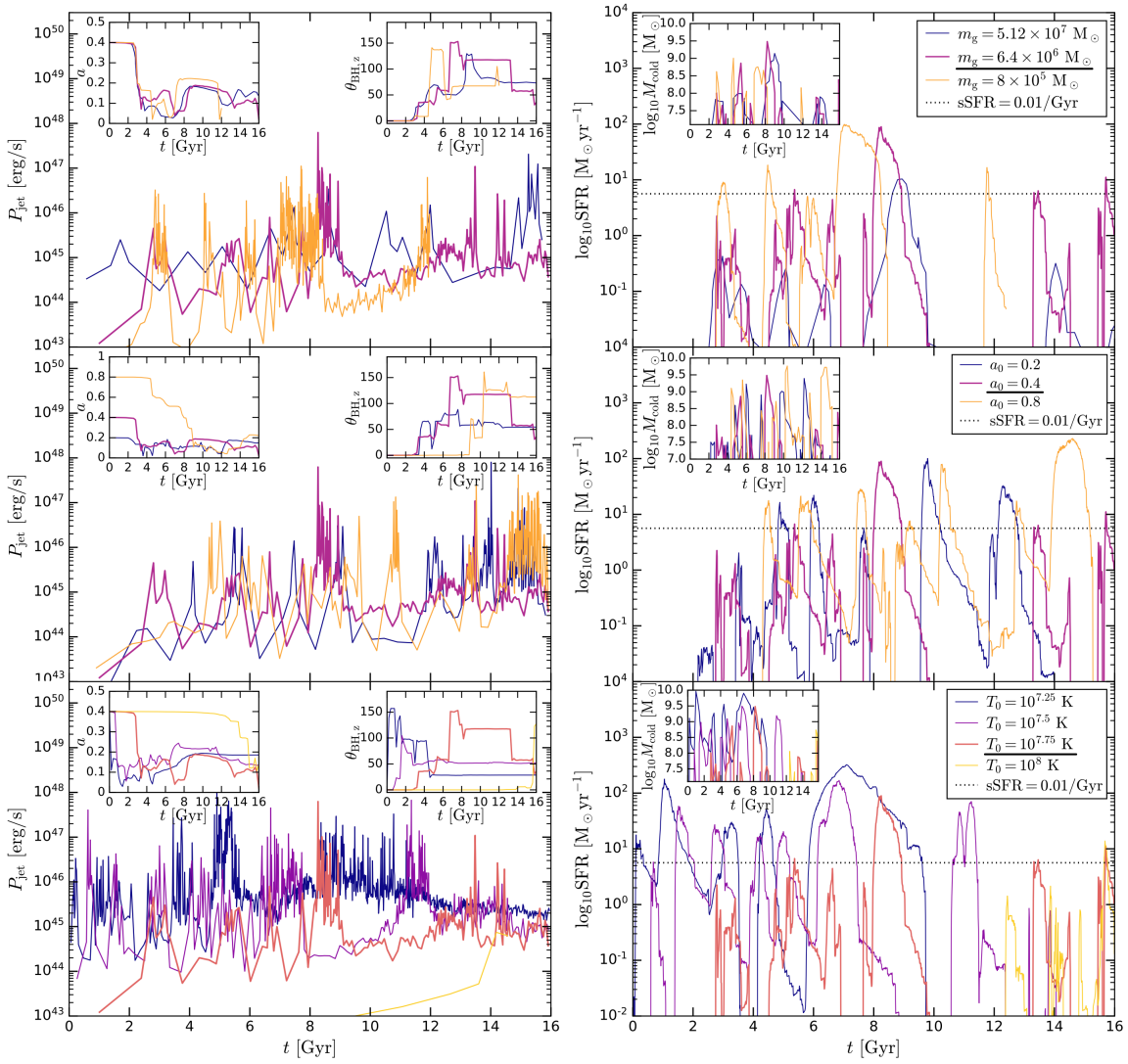

Figure 5.6: Time dependence of the quenching/feedback process in the high-mass galaxy cluster simulations ($M_{200} = 10^{15}$ M$_\odot$) with varying mass resolution (top row), initial SMBH spin (middle row) and initial central temperatures (bottom row), as per the legends in the right-hand panels. The left-hand panels show the jet power, while the right-hand panels show the star formation rate. Insets in the left-hand panels show the magnitude of SMBH spin and the angle between the spin vector and $z-$axis. The insets in the right-hand panels show the cold gas mass. The details of the fiducial case, relative to which these variations are made, are given in Table 6.1 (purple and orange lines in the top/middle and bottom panels, respectively; underlined parameter in each panel legend). The dotted black lines represent the upper limit of the specific star formation rate required to classify a galaxy as quenched. The yellow line in the top panel is discontinued at ≈ 12 Gyr since this simulation (the highest-resolution one) was not run for the full 16 Gyr.

hand, the cases with $a_0 = 0.2$ and $a_0 = 0.4$ both have spin vectors that are pointed in a different direction almost immediately during the first jet episode. Despite the differences in spin, all three cases exhibit a similar total injected jet energy as a function of time (not shown here), as well as similar star formation rates.

From the bottom panels we see the effects of varying the initial central temperature. The (relative) changes are similar to the low-mass galaxy cluster case. As expected, decreasing the temperature leads to more energy injection, cold gas and star formation, as well as more rapid spindown and reorientation. The case with the lowest initial central temperature ($T = 10^{7.25}$ K) has peak jet powers of a few times 10^{47} ergs^{-1}, corresponding to some of the strongest observed jets (Kino & Kawakatu 2005). The SFR reaches peaks of a few times 100 M$_\odot$yr^{-1}, which corresponds to SFRs of central galaxies in clusters with some of the strongest cooling flows, such as the Phoenix cluster (McDonald et al. 2015). The galaxy would be considered non-quenched most of the time. However, even in this case, after 11 Gyr the galaxy is completely quenched. In the case with the somewhat higher initial central temperature of $T_0 = 10^{7.5}$ K, the SFR is relatively high during the first 8 Gyr, but the galaxy is again quenched after that, with the exception of another episode at $t = 11$ Gyr. In the case where the central temperature is close to the virial temperature, there is almost no cold gas, star formation or jet activity.

5.4 Jet feedback in more detail

In the previous section we focused on the general morphology of self-consistent jets, as well as the details of the feedback cycle as measured through the jet power and SFR. Here we will look at some secondary features of these jets and their feedback. We focus on the most massive halo that we have simulated, the high-mass galaxy cluster ($M_{200} = 10^{15}$ M$_\odot$).

Fig. 5.7 shows visualizations of gas properties (in slices, and also including zoom-ins, see the caption) in our highest-resolution simulation ($m_{\rm g} = 8 \times 10^5$ M$_\odot$) of the massive halo, through its temperature, entropy, magnitude of the time derivative of the velocity divergence (this quantity is a shock/sound wave tracer) and the X-ray

surface brightness[3]. We have chosen these quantities since they highlight some of the main features of interest. The particular times (snapshots) shown were chosen for a similar reason.

5.4.1 Uplift of filaments

The jets in our simulations inflate bubbles that rise buoyantly due to gravity. Such bubbles can be seen clearly in the first three snapshots shown in Fig. 5.7, in maps of all of the properties to varying degree. We find that the rise of such bubbles is ubiquitously followed by the rise of colder, ambient medium in the form of filaments that connect the base of the bubbles to the centre of the halo. This gas is visible in the second and third snapshots in the temperature maps due to its low temperature ($\approx 10^7$ K), and the entropy maps show that the filaments are of a somewhat lower-entropy relative to the rest of the ambient medium. The filaments are also visible in the X-ray surface brightness, which shows actively cooling gas.

These filaments can be traced to two distinct physical processes (Pope et al. 2010), the drift (a hydrodynamical effect related to the displacement of the gas by the bubbles; Darwin 1953) and the wake (trapping of gas in eddies at the bottom of buouyantly rising bubbles; Yang 2003). The drift is visible as the main body of the filaments in Fig. 5.7, while the wake is visible as the 'petals' at the end of the filaments in the last three snapshots, most clearly in the X-ray maps.

The first snapshot in the X-rays shows the base of the cavities enveloped by cooling gas. This is qualitatively similar to filaments of cool gas enveloping the base of X-ray cavities, as observed with ALMA in the Phoenix cluster (Russell et al. 2017). The filamentary structures trailing bubbles in the second and third snapshot (and in our simulations in general, regardless of the resolution or mass of the system) are qualitatively in agreement with observations that find filaments trailing X-ray cavities or radio bubbles (e.g. Russell et al. 2016, Vantyghem et al.

[3]We calculate the X-ray surface brightness as appropriate for the ACIS detector on board the Chandra space telescope (Garmire et al. 2003) by using its effective area as a function of photon energy (corresponding to $0.2 - 7$ keV), which is convolved with a spectrum of bremsstrahlung cooling in an optically thin medium. The presence of metals is accounted for in the total cooling function, but metal lines are not included in the spectrum.

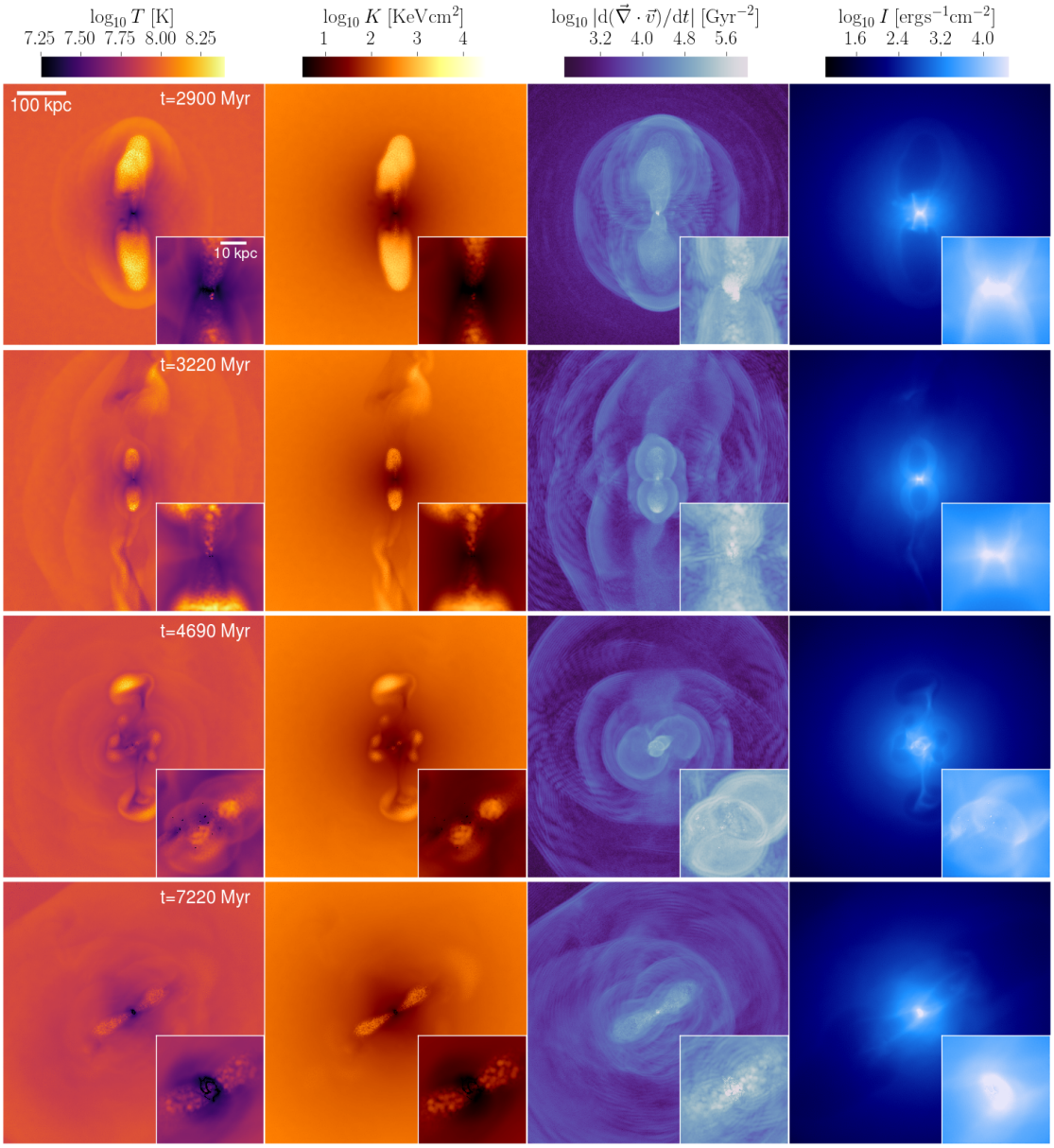

Figure 5.7: Gas properties (mass-weighted means) at different times in our fiducial simulation (see Table 6.1 for details) of the high-mass galaxy cluster ($M_{200} = 10^{15}$ $\mathrm{M}_\odot$). Each image is 800 kpc across, and shows slices 200 kpc in depth. Insets show a zoom-in of the central 50 kpc (10 kpc in depth). From left to right we show the temperature, entropy, shock/sound wave indicator and X-ray surface brightness (see text for details). From top to bottom we show different times. The video version of the X-ray plots is available to view at https://youtu.be/113F4ndbm1c.

2018). Observations with ALMA have found that filaments trailing bubbles may be ubiquitous wherever AGN bubbles are present (e.g. Olivares et al. 2019, Russell et al. 2019). Observations in other wavelengths have revealed many more examples of this correlation (e.g. Wilman et al. 2009, Salomé et al. 2011, Tremblay et al. 2015, Maccagni et al. 2021). In the Virgo cluster, a pair of filaments are visible in X-rays, and they are aligned with a pair of radio lobes (Feigelson et al. 1987, Bohringer et al. 1995, Gatuzz et al. 2021). Other observations also find X-ray filaments trailing X-ray cavities (e.g. Gendron-Marsolais et al. 2017), but these generally require long exposure times in order to resolve the filaments.

Simulations have been able to reproduce the uplift that results in these filaments (e.g. Churazov et al. 2001, Revaz et al. 2008, Li & Bryan 2014b, Brighenti et al. 2015, Qiu et al. 2019, Zhang et al. 2022), although it is not clear how common a feature they are. We have performed simulations of constant-power jets and jet-inflated bubbles in an idealised ICM (Huško et al. in prep.), where we found that the filaments are present after any bubble-inflation event. We also found that they are energetically significant, and that the process of uplift of ambient gas significantly reduces the central density of the ICM. This provides an alternative mechanism of feedback (alongside gas heating through shocks). It has even been suggested that jet feedback may represent a self-driven cycle: one jet episode results in the uplift of dense filaments that eventually cool and fall onto the central galaxy, triggering another jet episode (McNamara et al. 2016). We do find that these filaments eventually fall back onto the centre, but we leave a study of their role in the feedback cycle for a future study.

5.4.2 Structure of the cold gas

Our simulations of the most massive halo ($M_{200} = 10^{15}$ M$_\odot$) feature significant changes in the direction of the SMBH spin vector, as can be inferred from jets being launched in various directions. The evolution of the spin is primarily tied to the properties of the cold gas ($T < 2 \times 10^4$ K) surrounding the SMBH. We find that the cold gas is morphologically varied. At times, it takes the form of a relatively long-lived, rotationally-supported disc (e.g. the first and last snapshots,

visible mostly in the zoomed-in temperature and X-ray maps in Fig. 5.7). At other times, it is relatively clumpy, and can even be located far from the SMBH (third snapshot). These variations could be attributed to: i) the depletion of gas due to direct launching into the jet by the jet-launching algorithm, ii) the entrainment of gas into the jet, iii) the cooling of gas at large distances due to shock compression of gas induced by the jets, iv) the cooling of filaments drawn out by jet-inflated bubbles and v) poor sampling due to finite numerical resolution.

Observationally, it is not clear how ubiquitous cold gaseous discs are in massive galaxy clusters. For some galaxy clusters there is clear evidence of molecular gas discs (Hamer et al. 2014), while for others there is evidence of most of the molecular gas residing in precipitating filaments (Crawford et al. 2005). An analysis of a sample of clusters by Russell et al. (2019) suggests that there is a spectrum, with most clusters having both filaments and circumnuclear discs, with neither dominating. Newer observations with ALMA (Nagai et al. 2019) find that many of these discs may be unresolved in lower-resolution observations.

5.4.3 Driving of shocks and sound waves

As an anisotropic energy injection mechanism, jets are expected to deposit a significant fraction of their energy near the axis along which they are launched. In our most massive galaxy cluster simulation, this is not necessarily a problem since jets can reorient fairly quickly. In our lower-mass systems, such reorientation does not occur.

From the maps of the shock/sound wave tracer in Fig. 5.7 we see that jet launching is accompanied by ellipsoidal or spherical shocks and sound waves that propagate throughout the halo. The shocks from multiple jet episodes interact with each other in a complex way, producing ripples with a radial direction. This likely results from interference of waves from different jet episodes (or from the two sides of a single jet episode). Plumes tracing the jet material are visible due to strong shocking of the jet gas. Sound waves in our simulations do not heat the ICM, since it is relatively homogeneous (i.e. it does not feature realistic substructures, such as gas clumps, sloshing fronts, relics of accreted clusters, etc.), but they might do so in realistic

zoom-in cosmological simulations (Bambic & Reynolds 2019).

These plots show that jets that are directed along one axis can drive significant shocks in other directions. This is not surprising; many simulations have found that a significant fraction (usually of order 50%) of jet energy is imparted to the medium fairly isotropically while the jet is active, by driving a bow shock that deposits energy through thermalization at all angles (e.g. Weinberger et al. 2017b, Bourne & Sijacki 2017, Huško & Lacey 2022). After the jet is turned off, even more (if not all) of the previously injected energy is imparted to the ambient medium. This is consistent with our galaxy group and low-mass cluster simulations, where jets are launched almost perfectly along the $z-$axis, yet they successfully quench gas cooling and star formation in the haloes.

5.4.4 Impact of jet feedback on profiles of gas-related quantities

Observations indicate that, in terms of X-ray properties, galaxy clusters come in roughly two types: cool-core (CC) and non-cool core (NCC; McNamara et al. 2000, Lewis et al. 2002). In their outer regions these clusters are very similar (Voit et al. 2005), but in their centres, CC clusters exhibit a dip in temperature that can be a few times lower than the peak (Peterson et al. 2003). This distinction is also visible in entropy (Hudson et al. 2010), density (Peterson & Fabian 2006) and pressure (Arnaud et al. 2010) profiles. CC clusters have significantly shorter central cooling times, typically less than the Hubble time (Voit & Donahue 2015). Previous simulations have shown that the distinction between CC and NCC clusters can be explained as a result of AGN feedback (e.g. Dubois et al. 2011, Pike et al. 2014, Prasad et al. 2015, Barnes et al. 2017).

Fig. 5.8 shows the number density, temperature and entropy profiles of gas in our fiducial, medium-resolution simulation of the high-mass galaxy cluster ($M_{200} = 10^{15}$ $M_\odot$). Outside 200 kpc, the median profiles over 16 Gyr of evolution are similar to the initial ones, indicating that feedback mostly has an effect on the region within that radius. There are some variations at different times at all radii, but these are related to the relaxation of the halo, which is most easily visible in the temperature

profiles (shown here using a non-logarithmic axis), and also in an overall drop in the normalization of the density and entropy profiles.

Within 200 kpc there are significant variations in the profiles between snapshots, due to active cooling and feedback in this region. The median temperatures within $r < 10$ kpc reach values as low as a few times 10^6 K ($T \approx 0.1$ keV) and as high as 10^8 K ($T \approx 10$ keV), depending on whether the ICM is actively cooling or being heated by feedback. Entropies at the same time reach values as low as $K < 1$ keVcm^2 and as high as $K = 10^3$ keVcm^2. We also show median lines using all snapshots, as well as medians for when the cluster is considered CC or NCC for the entropy profiles, according to the definition of Cavagnolo et al. (2009) (a cluster is considered CC if its central entropy, K_0, measured within $r < 10$ kpc, satisfies $K_0 < 30$ keVcm^2, otherwise it is NCC). We find that our simulated cluster is considered CC for almost its entire evolution, with the CC median lines and the overall medians being very similar. Most of the time the cluster is more CC than when initialized, with densities being higher and temperatures and entropies lower. Our CC median entropy profile agrees fairly well with the sample from Cavagnolo et al. (2009), underestimating it by $\approx 50\%$ in the centre. However, our NCC median entropy profile, comprised of only ≈ 10 snapshots, falls short of the observed NCC median from Cavagnolo et al. (2009) by a factor of ≈ 4. These differences may be in part due to the haloes in the sample of Cavagnolo et al. (2009) differing in mass from $M_{200} = 10^{15}$ M$_\odot$. It is also likely that more realistic, cosmological simulations, with sloshing due to mergers, would feature higher-entropy cores, both for CC and NCC clusters (Ascasibar & Markevitch 2006, ZuHone et al. 2010).

5.4.5 Impact of parameter variations on the cooling and feedback cycle of galaxies

In § 5.3 we focused on general features of jets and the quenching process in all three systems that we simulated. We varied the initial SMBH spin, mass resolution and the central temperature in each case. In this section we present similar results, but for variations of other parameters or choices that we considered most significant; we discuss other variations in Appendix 5.B (where we find that they generally

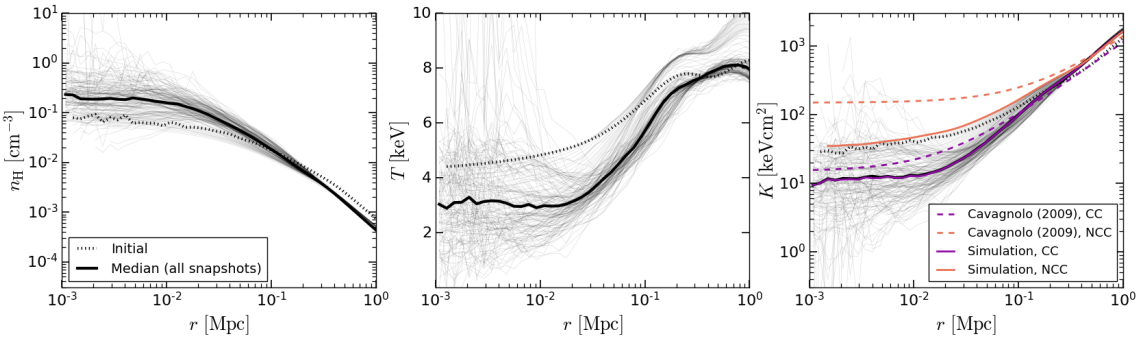

Figure 5.8: Profiles of gas density, tempreature and entropy from our fiducal high-mass galaxy cluster simulation at medium resolution ($M_{200} = 10^{15}$ M$_\odot$, $m_g = 6.4 \times 10^6$ M$_\odot$, see Table 6.1 for details). The initial profiles are shown by dotted lines, while thick solid lines are the median profiles using individual snapshots, which are shown with thin solid lines. The purple and orange lines show median profiles for our simulated cluster when it is cool-core (CC) and non-cool-core (NCC), respectively. The cluster is classified as the former if its central entropy (within $r < 10$ kpc) satisfies $K_0 < 30$ keVcm^2, and the latter if $K_0 > 30$ keVcm^2. This definition follows the observational sample of Cavagnolo et al. (2009); their median CC and NCC entropy profiles are shown with dashed purple and orange lines, respectively
.

have little impact). These variations were all done for the high-mass galaxy cluster ($M_{200} = 10^{15}$ M$_\odot$). In Fig. 5.9 we show the results of these variations for three different parameters/choices: the jet launching velocity, the scheme with which particles are kicked from the SMBH smoothing kernel, and finally a set of simulations where the jet direction is fixed along the $z-$axis, and the jet efficiency is also fixed in time.

The top row of Fig. 5.9 shows results of varying the velocity with which particles are kicked from the SMBH smoothing kernel. In terms of jet power, higher launching velocities result in more episodic feedback, which is especially pronounced with the highest launching velocity we tested, $v_j = 6 \times 10^4\,\mathrm{kms}^{-1} = 0.2c$. This simulation has four cooling episodes (which may feature one or more distinct jet episode each) that last for $0.5 - 1.5$ Gyr. Between these cooling episodes, the jet power is very low. The high-velocity case is likely more episodic due to its more explosive nature (due to a larger launching velocity, stronger shocks occur as the jet is being decelerated, and at smaller distances). This difference results in lower jet powers in the minima between jet episodes; this is likely due to the presence of hotter gas in the centre of the halo.

With lower launching velocities, the halo is heated more gently and at larger

distances, since shocks occur at larger distances. This is a result of the jets being more mass and momentum loaded, since the total mass launched into a jet with a total energy $E_{\rm j}$ (which we consider constant for the purpose of this argument) is $M_{\rm j} = 2E_{\rm j}/v_{\rm j}^2$, and the total momentum $p_{\rm j} = 2E_{\rm j}/v_{\rm j}$. The jets are thus able to drill through the ICM more easily, if they are launched with lower velocities, until they have swept up approximately as much mass as the mass in the jets, which is roughly when they transition from the ballistic phase to the self-similar one (see e.g. Kaiser & Best 2007 for a theoretical model, or Huško & Lacey 2022 for a confirmation of such behaviour in hydrodynamical tests). This transition roughly coincides with the scale where jets begin to experience strong shocking. Furthermore, since densities are smaller at larger radii, the shocks are also likely to be weaker.

The evolution of the SMBH spin magnitude and direction is similar in all three simulations, with perhaps the only exception being the somewhat more frequent changes in the spin for the lowest-velocity jet simulation, due to the jet being active throughout almost the entire simulation. Surprisingly, the peak star formation rates and cold gas masses are higher with larger launching velocities, which feature more explosive feedback. They also show more protracted decreases after their peaks during each episode. These differences are most likely due to explosive feedback being able to expel cold gas from the centre of the halo; the cold gas is then long-lived and star-forming until all of it is consumed (this behaviour was also found by Nobels et al. 2022 with thermal AGN feedback). The lower-velocity cases feature stronger cold gas evacuation from the centre of the halo through the jet launching mechanism, leading to lower SFRs. By this we are not referring to entrainment, but rather that the jet launching algorithm chooses the cold gas to be launched into the jet. The reason this effect depends on the jet launching velocity is that the mass loading of the jet increases as the velocity decreases: $\dot{M}_{\rm j} = 2P_{\rm j}/v_{\rm j}^2$.

When launching particles from the SMBH smoothing kernel, as part of our jet feedback implementation, a choice needs to be made as to which particles are launched (see Chaikin et al. 2022, in the context of stellar feedback). Our fiducial choice is to kick particles that are farthest from the SMBH on either hemisphere (relative to the spin vector). We compare this against kicking the closest two parti-

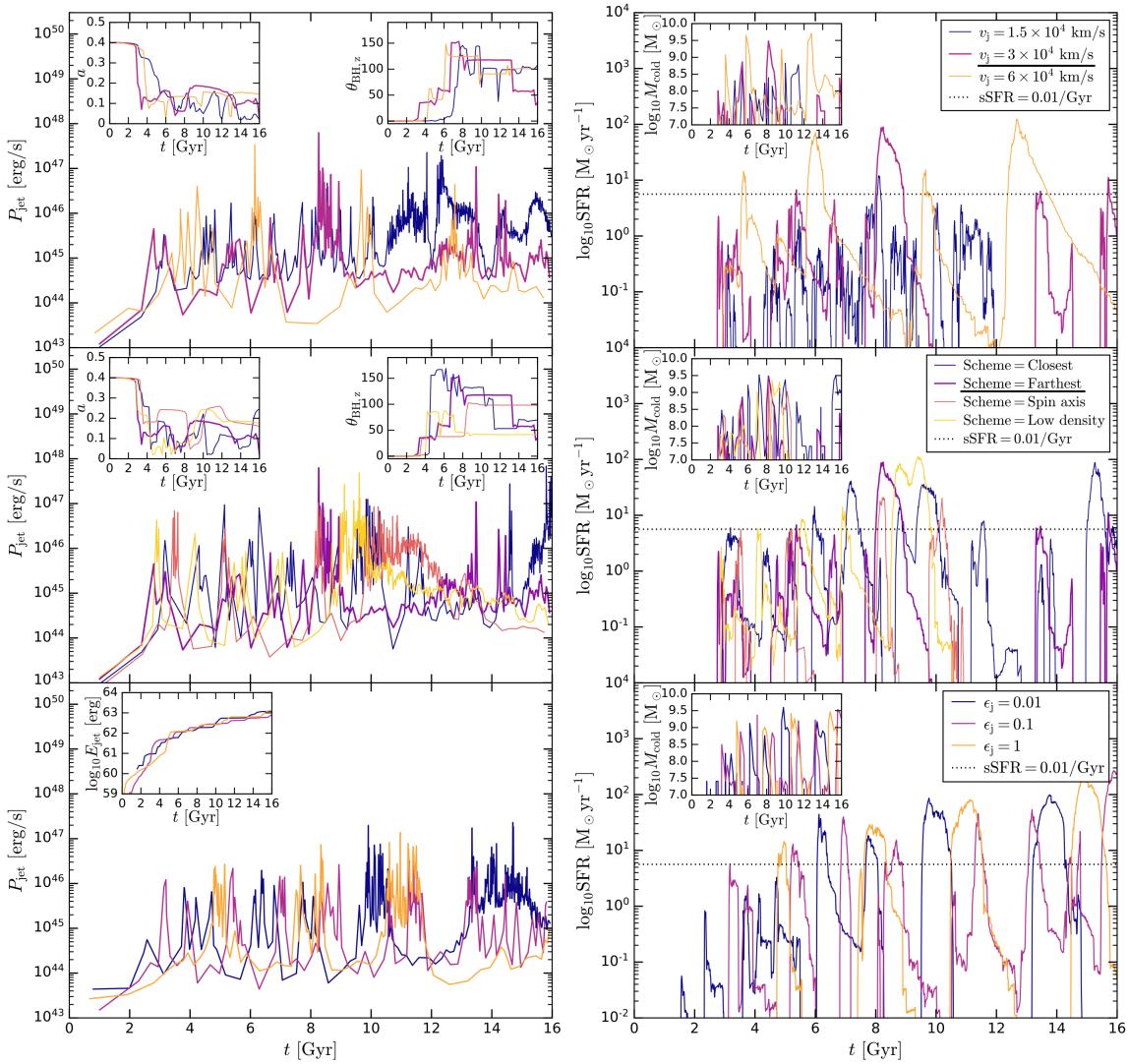

Figure 5.9: Time dependence of the quenching/feedback process in the high-mass galaxy cluster simulations ($M_{200} = 10^{15}$ M$_\odot$) with varying parameters/choices, as per the legends in the right-hand panels. In the top row we vary the jet launching velocity, and in the middle row the choice of which particles are kicked from the SMBH smoothing kernel. The bottom row shows a case with the jets fixed along the $z-$axis, with the jet power calculated using a fixed efficiency (see legend). The left-hand panels show the jet power, while the right-hand panels show the star formation rate. Insets in the left-hand panels show the magnitude of SMBH spin and the angle between the spin vector and $z-$axis in the top and middle panel, and the total injected jet energy in the bottom panel. The insets in the right-hand panels show the cold gas mass. The details of the fiducial case, relative to which these variations are made, are given in Table 6.1 (purple line in each panel and underlined parameter in each panel legend, with the exception of the bottom row). The dotted black lines represent the upper limit of the specific star formation rate required to classify a galaxy as quenched.

cles, as well as kicking the two particles closest to the spin axis (in terms of angular distance). We also compare against a case where the two particles with the lowest density are kicked, in an attempt to avoid launching cold gas into the jet. In Fig. 5.9 we show the effects of varying this choice. As we see, the consequences are minor but not negligible.

The scheme with the two closest particles being kicked is overall most similar to our fiducial choice, where the two farthest particles are kicked. However, the jet powers, SFRs and cold gas masses are more variable and less episodic in that scheme, since the cold gas structure near the SMBH is more prone to being disrupted. The scheme where low-density gas is targeted is overall similar to the previous two, but results in quicker 'final' quenching by $t = 10$ Gyr, due to a long-lived and strong cooling/jet episode, which is not easily disrupted since the launching scheme completely avoids the cold gas. The scheme where the gas closest to the spin axis is targeted appears to be most efficient at feedback. This scheme is most episodic and injects the energy required to quench cooling earlier than the other schemes. It completely quenches the halo by $t = 10$ Gyr as well (at least out to the end of the simulation).

In the bottom row of Fig. 5.9 we show results from simulations with jets that are fixed along the $z-$axis, and that inject energy with a constant efficiency (that we vary). We find that there is surprisingly little difference among simulations with efficiencies varying by factors of 10. Lower efficiency cases have more variable cooling/jet episodes and shorter delays between the episodes. Overall, however, we find that the amounts of energy injected by the jets is similar in all three simulations. The same is true for the amount of star formation. This similarity is likely due to the self-regulated nature of the system (see e.g. Booth & Schaye 2010); the SMBHs may inject less energy in the beginning of a cooling flow if they have lower efficiencies, but this will quickly be compensated by more cooling (and higher SMBH accretion rates) until the jet heating rate becomes sufficient to offset the cooling.

5.5 Summary and conclusions

In this chapter we presented a subgrid model for the spin evolution of SMBHs surrounded by unresolved thick accretion discs in hydrodynamical simulations of galaxy formation. This model is applicable for SMBHs accreting at low rates, as found in many galaxies in the local Universe, especially massive ones. Due to our modeling of spin evolution, the model naturally results in jet reorientation, as well as changes in jet efficiency.

We have applied our model to an idealised set-up that includes: 1) an external potential representing a dark matter halo 2) a central massive galaxy, 3) a realistic hot circumgalactic/intracluster medium in hydrostatic equilibrium and 4) a central black hole. We assume an accretion efficiency of 100%, so that the black hole accretion rate is equal to the Bondi accretion rate (no disc winds or other mass loss). The jet efficiencies that arise in our simulations are of order $1 - 10\%$, larger than most other similar simulations.

We have studied cases with three different dark matter halo masses: 10^{13} $M_\odot$, 10^{14} $M_\odot$ and 10^{15} $M_\odot$. These set-ups represent typical systems where jet feedback is expected to be important, including galaxy groups and clusters. We have simulated these systems at different resolutions and with varying parameters. From these simulations we conclude the following:

- Our jet feedback model is successful in quenching star formation in central galaxies across the mass scale, and with differing parameters related to jet feedback and initial conditions. Quenching is always achieved, but details of the feedback can depend on choices such as jet launching velocity and which particles are kicked from the SMBH smoothing kernel.

- The details of jet feedback are most sensitive to the mass of the system (as measured through the halo mass). In the $M_{200} = 10^{13}$ $M_\odot$ case (a typical elliptical galaxy in a galaxy group), an initial strong cooling flow and jet episode leads to quenching within $0.5 - 2$ Gyr. This galaxy remains quenched for a further 6 Gyr. A weak, constant-power jet is fed directly from the halo of hot gas. In the largest system that we simulate, the high-mass galaxy cluster

($M_{200} = 10^{15}$ $M_\odot$), the central galaxy experiences multiple cycles of cooling and jet activity. Jets fed by accretion from cold gas dominate in this system. In the intermediate-mass case ($M_{200} = 10^{14}$ $M_\odot$), representing a low-mass galaxy cluster, cold gas accretion typically dominates, with hot halo accretion being sufficient to keep the halo quenched only if jet efficiencies are very high, of order 100%.

- At fixed halo mass, we find that the results are most sensitive to the initial central temperature of the gaseous halo. We find the strongest jet activity (with jet powers a few times 10^{47} $\mathrm{erg s^{-1}}$) in our high-mass galaxy cluster ($M_{200} = 10^{15}$ $M_\odot$), if it is initialized as a strong cool-core cluster. Cold gas masses in this case reach peak values of 10^{10} $M_\odot$ and star formation rates reach peak values of a few times 100 $M_\odot \mathrm{yr^{-1}}$, in agreement with observations. Periods of such high cold gas masses, star formation rates and jet powers can last anywhere from 0.1 Gyr to 1 Gyr, depending on the jet efficiencies (i.e. spin) and the details of the system in question.

- In the galaxy group ($M_{200} = 10^{13}$ $M_\odot$) and low-mass cluster ($M_{200} = 10^{14}$ $M_\odot$), the cooling flows that develop do not lead to cold gas mass reservoirs large enough, or long-lived enough, to lead to significant SMBH accretion or spin evolution. Significant evolution of SMBH spin (both in terms of magnitude and direction) occurs in the $M_{200} = 10^{15}$ $M_\odot$ system. The accretion is chaotic and not well-aligned with the $z-$axis, with the gas sometimes forming a circumnuclear disc, and at other times clumps that may appear at large distances from the centre of the halo (> 10 kpc).

- Compared to simulations using thermal AGN feedback in the same set-up, performed by Nobels et al. (2022), we find that jets are more efficient at quenching the galaxies. They lead to overall less star formation and cold gas, as well as more rapid shutoff in star formation during a given cooling flow. Compared to thermal feedback, the jets are able to quench haloes with lower initial central gas temperatures. The cooling and feedback cycle is periodic in the case with thermal feedback, unlike the jet feedback case, where the time

elapsed between cooling episodes is less predictable. This is likely due to jet efficiencies that vary during a given simulation.

- The inflation of jet lobes/bubbles is always followed by the uplift of low-entropy gas from the centre of the gaseous halo. This gas forms dense, cooling filaments, in agreement with observations that suggest that these filaments are ubiquitous in galaxy clusters with evidence of jet activity.

Our simulations of the group and low-mass cluster regimes ($M_{200} = 10^{13}$ $M_{\odot}$ and $M_{200} = 10^{14}$ $M_{\odot}$) featured almost no spin evolution, which means that the jet efficiency and direction were effectively fixed. In addition, we performed some simulations of the high-mass galaxy cluster ($M_{200} = 10^{15}$ $M_{\odot}$) with the jet efficiency fixed at a few different values and the jet direction fixed along the $z-$axis. In all these simulations, successful quenching was achieved. These results indicate that variations of the jet efficiency and direction due to BH spin evolution may not be important if the main goal is to quench galaxies. However, some secondary effects are probably lost (e.g. non-periodicity of cooling flows).

Appendix 5.A: Black hole spin alignment timescale

Our procedure for modeling SMBH spin builds on the approach of several previous studies (Volonteri et al. 2007, King et al. 2008, Fanidakis et al. 2011, Griffin et al. 2019), with the main difference being that those studies focused on thin, radiatively efficient discs. This method is similar in many aspects to that implemented by Fiacconi et al. (2018) and Talbot et al. (2020), which also modeled the thin disc. However, we do not explicitly model the differential equation for the evolution of the SMBH spin direction due to LT torques between the accretion disk and the SMBH (e.g. Martin et al. 2007).

Furthermore, Fiacconi et al. (2018) measure the inflow of mass and angular momentum onto their sink particle, representing the SMBH and accretion disc system (without assuming e.g. Bondi accretion). This allows them to model the size, as well as total mass and angular momentum of their subgrid accretion disc (assuming some surface density profile, as well as Keplerian rotation). In turn this leads to the mass and angular momentum accretion rates onto the SMBH, using a system of equations that couple the SMBH with the large-scale accretion disc. These accretion rates onto the SMBH are in general different from the inflow rates onto the sink particle.

We instead assume Bondi accretion, and that the accretion rate onto the SMBH is equal to the Bondi rate at all times. For the angular momentum evolution, we use only the *direction* of angular momentum measured in the smoothing kernel of the SMBH. While it is beyond the scope of this study to compare our approach with the full approach of Fiacconi et al. (2018), we will compare the alignment timescale in our approach to that where LT torques are explicitly included in the angular momentum evolution equation. We do this for the radiatively-efficient thin disc assuming that gas pressure dominates over radiation pressure, and that free-free absorption dominates in the opacity (region C from Shakura & Sunyaev 1973). We make this choice since Fiacconi et al. (2018) studied this accretion regime, and since they use the derivation of Martin et al. (2007) to model the terms from the LT torque that contribute to the angular momentum evolution equation, which is applicable only for Keplerian rotation and thin discs. Note that while we assume the

thick accretion disc in this chapter, a comparison between the differential equation approach and the incremental accretion approach in any accretion regime should serve as a general validation of the incremental accretion approach (with the caveat that the differential equation itself should change depending on accretion regime).

In the Fiacconi et al. (2018) approach, the evolution of angular momentum is given by the equation

$$\begin{aligned}\frac{\mathrm{d}\mathbf{J}_{\mathrm{BH}}}{\mathrm{d}t} =& L_{\mathrm{ISCO}}\dot{M}_{\mathrm{BH,acc,0}}\hat{\mathbf{J}}_{\mathrm{BH}} - \\ & \frac{J_{\mathrm{BH}}}{\tau_{\mathrm{GM}}}\big[\tilde{K}_1\hat{\mathbf{J}}_{\mathrm{BH}}\times\hat{\mathbf{J}}_{\mathrm{d}} + \tilde{K}_2\hat{\mathbf{J}}_{\mathrm{BH}}\times(\hat{\mathbf{J}}_{\mathrm{BH}}\times\hat{\mathbf{J}}_{\mathrm{d}})\big],\end{aligned} \tag{5.4}$$

where $\mathbf{J}_{\mathrm{BH}}$ is the angular momentum vector of the BH, $\hat{\mathbf{J}}_{\mathrm{BH}}$ is its direction, $\hat{\mathbf{J}}_{\mathrm{d}}$ is the direction of the large-scale accretion disc surrounding the black hole (outside the warp radius), $\tilde{K}_1 = \sin(\pi/7)$, $\tilde{K}_2 = \cos(\pi/7)$ and τ_{GM} is a gravito-magnetic timescale which is given by

$$\tau_{\mathrm{GM}} = 0.17\mathrm{Myr}\left(\frac{M_{\mathrm{BH}}}{10^6\,\mathrm{M}_\odot}\right)^{-2/35}\dot{m}^{-32/35}|a|^{5/7}. \tag{5.5}$$

for the thin accretion disc. The first term in equation (5.4) corresponds to accretion onto the SMBH, and is identical to what we assume. Other terms represent the effects of LT torques in a warped accretion disc. Their form, including the forms of $\tilde{K}_1$, $\tilde{K}_2$ and τ_{GM}, follow from the derivation in Martin et al. (2007) under the assumption that the surface density scales as $\Sigma(R) \sim R^{-3/4}$, as appropriate for region C of the Shakura & Sunyaev (1973) thin disc, and that the tilt angle between the SMBH spin vector and the outer accretion disc is small.

The first term in the parentheses in equation (5.4) causes precession, whereas the second term leads to alignment. If we define the alignment timescale such that the alignment term in equation (5.4) takes the form $(\mathrm{d}\mathbf{J}_{\mathrm{BH}}/\mathrm{d}t)_{\mathrm{align}} = -(J_{\mathrm{BH}}/\tau_{\mathrm{align}})\hat{\mathbf{J}}_{\mathrm{BH}}\times(\hat{\mathbf{J}}_{\mathrm{BH}}\times\hat{\mathbf{J}}_{\mathrm{d}})$, the alignment timescale in this differential equation approach can be written as

$$\begin{aligned}\tau_{\mathrm{align,diff.eqn.}} &= \frac{\tau_{\mathrm{GM}}}{\cos(\pi/7)} = \\ &= 0.19\mathrm{Myr}\left(\frac{M_{\mathrm{BH}}}{10^6\,\mathrm{M}_\odot}\right)^{-2/35}\dot{m}^{-32/35}|a|^{5/7}.\end{aligned} \tag{5.6}$$

In the approach we use in this chapter (we refer to this as the warp increment approach), we use only the first term of equation (5.4) to evolve the magnitude of angular momentum (i.e. spin). To evolve its direction, at the end of every time-step we assume that the new direction of angular momentum matches that of $\mathbf{J}_{\rm BH} + \Delta\mathbf{J}_{\rm warp,tot}$, where $\Delta\mathbf{J}_{\rm warp,tot} = \Delta J_{\rm warp,tot}\hat{\mathbf{J}}_{\rm d}$ is the total angular momentum of all of the warp increments consumed over the time-step. This material is originally aligned with the outer accretion disc (in the direction of $\hat{\mathbf{J}}_{\rm d}$), but we assume that it becomes (counter-)aligned with the SMBH angular momentum vector through LT torques. In the process, the SMBH is also torqued in the opposite direction. The magnitude of the angular momentum exchanged with the BH is given by $\Delta J_{\rm warp,tot} = N_{\rm warp} J_{\rm warp}$, where $N_{\rm warp} = \Delta M_0/M_{\rm warp}$ is the number of warp increments consumed over the time-step, given the mass to be consumed, ΔM_0, and $J_{\rm warp}$ is the angular momentum of one warp increment. Equally, one can view this as the SMBH being torqued by gas with a specific angular momentum of $L_{\rm warp} = J_{\rm warp}/M_{\rm warp}$ as it accretes. For the general case of $\Sigma(R) \sim R^p$, we have $L_{\rm warp} = (2+p)/(5/2+p) \times \sqrt{M_{\rm BH} G R_{\rm warp}}$, where $R_{\rm warp}$ is the warp radius (see appendix in Fiacconi et al. 2018 for expression for region C of the thin disc). For the case of interest here, $\Sigma \sim R^{-3/4}$, and thus the numerical factor evaluates to 5/7. Using the above relations, we can define a similar alignment timescale to the one in the differential equation approach, namely

$$\begin{aligned} \tau_{\rm align,warp} &= \left(\frac{J_{\rm BH}\Delta t}{\Delta J_{\rm warp,tot}}\right) = \\ &= 0.21\,{\rm Myr}\left(\frac{M_{\rm BH}}{10^6\,{\rm M}_\odot}\right)^{-2/35} \dot{m}^{-32/35}|a|^{5/7}. \end{aligned} \tag{5.7}$$

This alignment timescale agrees with the differential equation apart from a ≈ 10 per cent difference in the numerical pre-factor. However, note that they are only directly comparable in the case that the SMBH angular momentum vector, and the angular momentum vector of the outer accretion disc, are perpendicular. Furthermore, we generally do not expect the two timescales to identical, since these two approaches appear inherently different.

In order to compare the two approaches in more detail, we use a very simple test set-up. We assume a SMBH mass of $M_{\rm BH} = 10^7$ M$_\odot$, spin of $a = 0.5$ directed along

the $z-$axis, and constant accretion rate of $\dot{m} = 0.1$. We assume that the angular momentum of the accretion disc on large scales, $\hat{\mathbf{J}}_{\rm d}$, is directed along the $x-$axis. Our aim is to compare how long it takes for the spin vector to be redirected in the direction of $\hat{\mathbf{J}}_{\rm d}$ in the two approaches. With our assumed parameters, we find that both the mass and spin magnitude remain very close to their initial values over the timescale of realignment, which is in this case of order a few Myr. We evolve the system using 100 time steps between $t = 0$ Myr and $t = 10$ Myr in both approaches.

In Fig. 5.10 we show the $x-$component of the angular momentum direction of the SMBH, i.e. the component in the direction of the outer accretion disc. The alignment is complete within $2 - 3$ Myr in both approaches, but it appears to be somewhat slower in our approach, using warp increments. We have attempted our approach with the warp angular momentum boosted slightly so that the alignment time-scale is exactly equal to the one in the differential equation approach (i.e. so that the numerical factor in equation 5.7 evaluates to 0.19 instead of 0.21, to match equation 5.6). This change leads to the two approaches of modeling SMBH spin alignment agreeing perfectly, showing that they are compatible.

Since we assume a thick disc in the model presented in this chapter, rather than the thin disc, it is worth addressing the alignment timescale for that accretion regime. The surface density in the self-similar thick solution of Narayan & Yi (1995) scales as $\Sigma(R) \sim R^{-1/2}$, so $L_{\rm warp} = (3/4)\Omega_0\sqrt{M_{\rm BH}GR_{\rm warp}}$, where we have also assumed that the orbital velocities are a fraction Ω_0 of their Keplerian values (see discussion in §**??**). Defining the alignment timescale in the same way as in equation (5.7) leads to

$$\tau_{\rm align,warp,thick} = \frac{4M_{\rm BH}}{3\dot{M}_{\rm BH,acc,0}}|a|\Omega_0\left(\frac{384|a|}{25(H/R)^2}\right)^{-1/5}, \tag{5.8}$$

where we have used equation (2.26) for the warp radius of the thick disc. Using our fiducial values for the parameters leads to $\tau_{\rm align,warp,thick} = 0.63|a|^{4/5}(M_{\rm BH}/\dot{M}_{\rm BH,acc,0})$. This shows that, for a high value of spin, the alignment timescale of a thick disc is of order the growth timescale of the SMBH. This is generally much slower than in the thin disc case, owing to the vast difference in the warp radii (several vs. thousands of $R_{\rm G}$, respectively), and therefore even larger differences in warp angular momenta. For a value of $a = 0.25$ (the equilibrium spin value, relevant in our high-mass galaxy

cluster simulations), the alignment timescale is shorter than the growth timescale; $\tau_{\rm align,warp,thick} \approx 0.2(M_{\rm BH}/\dot{M}_{\rm BH,acc,0})$, indicating that the SMBH can be redirected without having to significantly grow its mass.

Appendix 5.B: Additional parameter variations

Here we provide results on and discuss variations of different parameters related to jet feedback and our setup. These simulations were all of our high-mass galaxy cluster ($M_{200} = 10^{15}$ M$_\odot$), simulated at medium resolution ($m_{\rm g} = 6.4 \times 10^6$ M$_\odot$).

5.B.1 Direction of jet launching: opening angle and inclination

In the top row of Fig. 5.11 we show the effects of varying the half-opening angle of the jets (the fiducial value being $\theta_{\rm j} = 10°$). We find that all relevant quantities are very similar, even with a ballistic jet ($\theta_{\rm j} = 0°$). This is somewhat surprising, given the fact that jets with smaller opening angles are able to reach larger distances (e.g. Kaiser & Best 2007, Huško & Lacey 2022). The only visible difference we find is that the ballistic jet appears to feature less reorientation relative to the initial direction (visible in the plot of the misalignment angle). In addition, the spin of the SMBH takes on larger values, on average. In the bottom row of Fig. 5.11 we show results of varying the angle between the angular momentum vector of the halo and the initial SMBH spin vector of the SMBH (the fiducial angle being $\theta_0 = 0°$). The results are again very similar in terms of jet power, SFR and cold gas. There are no discernible differences among these quantities with different misalignment angles. This is likely indicative of the chaotic nature of these simulations.

5.B.2 Impact of ICM properties

In the top row of Fig. 5.12 we show results of varying the spin parameter of the gaseous halo of our galaxy cluster. Our fiducial value is $\lambda_{\rm g} = 0.05$, and here we show cases with values that are equal to half and double our fiducial, as well as no net rotation of the halo. The differences between these cases are minor, especially in terms of jet power, cold gas or SFR. The case with largest rotation ($\lambda_{\rm g} = 0.1$)

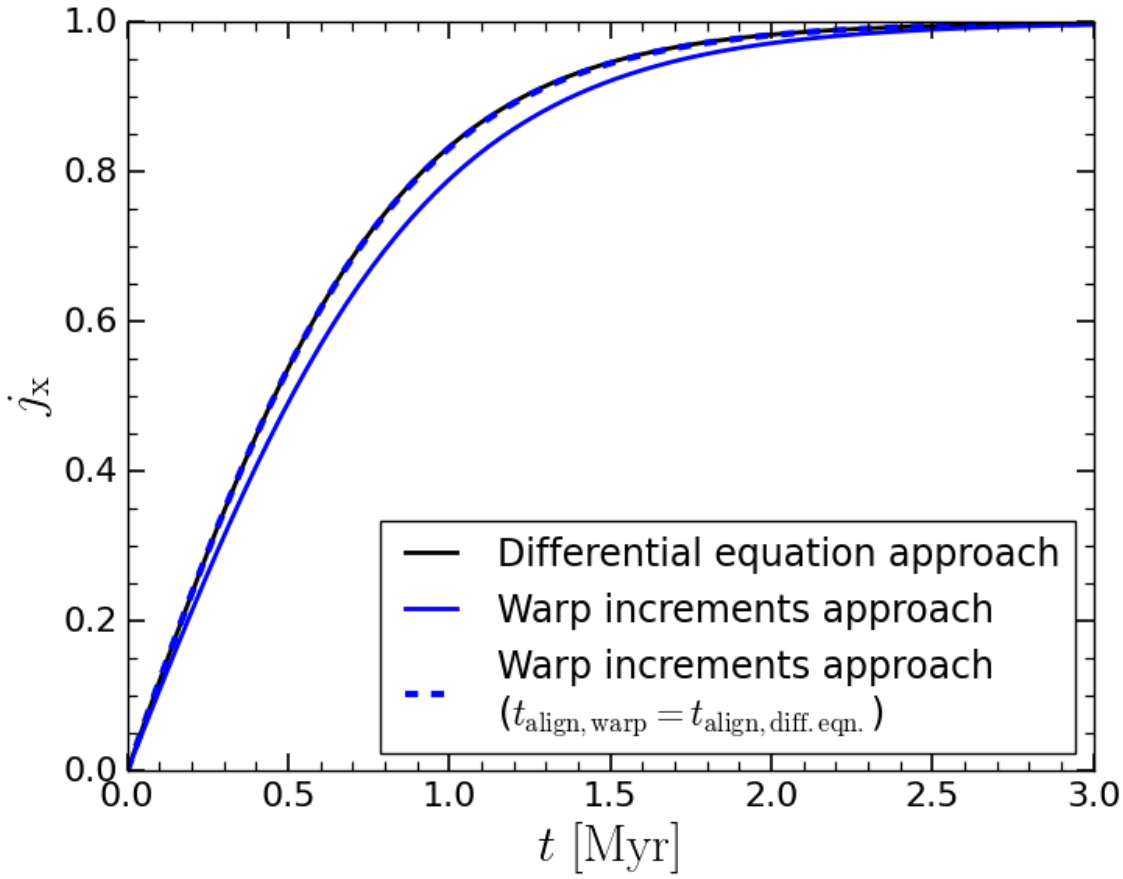

Figure 5.10: The alignment of an initially misaligned SMBH spin vector, calculated using two different approaches. We show the $x-$ component of the angular momentum direction vector, i.e. the component in the direction of the outer accretion disc. The initial SMBH spin is $a = 0.5$, and it is directed along the $z-$axis. The SMBH mass is $M_{\mathrm{BH}} = 10^7$ M$_\odot$, and the SMBH is accreting with a constant $\dot{m} = 0.1$. Black lines show the predicted alignment from the differential equation approach, using equations (5.4) and (5.6), while blue lines show predictions using our warp increment approach, with equation (5.7). The solid blue line shows the predicted alignment using the derived warp alignment timescale (equation 5.7), while the dashed blue line shows the prediction from the same approach, but using the alignment timescale from the differential equation approach, given by equation (5.6). The agreement between the black and dashed blue lines shows that the two approaches are (almost) equivalent.

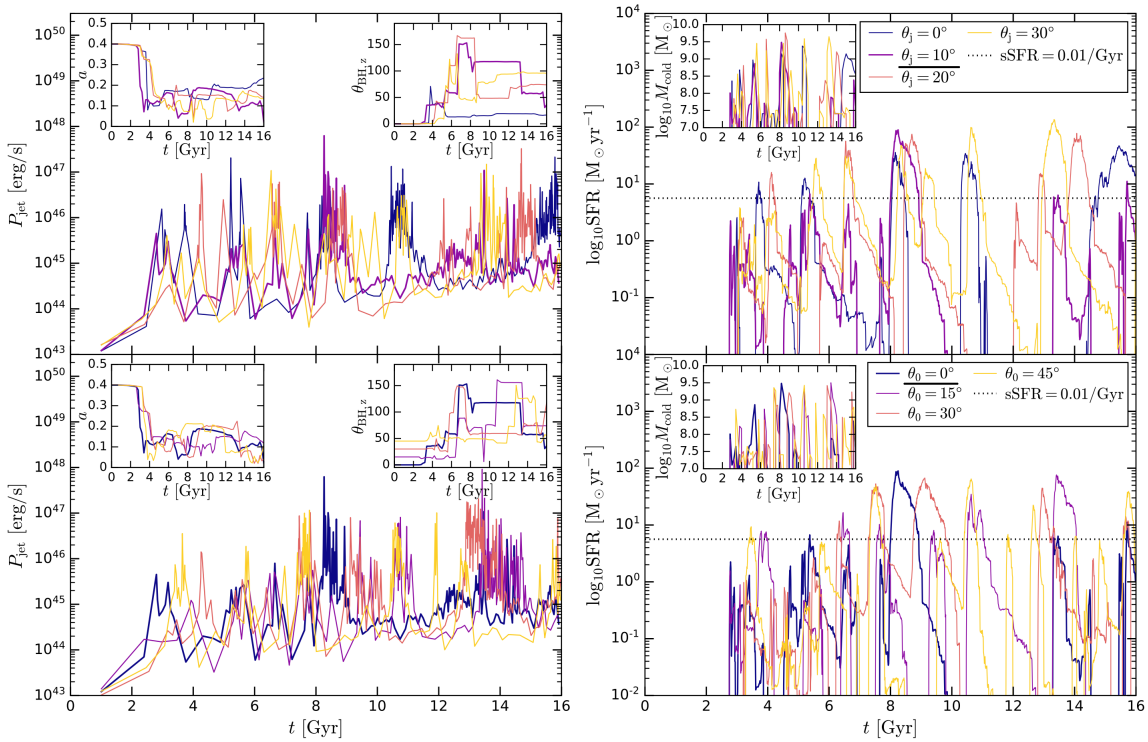

Figure 5.11: Time dependence of the quenching/feedback process in the high-mass galaxy cluster simulations ($M_{200} = 10^{15}$ M$_\odot$) with varying half-opening angles of the jet (top) and initial inclinations of the SMBH spin vector, relative to the angular momentum of the halo (bottom). The left-hand panels show the jet power, while the right-hand panels show the star formation rate. Insets in the left-hand panels show the magnitude of SMBH spin and the angle between the spin vector and $z-$axis. The insets in the right-hand panels show the cold gas mass. The fiducial simulation is the one with half-opening angle $\theta_{\rm j} = 10°$ and inclination $\theta_0 = 0°$ (purple and blue line, respectively, in the top and bottom panels); other details of the fiducial setup are given in Table 6.1. The dotted black lines represent the upper limit of the specific star formation rate required to classify a galaxy as quenched.

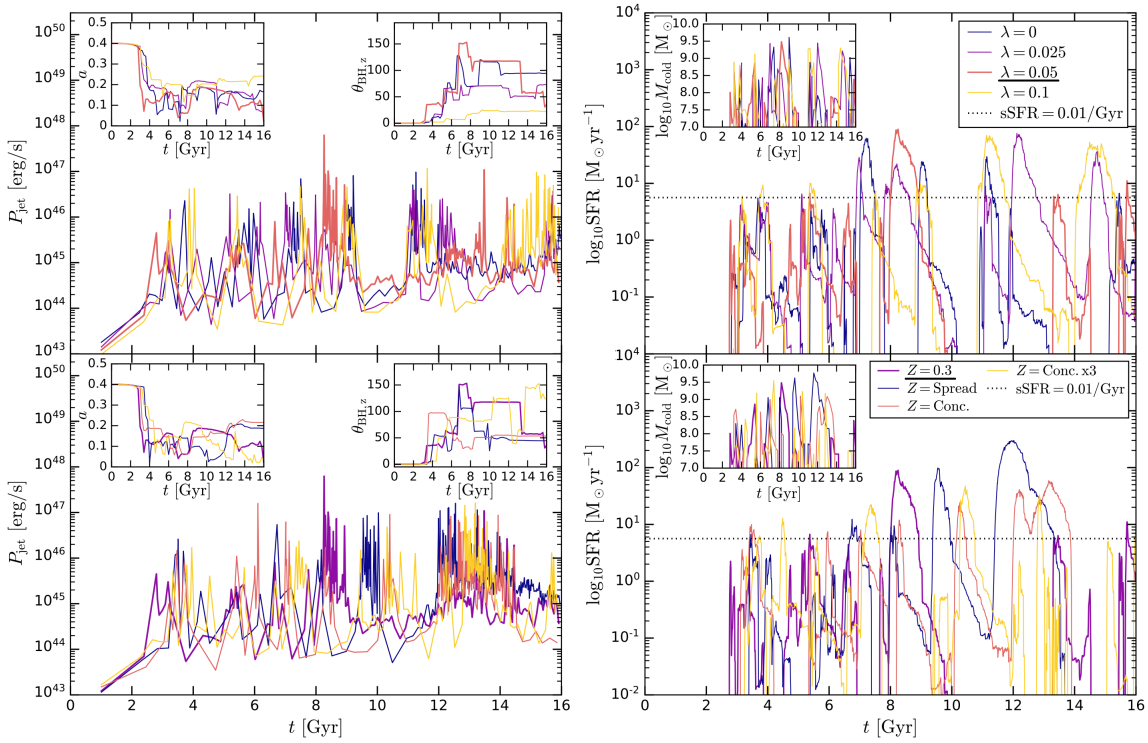

Figure 5.12: Time dependence of the quenching/feedback process in the high-mass galaxy cluster simulations ($M_{200} = 10^{15}$ M$_\odot$) with varying spin parameters (top) and metallicity profiles of the ICM (bottom). The left-hand panels show the jet power, while the right-hand panels show the star formation rate. Insets in the left-hand panels show the magnitude of SMBH spin and the angle between the spin vector and z-axis. The insets in the right-hand panels show the cold gas mass. The fiducial simulation is the one with an ICM spin parameter of $\lambda_{\rm g} = 0.05$ and constant metallicity $Z = 0.3Z_\odot$ (orange and purple lines, respectively, in the top and bottom panels); other details of the fiducial setup are given in Table 6.1. The dotted black lines represent the upper limit of the specific star formation rate required to classify a galaxy as quenched.

features on average somewhat higher spins and is never significantly misaligned from the z axis. Overall, these results imply that the rotation of the halo does not play a very significant role, and that the behaviour of the cooling gas is chaotic. These conclusions should be treated carefully, however, since these simulations were performed with a resolution of 6.4×10^6 M$_\odot$, which means that the cold gas is sampled with $100 - 1000$ particles at most.

In the bottom row of Fig. 5.12 we show variations in metallicity profiles of gas. We compare our fiducial case, with a constant metallicity of $0.3Z_\odot$, against a case with a 'spread' metallicity profile in accord with observations, $Z(r) = Z_\odot/(1 + r/20{\rm kpc})^{0.26}$ (which falls from solar values to $0.3Z_\odot$ at the virial radius), a 'con-

centrated' profile $Z(r) = Z_\odot/(1 + r/20\text{kpc})^{0.5}$ (which falls to $0.3Z_\odot$ by 100 kpc), and a similar one ('3xconcentrated') that has a central metallicity of $3Z_\odot$, but also falls to $0.3Z_\odot$ by 100 kpc. The 'spread' case features the highest SFR of all the simulations. The two other cases do not show significant differences relative to the fiducial case, despite the central metallicity being ≈ 3 and 10 times higher. This is likely because the higher metallicities cause faster cooling only for $T <$ a few $\times$ 10^6 K. However, gas that has already cooled down to such temperatures is already rapidly cooling, so the higher metallicities have an effect only on how quickly this portion of cooling occurs. The cooling gas spends the vast majority of its time at $T > 10^7$ K, so metallicity plays only a small role in these simulations.

5.B.3 Impact of other variations

In the top row of Fig. 5.13, we show the effects of reducing the gravitational softening length from 1200 pc, our fiducial choice, to 600 and 300 pc. These simulations are very similar. The one with the lowest softening length reaches the highest peak in SFR, but that is possibly incidental and due to the chaotic nature of these massive galaxy cluster simulations. The spin evolution in the three simulations is remarkably similar, despite the fact that the evolution of the misalignment between the spin vector and $z-$axis is not. Reducing the softening length does not appear to result in more coherent rotating, cold gas discs near the SMBH.

In the bottom row of Fig. 5.13 we compare two simulations with different initial conditions: random seeding (our fiducial choice) versus a uniform cubic lattice of particles, that is then stretched to produce the desired density profile. The differences are clearly visible. With uniform initial conditions, the gas cools more rapidly and there are generally more frequent jet/star formation episodes. This is likely because cooling caused by thermal instabilities from random seeding is not present, so the eventual cooling flows are stronger and harder to suppress (we find that overall more jet energy is injected in this simulation). Despite the lack of initial randomness, even the uniform simulation results in spindown and misalignment of the spin vector (with turbulence possibly being caused by jet feedback itself).

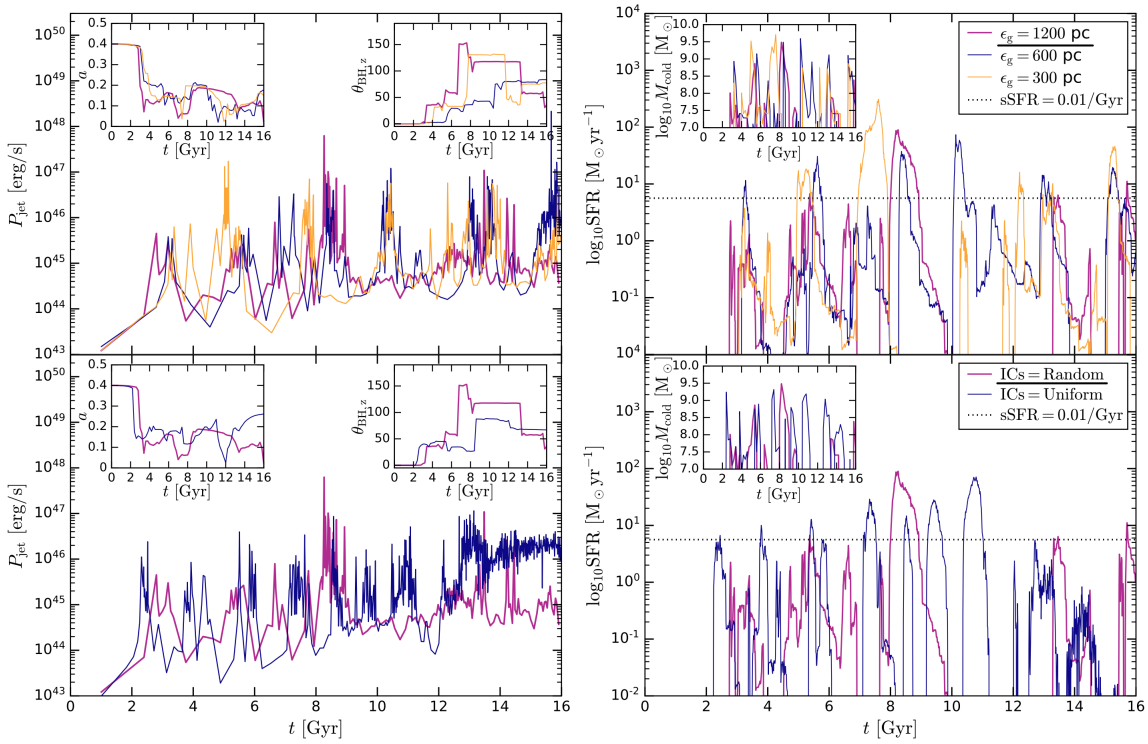

Figure 5.13: Time dependence of the quenching/feedback process in high-mass galaxy cluster simulations ($M_{200} = 10^{15}$ M$_\odot$) with varying gravitational softening lengths at fixed mass resolution (top) and particle position seeding (bottom). The left-hand panels show the jet power, while the right-hand panels show the star formation rate. Insets in the left-hand panels show the magnitude of SMBH spin and the angle between the spin vector and z-axis. The insets in the right-hand panels show the cold gas mass. The fiducial simulation is the one with a gravitational softening length of of $\epsilon_{\rm g} = 1.2$ kpc and random particle seeding (purple line in each panel); other details of the fiducial setup are given in Table 6.1. The dotted black lines represent the upper limit of the specific star formation rate required to classify a galaxy as quenched.

CHAPTER 6

Winds versus jets: a comparison of black hole feedback modes

6.1 Introduction

Hydrodynamical cosmological simulations of galaxy formation and evolution invariably find that AGN feedback is necessary in order to quench star formation in massive galaxies (e.g. Illustris: Vogelsberger et al. 2014 or EAGLE: Schaller et al. 2015). Most such simulations have implemented AGN feedback as isotropic heating of gas (thermal isotropic feedback), usually intended to represent the effects of radiatively-driven winds from quasars[1]. Examples of such simulations include Magneticum (Hirschmann et al. 2014), EAGLE (Schaye et al. 2015), MassiveBlack-II (Khandai et al. 2015), Romulus (Tremmel et al. 2017) and ASTRID (Bird et al. 2022), among others.

Other simulations have employed somewhat more complicated AGN feedback

[1]While this feedback mode is in principle similar in different simulations, the practical aspects of how it is implemented can lead to significant differences. Most significantly, if the feedback energy is injected in all particles/cells around the BH equally at every time-step ('thermal dump'), the heated gas can be prone to numerical overcooling, and the feedback is thus not very effective. In contrast, if the feedback energy is held in a reservoir until a sufficient amount of it has been accumulated to heat particles near the BH by some chosen heating temperature ΔT, these problems can be avoided (Booth & Schaye 2009). The feedback is most effective if only a single gas resolution element receives all of the accumulated energy.

prescriptions, using different mechanisms of energy injection at low BH accretion rates (alongside thermal isotropic feedback also being used at high accretion rates in all cases). In Illustris (Vogelsberger et al. 2014), pairs of thermal bubbles were injected at large distances in haloes (Sijacki et al. 2015). This feedback mode represents the late-time effects of relativistic jets that inflate lobes. However, the inflation process itself (which includes strong shocks that may be critical for heating the ICM) was not included, with the bubbles placed 'by hand', already inflated. IllustrisTNG (Nelson et al. 2019) instead uses kinetic isotropic feedback at low accretion rates (Weinberger et al. 2017a, Weinberger et al. 2018), representing the effects of winds that may be active alongside the jets (e.g. Blandford & Begelman 1999). For this feedback channel, the critical accretion rate below which it is used is assumed to be highly dependent on BH mass, leading to effectively no kinetic feedback for low-mass BHs and little thermal feedback for high-mass ones.

The SIMBA simulations (Davé et al. 2019) use kinetic jets (with high, supersonic velocities reached only at high BH masses, $M_{\rm BH} \geq 10^{7.5}$ $\rm M_{\odot}$, and at very low Eddington ratios) that are launched in the direction of the angular momentum of the gas surrounding the BH, alongside an additional X-ray feedback mechanism (implemented isotropically, as a mixture of heating and kicking particles), representing the equivalent of the kinetic wind used in IllustrisTNG at low accretion rates. In Horizon-AGN (Kaviraj et al. 2017), a similar prescription is used for the jets as in SIMBA (in that the jets are launched in the direction of the angular momentum of the gas close to the BH). Its successor New-Horizon (Dubois et al. 2021) uses a more sophisticated prescription based on a model presented in Dubois et al. (2014a), wherein the BH spin is evolved for all BHs using accretion disc models, and the jets are launched along the direction of the BH spin vectors, with spin-dependent efficiencies. In addition to being more realistic, this approach has the benefit (from a numerical perspective) that the BH spin vector is more stable against perturbations compared to the gas angular momentum (in the BH kernel), since the BH spin is a quantity that is integrated over the history of each BH. The radiative efficiency of AGN at high accretion rates also depends on BH spin in this model.

In this chapter, like in the previous ones, we will focus on modifications to the

AGN feedback prescription of the EAGLE galaxy formation model (Schaye et al. 2015, Crain et al. 2015), which is based on the Booth & Schaye (2009) AGN feedback scheme developed for the OWLS simulations (Schaye et al. 2010). The EAGLE simulations used a fairly simple AGN feedback prescription – despite this, the model correctly predicts the number of galaxies as a function of mass (as measured through the stellar mass function or the stellar mass-halo mass relation; Schaye et al. 2015) and redshift (Furlong et al. 2015) as well as many galaxy properties (e.g. the metallicities and sizes; Schaye et al. 2015, molecular gas content; Lagos et al. 2015, and colours; Trayford et al. 2017).

The Hydrangea simulations used the EAGLE model to evolve a sample of galaxy clusters (Bahé et al. 2017a). Despite the EAGLE model working well for the overall population of galaxies, these simulations found that BCGs were too massive, from about a factor of two for low-mass clusters (halo masses of order 10^{14} $M_{\odot}$) to a factor of nearly ten for high-mass clusters (halo masses of order 10^{15} $M_{\odot}$). The same galaxies were also found to be too highly star-forming compared to observations. This problem possibly originates from overly strong cooling flows in the simulations, which could be a consequence of insufficient heating by thermal isotropic AGN feedback at large radii (e.g. > 100 kpc).

The C-EAGLE project (Barnes et al. 2017) also used the EAGLE model to simulate a broadened sample (relative to Hydrangea) of galaxy clusters. Mock X-ray observations (Barnes et al. 2017) showed that these clusters appear to have central entropies of the ICM that are too high (a problem confirmed by Altamura et al. 2023 on a separate sample of galaxy groups and clusters, using an updated version of the EAGLE model). This is also true for the temperature, and the reverse is true for the density. A related problem is in the cool-core (CC) versus non-cool-core (NCC) dichotomy of clusters (e.g. Hudson et al. 2010): simulated clusters are likely too often NCC as compared to observed ones (the fraction of CC clusters is too low), although firm conclusions on this are complicated by varying definitions in the literature of what is a CC versus a NCC cluster (Barnes et al. 2018).

Nobels et al. (2022) studied AGN feedback using an updated version of the EAGLE model in idealized galaxy groups and clusters, and found that thermal isotropic

feedback can quench star formation in central galaxies for long times (many Gyr) only in galaxy groups, while in galaxy clusters, the BCGs have recurrent cooling flows. They found that clusters initialized as CC largely remain CC. This indicates that the potential lack of CC clusters, as measured through the central entropy, in realistic, cosmologically simulated samples of clusters (C-EAGLE) may be unrelated to AGN feedback, and could instead be a result of other physical processes in the evolution of these clusters. Alternatively, Altamura et al. (2023) found significant differences in entropy profiles between their clusters and those in the C-EAGLE sample. Their cosmological zoom-in simulations of groups and clusters used a slightly updated EAGLE model with, most significantly, a new hydrodynamics scheme (Borrow et al. 2022). They also found substantial differences when turning off artificial conduction in the hydrodynamics solver. These results indicate that the differences between observed and simulated clusters may be partly or wholly due to numerical issues.

If the differences between the observed clusters and ones simulated with EAGLE are not entirely due to numerics, including a more realistic feedback mechanism (representing the effects of relativistic jets) may be helpful, presumably by allowing more effective coupling of the feedback energy to larger radii instead of only to the core of the ICM. A similar modification may be beneficial in the IllustrisTNG model (see e.g. the results of the MillenniumTNG simulations, Pakmor et al. 2022). This is despite that model using kinetic feedback at low accretion rates (alongside thermal isotropic feedback at high accretion rates), and the reason may be that the feedback mechanism is also isotropic. As we will show in this chapter, kinetic isotropic and thermal isotropic feedback are fairly similar in their effects, at least in the context of idealized cluster simulations. The potential problems we have discussed may be present even for the SIMBA simulations (Davé et al. 2019), which also show somewhat too high entropies, albeit at intermediate radii rather than in the core of the ICM (Oppenheimer et al. 2021). While SIMBA includes AGN jets, they are launched in the direction of the angular momentum of the gas near the BH, which may not be very stable (especially in clusters and at low resolutions). As we will show in this chapter, the jet direction needs to be relatively stable for the jets to

lead to significant differences compared to isotropic feedback.

Here we will broaden the analysis from Chapter 5 and consider isotropic feedback as well – the AGN feedback mode used in EAGLE and all other large, cosmological hydrodynamical simulations (at least at high BH accretion rates). Our main goal here is to compare these two feedback modes in terms of their impact on the BCGs, their BHs and the ICM. Some previous works focusing on feedback in idealized galaxy clusters have studied different feedback implementations, with many of them comparing thermal and kinetic feedback (e.g. Barai et al. 2016, Meece et al. 2017, Su et al. 2021, Weinberger et al. 2023). Most of these works employed thermal feedback as a 'thermal dump', meaning that it will likely have been prone to numerical overcooling, unlike the kinetic variety.

The results we will present in this Chapter build on previous studies by broadening the comparison between AGN feedback modes to include both realistic feedback (with BH spin evolution) and a more simplified implementation (with fixed efficiencies and jet directions). In addition, we compare these feedback implementations for different halo masses, ranging from the galaxy group ($M_{200} = 10^{13}$ $\mathrm{M}_{\odot}$) to the high-mass galaxy cluster ($M_{200} = 10^{15}$ $\mathrm{M}_{\odot}$) scales. In our simplified feedback scenario, we systematically vary relevant parameters such as the heating temperatures and kick velocities, as well as feedback efficiencies. Furthermore, for both isotropic and jet feedback, we vary the type of energy being injected (thermal versus kinetic). In terms of results, we focus mostly on SFRs and entropy profiles, as stellar masses of BCGs and entropy profiles of the ICM appear to show the largest or most easily observable discrepancies between observed clusters and those simulated with EAGLE.

6.2 Simulations, methods and set-up

In this chapter we use the same set-up, code and physics modules (with the exception of differences in AGN feedback) as those presented in Chapter 5; we refer the reader to that chapter for further details. We simulate a subset of idealized galaxy groups and clusters from that chapter. For the AGN physics, we include a

more general model. In Chapter 5 we assumed that BHs are always in the thick accretion regime and launching kinetic jets. Here we add the thin disc mode with its radiative feedback (represented in our simulations by thermal isotropic heating), which is active at moderately high Eddington ratios. We perform some simulations where the BHs are always in either one of those two modes, as well as some where they switch modes at a critical Eddington ratio of $f_{\rm Edd,crit} = 0.01$. Note that, since we do not suppress the accretion rate due to winds in this chapter, the Eddington ratio $f_{\rm Edd}$ has the same meaning as $f_{\rm Edd,0}$. Note also that here, as in Chapter 5, we use the definition of the Eddington ratio in which the radiative efficiency is constant ($\epsilon_{\rm rad} = 0.1$), rather than the spin-dependent Novikov & Thorne (1973) one as in Chapter 2.

6.2.1 Implementation of AGN feedback

When implementing any feedback mechanism, several choices must be made: 1) how the energy is directed, 2) what is the feedback power, 3) how much energy is imparted per each feedback event and 4) what form the energy takes. In this chapter we compare two different forms of AGN feedback in terms of how it is directed: isotropic and jet feedback (the former of which is done as in Booth & Schaye 2009, at least for the thermal case). For both of these options, we thoroughly compare different choices related to points 2-4 above.

In the isotropic case, energy is imparted to the closest particle in the BH smoothing kernel. Note, however that this implementation is not precisely isotropic, since isotropic feedback would entail choosing random angles and imparting energy to the particles closest to those chosen angles. Chaikin et al. (2022) compared different numerical implementations of kinetic feedback (albeit stellar, but this makes no difference for the following argument), including 'Min distance' and 'Isotropic'. In the former, the closest particles to the BH are heated (corresponding to what we do here), while in the latter, particles were chosen in pairs along rays (that do not generally pass through the central star or BH that is injecting the energy) to ensure conservation of not only energy, but also linear and angular momentum. They found the results to be very similar in the two kicking schemes. Throughout the rest of this

chapter, for simplicity we refer to the scheme we use ('Min distance' from Chaikin et al. 2022) as 'isotropic', since we use it to represent the effects of isotropic winds, and since it is much different from jet feedback regardless of the details of how it is implemented.

In the jet case, energy is always imparted to two particles instead of one, and the same criterion is used to choose the particles as in our isotropic feedback. In order to find a pair of particles to kick in roughly opposite directions, we define two hemispheres within the BH smoothing kernel. The equatorial plane separating them is perpendicular to the vector that defines the launching direction of the jets (the $z-$axis or the BH spin vector).

Several parameters can be tuned to affect the behaviour of these feedback mechanisms (as described by points 2-4 in the beginning of this section). The first of these is the feedback efficiency ϵ, which controls how much feedback energy is injected given some amount of BH accretion. We use variable feedback efficiencies in the case where the BH spin and its evolution are used (§ 6.3), but also values fixed throughout the duration of a given simulation in a simplified model (§ 6.4).

The feedback power is funneled to a reservoir of energy. Once the reservoir exceeds some threshold value ΔE, a feedback event occurs (either one particle receiving energy in the isotropic case, or a pair in the jet case). The energy ΔE is imparted in either thermal, kinetic or mixed form (in the latter case, half of the energy is injected as thermal and half as kinetic). Thus, there are three choices to make in both the isotropic and jet case: 1) the feedback efficiency ϵ, 2) the energy threshold ΔE and 3) the type of energy being received. In all of our isotropic cases, we use large enough values of ΔE that the feedback is energy-dominated, rather than momentum-dominated (see e.g. Faucher-Giguère & Quataert (2012), Costa et al. 2014). We thus expect no additional radiative cooling (of a physical or numerical nature) in the regions immediately ahead or behind the outflows associated with feedback, as seen for momentum-driven outflows that appear if low velocities are used for kinetic feedback.

In the thin, radiatively efficient disc (used at high accretion rates), we use the thermal isotropic variant of AGN feedback to represent the effects of radiation-

driven winds[2]. This assumption is valid if the radiatively-driven winds shock and deposit their energy on small scales (e.g. $1 - 100$ pc) that we do not resolve in these simulations, leading to hot gas that expands on account of thermal pressure (e.g. Faucher-Giguère & Quataert 2012). For the thick, advection-dominated disc, we use kinetic jets to represent the effects of relativistic jets launched in this accretion regime. In both cases, our BH spin evolution model is used to evolve the radiative and jet feedback efficiencies, when we allow them to vary. For the jet case, this also results in a variation of the jet direction, which is assumed to be aligned with the BH spin axis.

In the case that particles are being isotropically heated, we refer to (and vary) the heating temperature ΔT instead of ΔE; the two are related by $\Delta E = (3m_{\rm g}/2\mu m_{\rm p})k_{\rm B}\Delta T$, where $m_{\rm g}$ is the gas particle mass, $\mu = 0.62$ the mean molecular weight of ionized gas and $k_{\rm B}$ the Boltzmann constant.

In the kinetic jet case, we express the energy being received by the particles through the jet velocity $v_{\rm j}$ as $\Delta E = 2 \times m_{\rm g} v_{\rm j}^2/2$, where the multiplication by two is present since we always kick in pairs. We do not kick particles perfectly along the jet direction, but instead implement a finite half-opening angle of $\theta_{\rm j} = 10^{\circ}$. This is accomplished by assigning a new kick direction every time a kick event occurs; this direction is given by a unit vector $\mathbf{n}_{\rm j}$ that is drawn randomly and uniformly in solid angle within a cone with a half-opening angle $\theta_{\rm j}$ directed along the chosen jet direction (either aligned with the BH spin vector or the $z-$axis). Since we always kick in pairs, the above procedure is done for one particle in the 'positive' direction (along the jet direction) and for another particle in the 'negative' direction (counteraligned with the jet direction).

[2]In the thermal isotropic case, we generally refer to the total feedback efficiency ϵ, which is different from the radiative efficiency $\epsilon_{\rm r}$ for the following reason. The BH radiates at a rate $\epsilon_{\rm r}\dot{M}_{\rm B}c^2$, but only a fraction $\epsilon_{\rm f}$ (the coupling, or feedback, efficiency) of that actually couples with the gas in the simulation. The total feedback efficiency is therefore $\epsilon = \epsilon_{\rm f}\epsilon_{\rm r}$. This distinction has a small effect in the simulations in that the BH accretes only $(1 - \epsilon_{\rm r})$ of the total accretion rate, rather than a fraction $(1 - \epsilon)$ of it. We fix $\epsilon_{\rm f} = 0.1$ and vary $\epsilon_{\rm r}$ in our simulations. For the jets we assume $\epsilon_{\rm f} = 1$ and drop the factor hereafter.

6.2.2 Physical set-up

In order to test the different implementations of AGN feedback discussed above, we simulate idealized galaxy groups and clusters as in Chapter 5. Our assumed properties (which are discussed at length in the mentioned chapter) for each of these idealized systems is listed in Table 6.1. These parameters do not vary in any of our simulations, other than with halo mass, as shown in the table.

The initial central temperature of the gas T_0 has a strong impact on the simulations (see Nobels et al. 2022 for the thermal isotropic feedback case, and Huško et al. 2022 for kinetic jet case). For this study we choose relatively low values that lead to significant cooling and feedback on the Gyr time-scales of the simulations we are performing here. In other words, these choices of T_0 correspond to a relatively CC set-up, rather than NCC (the majority of observed groups and clusters do not have appreciable amounts of ongoing cooling or AGN feedback). While this choice may not be representative of the entire population of galaxy clusters, we make it for a few reasons: 1) it leads to more AGN activity, allowing us to compare different AGN feedback schemes more easily, 2) the cooling flows are stronger, so the potential of various AGN feedback schemes to shut them off is tested to a stronger degree, 3) the BH accretion rates are higher, leading to the accretion regime more often corresponding to the thin, radiatively-efficient disc (the regime for which we have developed a model that we wish to test in detail using this setting). The BH spins we choose are relatively low; in galaxy groups and clusters we do not expect fully spun-up BHs due to spindown from jets and BH-BH merger activity.

Other choices also have to be made in setting up the ICM, although they are independent of halo mass (for our study). We assume a constant gas metallicity (as found in at least some observations, e.g. Werner et al. 2013 and McDonald et al. 2016) of $0.3Z_{\odot}$ (with the solar metallicity chosen as $Z_{\odot} = 0.0134$; Asplund et al. 2009). We also assume rotation of the ICM about the $z-$axis (see Nobels et al. 2022 for details on how this is set up) with a spin parameter of $\lambda = 0.05$ (Bullock et al. 2001), which is slightly larger than that of the DM (Oppenheimer 2018).

Table 6.1: List of parameters for the initial conditions (first eight columns) and numerical resolution (last two columns) of our idealized galaxy group and cluster simulations. These are, in order: 1) M_{200} - halo mass, 2) r_{200} - halo virial radius, 3) NFW halo concentration parameter $c_{\rm NFW}$, 4) baryonic mass fraction within R_{500}, $f_{\rm b,500}$, 5) central gas temperature T_0, 6) stellar mass of the BCG, 7) Hernquist scale length (half-light radius) of the galaxy, 8) mass of the central BH, 9) spin of the BH, 10) central gas mass resolution, 11) gravitational softening length.

M_{200} [$\rm M_\odot$]	R_{200} [kpc]	$c_{\rm NFW}$	$f_{\rm b,500}$	T_0 [K]	M_* [$10^{11}\,\rm M_\odot$]	a_* [kpc]
10^{13}	442.7	7.2	0.05	10^{6}	1	10
10^{14}	953.8	5.6	0.10	$10^{6.75}$	2.5	20
10^{15}	2054.8	4	0.15	$10^{7.5}$	6	30

$M_{\rm BH}$ [$10^9\,\rm M_\odot$]	a_0	$m_{\rm g,0}$ [$10^5\,\rm M_\odot$]	$\epsilon_{\rm g}$ [kpc]
0.25	0.2	1	0.25
0.5	0.2	8	0.5
6.5	0.4	64	1

6.2.3 Simulations

We perform a total of nine simulations using the BH spin evolution model presented in Chapter 2; three for each halo mass. The three for each case use different variations of BH spin evolution and feedback: 1) one simulation using the thin, radiatively efficient disc and thermal isotropic feedback, 2) one using the thick, advection-dominated disc with kinetic jets and 3) one with hybrid accretion and feedback modes, with the thin disc mode used at high accretion rates ($f_{\rm Edd} > f_{\rm Edd,crit}$) and the thick disc one at low accretion rates ($f_{\rm Edd} < f_{\rm Edd,crit}$). The details of these simulations are given in Table 6.2. This last model represents the most realistic one and should thus replicate the behaviour of BHs in the real Universe most closely.

In this chapter we use heating temperatures, ΔT, of order 10^9 K as motivated by many previous works (e.g. Schaye et al. 2015). For jet velocities, $v_{\rm j}$, we choose values of order 10^4 km s^{-1}, instead of relativistic ones, mainly due to limitations related to resolution. We increase the heating temperatures and jet velocities with halo mass, in order to sample feedback at a similar level (using the same values would result in the sampling of feedback being significantly better as halo mass is increased, which might thus lead to artificial numerical differences between the three

Table 6.2: List of simulations performed with the BH spin evolution model (see Chapter 2). For each halo mass, three simulations were performed with different feedback and accretion modes. In the hybrid mode, the thin disc and thermal isotropic feedback is used when the BH is accreting with $f_{\rm Edd} > f_{\rm Edd,crit} = 0.01$, while the thick disc and kinetic jets are used otherwise. The details of these simulations are given below.

M_{200} [$\rm M_\odot$]	Accretion disc	Feedback mode	Feedback efficiency ϵ
10^{13}	Thin	Thermal isotropic	$\epsilon_{\rm f}\epsilon_{\rm r}(a)$
10^{13}	Thick	Kinetic jets	$\epsilon_{\rm j}(a)$
10^{13}	Hybrid	Hybrid	$\epsilon_{\rm f}\epsilon_{\rm r}(a)$ or $\epsilon_{\rm j}(a)$
10^{14}	Thin	Thermal isotropic	$\epsilon_{\rm f}\epsilon_{\rm r}(a)$
10^{14}	Thick	Kinetic jets	$\epsilon_{\rm j}(a)$
10^{14}	Hybrid	Hybrid	$\epsilon_{\rm f}\epsilon_{\rm r}(a)$ or $\epsilon_{\rm j}(a)$
10^{15}	Thin	Thermal isotropic	$\epsilon_{\rm f}\epsilon_{\rm r}(a)$
10^{15}	Thick	Kinetic jets	$\epsilon_{\rm j}(a)$
10^{15}	Hybrid	Hybrid	$\epsilon_{\rm f}\epsilon_{\rm r}(a)$ or $\epsilon_{\rm j}(a)$

Heating temperature ΔT [K]	Jet velocity [$10^4\,\rm km s^{-1}$]
$10^{8.5}$	–
–	0.5
$10^{8.5}$	0.5
10^{9}	–
–	1.5
10^{9}	1.5
$10^{9.5}$	–
–	3
$10^{9.5}$	3

simulated haloes). The increase in jet velocity with halo mass is also motivated by previous simulations we have done, presented in Chapters 3-5, where we found that jets need to be highly supersonic relative to the external medium (by a factor $M = v_{\rm j}/c_{\rm s,ICM} \geq 10$) in order to inflate lobes. As the ICM temperature increases with increasing halo mass, this implies that an increase in jet velocity is well-motivated.

We also perform simulations with simplified feedback prescriptions. For these we fix the feedback efficiencies to constant values, as well as fixing the jet directions to be along the $z-$axis. The details of these simulations are given in Table 6.3. We perform these simulations only for the galaxy clusters ($M_{200} = 10^{14}$ $\rm M_\odot$ and $M_{200} = 10^{15}$ $\rm M_\odot$) since these simulations show more interesting (or variable) behaviour than the

galaxy group ones. The motivation for these simulations is to provide a comparison of different feedback modes by removing any differences due to variations in the feedback efficiency. To this end we include runs where we fix the efficiency to $\epsilon = 0.01$ in both the thermal isotropic and kinetic jet cases. For the kinetic jet case we test two options: 1) using jet velocities that are ≥ 10 times higher than the sound speed of the ICM and 2) using lower velocities (by a factor ≈ 3 relative to option 1) that, however, lead to the energy per feedback event ΔE being the same as in the equivalent thermal isotropic simulations. We consider option 1) our fiducial choice, for the reasons laid out in the paragraph above.

For the low-mass galaxy cluster ($M_{200} = 10^{14}$ M$_\odot$) case, we also perform a series of simulations whose parameters are specified in the last two rows Table 6.3. The purpose of these simulations is to vary all parameters of interest: the feedback efficiency, the energy per feedback event and the type of energy being injected. These variations were done for both the isotropic and jet cases. For the jet case, we also tested the importance of the jet direction by manually redirecting the jets in random directions with a given periodicity, and also by precessing them with varying opening angles and periods. These simulations, and their results, are discussed in detail in Appendix 6.A. We found the jet direction to be largely unimportant for the type of simulations being performed here.

6.2.4 Observational sample of entropy profiles

In this chapter, we mainly focus on the gas entropy when discussing the impact of feedback on the ICM. For this purpose we define the entropy as $K = k_\mathrm{B} T / n_\mathrm{e}^{2/3}$, where k_B is the Boltzmann constant and T and n_e are the gas temperature and electron number density, respectively. We will compare our simulated entropy profiles of the ICM (as a function of radius) to observed ones inferred from X-ray observations.

For high-mass clusters there are plentiful such samples due to the hot ICM gas falling well into the range observable by X-ray observatories such as *Chandra*, and since these clusters are easier to observe due to a larger intrinsic brightness. We compare the simulated high-mass galaxy cluster ($M_{200} = 10^{15}$ M$_\odot$) with the observed ones from Pratt et al. (2010), who studied 31 nearby clusters using *XMM-Newton*,

Table 6.3: List of simulations performed with simplified feedback prescriptions (without BH spin evolution, i.e. with fixed feedback efficiencies and jets in the direction of the $z-$axis). Three simulations were performed for the low- and high-mass galaxy clusters. For the low-mass galaxy cluster, further variations of all the parameters were performed in a total of 16 simulations. The parameters of these simulations are given in the last two rows. * Th. - thermal, Mix. - mixed (half thermal, half kinetic), Kin. - kinetic.

M_{200} [$M_\odot$]	Feedback mode	Energy type	Feedback efficiency ϵ	Heating temperature ΔT [K]	Jet velocity [$10^4\,\mathrm{km s^{-1}}$]
10^{14}	Isotropic	Thermal	0.01	10^9	–
10^{14}	Jet	Kinetic	0.01	–	0.65
10^{14}	Jet	Kinetic	0.01	–	1.5
10^{15}	Isotropic	Thermal	0.01	$10^{9.5}$	–
10^{15}	Jet	Kinetic	0.01	–	1.15
10^{15}	Jet	Kinetic	0.01	–	3
10^{14}	Isotropic	Th., Mix., Kin.*	$0.01-1$	$10^{8-9.5}$	–
10^{14}	Jet	Th., Mix., Kin.*	$0.01-1$	–	$0.47-2.66$

as well as those from Ghirardini et al. (2019) using the same telescope, but with a different sample of 12 galaxy clusters. We also compare with *Chandra* observations by Cavagnolo et al. (2009), who provide entropy profiles for a large sample of 239 high-mass galaxy clusters ($M_{500} \approx 10^{15}$ $M_\odot$, where M_{500} is the halo mass using a virial overdensity of factor 500 relative to the critical density). They also split their sample into CC and NCC clusters based on whether the central entropy is below or above 50 keV$\,$cm^2.

For galaxy groups and low-mass clusters ($M_{500} \leq 10^{14}$ $M_\odot$), such observations are inherently difficult (e.g. Werner et al. 2019, Eckert et al. 2021, Lovisari et al. 2021, Oppenheimer et al. 2021). The sample sizes tend to be small and/or they span a large range in halo mass. The halo masses of these galaxies cannot currently be measured through X-ray observations, since their ICM/CGM may not be in hydrostatic equilibrium, nor is the X-ray emission typically measured up to the virial radius (or an appreciable fraction of it so that one may extrapolate the pressure profile). The samples may also be biased towards CC (low-entropy) ones since such X-ray atmospheres are more likely to be bright and therefore observed. Finally, it is also likely that many of these observed X-ray atmospheres surround satellite galaxies rather than being the central ones of primary haloes. Tidal stripping may be affecting many such galaxies, or it may also be biasing the samples towards the X-ray bright ones.

Notwithstanding those currently unavoidable shortcomings, we compare the entropy profiles of our galaxy group ($M_{200} = 10^{13}$ $M_\odot$) and low-mass cluster ($M_{200} = 10^{14}$ $M_\odot$) simulations with a set of different observational papers. We use the data based on 28 and 43 observed galaxy groups and clusters by Johnson et al. (2009) (using *XMM-Newton*) and Sun et al. (2009) (using *Chandra*), which provide useful constraints on the entropy profiles between roughly $r = 30$ kpc and $r = 1$ Mpc. At relatively small radii ($r < 100$ kpc) we compare with data from Babyk et al. (2018), who compiled observed profiles of 40 galaxies/groups and 110 galaxy clusters, all observed with *Chandra*. For all these systems, Babyk et al. (2018) find a universal median entropy profile, which they fit with $K \propto r^{2/3}$ at small radii and $K \propto r^{1.1}$ at large ones. Finally, we compare with Lakhchaura et al. (2018), who presented

entropy profiles of 49 bright elliptical galaxies observed with *Chandra*. These data are largely consistent with the Babyk et al. (2018) ones, although they tend to follow a single slope with radius.

6.3 Results I: feedback with black hole spin evolution

We first consider the results of using the BH spin evolution model for all three of the halo masses, from the galaxy group ($M_{200} = 10^{13}$ M$_\odot$) to the high-mass cluster ($M_{200} = 10^{15}$ M$_\odot$) scale. For each of the halo masses, we performed three simulations: 1) using the thin, radiatively-efficient disc and thermal isotropic feedback, 2) using the thick, advection-dominated disc and kinetic jet feedback and 3) a hybrid case where the two accretion and feedback modes interchange at $f_{\rm Edd} = f_{\rm Edd,crit} = 0.01$. The details of these simulations are given in § 6.2.2 and Table 6.1 (in terms of physical set-up and halo mass) as well as § 6.2.3 and Table 6.2 (in terms of feedback implementation).

In Fig. 6.1 we show visualizations of the gas temperature in our hybrid simulation of the high-mass cluster. These show the qualitative behaviour of the feedback and cooling cycle, which we consider to be representative of all our simulations. These visualizations highlight the rich variety of structures we find, with many of them similar to features observed in the ICM of real galaxy clusters. The bulk of the ICM on the spatial scales shown in Fig. 6.1 has a temperature of order $T \approx 10^{7.5} - 10^{8}$ K (light-blue to dark-purple colours), varying with radius. Black colours indicate gas that is slightly hotter (mostly due to shock waves), while orange-to-white colours indicate gas that is a factor of several times hotter than the ambient medium (the gas launched as part of feedback or entrained in the same process). These visualizations also show gas that is strongly cooling (white colours).

The two left-hand panels show simulation times when the kinetic jet activity is peaking, while the two right-hand panels show the same for thermal isotropic feedback. From the two left-hand panels, we see that jet feedback can lead to asymmetrical large-scale outflows, as a result of several processes, some of which

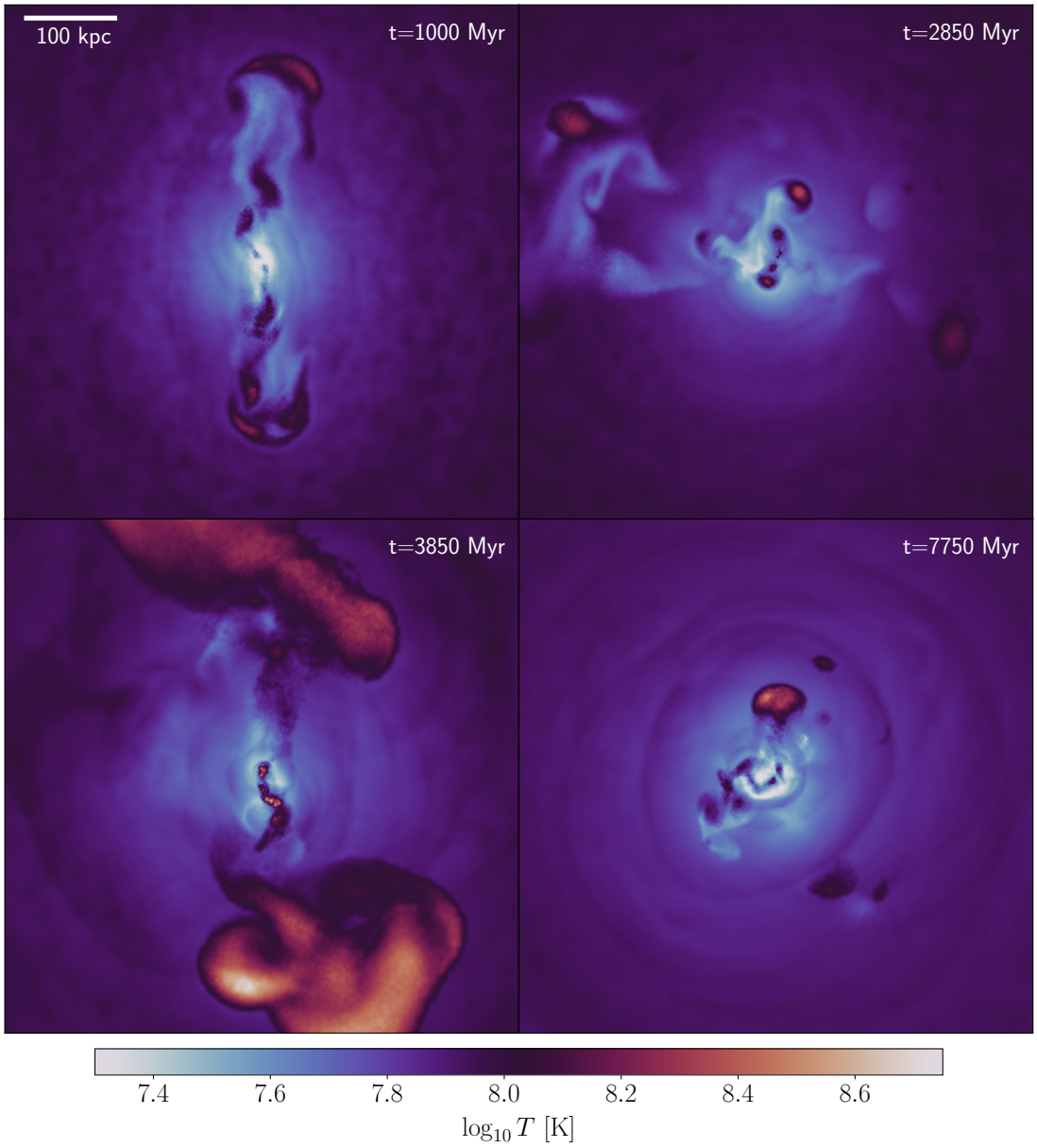

Figure 6.1: A visualization of the gas temperature at four representative times in our hybrid simulation (with both kinetic jets and thermal isotropic feedback, interchanging at an Eddington ratio $f_{\mathrm{Edd,crit}} = 0.01$) of the high-mass galaxy cluster ($M_{200} = 10^{15}$ $\mathrm{M}_{\odot}$). The colours indicate the projected, mass-weighted gas temperature, as indicated by the colour bar, and we include all gas in a 50 kpc-deep slice. The left-hand panels show times when kinetic jet feedback dominates, while the right-hand panels show times when thermal isotropic feedback is dominant. The bottom two panels show that both types of feedback lead to spherical shock waves. At all times shown here, ambient gas uplifted by feedback-induced outflows is visible in the form of cool filamentary structures.

are: 1) jet redirection and/or precession, 2) variability in the jet power and 3) the complex structure of the ICM in the jets' path (including uplifted low-entropy gas due to previous feedback episodes; we discuss this below). From the right-hand panels, we see that thermal isotropic feedback generally does *not* lead to isotropic outflows. This is partly a result of how it is implemented in our simulations: gas is heated to large temperatures ($\Delta T = 10^{9.5}$ K in this case). This hot gas tends to not expand isotropically, but rather in the 'path of least resistance' away from the BCG. The first few heating events in a given feedback episode create a channel that represents the preferred direction in which the subsequently heated gas will expand.

For both thermal isotropic and kinetic jet feedback, we see that the typical temperature of the hot gas outflows and bubbles is not similar to the temperature associated with the launching events ($\Delta T = 10^{9.5}$ K and $\Delta T_{\rm j} \approx 10^{10}$ K[3], respectively). It is instead a factor of 10 or so lower in temperature, which is likely on account of several processes, including the transferal of energy from the outflows to the ambient medium (through shocks or other processes), as well as adiabatic expansion and entrainment of ambient gas.

From the bottom two panels we see that both kinetic jets and thermal isotropic feedback lead to the generation of roughly spherical shock waves, which is one of the ways in which AGN feedback can heat the ambient medium (e.g. Li et al. 2017, see also review by Fabian 2012). From all four panels we see that the ICM has a generally very complex structure, with actively cooling gas draping and trailing the outflows and bubbles associated with feedback (to distances as large as 300 kpc). Particularly noticeable are filamentary structures that arise from the feedback-induced uplift of the low-entropy ICM from the core of the ICM to larger radii (see Chapter 4 for a discussion on AGN-induced uplift of gas). The process of gas uplifting is one of the ways feedback is done, by reducing the central gas density and therefore delaying

[3]This temperature represents the typical temperature of hot gas making up the jet-inflated lobes if one assumes that all of the kinetic energy of a single jet kicking event, with a velocity of $v_{\rm j} = 3 \times 10^4$ km s^{-1} in this case, is transformed to thermal energy through shocks, as well as that none of it is transferred to the ambient medium through the shocks, and that no ambient ICM is entrained. This typical temperature, obtained through $(3/2)k_{\rm B}\Delta T_{\rm j} = (1/2)\mu m_{\rm p} v_{\rm j}^2$, is expected to be an overestimate for the aforementioned reasons, but it is a useful order-of-magnitude estimate, especially when comparing to thermal feedback.

radiative cooling. However, the uplifted gas rises to some radius where the thermal pressure is lower, so its thermal pressure also reduces. The gas cools adiabatically and it thus may be more prone to further radiative cooling. It is thus possible that a positive AGN feedback loop exists, at least to some degree (not necessarily dominant over the negative feedback), in the systems we are simulating.

6.3.1 Feedback powers

We begin our quantitative comparison of the different simulations with BH spin evolution by considering the variation of feedback powers with time. In Chapter 5 we showed the power to be high when the central regions of these simulated haloes are strongly cooling, i.e. undergoing a cooling flow that leads to significant amounts of cool gas (which we define to be $T < 2 \times 10^4$ K for the purposes of this paper) and a non-zero SFR (see Nobels et al. 2022 for a discussion of the small delay between cooling and feedback). On the other hand, if the central regions of these haloes have been sufficiently heated by feedback, or if gas has been transported outwards through feedback-induced uplift, the feedback powers are low since the BHs are accreting directly from the hot halo, rather than the cold gas. As a result, the feedback power serves as a good tracer of the overall behaviour of the cooling and feedback cycle of these haloes.

In the top two rows of Fig. 6.2 we show the feedback power as a function of time in simulations with different feedback prescriptions, for all three of our studied halo masses. The top two left-hand panels show the feedback powers for the galaxy group. In all cases there is an initial feedback episode, after which the feedback power settles down to much lower, roughly constant values for the rest of the simulations. This constant value is around 5 times lower for the thermal isotropic case (bottom panel) than the kinetic jet case. The difference can be explained by considering the feedback efficiencies in these simulations, which are set by the spins of the BHs (see § 2.4 and Fig. 6.3 for a detailed discussion of the evolution of the BHs in these simulations). In the jet case, the feedback efficiency is $\epsilon_{\rm j} \approx 0.025$, whereas the radiative efficiency in the thermal case is $\epsilon_{\rm r} \approx 0.06$. The thermal isotropic feedback power is 10 times lower than that due to a coupling efficiency factor of $\epsilon_{\rm f} = 0.1$,

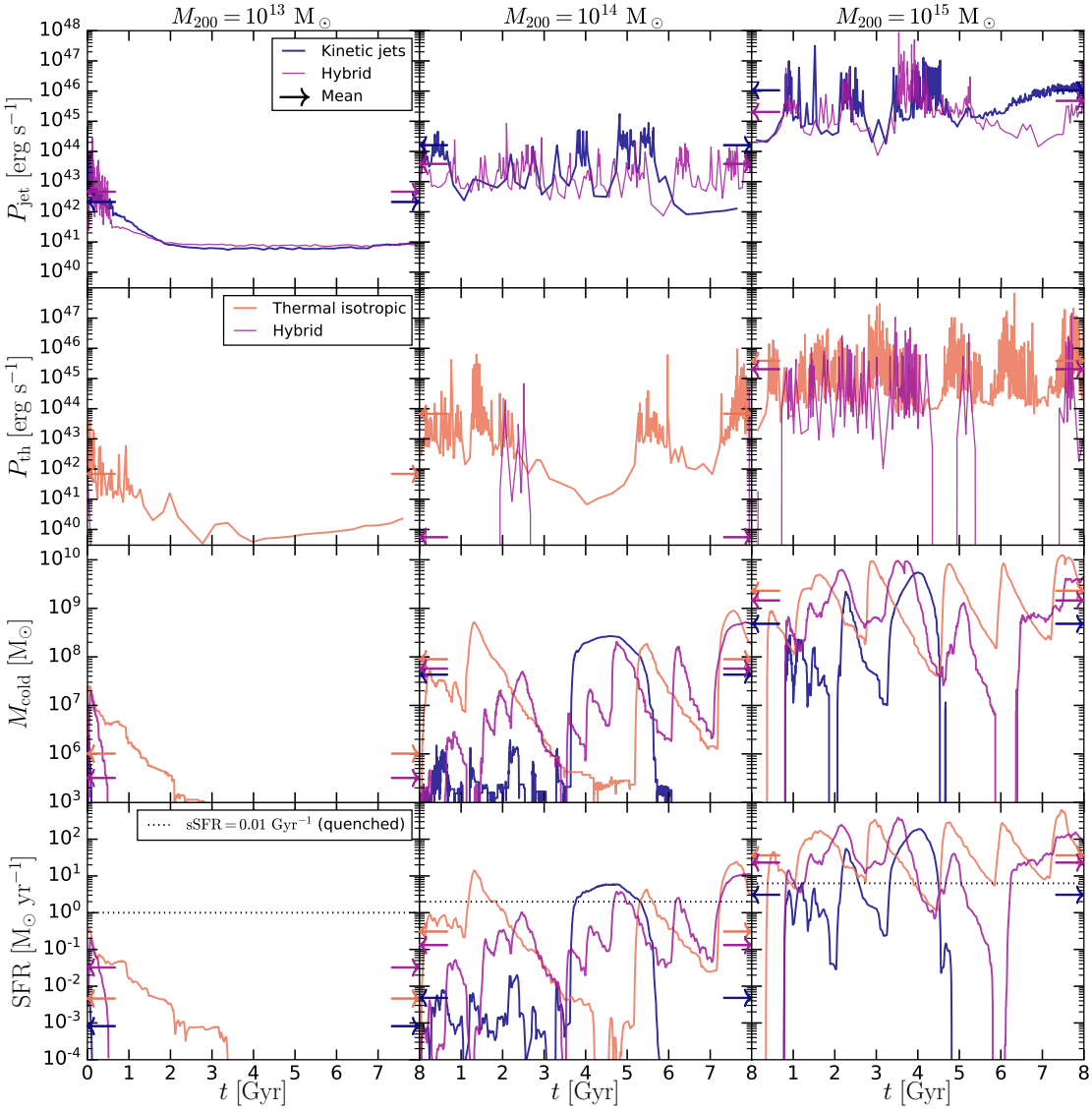

Figure 6.2: Comparison of the cooling and feedback cycle in simulations using the BH spin evolution model for our idealized galaxy group ($M_{200} = 10^{13}$ M$_\odot$), low-mass cluster ($M_{200} = 10^{14}$ M$_\odot$) and high-mass cluster ($M_{200} = 10^{15}$ M$_\odot$), from left to right. From top to bottom we show the kinetic jet power, the thermal heating power, the cold gas masses ($T < 2 \times 10^4$ K) and the star formation rates. The details of these simulations are given in § 6.2.2 and Table 6.1 (in terms of physical set-up and halo mass) as well as § 6.2.3 and Table 6.2 (in terms of the feedback implementation). The model uses the thin, radiatively-efficient accretion disc with thermal isotropic feedback (orange lines) and/or the thick, advection-dominated accretion disc with kinetic jet feedback (blue lines). The purple lines show cases with hybrid feedback, in which the feedback and accretion modes interchange at an Eddington ratio $f_{\rm Edd,crit} = 0.01$ (below this value kinetic jets are used, above it thermal isotropic feedback). The feedback powers are calculated using adaptive time bins such that during each bin, 10 feedback events (heating or kicking particles) occurred. The cold gas masses and star formation rates are calculated as moving averages in 5 Myr-wide bins. The arrows indicate averages over the 8 Gyr simulation run time.

so the total thermal isotropic efficiency is $\epsilon = \epsilon_{\rm f}\epsilon_{\rm r} \approx 0.006$. This value is around 5 times lower than the jet one, $\epsilon_{\rm j} \approx 0.025$, leading to a 5 times lower feedback power at late times (given similar accretion rates, see Fig. 6.3). The thermal isotropic power is also (on average) lower at all except very early times ($t > 100$ Myr). This indicates that these haloes go through a very similar thermodynamic state as the feedback is in the process of quenching them. In other words, the system is not self-regulated. Instead, any feedback mechanism is sufficient to quench the cooling flow in the centre very quickly, and any residual feedback is merely an 'after-effect'. While this is not easily visible from the plot, the thermal power is higher than the jet power at very early times. This could be either due to the lower feedback efficiency in that case or due to thermal isotropic feedback generally being less effective at quenching cooling flows than kinetic jets even with the same efficiency (as we show in § 6.4.2), so a stronger initial cooling flow develops. As a consequence, there is more cold gas in the centre of the halo (visible in the third row) at these times, feeding the BH more strongly. The feedback power is also more variable in that case as compared to the jet case. This difference is a result of isotropic feedback regularly blowing away clumps of cool gas from the centre of the halo, which eventually fall back and periodically feed the BH.

In the same two panels (top two left-hand ones) we show the feedback powers in a simulation with hybrid feedback and interchanging accretion modes. We find that there is only a small amount of thermal feedback in the very beginning in this simulation, with jets dominating at all other times (because the accretion rate in terms of the Eddington ratio is generally $f_{\rm Edd} < f_{\rm Edd,crit} = 0.01$; see Fig. 6.3). The jet power in this case is very similar to the jet-only case, although it appears to be more variable, possibly as a result of more cold gas being present (see third row).

We now turn to the more massive, galaxy cluster-size haloes ($M_{200} \geq 10^{14}$ M$_\odot$), which quickly become self-regulated. We begin with the low-mass cluster ($M_{200} = 10^{14}$ M$_\odot$), the results for which are shown in the top two middle panels of Fig. 6.2. In all cases we see multiple cycles of cooling and feedback. The peaks in the feedback powers do not occur at the same times for the different simulations, for two reasons: 1) the feedback implementation is inherently different and 2) these simulations are

chaotic (see Appendix A of Nobels et al. 2022). The feedback powers averaged over the 8 Gyr simulation run times, shown with arrows on the plot, are $P \approx 10^{44}$ erg s^{-1} in both the kinetic-only and thermal-only cases (slightly above that value for the former and slightly below it for the latter). The hybrid case again shows very little thermal feedback, except some activity at $t = 2 - 3$ Gyr. The mean jet power in this simulation is, however, roughly a factor of two lower than in the kinetic-only one.

Despite the overall similarity in the mean feedback powers between these three simulations, there are differences in their variability. The kinetic-only case has 3-7 distinct episodes of feedback (depending on how one counts them)[4] with some activity at all times except at the end of the simulation. The thermal-only one has 3-4 episodes (depending on whether the first bout of activity, between $t = 0$ Gyr and $t = 2$ Gyr, is considered as one or two episodes) with very clear quiescent periods at $t \approx 4$ Gyr and $t \approx 7$ Gyr. This difference is likely a result of jet feedback being able to react more quickly to the formation of a cooling flow, possibly due to the higher feedback efficiency (see § 2.4 and Fig. 6.3), which allows a cooling flow to be shut off before it becomes overly strong. In the hybrid case, jet feedback appears yet more variable. Instead of multiple coherent episodes being discernible in the variability of the jet power, we see relatively frequent variations around a jet power of $P \approx 3 \times 10^{43}$ erg s^{-1}. This difference is likely caused by the higher jet efficiency in this case, since in the jet-only mode the BH can be and does become spun down to very low BH spins (see Chapter 2, § 6.3.3 and Fig. 6.3).

We now move to our most massive galaxy cluster, with $M_{200} = 10^{15}$ $M_\odot$, the results for which are shown in the top two right-hand panels of Fig. 6.2. Similar to the low-mass cluster, the feedback powers show multiple cycles of activity, with the thermal-only case this time showing significant variability, while the jet-only case has a few distinct episodes of activity. From the hybrid case we see that that thermal

[4]The shape of the curves in these plots is dependent on how we calculate the feedback power and on the binning. However, episodes of activity can, regardless of how the power is calculated, be gleaned as features taking the form of a clear increase from the global minimum power, peak and subsequent decrease (with possible variability in between) to the minimum power. This is what we mean when we refer to feedback episodes.

feedback is often active. While it may appear that thermal isotropic and kinetic jet feedback are often active at the same time, this is merely a consequence of the feedback modes interchanging more frequently than our sampling of the feedback powers (which are in this case plotted using adaptive bin widths containing 10 feedback events), as well as other quantities (e.g. Eddington ratios shown in Fig. 6.3)

Comparing the jet powers in the jet-only and hybrid case, we find that they are overall similar (even in the positions of the peaks), but there is a difference towards the end of the simulations. The jet-only one has a jet power that increases towards $P_{\rm j} \approx 10^{46}$ erg s^{-1} by the end – this is a result of jet-induced spindown leading to a very low BH spin and therefore low jet efficiency, which in turn leads to a very high (unrealistically so) BH mass (see § 6.3.3 and Fig. 6.3). With such a high mass, the BH is able to launch strong jets by accreting from the hot gas halo, leaving the system fully quenched (see bottom panels). From the thermal power, we see that thermal feedback is active more often in this case than in the low-mass galaxy cluster. This is a result of the massive galaxy cluster having significant amounts of gas cooling and star formation, which is connected to the accretion rate of the BH, which is also higher (similar as in Chapter 5; see bottom panels and Fig. 6.3).

We can also compare the mean feedback powers in all of the simulations we have discussed thus far (see arrows in Fig. 6.2). We find that the kinetic jet power is higher than the thermal power in all cases. We interpret this as a result of a larger fraction of the energy related to jet feedback reaching larger radii (regions that do not 'need' to be heated, since they already have long cooling times) than in the thermal isotropic case, which generally has more central heating. A larger fraction of feedback energy coupling to larger radii thus leads to overall more energy needing to be injected to shut off the central cooling flows.

6.3.2 Impact of feedback on galaxy growth

We will now discuss quantities related to the BCGs and their growth in our simulations with BH spin evolution, which are shown in the bottom two panels of Fig. 6.2. These are the cold gas masses (defined as the total masses of all gas with $T < 2 \times 10^4$ K, at all radii) and SFRs. We consider galaxies as quenched if their specific SFR

(sSFR), i.e. the SFR divided by M_*, is below 0.01 Gyr^{-1} (e.g. Weinmann et al. 2006). We find that our results are largely insensitive to this exact choice. We calculate both the SFR and M_{cold} as moving averages in 5 Myr wide time bins.

We again begin with the left-hand panels, showing the results for the lowest-mass simulations ($M_{200} = 10^{13}$ $\mathrm{M}_\odot$). In the kinetic-only case, there is barely any cold gas and star formation, and then only at the very beginning (hardly discernible in the plot). The thermal-only and hybrid cases show a similar amount of cold gas ($M_{\mathrm{cold}} \approx 3 \times 10^7$ $\mathrm{M}_\odot$) and star formation (SFR = 0.1 $\mathrm{M}_\odot$ yr^{-1}) at the peak, although the hybrid case more quickly reaches a state of no cold gas being present and therefore no star formation. In all three cases, the system is considered quenched at all times.

We now move to the low-mass galaxy cluster case with $M_{200} = 10^{14}$ $\mathrm{M}_\odot$ (middle panels). The cold gas and SFR exhibit multiple episodes that generally coincide with the peaks in the feedback powers (see top rows). The cold gas mass has peak values close to $M_{\mathrm{cold}} = 10^9$ $\mathrm{M}_\odot$, with the peaks being slightly lower in the cases with jet feedback (see also the mean values, indicated on the plot with arrows). The SFR peaks at ≈ 10 $\mathrm{M}_\odot$ yr^{-1}, which is sufficient to consider the galaxies non-quenched at these rare times. The kinetic jet case exhibits very little cold gas or star formation at early times (before $t = 3.5$ Gyr). This indicates that hot halo accretion is sufficient to keep the halo quenched with this feedback mode for quite a long time. By $t = 3.5$ Gyr, a strong cooling flow develops, and it lasts ≈ 2 Gyr. During this time, the BH experiences a significant amount of growth. Since it was spun down to a very low value of the BH spin even earlier (see § 6.3.3 and Fig. 6.3), it means that the BH cannot quickly react to the development of a cooling flow. As a result, a strong cooling flow develops, to the degree that it results in feedback strong enough to heat the ICM at large radii, thus preventing any cooling flows from occurring in at least the next 2.5 Gyr (until the end of the simulation). The thermal isotropic case has the largest amounts of cold gas and star formation, and its first cooling flow develops in the very beginning of the simulation (whereas jet feedback, in both the jet-only and hybrid simulations, is able to delay the initial cooling flow). The hybrid case has a moderate amount of cool gas and star formation. The shape

of each peak is similar to the thermal-only case. Whereas the jet-only case has sharp declines in the cold gas mass and SFR after every peak, these two cases have gradual declines that can last up to 2 Gyr. We interpret this as possibly being due to thermal feedback blowing away clumps of cold gas, which thus take a longer time to be consumed through SF, and in the meantime they are not feeding the BH and producing feedback.

Finally, we discuss the massive galaxy cluster case ($M_{200} = 10^{15}$ $\mathrm{M}_\odot$). The cold gas mass reaches peaks of up to 10^{10} $\mathrm{M}_\odot$ in all three cases, with the SFR reaching several hundred $\mathrm{M}_\odot$ yr^{-1}. The hybrid case has only a mildly lower mean cold gas mass and SFR than the thermal-only case, since the operating feedback mode is quite often thermal (Fig. 6.2). The jet-only simulation has an appreciably lower cold gas masses and SFR, and is fully quenched at around $t = 4.5$ Gyr.

In Appendix 6.B we discuss whether BH growth and feedback interferes with star formation directly or indirectly. We probe this by considering the ratio $M_\mathrm{i}/M_{*,\mathrm{formed}}$ as a function of time, where M_i is the total mass accreted, launched into the jets or heated by the BH, and $M_{*,\mathrm{formed}}$ is the total mass of all stars formed. We find that this ratio is often comparable to or larger than unity, suggesting that BH growth and feedback do indeed directly interfere with star formation in our simulations, by depriving it of its fuel (cold gas) through direct processes (algorithmically choosing it to be heated or kicked), rather than, for example, through entrainment.

The implications of this finding for realistic, cosmological simulations may not be problematic for BH accretion, as long as we assume that BH growth is not excessive in these simulations. However, the high mass flux of particles associated with feedback may be more problematic, especially since these fluxes are also typically higher than those associated with BH accretion. The rate at which the BH is heating or kicking gas particles depends not only on the feedback powers, but also on the heating temperature ΔT and jet velocity v_j. Both of these parameters are at least partially numerical in nature. Decreasing their values (at a fixed feedback power) increases the mass flux of particles being heated/kicked. If too low values are chosen, the mass flux of particles associated with feedback may be close in magnitude to the SFR, which we sometimes find to be the case in our simulations. One

would ideally want to avoid this situation, and ensure that the mass flux of particles being heated/kicked is always much smaller than the rate at which the gas is being converted into stars. In practice, this limit may be hard to avoid, at least at low resolutions, since decreasing the mass flux of the particles being heated/kicked also decreases how well sampled the feedback is, which then means that feedback is resolved more poorly. We do not propose a particular solution here, but merely point out that the mass flux in question is probably quite large (close to the SFR) in most implementations of AGN feedback in cosmological simulations.

6.3.3 Evolution of black hole properties

In Fig. 6.3 we show the evolution of various BH-related properties, including from top to bottom the BH mass (both the subgrid and the dynamical mass, which are the same in this case), Eddington-normalised mass accretion rate, the BH spin magnitude, the angle between the BH spin vector and the z-axis, and finally the jet and radiative efficiencies. We discuss each of these quantities in turn.

The BH mass (first row of Fig. 6.3) remains unchanged in the galaxy group case, whereas in the galaxy cluster cases, there is always some appreciable growth. The low-mass cluster exhibits BH growth by more than a factor of ten in the kinetic-only case, partly as a result of low efficiencies (due to jet-induced spindown). The thermal-only and hybrid cases show much less growth – about a factor of two for both cases. The results are similar for the high-mass galaxy cluster, but these simulations show even more growth. The kinetic-only one shows BH growth beyond $M_{\rm BH} = 10^{11}$ $\rm M_{\odot}$ by $t = 2.5$ Gyr (the final BH mass reached in this simulation, which we do not show here, is $\approx 5 \times 10^{11}$ $\rm M_{\odot}$, which highlights the unrealistic nature of using the jet mode in isolation, at least with the strong jet spindown rates we have assumed). The other two cases both show growth by a factor of 5-10, with the hybrid one, interestingly, showing the least amount of growth (which may be interpreted as the hybrid feedback being most effective at self-regulation of BH growth).

The Eddington-normalized accretion rates (second row of Fig. 6.3) peak near $f_{\rm Edd,crit} = 0.01$ for all three galaxy group simulations. They also all reach $f_{\rm Edd} = 10^{-5}$ by the end, although the thermal-only case takes the longest time to reach that value.

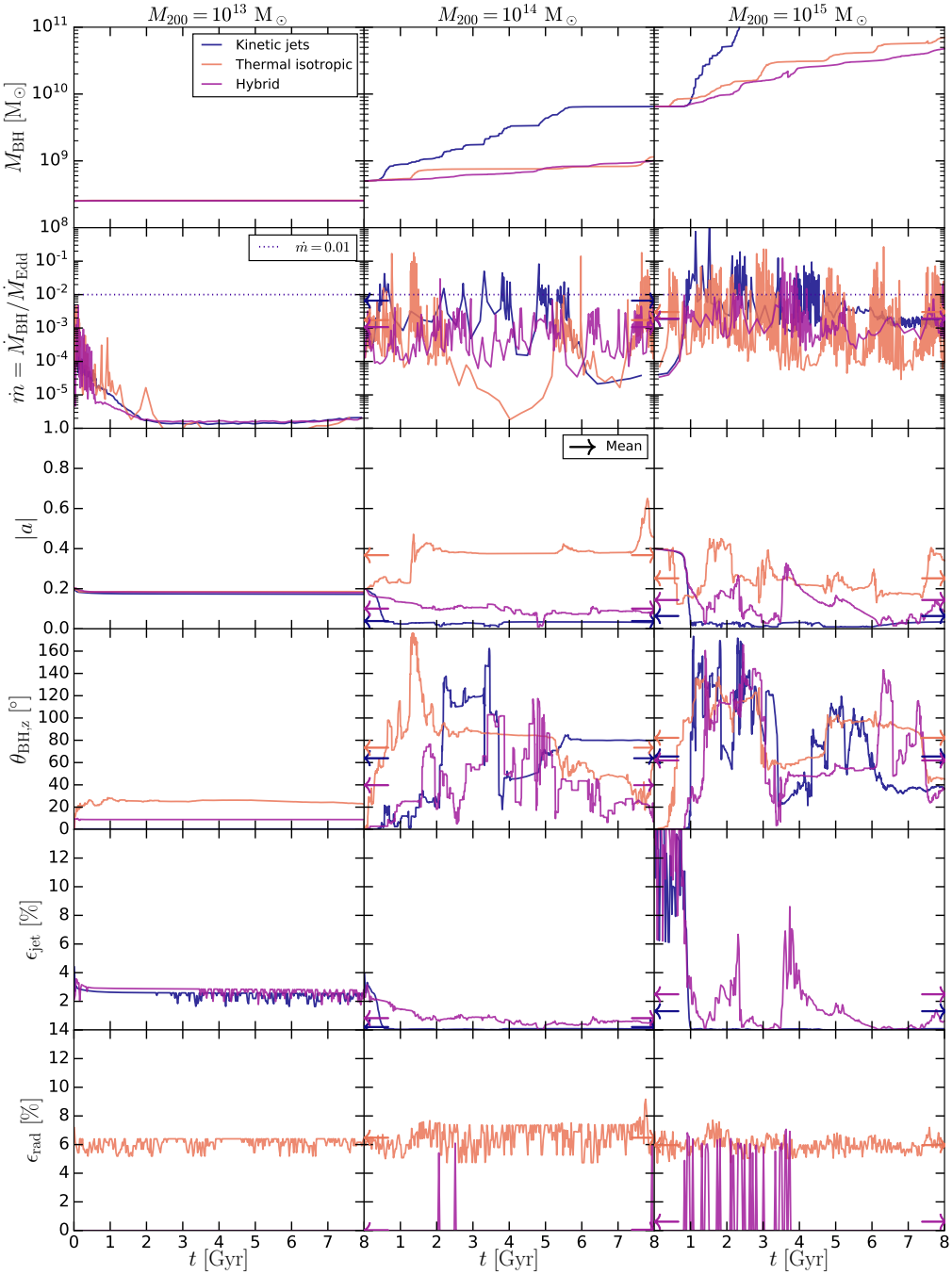

Figure 6.3: The properties of the BHs and their evolution in simulations using the BH spin evolution model. From top to bottom, we show the BH masses, the Eddington fractions, the BH spin magnitudes, the angles between the BH spin vectors and the $z-$axis, and the jet and radiative efficiencies. All quantities except the feedback efficiencies are sampled every 5 Myr. The feedback efficiencies are sampled every 1 Myr and then a moving average in a 5 Myr-wide bin is calculated using only times when the BH is in the appropriate accretion state (the thick disc for the jet efficiency and the thin disc for the radiative efficiency), and they are weighted by the accretion rate. The arrows indicate averages over the 8 Gyr simulation run time. Everything else is the same as in Fig. 6.2.

The two higher-mass cases show much more variability in the accretion rate, with it often peaking above $f_{\rm Edd,crit}$ (which is why the hybrid cases have the feedback modes often interchanging). Interestingly, the hybrid simulations do not feature high values of the accretion rate (e.g. $f_{\rm Edd} = 0.1$ or approaching $f_{\rm Edd} = 1$) as often as the two other simulations, which again may be related to more effective self-regulation.

From the evolution of the Eddington ratios, it is clear that BHs sometimes have an accretion rate high enough for the accretion mode to correspond to the thin disc, instead of the thick disc, and feedback to be thermal isotropic ($f_{\rm Edd} > f_{\rm Edd,crit} = 0.01$), at least in the galaxy cluster cases ($M_{200} \geq 10^{14}$ M$_\odot$). However, it is not clear from these plots how much growth actually occurs in which accretion regime. While the Eddington ratio appears to be $f_{\rm Edd} < 0.01$ most of the time for all 9 simulations shown in Fig. 6.3, it is possible for most of the growth to occur at $f_{\rm Edd} > 0.01$ due to the accretion rates being higher.

In Appendix 6.C we discuss the cumulative mass fractions of growth that occur at low versus high Eddington ratios. We find that neither regime is negligible in terms of growth. Perhaps surprisingly, we find that most growth occurs when $f_{\rm Edd} > 0.01$ in the galaxy cluster cases, despite the accretion rate satisfying $f_{\rm Edd} < 0.01$ most of the time. This implies that radiatively-efficient accretion and its associated 'quasar feedback' should not be ignored for galaxy clusters (at least not CC ones), despite its rarity. This finding is likely a consequence of cooling flows becoming progressively stronger for more massive clusters. The picture of 'maintenance-mode' feedback (by relativistic jets) that keeps BCGs quenched is thus probably an oversimplification for relatively CC clusters, such as the ones we are simulating here. This is in agreement with the analysis of a wide range of observations done by McDonald et al. (2018), who found that the systems with the largest cooling flows (and star formation rates) tend to have the highest star formation efficiencies, which could be explained by the central BH more often being in the radiative versus mechanical feedback mode (the former of which is less efficient as a feedback mechanism, as we have found already in this section, and which we also confirm more robustly in § 6.4).

The BH spin magnitude (third row of Fig. 6.3) exhibits very little evolution in the galaxy group case (except a small amount of spindown at the very beginning),

which is a direct result of little-to-no BH mass growth. In the other two cases there is significant BH spin evolution. The low-mass cluster shows spindown in the kinetic-only simulation (down to values $|a| < 0.05$, as a result of using a GRMHD spindown formula, see § 2), as well as in the hybrid one, where larger values of the BH spin are reached (although still very low ones, $|a| \approx 0.05 - 0.1$). The thermal-only case instead shows occasional spin-up to values around $|a| = 0.4$. In the massive galaxy cluster case, all three simulations have a median BH spin that is below the initial value ($a_0 = 0.4$). The kinetic-only one behaves similar to the low-mass cluster case, although the mean BH spin is even lower. The hybrid one has the BH spin varying between $a = 0$ and $a = 0.3$ – higher values are achieved than in the low-mass cluster case due to more spinup, as the BH spends more time in the thin disc regime due to high accretion rates. The thermal-only case, on the other hand, shows a lower mean BH spin than in the low-mass cluster simulation. This could be due to the cold gas being more chaotic in terms of its angular momentum (or due to the high-mass simulation having poorer resolution), which would lead to more frequent retrograde accretion of the BH, and therefore more frequent spindown.

The angle between the BH spin vector and the z-axis (fourth row of Fig. 6.3) contains information on how much redirection the BH spin vector has experienced. In the galaxy group case, there is some redirection that occurs in the very beginning of both the thermal-only and hybrid simulations. In the two higher-mass cases, there is much more redirection – these plots highlight the chaotic nature of the angular momentum of the accreting gas in these simulations. Our results are in qualitative agreement with the 'chaotic cold accretion' (CCA) scenario presented by Gaspari et al. (2013). This is despite the fact that we use Bondi accretion, which is often portrayed as being mutually exclusive with CCA. We argue instead that a version of CCA naturally emerges if cold gas is included in the Bondi formula (instead of restricting it to hot, X-ray emitting gas). This mixed approach can reproduce the main features of CCA, including the chaotic nature of the cold gas that is accreting onto the BH and the boosting of the BH accretion rate (relative to the Bondi rate inferred from hot gas).

In the final two rows of Fig. 6.3 we show the feedback efficiencies in these simu-

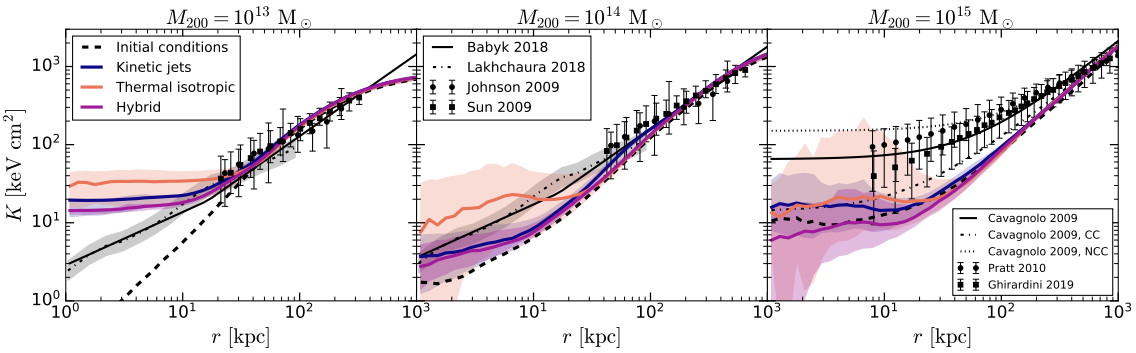

Figure 6.4: The radial gas entropy profiles (volume-weighted) of the ICM using the BH spin evolution model, from the same set of simulations as in Figs. 6.2 and 6.3. The solid lines show medians calculated using 160 snapshots between $t = 0$ and $t = 8$ Gyr, while the shadings indicate the $16^{\rm th} - 84^{\rm th}$ percentile ranges. The profiles in the initial conditions are shown with the dashed lines. The observational data sets are described in § 6.2.4. The profiles from Johnson et al. (2009) and Sun et al. (2009) are converted from their dimensionless form to physical form for the two left-hand panels separately, which is why these data differ in the two panels. The sample from Cavagnolo et al. (2009) is split onto cool-core (CC) and non-cool-core (NCC) clusters.

lations. These are calculated as moving averages over 5 Myr wide bins, but we only include times when the BH is in the appropriate accretion state (the thick disc for the jet efficiency and the thin disc for the radiative efficiency), and they are also weighted by the accretion rate at every time-step. In the galaxy group case, the efficiencies show some variability–this can occur despite the magnitude of the BH spin not evolving because the feedback efficiencies also depend on the sign of the BH spin, which itself depends on the angular momentum direction of the gas in the BH smoothing kernel. The jet efficiency quickly drops to per cent-level values for the kinetic-only case in both galaxy cluster simulations. In the hybrid cases, the jet efficiencies depend highly on the current BH spin; in the low-mass case it is below 2 per cent, while in the high-mass case it sometimes grows to several per cent. The radiative efficiency in the thermal-only simulations is in all cases between 4 and 8 per cent. This lack of strong variability is a result of the radiative efficiency being weakly dependent on BH spin, except at $a > 0.9$.

6.3.4 Entropy profiles

We now turn to the entropy profiles in these simulations, which are shown in Fig. 6.4. These profiles are compared to the observed ones, which are described in § 6.2.4. We do not expect the simulated profiles to agree perfectly with the observed ones, for several reasons. Firstly, our simulations represent only single realizations in terms of how CC they are, i.e. we could vary the initial central ICM temperature parameter T_0 to obtain different profiles. We chose low values (relatively CC systems) for reasons laid out in § 6.2.2. Secondly, real clusters undergo merging activity, which is not included in our idealized simulations. Thirdly, observed profiles are deprojected given some assumed model. Fourthly, the profiles are not volume-weighted, but X-ray emission-weighted. Finally, for the galaxy group and low-mass cluster simulations, the observed profiles we are comparing these simulations with span the mass range $M_{200} = 10^{13}$-10^{14} $\mathrm{M}_{\odot}$, i.e. they are centred on a median halo mass of $M_{200} \approx 10^{13.5}$ $\mathrm{M}_{\odot}$. Additional shortcomings of these observations (in the context of applying them here for purposes of comparison) are discussed in § 6.2.4. For these reasons, care should be taken when comparing the galaxy group ($M_{200} \approx 10^{13}$ $\mathrm{M}_{\odot}$) and low-mass cluster ($M_{200} \approx 10^{14}$ $\mathrm{M}_{\odot}$) simulations with these observations (the observed profiles shown in the left-hand and middle panels of Fig. 6.4 are the same). Furthermore, this sample of observed galaxies does not only include centrals, but also satellites. Given these considerations, we use the observed profiles as a baseline to compare the shapes of the profiles (and their differences between models), rather than seeking full agreement.

Before discussing the cases individually (and comparing with the observed profiles), we first comment on some common features seen in all three cases. From Fig. 6.4 we see that the hybrid simulations have the lowest central entropy, even lower than the kinetic-only simulations. This is potentially caused by a combination of two effects whose impacts on the central entropy are opposite. Firstly, jets are able to heat the halo at larger distances than thermal isotropic feedback, and they deposit less of their energy in the very central regions (see also Fig. 6.6). This means that the cores in simulations with jets should be cooler. Secondly, the haloes are more effectively quenched by jets than by thermal isotropic feedback, which means

that the central ICM undergoes strong cooling flows less frequently, or they are weaker and/or shorter-lived. This in turn means that the central entropy should, on average, be higher if jets are used. When comparing our kinetic-only and thermal-only simulations, it appears that the first of these two effects dominates, at least for the two lower-mass cases. Allowing the two feedback modes to interchange, as in the hybrid simulations, leads to the lowest central entropies for all three halo masses since these simulations exhibit both strong cooling flows and less central heating. Another common feature between all three feedback cases is the difference in scatter. The thermal-only simulations show the largest scatter because they have both central ICM heating and strong cooling flows, whereas the opposite is true for the kinetic-only simulations. The hybrid ones have an intermediate amount of scatter.

For the galaxy group case, shown in the left-hand panel of Fig. 6.4, all three simulations (with differing feedback implementations) fail to reproduce the shape (slope) of the observed entropy profiles within 10 kpc, but agree with them at larger distances (by construction). Within 10 kpc, the observed profiles behave as $K \propto r^{2/3}$, whereas our simulated entropy profiles all have cores. This is unlikely to be affected strongly by the T_0 parameter (Nobels et al. 2022, Chapter 5). Instead we interpret this disagreement as showing that lower jet velocities may need to be used (the velocity used for these simulations was $v_\mathrm{j} = 5 \times 10^3$ km s^{-1}). As we show in Fig. 6.9, lower velocities lead to lower central entropies and more sloped profiles. Alternatively, as already explained, it is possible (if not likely) that the observations used for comparison here are biased towards brighter groups that therefore have lower central entropies. If the satellites were removed from the observational samples, it is likely that the disagreement would be worse, since satellites are less likely to be undergoing cooling flows, due to stripping of their CGM.

For the low-mass cluster simulations (middle panel of Fig. 6.4), we again find agreement with the observed profiles at large distances (in this case $r > 50$ kpc). In the central regions, the thermal-only case appears to have the correct slope at small distances ($r < 10$ kpc), but it has a flat section extending from $r = 10$ kpc to $r = 30$ kpc – a feature not visible in the observed entropy profiles. Our kinetic-only and hybrid simulations show similar slopes as the observed profiles, with perhaps a

slightly too shallow slope in the very centre. This could be mitigated by a different choice of T_0 or a slightly lower jet velocity.

Finally, we move to the high-mass galaxy cluster case, shown in the right-hand panel of Fig. 6.4. In the inner regions, all of our entropy profiles are lower than those in observations of Pratt et al. (2010), Cavagnolo et al. (2009) and Ghirardini et al. (2019) (although this could have been prevented by choosing a higher T_0, but we instead chose a highly CC setup to maximize differences between the AGN feedback implementations). They also show a central entropy core, but signs of such a core appear to be present in observations as well. All three of the simulations are consistent with being CC at most times (in agreement with the CC sample of Cavagnolo et al. 2009, as well as with the lower end of the scatter from Pratt et al. 2010 and Ghirardini et al. 2019). Out of the three simulations, only the thermal feedback case sometimes has a central entropy approaching the median entropy of the NCC sample from Cavagnolo et al. (2009). However, NCC clusters may also be explained as a result of mergers (e.g. Poole et al. 2008, Hudson et al. 2010).

We note that changing the implementation of AGN feedback is not the only way of affecting simulated entropy profiles (e.g. Altamura et al. 2023). The details of the hydrodynamics scheme appear to be at least as important (e.g. Borrow et al. 2022, Altamura et al. 2023). In particular, turning off artificial conduction in the SPH solver appears to lead to significantly more sloped entropy profiles.

Entropy profiles are often compared in a rescaled form, such that instead of plotting K versus r, one plots K/K_{500} versus r/r_{500}, where K_{500} is a typical entropy that depends only on the halo mass. We discuss such profiles in Appendix 6.D. We find that they are fairly similar between the different simulated haloes, and all of them lie below the median observed entropies, likely because we simulate relatively CC systems.

6.4 Results II: simplified feedback

In the previous section we presented results of our model with BH spin evolution, for both thermal isotropic and kinetic jet feedback. Here we will simplify our im-

plementation by instead fixing the efficiencies, as well as the direction for the jets (along the $z-$axis). In Appendix 6.A we show that the latter is justified as long as jet redirection occurs less frequently than ≈ 1000 Myr, and if jets precess with small opening angles ($\leq 15°$) and long time-scales ($\Delta t \geq 20$ Myr). The typical redirection time-scale, if redirection is allowed, is indeed typically longer than this (see the hybrid feedback cases in Fig. 6.3), since it occurs only a few times during an 8 Gyr long simulation (if we define 'redirection' as a change in direction that is larger than a few dozen degrees).

These simplifications are motivated by a desire to isolate the effects of varying efficiencies, as well as to make the simulations with different feedback implementations as similar as possible. To this end we fix the efficiencies to a value $\epsilon = 0.01$ for both the thermal isotropic and kinetic jet feedback. We do not test hybrid cases in these simplified simulations, and instead assume the feedback to be either thermal isotropic or kinetic jets regardless of accretion rate. We test the case where the feedback energies per heating/kicking event are the same for thermal isotropic and kinetic jet feedback, but this is not our fiducial choice. We instead typically use much higher jet velocities, since they are required in order to lead to inflation of lobes that turn into bubbles and create cavities in X-ray emitting gas, as seen in observations. We present results for the low- and high-mass galaxy clusters here ($M_{200} = 10^{14}$ M$_\odot$ and $M_{200} = 10^{15}$ M$_\odot$, respectively). We then vary the feedback efficiency, heating/kicking energy and energy type (thermal versus kinetic, as well as mixed) for both isotropic and jet feedback. These variations are intended to show the effects of choosing a particular implementation of feedback. For simplicity we vary these only for the low-mass galaxy cluster.

6.4.1 General results

In Fig. 6.5 we show the feedback powers and SFRs in the galaxy cluster simulations with the simplified feedback prescriptions. We find that the thermal isotropic simulations are quite similar to those presented in § 6.3, i.e. with BH spin evolution. This is likely due to the radiative efficiencies being near-constant in the case with BH spin evolution (Fig. 6.3). The kinetic jet simulations (with fiducial jet velocities,

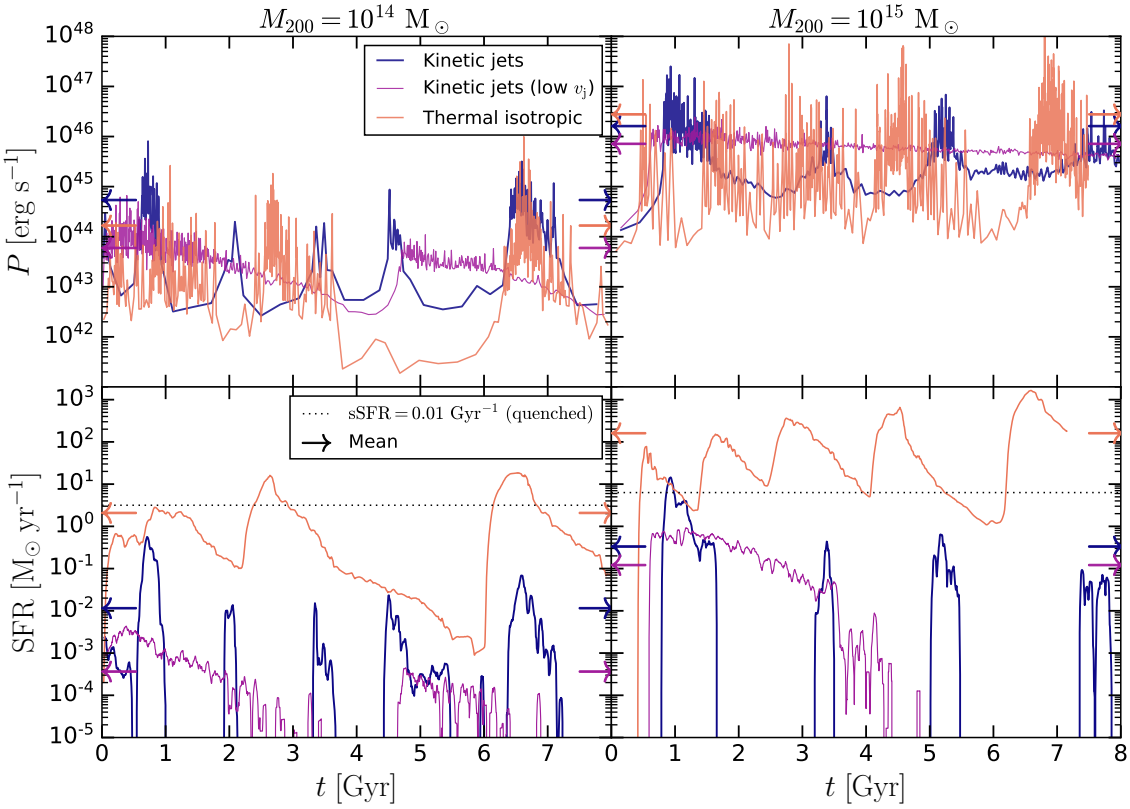

Figure 6.5: The feedback cycle for our simulations with fixed feedback efficiencies (as well as fixed jet directions in the jet feedback case, where they are launched in the $z-$direction). The left-hand panels show results for the low-mass galaxy cluster case ($M_{200} = 10^{14}$ M$_\odot$), while the right-hand ones show the results for the high-mass galaxy cluster ($M_{200} = 10^{15}$ M$_\odot$). In the top panels we show the feedback powers, while the bottom panels show the SFRs. For the jet case, we perform fiducial simulations that have velocities high enough to lead to the inflation of hot lobes of gas (blue lines), as well as lower-velocity ones (purple lines) that instead have an equal energy per kicking event as the thermal isotropic simulations (orange lines). The feedback powers are calculated using adaptive time bins such that during each bin, 10 feedback events (heating or kicking particles) occurred, while the star formation rates are calculated as moving averages using 5 Myr-wide bins. The arrows indicate averages over the 8 Gyr simulation run time. Further details of the simulations are given in § 6.2.3 and Table 6.3.

1.5×10^4 km s^{-1} and 3×10^4 km s^{-1} for the two halo masses) are somewhat different from the BH spin evolution case. This is largely due to the jet efficiency not dropping below 1 per cent (unlike in the BH spin evolution case; Fig. 6.3), which means that very strong cooling and BH growth are prevented. As in Chapter 5, we find that fixing the jet direction to be along the $z-$axis does not prevent efficient feedback.

Comparing the thermal isotropic and kinetic jet simulations, we find that the former reach lower minima of the feedback power, despite the fact that the same constant efficiency is used. This means that the BH reaches lower accretion rates in the thermal isotropic case (same as in the cases with BH spin evolution, see Fig. 6.3). This is caused by the thermal feedback simulations often featuring a significant presence of hot gas near the BH (originating from the feedback itself), which reduces its accretion rate. We find that using a constant efficiency leads to periodicity between cooling flow episodes, which seems more pronounced in the high-velocity jet cases. In these cases, we see periods of ≈ 1.5 Gyr in the low-mass cluster and ≈ 2 Gyr in the high-mass cluster. This periodicity occurs because AGN feedback effectively heats all gas out to a radius at which the ratio of the cooling time, $t_{\rm cool}$, and the dynamical time, $t_{\rm dyn}$, is $t_{\rm cool}/t_{\rm dyn} \approx 10$. The period between cooling flows is then roughly equal to the cooling time at that radius. These findings are illustrated in Appendix 6.E and are supported by previous works (e.g. Nobels et al. 2022, see also discussion therein).

In Fig. 6.5 we also show the results of using low jet velocities (6.5×10^3 km s^{-1} and 1.15×10^4 km s^{-1} for the low-mass and high-mass cluster, respectively), which are supersonic by only a factor of a few relative to the ICM. These velocities are chosen such that the energy per kicking event is equal to the heating energies used in the corresponding thermal isotropic simulations ($\Delta T = 10^9$ K and $\Delta T = 10^{9.5}$ K for the low-mass and high-mass cluster, respectively). We find that such low velocities lead to the period between cooling flow episodes increasing (to the point that the high-mass cluster shows no periodicity in this case, at least within 8 Gyr), and the SFR reaching smaller peaks, as well as being lower on average.

In Fig. 6.6 we show radial profiles of the ICM density, temperature and entropy

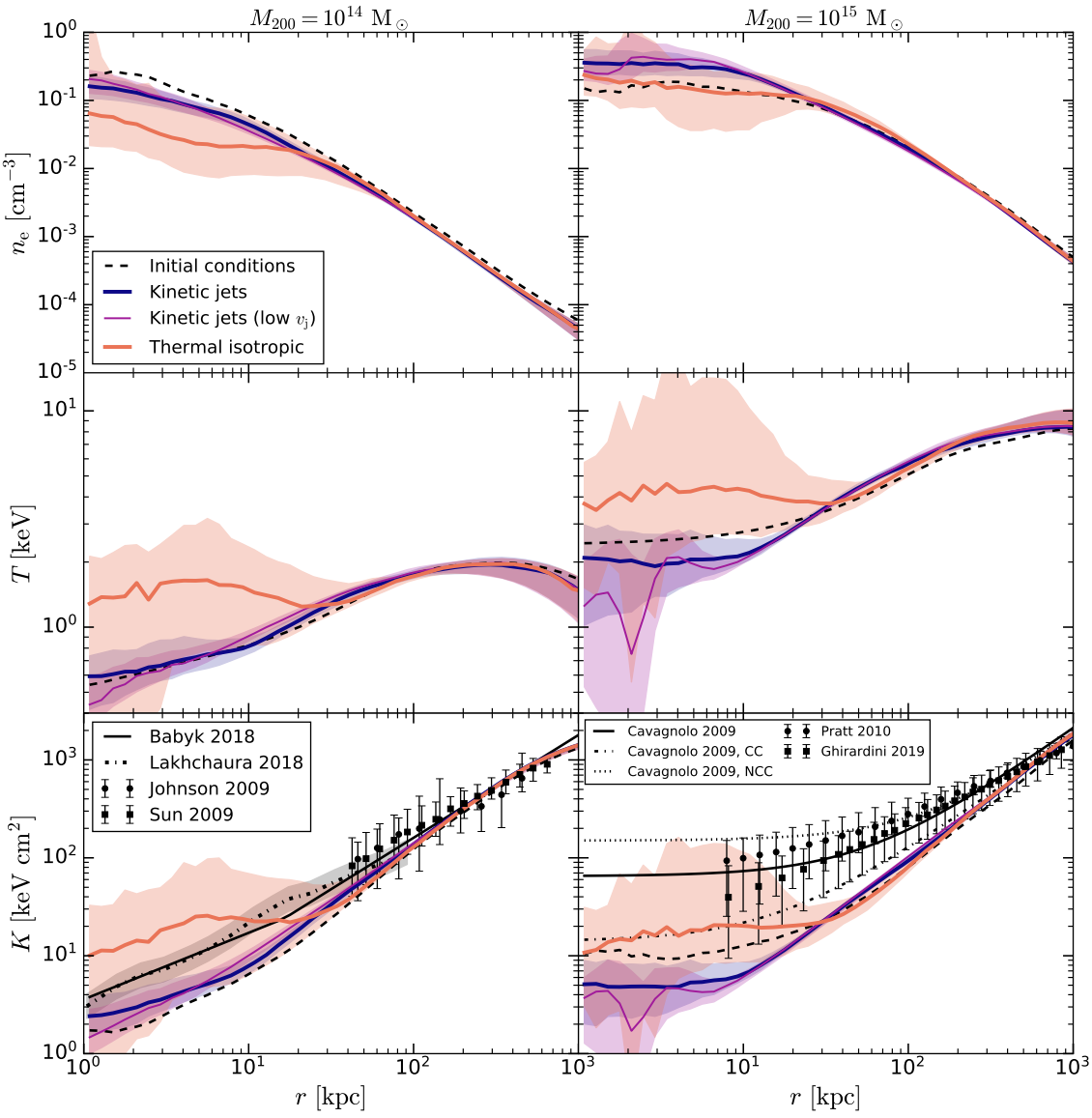

Figure 6.6: Radial gas profiles (volume-weighted) of the ICM for the same set of simulations as shown in Fig. 6.5. From top to bottom we show the electron number density, the temperature and the entropy. The solid lines are medians calculated using 160 snapshots between $t = 0$ and $t = 8$ Gyr, while the shadings indicate the $16^{\text{th}} - 84^{\text{th}}$ percentile ranges. The profiles in the initial conditions are shown with dashed lines. The observational data sets are described in § 6.2.4. The sample from Cavagnolo et al. (2009) is split onto cool-core (CC) and non-cool-core (NCC) clusters.

for these same simulations. From the top panels we see that using jets leads to higher central densities (within $20 - 40$ kpc), by a factor of a few. There is only a small difference between the fiducial and low-velocity jet cases. In the middle panels we compare the temperatures. The jet cases have lower central temperatures (within the same radii as for the densities) than the thermal isotropic ones, by up to a factor of two. At intermediate radii (up to $r = 100$ kpc), the jet cases have higher temperatures, indicating that more of the feedback energy couples to larger radii in the jet cases. In the bottom panels we compare the entropy profiles. Due to a combination of higher central densities and lower central temperatures, the central entropies in the jet cases are lower by a factor of ≈ 5 and ≈ 2 for the two halo masses, respectively. In the low-mass case, the low-velocity simulation appears to have the same slope as the observed profiles, which are also shown in the figure. This potentially indicates that lower velocities should be used (rather than highly supersonic ones with Mach numbers ≥ 10, which we find to be required for the inflation of hot lobes and for X-ray cavities to be present), at least in these lower-mass systems. For the high-mass case, we again find that using thermal isotropic or kinetic jet feedback leads to similarly-shaped profiles as the observed ones (the same conclusion as found from Fig. 6.4, showing the BH spin evolution case). The entropies are visibly higher for jet feedback at $r = 30-100$ kpc and $r = 40-300$ kpc in the two mass cases, respectively. This supports the interpretation that kinetic jets are able to heat at larger radii than thermal isotropic feedback. In all of the presented profiles we see less scatter in the kinetic jet cases than with thermal isotropic feedback – this is a result of fewer or weaker cooling flows, and less violent central heating. The thermal isotropic form of feedback leads to very similar results in terms of the entropy profiles as the cases with BH spin evolution (Fig. 6.4). This is likely due to very similar feedback efficiencies (Fig. 6.3), although as we show in the next section, the entropy profiles are also largely insensitive to a much larger variation of the efficiency.

6.4.2 Varying the implementation of feedback

Visual differences

We now turn to variations on the cases presented above. We vary the efficiencies of both types of feedback (isotropic and jet), energy per each feedback event and the type of energy used for feedback – thermal[5], mixed or kinetic. We performed all of these for the low-mass galaxy cluster ($M_{200} = 10^{14}$ M$_\odot$).

In Fig. 6.7 we show visualizations of some of these simulations. In particular, we show jets with different energy types and velocities (top row, left- and right-hand sides, respectively), and the same for isotropic feedback (bottom row, with the latter variation corresponding to the heating temperature). These are shown on the same spatial scales for purposes of comparison, but we find that isotropic feedback is generally more confined to the central regions than jet feedback. We also note that these visualizations are generally *not* shown for the same simulation time. Doing so would result in very little visible activity in some of the cases, since all of these simulations peak in feedback activity at different times. We have therefore attempted to show these visualizations at representative times for each of the cases.

We begin our comparison of different types of feedback with variations of energy type for jet feedback (left-hand side of the top row in Fig. 6.7). Kinetic jets inflate well-defined ellipsoidal lobes, and they also create strong bow shocks. Using mixed jets also leads to fairly symmetrical lobes that create bow shocks, although they appear to be weaker (judging by the typical temperature in the shock fronts). Thermal jets do lead to biconical outflows, but these are asymmetrical since they are much more susceptible to perturbations. Relatively weak shocks are visible in this case.

In the right-hand side of the top row of Fig. 6.7 we show variations of the jet velocity in the kinetic jet case. The lowest-velocity case ($v_\mathrm{j} \approx 8500$ km s^{-1}) does not appear to feature hot, ellipsoidal lobes. Instead, the outflows resemble Fanaroff

[5]In the thermal jet variant, particles are preferentially heated along a particular direction (the $z-$axis in this case). No kinetic energy is imparted to the gas, but it can still form outflows in the form of jets.

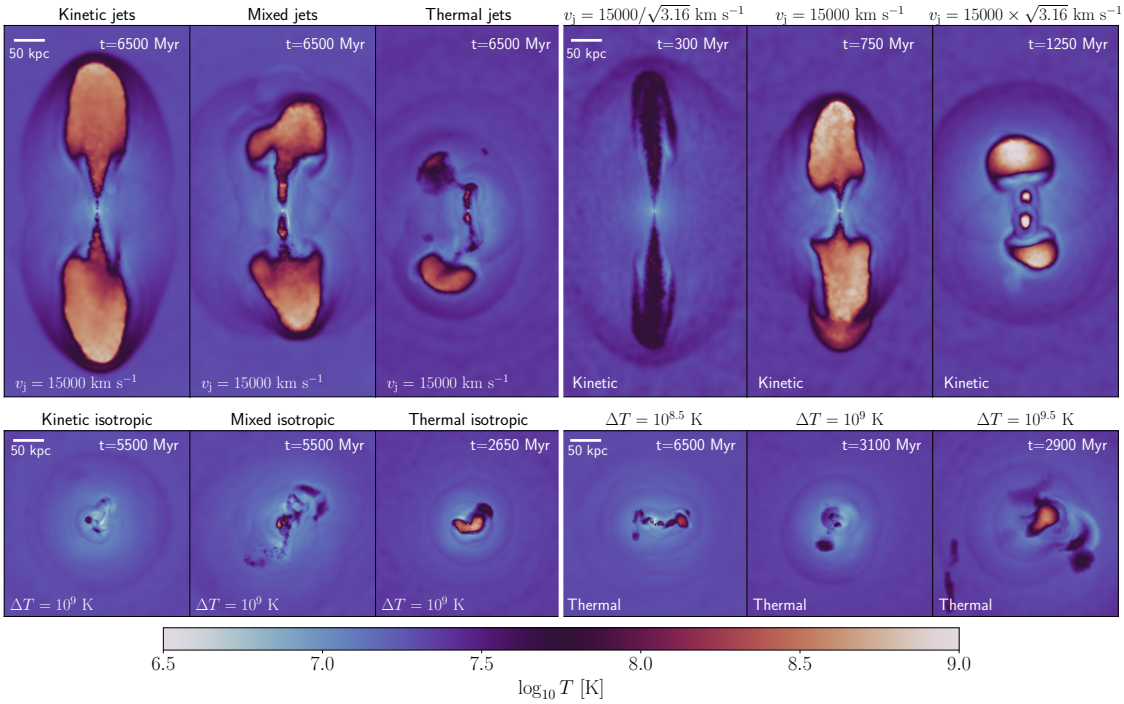

Figure 6.7: A mosaic of different jet (top row) and isotropic (bottom row) feedback simulations with varying feedback parameters, for the low-mass galaxy cluster ($M_{200} = 10^{14}$ M$_\odot$). The colours indicate the gas temperature, as shown by the colour bar, and we include all gas in a 50 kpc-deep slice. The panels all show the same spatial scales. The simulation times shown here are generally different since the timing of the feedback activity is highly chaotic. For both the jets and isotropic feedback we vary: 1) the fraction of energy injected as thermal as opposed to kinetic (values of 0, 0.5 and 1), shown on the left-hand side, and 2) the energy increment received by the particles (by factors of $\sqrt{10} \approx 3.16$), shown on the right-hand side. The variations of the jet energy type use a jet velocity of 1.5×10^4 km s^{-1} (or its corresponding heating temperature if feedback is mixed or purely thermal), while the corresponding isotropic variations use a corresponding temperature increase of $\Delta T = 10^9$ K. The variations of the energetics are done for kinetic feedback in the jet case and thermal feedback in the isotropic case.

& Riley (1974) type I (conical) jets. Increasing the jet velocity leads to the inflation of lobes and stronger generation of spherical shocks, and this activity tends to be concentrated to smaller radii. The highest-velocity case shows lobes that appear similar to observed X-ray cavities, although we caution that this may be merely a consequence of low resolution (increasing the jet velocity at fixed power decreases the number of jet particles inside the lobes/bubbles, making them more spherical).

In the left-hand side of the bottom row of Fig. 6.7 we show results of varying the type of energy in the isotropic case. Using less kinetic energy leads to weaker spherical shocks, but typically hotter outflows. In the last row of Fig. 6.7 we show the results of varying the heating temperature in the thermal isotropic case. These simulations all appear similar, and we do not find that increasing the heating temperature leads to hotter outflows, as one might have expected. From the visualizations shown here, it is also apparent that thermal isotropic feedback can sometimes lead to the emergence of biconical outflows – this is typically a result of a cold gas disc forming in the centre and feeding the BH. The feedback then results in the launching of biconical outflows that are perpendicular to the disc (see also Nobels et al. 2022), since the heated gas tends to expand along the 'path of least resistance'.

Differences in feedback powers and SFRs

In Fig. 6.8 we show the feedback power and SFR for all of the cases discussed above, as well as cases with varying feedback efficiency. We begin by discussing the jet cases (left-hand column), and then the isotropic ones (right-hand column). We find that varying the type of jet energy (top-left panel) does not lead to very large differences in the jet powers. The mean jet power does increase slightly, however, by making it more kinetic rather than thermal. In addition, thermal jets lead to lower minima in the jet power, similar as in the thermal isotropic case, due to the gas near the BH often being hotter (which leads to lower accretion rates). From the SFR plot we see that kinetic jets are the most efficient at quenching, with the purely thermal ones quite similar to isotropic feedback (discussed below), and the mixed ones somewhere in between.

In the middle-left panel of Fig. 6.8 we show results of varying the jet velocity

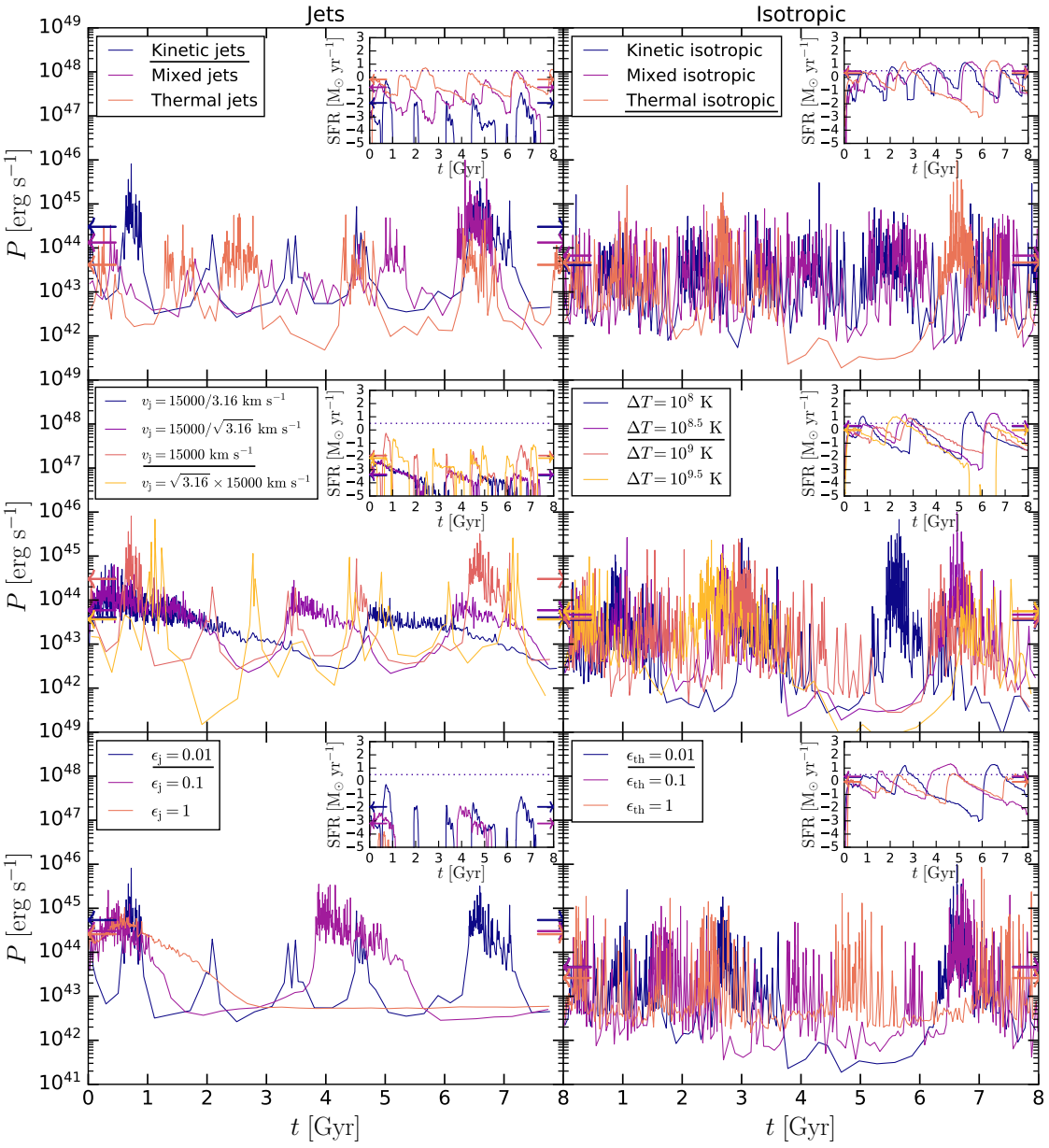

Figure 6.8: Impact of parameter variations on the feedback cycle for both jet (left) and isotropic (right) feedback as measured through the feedback power and the star formation rate (insets in each panel), for the low-mass galaxy cluster ($M_{200} = 10^{14}$ M$_\odot$ halo). The feedback powers are calculated using adaptive time bins such that during each bin, 10 feedback events (heating or kicking particles) occurred, while the star formation rates are calculated as averages in bins with a fixed width of 5 Myr. The arrows indicate averages over the 8 Gyr simulation run time. The dotted horizontal lines in the inset panels show the SFR at which the BCG is classified as marginally quenched (sSFR = 0.01 Gyr^{-1}). The details of the simulations are given in § 6.2.3 and Table 6.3. The parameters that are varied are shown in the legend of each panel, and they are: 1) the fraction of energy injected in thermal as opposed to kinetic form (top row, values of 0, 0.5 and 1), 2) the kicking/heating energy increments, given by the choice of jet velocity and heating temperature (middle row, by factors of $10^{1/4} \approx 1.78$ and $\sqrt{10} \approx 3.16$, which corresponds to logarithmic intervals of 0.25 and 0.5 dex, respectively) and 3) the feedback efficiency (bottom row, by factors of 10). The fiducial cases are those with thermal isotropic and kinetic jet feedback, using efficiencies of $\epsilon = 0.01$, heating temperatures of $\Delta T = 10^{8.5}$ K and jet velocities of $v_j = 1.5 \times 10^4$ km s^{-1}. These parameters are underlined in the legend of each panel.

of kinetic jets. We already showed a variation of this kind in Figs. 6.5 and 6.6, although we do it here more systemically. We find that using higher jet velocities results in more episodic feedback cycles, with higher peaks in the jet power and lower minima. The former is a result of more cold gas feeding stronger feedback, while the latter is a result of stronger shocking or shocking at smaller distances, which leads to more hot gas feeding the BH and reducing its accretion rate. Decreasing the velocity leads to a decrease in the SFR. Note, however, that decreasing the jet velocity at fixed resolution also improves the sampling of feedback (leading to more particles making up the jets and lobes), an effect that might be the main cause of these differences.

In the bottom-left panel of Fig. 6.8 we show results of varying the feedback efficiency of the kinetic jets. As we can see, the differences are significant. Increasing the feedback efficiency results in fewer and fewer feedback episodes. With an efficiency of 100 per cent, there is only one initial episode and effectively no star formation. Using an intermediate efficiency leads to two feedback and SFR episodes. It should be noted, however, that all three cases are quenched and thus show negligible star formation as compared to star-forming galaxies. Interestingly, all three simulations show the same minimum in the jet power ($P_{\rm j} \approx 3 \times 10^{42}$ erg s^{-1}). This minimum corresponds to hot halo accretion.

In the right-hand panels of Fig. 6.8 we show the corresponding variations of isotropic feedback. We find that all of the simulations are fairly similar, especially when compared with the variations in the jet case. It should be kept in mind that these simulations are chaotic in nature, so differences in the timing of peaks in the SFR and feedback power may not be very significant. With this in mind, we find that changing the energy type (top right panel) is the variation that has the most significant impact, in the form of changing the periodicity of the feedback events – the purely thermal case appears to have the longest period between feedback events. It also reaches the lowest value in the feedback power and SFR at $t \approx 6$ Gyr. Regardless of these small differences, the typical powers and SFRs are still similar.

The similarity of thermal and kinetic isotropic feedback, as implemented here,

has bearing for cosmological simulations. In particular, the EAGLE simulations (Schaye et al. 2015) used a thermal isotropic AGN feedback implementation, whereas in IllustrisTNG (Nelson et al. 2019), feedback by AGN is mostly done through kinetic isotropic winds. The results shown here imply that these two feedback implementations are quite similar in their effects (and both of them quite different from kinetic jets). A caveat to this is that our simulations are of idealized clusters. In reality, feedback is expected to occur in various contexts, such as during and after galaxy mergers (see e.g. Gao et al. 2020 for observational evidence or McAlpine et al. 2018 for indications of the same in cosmological simulations) or triggered by disc instabilities (e.g. Menci et al. 2014). In these situations the effects of AGN feedback might be more sensitive to the various parameters and choices we have discussed.

In the middle panel of Fig. 6.8 we show the results of varying the heating temperature in the thermal isotropic case. The results are again very similar, although the two higher-temperature cases ($\Delta T \geq 10^9$ K) show a somewhat lower recurrent peak in the feedback power and SFR at $t \approx 6-7$ Gyr. This result may be due to stochastic noise, rather than an indication of an actual trend. In the bottom right-hand panel, we see the results of varying the feedback efficiency. The highest-efficiency case has both lower maxima and higher minima in the power and SFR (more easily visible in the latter), which is likely due to the BH reacting more quickly to the development of a cooling flow: the maxima reached are lower because the feedback can shut off the cooling flow before too much cooling occurs, while the minima are higher because the feedback is then not as explosive.

Entropy profiles

Finally, in Fig. 6.9 we show the entropy profiles for the variations discussed above. From the top-left panel we see that increasing the fraction of kinetic energy in the jets leads to steeper inner entropy profiles, which are in closer agreement to observed ones (in terms of the slope). From the middle-left panel we see that decreasing the jet velocity can also bring the entropy profiles into closer agreement with observations. This may appear counterintuitive considering that real AGN jets are relativistic, and thus high-velocity (see e.g. review by Blandford et al. 2019). However, one

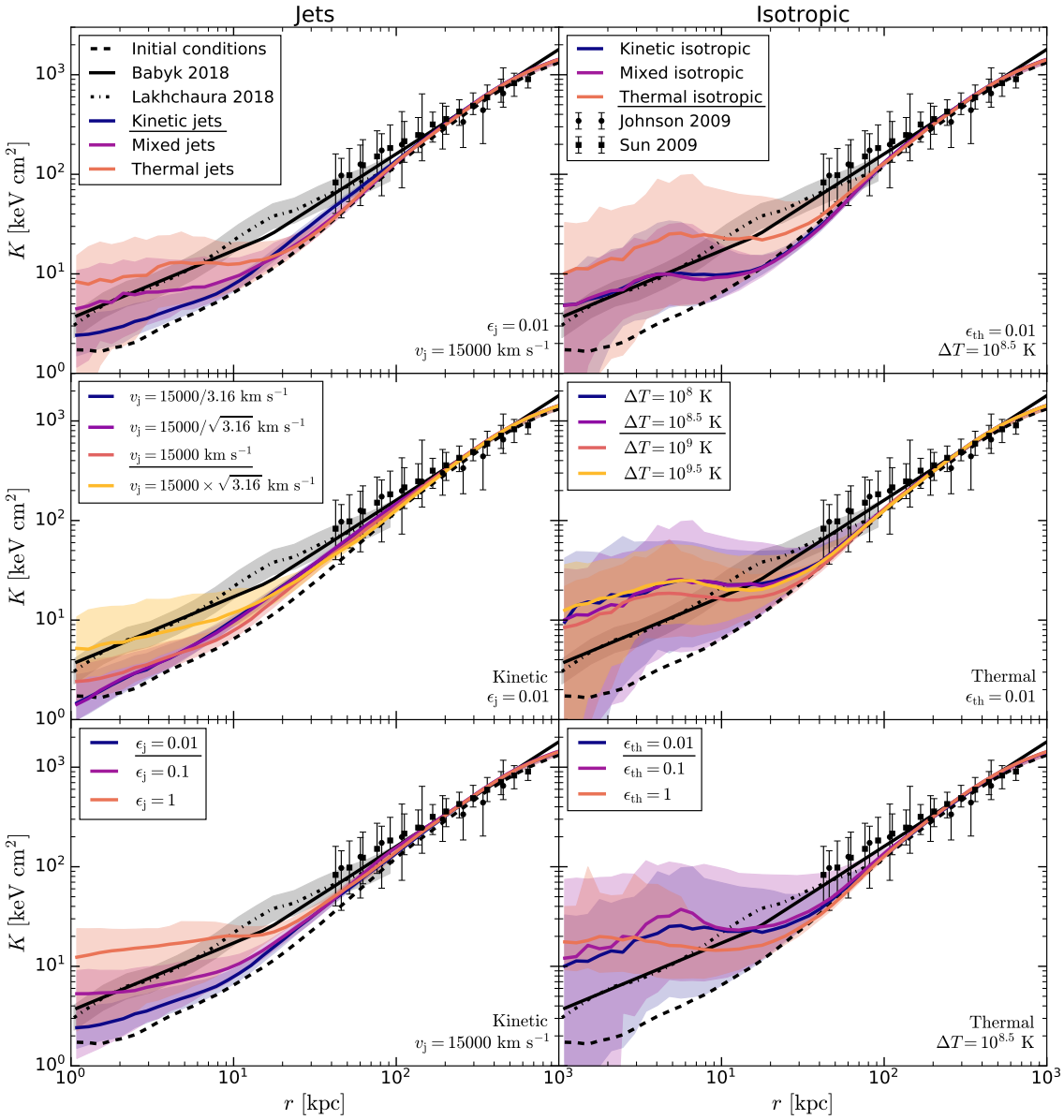

Figure 6.9: Impact of parameter variations on the gas entropy profiles (volume-weighted) of the ICM using both jet (left) and isotropic (right) feedback, for the low-mass galaxy cluster ($M_{200} = 10^{14}$ M$_\odot$). The solid lines are medians calculated using 160 snapshots between $t = 0$ and $t = 8$ Gyr, while the shadings indicate the $16^{\rm th} - 84^{\rm th}$ percentile ranges. The fiducial parameters (underlined and printed in each panel), as well as the parameters being varied, are the same as shown in Fig. 6.8 and described in its caption. The observational data sets are described in § 6.2.4.

should keep in mind that the bulk of the jet material (or energy associated with the jets) is not necessarily relativistic on all scales; the jets are often mostly transrelativistic[6] (e.g. Jetha et al. 2006 and Mullin & Hardcastle 2009) or subrelativistic (e.g. Shulevski et al. 2019) on kpc scales, the ones we are simulating in this chapter. The subrelativistic launching velocities ($v_{\rm j} < 0.05c$) favoured by these simulations may be indicative of observed jets experiencing significant amounts of entrainment on subgrid scales relative to what we are resolving here (i.e. below ≈ 300 pc). We find that the two lower-velocity cases shown in the panel have an almost identical entropy profile, indicating that the profiles converge to the same one as the velocity is decreased. From the two higher-velocity cases, we see that increasing the velocity leads to differences in the profiles: the central entropies are higher, and the slope is changed. In addition, the scatter between the different snapshots is increased. Overall, these results indicate that increasing the velocity leads to entropy profiles that are progressively more similar to those found with thermal isotropic feedback, likely due to shock heating (thermalisation) of the jets and inflation of lobes/bubbles at smaller radii.

In the bottom-left panel we show variations of the feedback efficiency. These results indicate that higher efficiencies lead to entropies that are too flat in the centre. The CC/NCC dichotomy could thus partially or wholly be a result of the BH population differing in BH spin – the low spin ones having lower feedback efficiencies and therefore lower central entropies, whereas the higher-spin ones would be the opposite in this picture.

In the right-hand panels of Fig. 6.9 we show the same variations for the isotropic case. Overall these are very similar to each other, with the energy type variations (top right-hand panel) being the only ones that show appreciable differences. In particular, the mixed or purely kinetic isotropic wind cases have lower entropies than the purely thermal one, by roughly a factor of two. However, the overall shape of the entropy profile is still the same, and it still disagrees with the observed profiles in terms of the slope.

[6]Velocities at which relativistic effects begin to become important, $v_{\rm j} \approx 0.1 - 0.5c$.

Comparison with previous simulations

We will compare our variations of the feedback implementation with previous work, mostly on idealized galaxy clusters and mainly for the low-mass cluster case ($M_{200} = 10^{14}$ $M_\odot$), since other studies have largely focused on such haloes. We discuss specifically studies that have implemented more than one AGN feedback variant, or that have varied parameters that also correspond to our simulations.

Barai et al. (2016) performed SPH simulations and compared several implementations of kinetic feedback, as well as one thermal variation. Their feedback implementation is intermediate to our isotropic and jet feedback, since it is bipolar in nature, but with a large opening angle (45°). They found that using kinetic feedback leads to less star formation than if thermal feedback is used, in agreement with our findings. However, their entropy profiles with thermal feedback are lower than the ones with kinetic feedback, a conclusion opposite to ours (both for the isotropic and jet cases). This is likely a result of their thermal feedback being implemented as a 'thermal dump' (see footnote 1), which likely resulted in numerical overcooling. They find that lower-velocity feedback leads to higher central entropies, again in disagreement with our finding. This could be due to differences in the hydrodynamics schemes (GADGET-3 vs. SPHENIX). Weinberger et al. (2023) compared kinetic jets with the kinetic wind implemented in IllustrisTNG; they found that jets are slightly more efficient at quenching star formation, in agreement with our results. They also found that the feedback powers are less time-variable in the jet case than in the kinetic wind case, which is again in agreement with our results. Their interpretation of this is that jets act more on the strongly cooling (but not yet star-forming gas), while the wind acts on the star-forming ISM, including in the vicinity of the BH.

The remaining simulations we compare with were performed using grid-based codes. Gaspari et al. (2014) compared mechanical (kinetic) jet feedback and thermal isotropic feedback across a range of halo masses ($10^{13} - 10^{15}$ $M_\odot$), finding that the former leads to cooler cores, in agreement with our results. However, they implemented kinetic jets as self-regulated (with the accretion rate determined from the properties of gas), while their thermal feedback was implemented as a blast with

a fixed power (heating all gas near the BH), which is not a fair comparison. Meece et al. (2017) compared different feedback models in a massive halo ($M_{200} \approx 10^{15}$ M$_\odot$). They found that purely thermal jets are less efficient at preventing cooling flows from developing than either mixed or purely kinetic ones, in agreement with our findings. However, in disagreement with our results, they find lower central entropies with thermal feedback, similar to Barai et al. (2016) (this is, again, probably a result of using low heating temperatures as part of a 'thermal dump' that likely led to too much numerical overcooling). Ehlert et al. (2023) compared dense (i.e. low-velocity) and light (high-velocity) jets, finding that the results are relatively similar. However, it should be pointed out that the majority of these papers, including the last one, perform their simulations for a relatively short time (usually $1-2$ Gyr or less). This is of order the length of the typical cycle of activity (cooling and feedback) we find in our simulations. Thus, most of these papers may be biasing their results to the first episode of high-activity.

Finally, while we found that the choice of heating temperature used for thermal isotropic feedback has little effect on our results, especially for the entropy profiles, this is in disagreement with previous work in a cosmological context (e.g. Le Brun et al. 2014, Hahn et al. 2017). Those studies found that the choice of heating temperature affects both the total mass of the ICM (the gas fraction) as well as its distribution and properties (the thermodynamical profiles). This difference between our results and cosmological studies is likely due to our simulations focusing on isolated and self-regulated systems (assumptions that break down for realistic haloes).

6.5 Summary and conclusions

In this chapter we presented an extension of our study of jet feedback in idealized galaxy groups and clusters, which was discussed in Chapter 5. Here, we compared different types of AGN feedback (in terms of energy, directionality, heating versus kicking) in idealized haloes spanning the $M_{200} = 10^{13} - 10^{15}$ M$_\odot$ range, which we initialized in a relatively cool-core state. We focused specifically on comparing

thermal isotropic and kinetic jet feedback – the former representing the effects of radiatively-driven wind (i.e. quasar) feedback, and the latter the effects of feedback by relativistic jets.

We first tested these AGN feedback implementations in unison with our BH spin evolution model (Chapter 2). This has the advantage of giving realistic, variable feedback efficiencies, as well as variable jet directions. We assumed that thermal isotropic feedback occurs at high normalized accretion rates (Eddington ratios $f_{\rm Edd} > 0.01$), when the disc is thin and radiatively efficient, whereas kinetic jets are assumed to be launched at low Eddington ratios ($f_{\rm Edd} < 0.01$), when the disc is thick and advection-dominated. We compared this hybrid model with one where the disc is always thin and launching isotropic winds, as well one where the disc is always thick and launching jets. We then simplified the set-up by assuming constant feedback efficiencies and fixing the jet direction. In this simplified set-up, we further varied the feedback efficiency, the energy per feedback event, as well as the type of energy being used for feedback (thermal vs. kinetic) for both the isotropic and jet cases. From the simulations performed and the analysis presented in this chapter, we find the following:

- Kinetic jet feedback leads to more efficient quenching of star formation in the central galaxies than thermal isotropic (wind) feedback. This applies across the whole mass scale range we have tested. It is true in simulations using detailed models of BH spin evolution (resulting in variable feedback efficiencies/jet directions), as well as ones without (using constant feedback efficiencies/jet directions). A larger fraction of the feedback energy couples to large radii in the jet case, resulting in overall more energy being injected in that case in order to quench cooling flows.

- Due to a smaller fraction of the feedback energy coupling to the intracluster gas at smaller radii, and a larger fraction at larger radii, the central gas entropies are significantly lower with kinetic jet feedback than with thermal isotropic feedback. They are also in closer agreement with observations in terms of the inner slope. In addition to the median central entropies being lower, median

central densities are higher and median central temperatures lower, despite cooling flows being weaker and/or shorter-lived.

- We find that isotropic feedback is largely insensitive to the choice of feedback efficiency and energy per feedback event. By varying the type of energy being injected (kinetic, mixed and thermal), we find that the thermal isotropic case has a somewhat higher central entropy and a feedback cycle with the longest periodicity. However, all of these isotropic feedback implementations are still more similar to each other than any of them is to kinetic jet feedback. This may indicate that the isotropic kinetic feedback employed in some cosmological simulations (e.g. IllustrisTNG) is quite similar in its effects to the isotropic thermal feedback employed in other simulations (e.g. EAGLE). However, all of our isotropic feedback is energy-dominated, so the conclusions may change somewhat for momentum-dominated winds.

- Jet feedback is sensitive to all of the choices mentioned in the previous point. High feedback efficiencies can prevent any cooling flows from developing, leading to higher central entropies. Increasing the jet velocity leads to more frequent cooling flows (and more star formation), but it also leads to higher mean central entropies with shallower slopes, due to strong shocks and heating at small radii. In other words, kinetic jet feedback is progressively more similar to thermal isotropic feedback as the jet velocity is increased. Jet feedback is most efficient if it is kinetic, rather than thermal or mixed. The jet direction is unimportant, as long as it does not change more frequently than every ≈ 1 Gyr, which it is unlikely to do in galaxy clusters with realistic BH spin evolution. Constant jet efficiencies lead to highly periodic cooling flows, unlike in the variable-efficiency cases.

- In order to recover the observed entropy profiles across a large range of masses (galaxy group to rich cluster scales), it may be necessary to choose jet velocities carefully. In particular, low velocities may be required in galaxy groups/low-mass clusters in order to yield steep entropy profiles, while high jet velocities may be required to reproduce cored entropy profiles and X-ray cavities in rich

galaxy clusters. Alternatively, variable jet efficiencies from a BH spin evolution model, in conjunction with different accretion/merger histories, might naturally lead to some of these differences. We find that a hybrid model with both thermal isotropic and kinetic jet feedback (depending on the BH accretion rate) has the lowest central entropies, and may thus be the most promising. On the other hand, our jet-only model is disfavoured on account of excessive BH mass growth. This growth is due to strong jet-induced spindown of BHs, leading to very low BH spins (and therefore jet efficiencies of order 0.1 per cent).

- The differences between simulated entropy profiles with varying AGN feedback implementations are similar in magnitude to differences that arise if the numerical details are varied (e.g. the artificial conductivity and viscosity of the hydrodynamics code). This means that these physical and numerical variations are somewhat degenerate with regards to entropy profiles. Bringing different numerical codes in agreement would thus significantly improve the potential of simulations to discriminate between different AGN feedback implementations.

We caution that these conclusions may only be valid for isolated systems such as the ones studied in this chapter. Thus, some of them may not fully apply in the context of cosmological simulations. Despite this caveat, the results presented in this chapter should be valuable when considering different implementations of AGN feedback in cosmological simulations of galaxy formation and evolution.

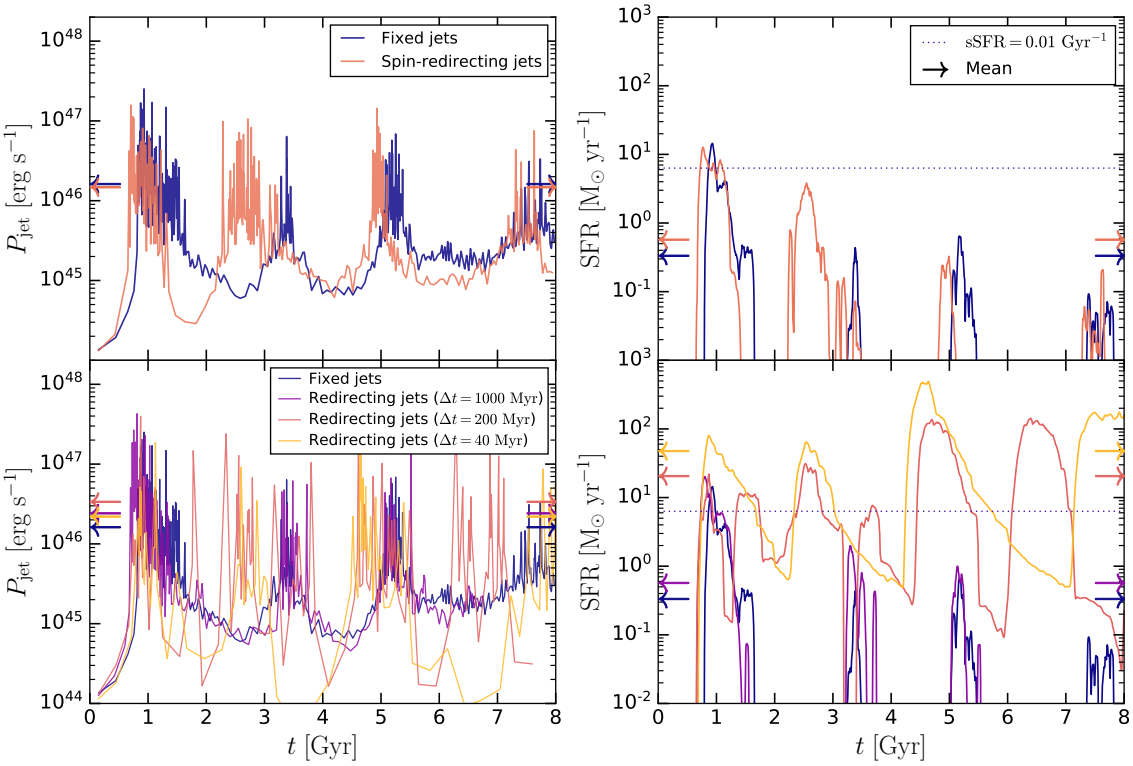

Figure 6.10: Time dependence of the jet powers (left) and star formation rates (right) in the high-mass galaxy cluster ($M_{200} = 10^{15}$ M$_\odot$) simulations that feature jet redirection, compared with a case that has a fixed jet direction (along the $z-$axis). In the top panels we compare with a case that features jet redirection using the spin evolution model. The bottom panels show several cases where the jets are held fixed in a direction that randomly changes, with the period of these redirections shown in the legend. The arrows indicate averages over the 8 Gyr simulation run time. The parameters of the simulations correspond to the sixth row of Table 6.3.

Appendix 6.A: Effects of jet redirection and precession

For the purposes of the main results in this paper, we fixed the jets to be along the $z-$axis when considering simplified feedback without BH spin evolution. This immediately leads to the following questions: how justified is this assumption, and how important is the change of the jet direction for the effects of feedback? We ran some additional simulations in order to answer these questions. These simulations employed either manually redirecting or precessing jets. There are many ways in which both of these processes could be implemented. We used a fairly simple implementation, since these results are meant to be illustrative. We tested these cases

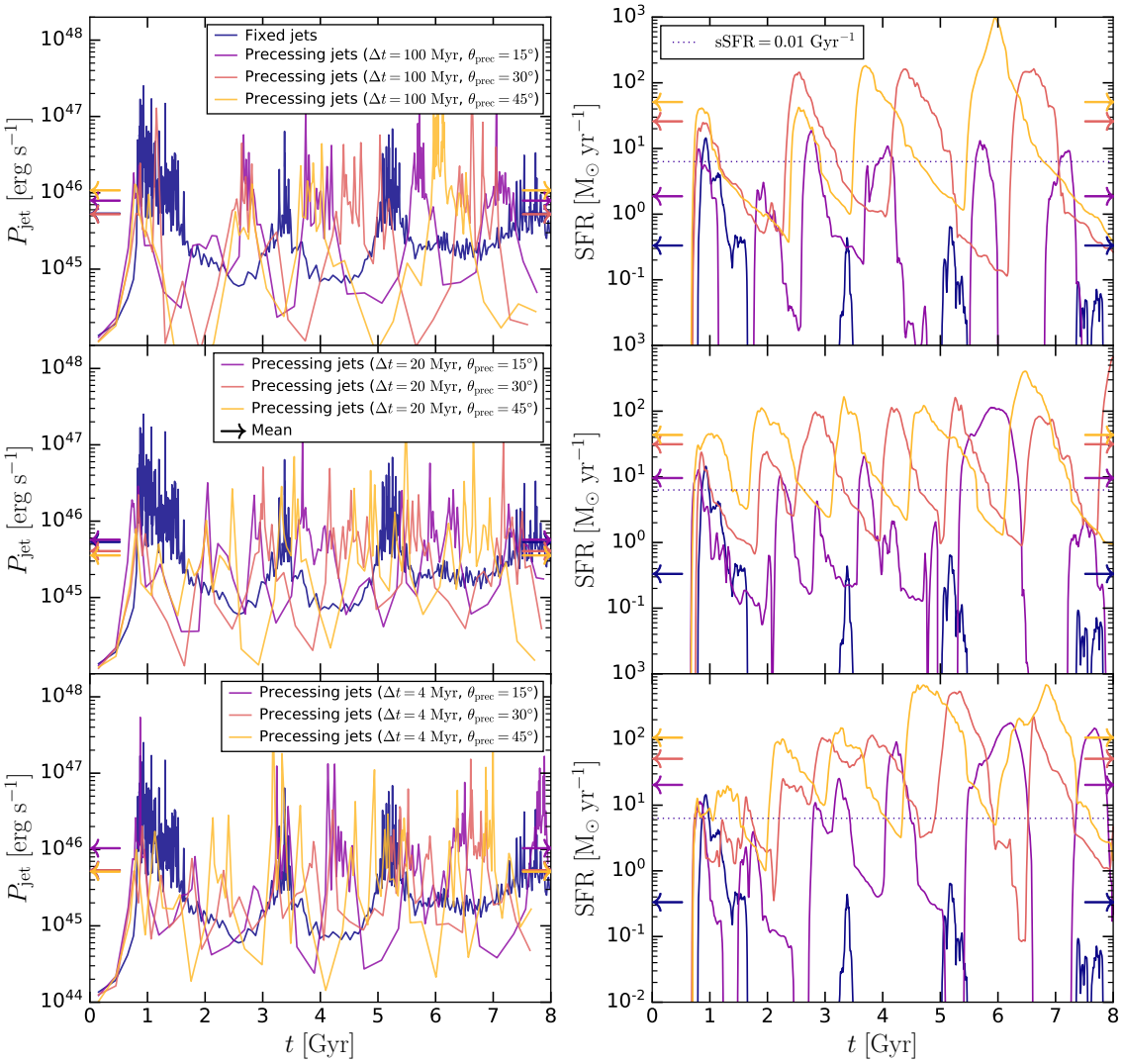

Figure 6.11: Same as Fig. 6.10, but showing cases with precessing rather than redirecting jets. From top to bottom we show several cases with different periods of jet precession. In each row (i.e. at every fixed precession period) we also vary the precession angle.

in our fiducial high-mass galaxy cluster set-up ($M_{200} = 10^{15}$ M$_\odot$), since we found redirection to be more likely for this halo mass (if BH spin evolution is used).

In the redirecting case, the jets were initially directed along the $z-$axis. With a period of Δt, they were then instantaneously redirected to another, randomly chosen axis. We tested three periods: $\Delta t = 1000$ Myr, $\Delta t = 200$ Myr, and $\Delta t = 40$ Myr. These are compared with the fixed-direction case in Fig. 6.10, alongside a case that has spin-driven jet redirection, but a constant jet efficiency ($\epsilon_\mathrm{j} = 0.01$, as in all of these simulations). The spin-redirecting case appears to show similar behaviour as the fixed-axis case, despite the jets being redirected during each of the cooling episodes (for a total of 4 times, i.e. once per each cooling episode, although this is not shown here). The case with manual redirection every $\Delta t = 1000$ Myr is again very similar to the fixed case, and therefore to the spin-redirecting case. However, if redirection is done more often ($\Delta t \leq 200$Myr), the jet powers are more variable and the SFRs are more similar to the thermal isotropic case. We interpret this to be a result of the redirection time-scale being similar to (of the same order of magnitude as) the typical duration of a jet episode, which can be up to 100 Myr. We speculate that this may be due to jets often being redirected while they are in the process of inflating a pair of lobes, or otherwise moving to large radii (where effective heating seems to be necessary in order for cooling flows to be shut off effectively).

In the precessing cases, we manually precessed the jets with a period of Δt about the $z-$axis, with a precession angle of θ_prec. We did not nutate the jets as well, i.e. they did not 'cover' the region between the $z-$axis and the circle on which they were precessing. Note that the effects of jet precession are probably quite similar to the effects of using a larger opening angle. We tested three values of Δt: $\Delta t = 100$ Myr, $\Delta t = 20$ Myr, and $\Delta t = 4$ Myr. These are relatively shorter than in the redirecting case, because we expect that the BH spin vector can change in direction by small values (e.g. 15°) with very little mass accretion, which is not true for full redirection. For each of the precession time-scales, we tested three precession angles: $\theta_\mathrm{prec} = 15°$, $\theta_\mathrm{prec} = 30°$ and $\theta_\mathrm{prec} = 45°$. The results of these tests are shown in Fig. 6.11. It appears that jet precession leads to significant differences in all cases shown here. The only combination(s) that result in fairly low SFRs are those with

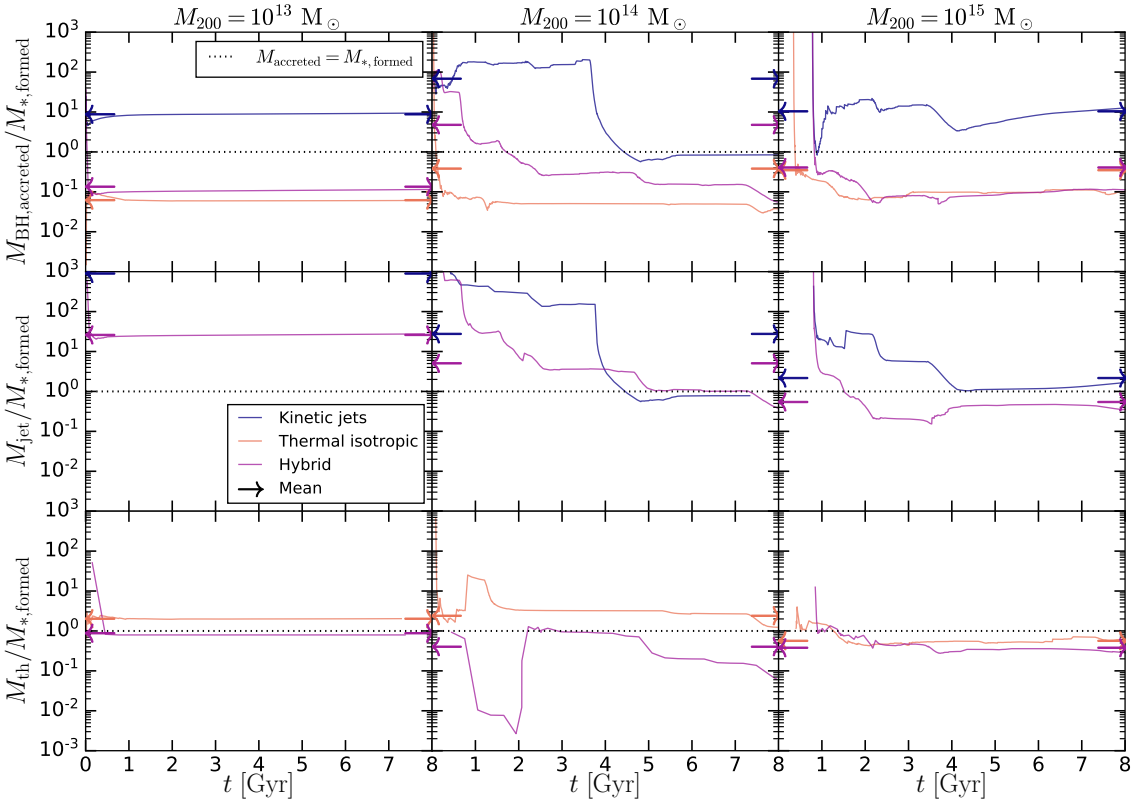

Figure 6.12: Ratio of total mass accreted (top row), launched into the jets (middle row) and heated (bottom row) by the BH, and the total stellar mass formed. The arrows indicate averages over the 8 Gyr simulation run time. This figure is an extension of Fig. 6.2.

$\theta_{\rm prec} = 15°$ and $\Delta t \geq 20$ Myr. However, even these cases show higher SFRs than the fixed-axis case. Cases with larger precession angles appear quite similar in their effects to thermal isotropic feedback. The precession time-scale does not appear to have a large impact.

Appendix 6.B: Mass flux associated with accretion and feedback

In Fig. 6.12 we show some additional quantities from the same simulations as in Fig. 6.2, namely: the ratio of total mass accreted, launched into the jets and heated by the BH, to the total stellar mass formed. These ratios are plotted for our simulations with spin evolution spanning the galaxy group ($M_{200} = 10^{13}$ M$_\odot$) to high-mass cluster scale ($M_{200} = 10^{15}$ M$_\odot$). We plot these quantities in order to glean in-

formation on whether BH accretion and feedback are directly interfering with star formation (by depriving it of cool gas either by accreting, kicking or heating it), or indirectly by e.g. causing outflows of the same gas or shutting off cooling flows that supply this gas. These ratios should be treated as meaningful only once the amount of stars that have formed is appreciable, and not very low due to feedback being effective. For this reason, the results from the left-hand column should not be considered too meaningful (since very little star formation occurs in the galaxy group case), while for the galaxy cluster cases, they become meaningful only at $t = 2 - 4$ Gyr, depending on the case.

From the galaxy cluster cases we see that the amount of mass accreted by the BH is significant in all cases, with the mass flux associated with feedback even more significant (for at least one of the feedback channels in the given simulation). This is true even for the high-mass cluster, which is the most star-forming of the systems we study, and where we find that the combined mass of all the heated and kicked particles in the hybrid case (as an example) to be roughly as large as the total mass of all stars formed ($\approx 3 \times 10^{11}$ $M_{\odot}$). Overall, these plots indicate that feedback mechanisms in simulations may directly interfere with the formation of stars (by depriving it of cold gas), even when the rate of star formation is relatively high. This effect may, however, still be subdominant to the indirect effects of feedback. These plots also show that BHs in the kinetic jet-only case cannot self-regulate their growth, due to low jet efficiencies as a result of spindown.

Appendix 6.C: Fraction of black hole growth at low vs. high Eddington ratios

In Fig. 6.13 we show the cumulative fraction of mass accreted when $f_{\rm Edd} < f_{\rm Edd,crit} = 0.01$ (corresponding to the thick disc in the hybrid and kinetic-only case) as a function of time, for all 9 simulations discussed in § 6.3. This figure is an extension of Fig. 6.3. We see that in the galaxy group case, most of the growth is at low Eddington ratios, except at the very beginning. However, this reflects the fact that there is an initial burst of high accretion rate growth at the beginning of the simulation,

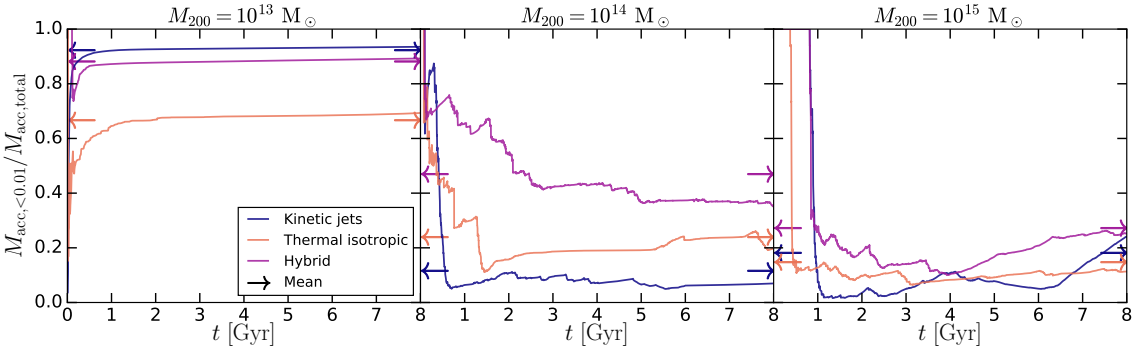

Figure 6.13: BH mass growth that occurs at low Eddington ratios ($f_{\rm Edd} < 0.01$) as a fraction of the total mass growth, for our simulations with BH spin evolution. This figure is an extension of Fig. 6.3.

after which the system is fully quenched. In the galaxy cluster cases, we see that most of the BH growth occurs when $f_{\rm Edd} > 0.01$, despite the fact that this condition is not fulfilled most of the time. The growth at low Eddington ratios, however, is by no means negligible.

Appendix 6.D: Dimensionless entropy profiles

In Fig. 6.14 we show the dimensionless entropy profiles K/K_{500} as a function of the scaled radius r/r_{500}, for the 9 simulations with BH spin evolution, discussed in § 6.3.4 (this plot may be considered an alternative way of showing the data in Fig. 6.4). We define the entropy K_{500} as $k_{\rm B}T_{500}/n_{\rm e,500}^{2/3}$, where $T_{500} = GM_{500}\mu m_{\rm p}/2r_{500}$ and $n_{\rm e,500} = 500 f_{\rm b,0}\rho_{\rm c}/\mu_{\rm e}m_{\rm p}$. Here, $\rho_{\rm c}$ is the critical density, $\mu_{\rm e} = 1.14$ the mean molecular weight per free electron and $f_{\rm b,0} \approx 0.16$ the cosmic baryon fraction (e.g. Barnes et al. 2017). Overall, from Fig. 6.14 we see that all of the simulated dimensionless profiles are similar, although there is some disagreement in normalisation at large radii. This can be avoided (and the profiles made even more similar) if the cosmic baryon fraction $f_{\rm b,0}$ in the definition of K_{500} is replaced by the actual baryon fraction of each of the haloes, $f_{\rm b,500}$, although we do not show those profiles here. We find that the low-mass clusters ($M_{200} = 10^{14}$ M$_\odot$) with jets show the lowest dimensionless entropy. This result may not be significant, however, given that these are single realizations of idealized and isolated clusters. Most of our profiles lie below the observations shown in the figure, although this is by construction (we simulate relatively CC

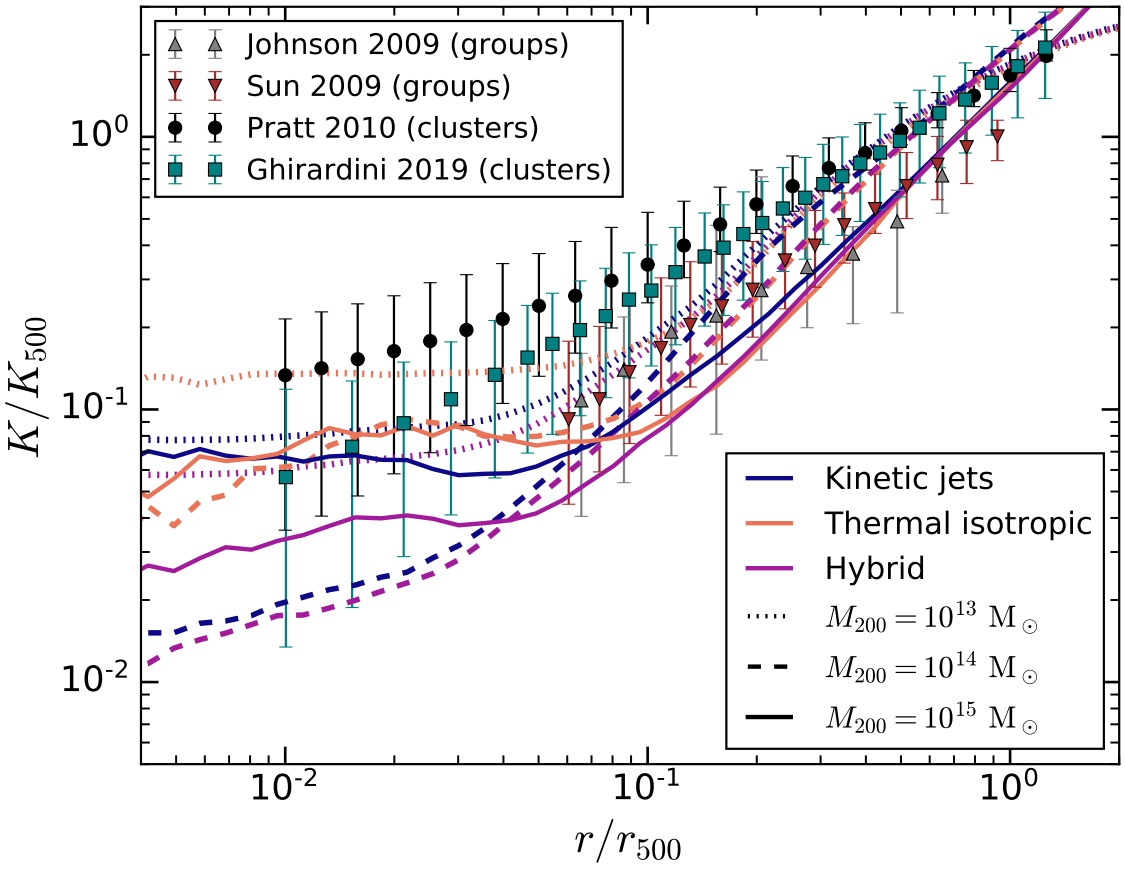

Figure 6.14: Dimensionless entropy profiles for our simulations with BH spin evolution. This figure may be considered an alternative to Fig. 6.4. Note that we define the entropy K_{500} using the actual baryon fractions of our simulated haloes, rather than the cosmic baryon fraction (the usual choice). We find that this leads to better agreement between the profiles at large distances.

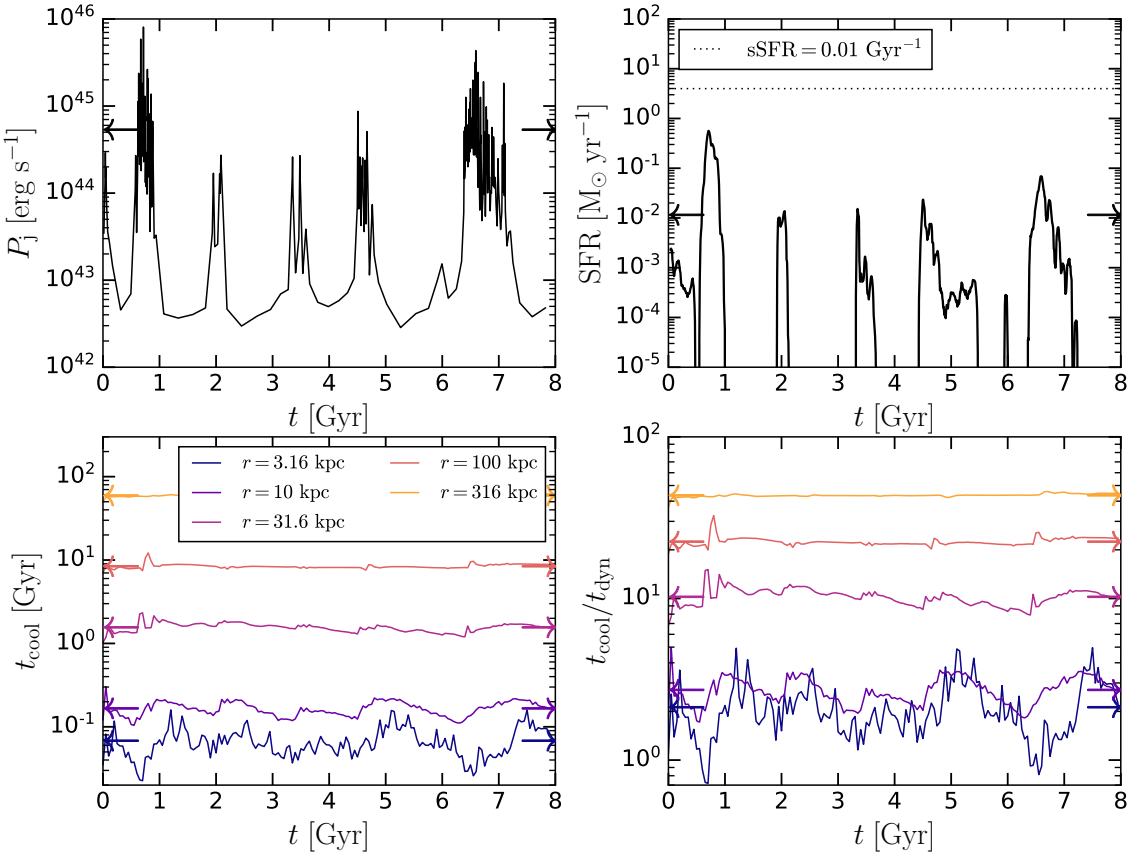

Figure 6.15: Time dependence of quantities related to the quenching/feedback process in our fiducial $M_{200} = 10^{14}$ M$_\odot$ simulation with fixed jet feedback (the parameters are given in the third row of Table 6.3). From top left to bottom right we show the jet power, SFR, cooling time at several radii (see legend) and cooling time to dynamical time ratio for the same radii. These plots show that the periodicity between jet/cooling episodes is set by the cooling time of the gas with $t_{cool}/t_{dyn} \approx 10$, due to all gas with that ratio below 10 undergoing cooling.

systems).

Appendix 6.E: Periodicity between jet episodes

In Fig. 6.15 we show the approximate periodicity in relevant quantities related to the feedback cycle for our fiducial simulation (with a fixed feedback efficiency $\epsilon_j = 0.01$ and the jets directed along the $z-$axis) of the low-mass galaxy cluster ($M_{200} = 10^{14}$ M$_\odot$). The top left-hand panel shows the jet power: it has 5 peaks that appear to be roughly equally separated in time, while the top right-hand panel shows the same for the star formation rate. The peaks in jet power and SFR roughly coincide. The

bottom row shows the cooling time and the cooling time to dynamical time ratio ratio at several radii from $r = 3.16$ kpc to $r = 316$ kpc. According to the hypothesis of Nobels et al. (2022) (and references therein), all gas with $t_{\rm cool}/t_{\rm dyn} < 10$ will cool effectively and contribute to the cooling flow. From the right-hand panel we see that the gas at $r = 31.6$ kpc has a roughly constant value of the ratio, $t_{\rm cool}/t_{\rm dyn} \approx 10$. If we then look at the left-hand panel, that same gas has a roughly constant cooling time of ≈ 1.5 Gyr. This is also roughly the period between the cooling flow episodes. Our results are thus in agreement with the above-mentioned hypothesis. While we have shown only this one case, we find that the same holds true across all our simulations.

CHAPTER 7

Conclusions and future work

Modern simulations of galaxy formation and evolution are becoming ever more sophisticated, and including more detailed and physically realistic prescriptions for various processes, including BH growth and feedback. Simultaneously, simulations of accretion processes onto BHs are confirming or improving our understanding of BH growth and feedback based on theoretical explorations since the latter half of the 20th century.

It is becoming clear, from both an observational and theoretical perspective, that BH accretion discs operate in at least two (probably three) modes: 1) a radiatively-efficient mode where the BH grows from a thin accretion disc and 2) a radiatively-inefficient, advection dominated mode with a thick accretion disc. In the former case, the AGN is visible as a quasar in multiple wavelengths (e.g. optical, UV, X-ray), while in the latter case, the AGN itself is quite faint, but prominent jets and lobes are visible on large scales at radio wavelengths. Most simulations of galaxy formation and evolution are beginning to include BH growth and AGN feedback models that emulate at least these two feedback modes. However, in order for realistic jets to be launched, one needs to track the evolution of BH spin for every BH in the simulation. This has not yet been done in large cosmological simulations

of galaxy formation and evolution.

In Chapter 2 I presented a model for the evolution of BHs, including their mass growth, spin evolution, and the feedback that they produce as they grow. In addition to the thin and thick disc mentioned above, which are active at low and moderate accretion rates (as determined by the Eddington ratios), the model includes a slim disc component that is active during super-Eddington phases of BH growth. The model includes the effects of winds launched by different mechanisms (and therefore featuring different efficiencies) in each of the three regimes. Jets are also present in all three regimes, but they are most efficient in the thick disc and in the slim disc for highly super-Eddington accretion. BH spin is evolved self-consistently in each accretion mode, with spindown of the BH by jets particularly important for a realistic evolution of spin. The jets are launched in the direction of the BH spin vector, which leads to natural precession and redirection of the jets. The effects of Lense-Thirring torques on BH spin evolution are also included, as well as that of BH-BH mergers. Finally, by means of an accretion efficiency, the effects of disc winds that blow away most of the accreting mass are included. The full model, as just described, is included in the publicly-available SWIFT code. It will be used in next-generation cosmological simulations of galaxy formation and evolution that will succeed the EAGLE model.

Alongside the development of the above model, the majority of the research presented in this Thesis concerns tests of various parts of the model, and its implementation. In this Thesis we do not include tests of the slim disc regime and super-Eddington feedback, since it is beyond the scope of the Thesis, but such tests are underway. All tests of the model were performed in idealized settings. The purpose of these tests is to validate the model, as well as to understand its behaviour and predictions for single objects, before the model is implemented for many galaxies and BHs in a cosmological simulation.

In Chapters 3 and 4 I began with tests of single, individual episodes of jet launching, whose purpose was to validate the behaviour of the jets and lobes that they produce using the SWIFT code. This was particularly necessary as SWIFT uses the smoothed particle hydrodynamics (SPH) method, with which AGN jets

have not been simulated to date. The jets in these simulations were launched from initially placed reservoirs of particles, and did not include any BHs.

In Chapter 3 I presented results of simple hydrodynamical tests, where jets were launched into an ambient medium of a constant density, and in a few cases into ambient media with a power-law density profile. The jets in these simulations were initially ballistic, but eventually reached a phase where they inflated lobes of a self-similar shape, and also launched a bow shock. The energies in both the lobes and imparted to the ambient medium (through the bow shock) were found to both be significant, the same being true for both the kinetic and thermal components. The jet velocity was found to be an important physical parameter, since it affects when the self-similar phase is reached. It is also an important numerical parameter (in the SPH approach), because it changes how many particles constitute the jets and lobes (at a fixed power). The results of these simulations were in good agreement with analytical predictions. Surprisingly, the lobes and bow shock were found to be very similar at different numerical resolutions (even down to only ≈ 400 particles constituting the lobes). This indicates that the basic physics of jet feedback can be correctly simulated even in low-resolution cosmological simulations, at least in galaxy clusters (and assuming that most of the feedback occurs through the inflation of lobes and driving of bow shocks).

Chapter 4 presents the results of a broadened study similar to the above, but where jets were launched into more realistic ambient media, representing idealized galaxy clusters in hydrostatic equilibrium. Furthermore, the focus was not only on the initial phase of the interaction between the jets and lobes with the ambient medium (during the jet launching phase), but also on the interaction between the jet-inflated bubbles and the intracluster medium (ICM) in the post-launching phase. It was found that jet-inflated bubbles draw out low-entropy ICM gas from the central portions of the ICM outwards (in the form of the Darwin drift and the wake). This results in a permanent rearrangement of the ICM, which is visible as changes in the radial profiles of gas properties such as temperature and density. In particular, the central temperature and density of the ICM are higher and lower (compared to the initial state), respectively, after the jet-inflated bubbles have buoyantly risen

out of the ICM. In agreement with this picture, all of the initially launched jet energy ends up in reducing the magnitude of the (negative) gravitational potential energy of the ICM, indicating that the ICM has overall expanded. By comparing the simulations with an analytical model, we found that the behaviour of jet-inflated bubbles is impacted by a complex mixture of different physical processes, including: 1) buoyancy, 2) drag, 3) entrainment of ambient material, 4) Darwin drift, 5) wake.

In Chapters 5 and 6 the tests were broadened to a similar set-up (idealized galaxy clusters), but the focus was on testing the BH spin evolution and AGN feedback model presented in Chapter 2. For this purpose, more physics was turned on, including radiative gas cooling and star formation (using the EAGLE galaxy formation and evolution model). The set-up included a wide array of idealized galaxy groups and clusters, spanning the full range of mass and central temperature (allowing for both cool-core and non-cool-core clusters to be simulated, as well as anything in between).

In Chapter 5 the focus was on testing the low-accretion rate regime (the thick disc) and its primary form of AGN feedback: kinetic AGN jets whose direction is in the BH spin direction, and whose efficiency depends on spin. We found that AGN jets successfully quench cooling flows across the full range of halo masses, from the galaxy group to the massive galaxy cluster scale. All relevant parameters were varied, but quenching was efficient in almost all cases, except for very cool-core, massive clusters. Theses tests, however, were not fully realistic, as jet feedback was allowed at moderate Eddington ratios using the same feedback efficiency as at low Eddington ratios. Furthermore, BH spindown by jets was intentionally weaker than it realistically should have been, to prevent spindown to effectively zero spin.

In Chapter 6 we performed similar simulations, but with a focus on comparing the above case (with only jets) against thermal isotropic feedback (representing feedback by quasars) in the thin accretion disc regime, including its BH spin evolution. In addition, we performed hybrid simulations, where the thick disc and kinetic jets were used at low accretion rates, and the thin disc and thermal isotropic feedback at high accretion rates. We found that kinetic jets were more efficient at quenching and led to lower central entropies, although the hybrid model performed best on the

latter measure and is likely the most promising option, from those we tested, for use in cosmological simulations. We also performed simpler simulations where we compared isotropic and jetted feedback using fixed efficiencies (and jet directions). We systemically varied three relevant parameters: 1) the constant feedback efficiency, 2) the heating/kicking energy and 3) the fraction of energy in the thermal and kinetic components. We found that the most efficient combination was that of kinetic jet feedback.

The model presented in this Thesis represents an important step forward for realistic inclusion of BH physics in hydrodynamical, cosmological models of galaxy formation and evolution. The results from the array of idealized tests presented here are not only insightful for our understanding of AGN physics, but are also crucial to perform before such a model is employed in cosmological simulations.

7.1 Ongoing and future work

The tests presented in this Thesis concerned aspects of the BH growth and feedback model that are relevant at sub-Eddington accretion rates. Tests of the slim disc, relevant at super-Eddington rates, were not included. These tests are currently ongoing. Since super-Eddington accretion appears extremely rarely in the local Universe, or in very specific circumstances at higher redshifts (about which we do not know much), these tests are being performed using cosmological simulations. Specifically, they are being done using the zoom-in method, where a specific region of a large cosmological volume is resimulated at a high resolution. The region of interest is that surrounding a massive protocluster ($M_{\rm halo} \approx 10^{15}$ M$_\odot$ at $z = 0$, $M_{\rm halo} \approx 10^{13}$ M$_\odot$ at $z = 4$). The central galaxy starts forming very early, as does its BH. Using such a set-up, multiple simulations are being performed, comparing the fiducial case (with an Eddington cap and only thermal isotropic feedback) with that where super-Eddington accretion is allowed, as well as the case with feedback implemented as relevant for the slim disc (using its wind and jet efficiencies).

Once the slim disc aspect of the model is tested and validated, the model is ready for use in cosmological simulations of galaxy formation and evolution. For

this purpose, it has already been included into the SWIFT code, which is used for both current versions of EAGLE-like models ('SWIFT-EAGLE'), as well as the next-generation successor to EAGLE (the COLIBRE simulations). The COLIBRE simulations will span a wide range of resolutions and box sizes, and its 'fiducial' AGN feedback mode will be the same as in EAGLE: thermal isotropic heating at all accretion rates. The current plan is to use our AGN feedback model for at least some of the COLIBRE simulations, and possibly in the largest runs in the suite, depending on how it performs. For this reason, tests and calibration of the model are already ongoing for cosmological simulations, in parallel with the same calibration procedure for the 'fiducial' COLIBRE simulations. These tests are already highlighting the non-trivial nature of making changes to AGN feedback. Adding a feedback mode (kinetic jets) introduces changes to both galaxy and BH properties, as do any changes to feedback efficiencies. Test and calibration runs so far indicate that many parameters need to be (re-)tuned carefully, including: 1) jet velocities, 2) coupling efficiencies of thermal feedback, 3) accretion efficiencies (in both the thick and slim disc, with the former having larger effects), 4) BH seed masses and 5) possibly other SNe-related parameters.

Work is also ongoing to include synchrotron radio emission from AGN jet particles launched in the simulations that use the model. The acceleration of electrons to relativistic energies (and the amplification of magnetic fields) can be tied directly to the internal shocking rates of gas, so in principle, we can directly track where such injection occurs. Once injected/amplified, the relativistic electron and magnetic field energies evolve due to adiabatic expansion or compression, as well as synchrotron and inverse-Compton emission (on both the CMB and the synchrotron photons themselves) in the case of the electrons. For every jet particle in SWIFT, this yields an energy distribution ('spectrum') of relativistic electrons as a function of Lorentz factor that has a non-trivial shape. It is not feasible to track this distribution for every jet particle, so work is ongoing to use an approximate model and auxilliary quantities to reconstruct such distributions in post-processing. Given such a model, we can predict synchrotron emissivities for every jet particle at arbitrary frequency. In other words, we can construct not only radio maps, but also radio

spectral energy distributions (SEDs) for the jets launched in the simulations, and the lobes they inflate. This will be useful not only in providing predictions and therefore enabling comparisons with observed radio galaxies, but it will also help explain the properties of radio galaxies. In addition to radio jets, work is ongoing to generalize the model to provide predictions for synchrotron radio emission from all other processes relevant for galaxy formation and evolution simulations, including supernovae, AGN winds, as well as accretion and merger shocks in galaxy clusters.

Bibliography

Agertz O., et al., 2007, , 380, 963

Akiyama K., et al., 2022, , 930, L16

Altamura E., Kay S. T., Bower R. G., Schaller M., Bahé Y. M., Schaye J., Borrow J., Towler I., 2023, ,

Arnaud M., Pratt G. W., Piffaretti R., Böhringer H., Croston J. H., Pointecouteau E., 2010, , 517, A92

Ascasibar Y., Markevitch M., 2006, , 650, 102

Asplund M., Grevesse N., Sauval A. J., Scott P., 2009, , 47, 481

Babcock H. W., 1939, Lick Observatory Bulletin, 498, 41

Babyk I. V., McNamara B. R., Nulsen P. E. J., Russell H. R., Vantyghem A. N., Hogan M. T., Pulido F. A., 2018, , 862, 39

Bahé Y. M., et al., 2017a, , 470, 4186

Bahé Y. M., et al., 2017b, , 470, 4186

Bahé Y. M., et al., 2022, ,

Baldi A., Forman W., Jones C., Kraft R., Nulsen P., Churazov E., David L., Giacintucci S., 2009, , 707, 1034

Baldry I. K., et al., 2012, , 421, 621

Bambic C. J., Reynolds C. S., 2019, , 886, 78

Bamford J. T., Komissarov S. S., 2018, arXiv e-prints, p. arXiv:1811.06764

Bandara K., Crampton D., Simard L., 2009, , 704, 1135

Barai P., Murante G., Borgani S., Gaspari M., Granato G. L., Monaco P., Ragone-Figueroa C., 2016, , 461, 1548

Barausse E., Rezzolla L., 2009, , 704, L40

Barausse E., Morozova V., Rezzolla L., 2012, , 758, 63

Bardeen J. M., 1980, , 22, 1882

Bardeen J. M., Petterson J. A., 1975, , 195, L65

Barnes D. J., et al., 2017, , 471, 1088

Barnes D. J., et al., 2018, , 481, 1809

Becker R. H., White R. L., Helfand D. J., 1995, , 450, 559

Beckmann R. S., et al., 2019, , 631, A60

Beckmann R. S., Dubois Y., Pellisier A., Olivares V., Polles F. L., Hahn O., Guillard P., Lehnert M. D., 2022, arXiv e-prints, p. arXiv:2204.03629

Begelman M. C., 2012, , 420, 2912

Begelman M. C., Cioffi D. F., 1989, , 345, L21

Begelman M. C., Scepi N., Dexter J., 2021, arXiv e-prints, p. arXiv:2111.02439

Behroozi P. S., Wechsler R. H., Conroy C., 2013, , 770, 57

Benjamin T. B., 1986, Journal of Fluid Mechanics, 169, 251

Benson A. J., Babul A., 2009, , 397, 1302

Benson A. J., Bower R. G., Frenk C. S., Lacey C. G., Baugh C. M., Cole S., 2003, , 599, 38

Bicknell G. V., 1995, , 101, 29

Bird S., Ni Y., Di Matteo T., Croft R., Feng Y., Chen N., 2022, , 512, 3703

Biretta J. A., Sparks W. B., Macchetto F., 1999, , 520, 621

Bîrzan L., Rafferty D. A., McNamara B. R., Wise M. W., Nulsen P. E. J., 2004, , 607, 800

Blake C., et al., 2011, , 418, 1707

Blandford R. D., Begelman M. C., 1999, , 303, L1

Blandford R. D., Königl A., 1979, , 232, 34

Blandford R. D., Znajek R. L., 1977, , 179, 433

Blandford R., Meier D., Readhead A., 2019, , 57, 467

Blondin J. M., Fryxell B. A., Konigl A., 1990, , 360, 370

Bocquet S., Saro A., Dolag K., Mohr J. J., 2016, , 456, 2361

Bodo G., Tavecchio F., 2018, , 609, A122

Bohringer H., Nulsen P. E. J., Braun R., Fabian A. C., 1995, , 274, L67

Bondi H., 1952a, , 112, 195

Bondi H., 1952b, , 112, 195

Bondi H., Hoyle F., 1944, , 104, 273

Booth C. M., Schaye J., 2009, , 398, 53

Booth C. M., Schaye J., 2010, , 405, L1

Borrow J., Anglés-Alcázar D., Davé R., 2020, , 491, 6102

Borrow J., Schaller M., Bower R. G., Schaye J., 2022, , 511, 2367

Bosma A., 1978, PhD thesis, University of Groningen, Netherlands

Bourne M. A., Sijacki D., 2017, , 472, 4707

Bourne M. A., Sijacki D., 2020, arXiv e-prints, p. arXiv:2008.12784

Bourne M. A., Sijacki D., Puchwein E., 2019, , 490, 343

Bower R. G., Benson A. J., Malbon R., Helly J. C., Frenk C. S., Baugh C. M., Cole S., Lacey C. G., 2006, , 370, 645

Boylan-Kolchin M., Ma C.-P., Quataert E., 2008, , 383, 93

Bregman J. N., Fabian A. C., Miller E. D., Irwin J. A., 2006, , 642, 746

Brighenti F., Mathews W. G., Temi P., 2015, , 802, 118

Bromberg O., Nakar E., Piran T., Sari R., 2011, , 740, 100

Brüggen M., Kaiser C. R., Churazov E., Enßlin T. A., 2002, , 331, 545

Brüggen M., Heinz S., Roediger E., Ruszkowski M., Simionescu A., 2007, , 380, L67

Bullock J. S., Dekel A., Kolatt T. S., Kravtsov A. V., Klypin A. A., Porciani C., Primack J. R., 2001, , 555, 240

Carazzo G., Kaminski E., Tait S., 2006, Journal of Fluid Mechanics, 547, 137

Castignani G., Pandey-Pommier M., Hamer S. L., Combes F., Salomé P., Freundlich J., Jablonka P., 2020, , 640, A65

Catinella B., et al., 2010, , 403, 683

Cavagnolo K. W., Donahue M., Voit G. M., Sun M., 2009, , 182, 12

Chaikin E., Schaye J., Schaller M., Bahé Y. M., Nobels F. S. J., Ploeckinger S., 2022, ,

Chatterjee K., Liska M., Tchekhovskoy A., Markoff S. B., 2019, , 490, 2200

Choi E., 2017, , 469, 4148

Choi E., Ostriker J. P., Naab T., Johansson P. H., 2012, , 754, 125

Choi E., Ostriker J. P., Naab T., Oser L., Moster B. P., 2015, , 449, 4105

Churazov E., Brüggen M., Kaiser C. R., Böhringer H., Forman W., 2001, , 554, 261

Cielo S., Antonuccio-Delogu V., Macciò A. V., Romeo A. D., Silk J., 2014, , 439, 2903

Ciotti L., Ostriker J. P., 1997, , 487, L105

Colless M., et al., 2001, , 328, 1039

Collin-Souffrin S., Dumont A. M., 1990, , 229, 292

Costa T., Sijacki D., Haehnelt M. G., 2014, , 444, 2355

Crain R. A., et al., 2015, , 450, 1937

Crawford C. S., Sanders J. S., Fabian A. C., 2005, , 361, 17

Croston J. H., et al., 2008, , 487, 431

Croton D. J., et al., 2006, , 365, 11

Crowe C. T., 2005, Multiphase Flow Handbook

Dabiri J. O., 2006, Journal of Fluid Mechanics, 547, 105

Darwin C., 1953, Proceedings of the Cambridge Philosophical Society, 49, 342

Davé R., Anglés-Alcázar D., Narayanan D., Li Q., Rafieferantsoa M. H., Appleby S., 2019, , 486, 2827

Davies L. J. M., et al., 2016, , 461, 458

Davis T. A., Greene J. E., Ma C.-P., Blakeslee J. P., Dawson J. M., Pandya V., Veale M., Zabel N., 2019, , 486, 1404

Davis F., et al., 2022, arXiv e-prints, p. arXiv:2201.09903

Dellino P., et al., 2014, Bulletin of Volcanology, 76

Diehl S., Rockefeller G., Fryer C. L., Riethmiller D., Statler T. S., 2015, , 32, e048

Done C., Gierliński M., Kubota A., 2007, , 15, 1

Donohoe J., Smith M. D., 2016, , 458, 558

Doria A., Gitti M., Ettori S., Brighenti F., Nulsen P. E. J., McNamara B. R., 2012, , 753, 47

Dreher J. W., Feigelson E. D., 1984, , 308, 43

Driver S. P., et al., 2011, , 413, 971

Dubois Y., Devriendt J., Slyz A., Teyssier R., 2010, , 409, 985

Dubois Y., Devriendt J., Teyssier R., Slyz A., 2011, , 417, 1853

Dubois Y., Devriendt J., Slyz A., Teyssier R., 2012, , 420, 2662

Dubois Y., Volonteri M., Silk J., 2014a, , 440, 1590

Dubois Y., et al., 2014b, , 444, 1453

Dubois Y., et al., 2021, , 651, A109

Eckert D., et al., 2012, , 541, A57

Eckert D., Gaspari M., Gastaldello F., Le Brun A. M. C., O'Sullivan E., 2021, Universe, 7, 142

Edge A. C., 2001, , 328, 762

Edge A. C., Stewart G. C., 1991, , 252, 414

Efstathiou G., Ellis R. S., Peterson B. A., 1988, , 232, 431

Ehlert K., Weinberger R., Pfrommer C., Pakmor R., Springel V., 2018, , 481, 2878

Ehlert K., Weinberger R., Pfrommer C., Pakmor R., Springel V., 2023, , 518, 4622

Einstein A., 1916, Annalen der Physik, 354, 769

English W., Hardcastle M. J., Krause M. G. H., 2016, , 461, 2025

Erfanianfar G., et al., 2019, , 631, A175

Event Horizon Telescope Collaboration et al., 2021, , 910, L13

Fabian A. C., 1994, , 32, 277

Fabian A. C., 2012, , 50, 455

Fabian A. C., Sanders J. S., Allen S. W., Crawford C. S., Iwasawa K., Johnstone R. M., Schmidt R. W., Taylor G. B., 2003, , 344, L43

Falle S. A. E. G., 1991, , 250, 581

Fanaroff B. L., Riley J. M., 1974, , 167, 31P

Fanidakis N., Baugh C. M., Benson A. J., Bower R. G., Cole S., Done C., Frenk C. S., 2011, , 410, 53

Fattahi A., et al., 2016, , 457, 844

Faucher-Giguère C.-A., Quataert E., 2012, , 425, 605

Feigelson E. D., Wood P. A. D., Schreier E. J., Harris D. E., Reid M. J., 1987, , 312, 101

Fiacconi D., Sijacki D., Pringle J. E., 2018, , 477, 3807

Fiore F., et al., 2017, , 601, A143

Forman W., et al., 2007, , 665, 1057

Frenk C. S., White S. D. M., Davis M., Efstathiou G., 1988, , 327, 507

Furlong M., et al., 2015, , 450, 4486

Gao F., et al., 2020, , 637, A94

Garmire G. P., Bautz M. W., Ford P. G., Nousek J. A., Ricker George R. J., 2003, in Truemper J. E., Tananbaum H. D., eds, Society of Photo-Optical Instrumentation Engineers (SPIE) Conference Series Vol. 4851, X-Ray and Gamma-Ray Telescopes and Instruments for Astronomy.. pp 28–44, doi:10.1117/12.461599

Garofalo D., Singh C. B., Zack A., 2018, Scientific Reports, 8, 15097

Gaspari M., Brighenti F., D'Ercole A., Melioli C., 2011, , 415, 1549

Gaspari M., Ruszkowski M., Sharma P., 2012, , 746, 94

Gaspari M., Ruszkowski M., Oh S. P., 2013, , 432, 3401

Gaspari M., Brighenti F., Temi P., Ettori S., 2014, , 783, L10

Gatuzz E., Sanders J. S., Dennerl K., Pinto C., Fabian A. C., Tamura T., Walker S. A., ZuHone J., 2021, ,

Gendron-Marsolais M., et al., 2017, , 848, 26

Genzel R., Hollenbach D., Townes C. H., 1994, Reports on Progress in Physics, 57, 417

Georgakakis A., Hopkins A. M., Caulton A., Wiklind T., Terlevich A. I., Forbes D. A., 2001, , 326, 1431

Ghirardini V., et al., 2019, , 621, A41

Ghisellini G., Padovani P., Celotti A., Maraschi L., 1993, , 407, 65

Gillessen S., Eisenhauer F., Trippe S., Alexander T., Genzel R., Martins F., Ott T., 2009, , 692, 1075

Gourgouliatos K. N., Komissarov S. S., 2018, Nature Astronomy, 2, 167

Grand R. J. J., Springel V., Gómez F. A., Marinacci F., Pakmor R., Campbell D. J. R., Jenkins A., 2016, , 459, 199

Griffin A. J., Lacey C. G., Gonzalez-Perez V., Lagos C. d. P., Baugh C. M., Fanidakis N., 2019, , 487, 198

Guo F., Mathews W. G., 2011, , 728, 121

Guo F., Mathews W. G., 2012, , 756, 181

Guo F., Duan X., Yuan Y.-F., 2018, , 473, 1332

Hahn O., Martizzi D., Wu H.-Y., Evrard A. E., Teyssier R., Wechsler R. H., 2017, , 470, 166

Hamer S. L., et al., 2014, , 437, 862

Hardcastle M. J., Krause M. G. H., 2013, , 430, 174

Hardcastle M. J., Krause M. G. H., 2014, , 443, 1482

Hardcastle M. J., Worrall D. M., Kraft R. P., Forman W. R., Jones C., Murray S. S., 2003, , 593, 169

Heckman T. M., Best P. N., 2014, , 52, 589

Heckman T. M., Smith E. P., Baum S. A., van Breugel W. J. M., Miley G. K., Illingworth G. D., Bothun G. D., Balick B., 1986, , 311, 526

Henriques B. M. B., White S. D. M., Thomas P. A., Angulo R., Guo Q., Lemson G., Springel V., Overzier R., 2015, , 451, 2663

Hernquist L., 1990, , 356, 359

Hervet O., Meliani Z., Zech A., Boisson C., Cayatte V., Sauty C., Sol H., 2017, , 606, A103

Hirschmann M., Dolag K., Saro A., Bachmann L., Borgani S., Burkert A., 2014, , 442, 2304

Hlavacek-Larrondo J., Fabian A. C., Edge A. C., Ebeling H., Sanders J. S., Hogan M. T., Taylor G. B., 2012a, , 421, 1360

Hlavacek-Larrondo J., Fabian A. C., Edge A. C., Ebeling H., Sanders J. S., Hogan M. T., Taylor G. B., 2012b, , 421, 1360

Hopkins P. F., 2015, , 450, 53

Hopkins P. F., Quataert E., 2011, , 415, 1027

Hopkins P. F., Kereš D., Oñorbe J., Faucher-Giguère C.-A., Quataert E., Murray N., Bullock J. S., 2014, , 445, 581

Hopkins P. F., et al., 2018, , 480, 800

Horton M. A., Krause M. G. H., Hardcastle M. J., 2020, , 499, 5765

Hoyle F., Lyttleton R. A., 1941, , 101, 227

Hubble E. P., 1926a, , 63, 236

Hubble E. P., 1926b, , 64, 321

Hubble E., 1929, Proceedings of the National Academy of Science, 15, 168

Hudson D. S., Mittal R., Reiprich T. H., Nulsen P. E. J., Andernach H., Sarazin C. L., 2010, , 513, A37

Huško F., Lacey C. G., 2022, arXiv e-prints, p. arXiv:2205.08884

Huško F., Lacey C. G., Schaye J., Schaller M., Nobels F. S. J., 2022, , 516, 3750

Ivison R. J., et al., 2012, , 425, 1320

Jeans J. H., 1915, , 76, 70

Jetha N. N., Hardcastle M. J., Sakelliou I., 2006, , 368, 609

Johnson R., Ponman T. J., Finoguenov A., 2009, , 395, 1287

Kaiser C. R., Alexander P., 1997, , 286, 215

Kaiser C. R., Best P. N., 2007, , 381, 1548

Kaviraj S., Shabala S. S., Deller A. T., Middelberg E., 2015, , 454, 1595

Kaviraj S., et al., 2017, , 467, 4739

Kellermann K. I., Pauliny-Toth I. I. K., Williams P. J. S., 1969, , 157, 1

Kennicutt Robert C. J., 1998, , 36, 189

Kerr R. P., 1963, , 11, 237

Khandai N., Di Matteo T., Croft R., Wilkins S., Feng Y., Tucker E., DeGraf C., Liu M.-S., 2015, , 450, 1349

Kim J.-h., et al., 2014, , 210, 14

King A. R., Lubow S. H., Ogilvie G. I., Pringle J. E., 2005, , 363, 49

King A. R., Pringle J. E., Livio M., 2007, , 376, 1740

King A. R., Pringle J. E., Hofmann J. A., 2008, , 385, 1621

Kino M., Kawakatu N., 2005, , 364, 659

Kirkpatrick C. C., Gitti M., Cavagnolo K. W., McNamara B. R., David L. P., Nulsen P. E. J., Wise M. W., 2009, , 707, L69

Komatsu E., Seljak U., 2001, , 327, 1353

Komissarov S. S., Falle S. A. E. G., 1998, , 297, 1087

Konar C., Saikia D. J., Jamrozy M., Machalski J., 2006, , 372, 693

Konar C., Hardcastle M. J., Croston J. H., Saikia D. J., 2009, , 400, 480

Kormendy J., Ho L. C., 2013, , 51, 511

Krause M., Alexander P., Riley J., Hopton D., 2012, , 427, 3196

Krumholz M. R., McKee C. F., Klein R. I., 2005, , 618, 757

Krumholz M. R., McKee C. F., Klein R. I., 2006, , 638, 369

Lacey C., Cole S., 1993, , 262, 627

Lacey C. G., et al., 2016, , 462, 3854

Lagos C. d. P., et al., 2015, , 452, 3815

Lagos C. d. P., Tobar R. J., Robotham A. S. G., Obreschkow D., Mitchell P. D., Power C., Elahi P. J., 2018, , 481, 3573

Lakhchaura K., et al., 2018, , 481, 4472

Lange R., et al., 2015, , 447, 2603

Le Brun A. M. C., McCarthy I. G., Schaye J., Ponman T. J., 2014, , 441, 1270

Ledlow M. J., Owen F. N., Yun M. S., Hill J. M., 2001, , 552, 120

Lense J., Thirring H., 1918, Physikalische Zeitschrift, 19, 156

Lewis A. D., Stocke J. T., Buote D. A., 2002, , 573, L13

Li Y., Bryan G. L., 2014a, , 789, 54

Li Y., Bryan G. L., 2014b, , 789, 153

Li Y., Bryan G. L., Ruszkowski M., Voit G. M., O'Shea B. W., Donahue M., 2015, , 811, 73

Li Y., Ruszkowski M., Bryan G. L., 2017, , 847, 106

Li Y., Wiita P. J., Schuh T., Elghossain G., Hu S., 2018, , 869, 32

Licquia T. C., Newman J. A., 2015, , 806, 96

Lin Y.-T., Stanford S. A., Eisenhardt P. R. M., Vikhlinin A., Maughan B. J., Kravtsov A., 2012, , 745, L3

Lind K. R., Payne D. G., Meier D. L., Blandford R. D., 1989, , 344, 89

Liska M., Tchekhovskoy A., Ingram A., van der Klis M., 2019, , 487, 550

Liska M., Tchekhovskoy A., Quataert E., 2020, , 494, 3656

Liu H., Wu Q., 2013, , 764, 17

Lodato G., 2007, Nuovo Cimento Rivista Serie, 30, 293

Lodato G., Price D. J., 2010, , 405, 1212

Lodato G., Pringle J. E., 2007, , 381, 1287

Loveday J., Peterson B. A., Efstathiou G., Maddox S. J., 1992, , 390, 338

Loveday J., et al., 2012, , 420, 1239

Lovisari L., Ettori S., Gaspari M., Giles P. A., 2021, Universe, 7, 139

Maccagni F. M., et al., 2021, , 656, A45

Machalski J., Chyży K. T., Stawarz Ł., Kozieł D., 2007, , 462, 43

Madau P., Ferguson H. C., Dickinson M. E., Giavalisco M., Steidel C. C., Fruchter A., 1996, , 283, 1388

Madau P., Haardt F., Dotti M., 2014, , 784, L38

Mahadevan R., 1997, , 477, 585

Mahatma V. H., Hardcastle M. J., Croston J. H., Harwood J., Ineson J., Moldon J., 2020, , 491, 5015

Maiolino R., et al., 2023, arXiv e-prints, p. arXiv:2308.01230

Martin R. G., Pringle J. E., Tout C. A., 2007, , 381, 1617

Martin R. G., Nixon C. J., Pringle J. E., Livio M., 2019, , 70, 7

Martizzi D., Jimmy Teyssier R., Moore B., 2014, , 443, 1500

Martizzi D., Quataert E., Faucher-Giguère C.-A., Fielding D., 2019, , 483, 2465

Matsumoto J., Masada Y., 2019, , 490, 4271

McAlpine S., Bower R. G., Rosario D. J., Crain R. A., Schaye J., Theuns T., 2018, , 481, 3118

McCarthy I. G., Schaye J., Bird S., Le Brun A. M. C., 2017, , 465, 2936

McConnell N. J., Ma C.-P., 2013, , 764, 184

McDonald M., et al., 2015, , 811, 111

McDonald M., et al., 2016, , 826, 124

McDonald M., Gaspari M., McNamara B. R., Tremblay G. R., 2018, , 858, 45

McKinney J. C., Tchekhovskoy A., Blandford R. D., 2012, , 423, 3083

McNamara B. R., Nulsen P. E. J., 2012, New Journal of Physics, 14, 055023

McNamara B. R., et al., 2000, , 534, L135

McNamara B. R., Nulsen P. E. J., Wise M. W., Rafferty D. A., Carilli C., Sarazin C. L., Blanton E. L., 2005, , 433, 45

McNamara B. R., et al., 2014, arXiv e-prints, p. arXiv:1403.4249

McNamara B. R., Russell H. R., Nulsen P. E. J., Hogan M. T., Fabian A. C., Pulido F., Edge A. C., 2016, , 830, 79

Meece G. R., Voit G. M., O'Shea B. W., 2017, , 841, 133

Meier D. L., 2002, , 46, 247

Menci N., Gatti M., Fiore F., Lamastra A., 2014, , 569, A37

Menon H., Wesolowski L., Zheng G., Jetley P., Kale L., Quinn T., Governato F., 2015, Computational Astrophysics and Cosmology, 2, 1

Merritt D., Ekers R. D., 2002, Science, 297, 1310

Mezcua M., Suh H., Civano F., 2019, , 488, 685

Mizumoto M., Nomura M., Done C., Ohsuga K., Odaka H., 2021, , 503, 1442

Mizuno Y., Gómez J. L., Nishikawa K.-I., Meli A., Hardee P. E., Rezzolla L., 2015, , 809, 38

Moderski R., Sikora M., 1996, , 283, 854

Moffett A. J., et al., 2016, , 457, 1308

Monaghan J. J., 1992a, , 30, 543

Monaghan J. J., 1992b, , 30, 543

Morsony B. J., Heinz S., Brüggen M., Ruszkowski M., 2010, , 407, 1277

Morton B. R., Taylor G., Turner J. S., 1956, Proceedings of the Royal Society of London Series A, 234, 1

Moster B. P., Naab T., White S. D. M., 2018, , 477, 1822

Mukherjee D., Bicknell G. V., Wagner A. Y., Sutherland R. S., Silk J., 2018, , 479, 5544

Mukherjee D., Bodo G., Mignone A., Rossi P., Vaidya B., 2020, , 499, 681

Müller A., 2004, PhD thesis, -

Mullin L. M., Hardcastle M. J., 2009, , 398, 1989

Nagai H., et al., 2019, , 883, 193

Nakamura M., Uchida Y., Hirose S., 2001, , 6, 61

Narayan R., Yi I., 1994, , 428, L13

Narayan R., Yi I., 1995, , 452, 710

Narayan R., Igumenshchev I. V., Abramowicz M. A., 2003, , 55, L69

Narayan R., SaĬ§dowski A., Soria R., 2017, , 469, 2997

Narayan R., Chael A., Chatterjee K., Ricarte A., Curd B., 2022, , 511, 3795

Navarro J. F., Frenk C. S., White S. D. M., 1996a, , 462, 563

Navarro J. F., Frenk C. S., White S. D. M., 1996b, , 462, 563

Nelson D., Vogelsberger M., Genel S., Sijacki D., Kereš D., Springel V., Hernquist L., 2013, , 429, 3353

Nelson D., et al., 2019, Computational Astrophysics and Cosmology, 6, 2

Nemmen R. S., Tchekhovskoy A., 2015, , 449, 316

Nesvadba N. P. H., et al., 2021, , 654, A8

Nobels F. S. J., Schaye J., Schaller M., Bahé Y. M., Chaikin E., 2022, , 515, 4838

Noda H., Done C., 2018, , 480, 3898

Nomura M., Ohsuga K., Takahashi H. R., Wada K., Yoshida T., 2016, , 68, 16

Novikov I. D., Thorne K. S., 1973, in Black Holes (Les Astres Occlus). pp 343–450

Nulsen P., Jones C., Forman W., Churazov E., McNamara B., David L., Murray S., 2009, in Heinz S., Wilcots E., eds, American Institute of Physics Conference Series Vol. 1201, The Monster's Fiery Breath: Feedback in Galaxies, Groups, and Clusters. pp 198–201 (arXiv:0909.1809), doi:10.1063/1.3293033

O'Dea C. P., et al., 2008, , 681, 1035

O'Dea C. P., Daly R. A., Kharb P., Freeman K. A., Baum S. A., 2009, , 494, 471

O'Sullivan E., Combes F., Hamer S., Salomé P., Babul A., Raychaudhury S., 2015, , 573, A111

O'Sullivan E., Combes F., Babul A., Chapman S., Phadke K. A., Schellenberger G., Salomé P., 2021, , 508, 3796

Ogilvie G. I., 1999, , 304, 557

Olguín-Iglesias A., Kotilainen J., Chavushyan V., 2020, , 492, 1450

Olivares V., et al., 2019, , 631, A22

Omma H., Binney J., Bryan G., Slyz A., 2004, , 348, 1105

Oort J. H., 1932, , 6, 289

Oppenheimer B. D., 2018, , 480, 2963

Oppenheimer B. D., Babul A., Bahé Y., Butsky I. S., McCarthy I. G., 2021, Universe, 7, 209

Orellana G., et al., 2017, , 602, A68

Pakmor R., et al., 2022, arXiv e-prints, p. arXiv:2210.10060

Pakull M. W., Soria R., Motch C., 2010, , 466, 209

Papaloizou J. C. B., Pringle J. E., 1983, , 202, 1181

Park J., et al., 2019, , 887, 147

Pavlovski G., Kaiser C. R., Pope E. C. D., Fangohr H., 2008, , 384, 1377

Perlmutter S., et al., 1999, , 517, 565

Perucho M., Lobanov A. P., Martí J. M., Hardee P. E., 2006, , 456, 493

Perucho M., Martí J. M., Cela J. M., Hanasz M., de La Cruz R., Rubio F., 2010, , 519, A41

Perucho M., Martí J.-M., Quilis V., 2022, , 510, 2084

Peterson J. R., Fabian A. C., 2006, , 427, 1

Peterson J. R., Kahn S. M., Paerels F. B. S., Kaastra J. S., Tamura T., Bleeker J. A. M., Ferrigno C., Jernigan J. G., 2003, , 590, 207

Pier E. A., Krolik J. H., 1992, , 399, L23

Pike S. R., Kay S. T., Newton R. D. A., Thomas P. A., Jenkins A., 2014, , 445, 1774

Pillepich A., et al., 2018, , 475, 648

Ploeckinger S., Schaye J., 2020, , 497, 4857

Poole G. B., Babul A., McCarthy I. G., Sanderson A. J. R., Fardal M. A., 2008, , 391, 1163

Pope E. C. D., Babul A., Pavlovski G., Bower R. G., Dotter A., 2010, , 406, 2023

Prasad D., Sharma P., Babul A., 2015, , 811, 108

Pratt G. W., Croston J. H., Arnaud M., Böhringer H., 2009, , 498, 361

Pratt G. W., et al., 2010, , 511, A85

Predehl P., et al., 2020, , 588, 227

Press W. H., Schechter P., 1974, , 187, 425

Pringle J. E., 1992, , 258, 811

Pushkarev A. B., Kovalev Y. Y., Lister M. L., Savolainen T., 2009, , 507, L33

Pushkarev A. B., Kovalev Y. Y., Lister M. L., Savolainen T., 2017, , 468, 4992

Qiu Y., Bogdanović T., Li Y., McDonald M., 2019, , 872, L11

Quera-Bofarull A., Done C., Lacey C. G., Nomura M., Ohsuga K., 2023, , 518, 2693

Rafferty D. A., McNamara B. R., Nulsen P. E. J., Wise M. W., 2006, , 652, 216

Randall S. W., et al., 2011, , 726, 86

Rees M. J., 1978, , 184, 61P

Revaz Y., Combes F., Salomé P., 2008, , 477, L33

Reynolds C. S., Heinz S., Begelman M. C., 2001, , 549, L179

Reynolds C. S., Garofalo D., Begelman M. C., 2006, , 651, 1023

Ricarte A., Narayan R., Curd B., 2023, arXiv e-prints, p. arXiv:2307.04621

Richardson M. L. A., Scannapieco E., Devriendt J., Slyz A., Thacker R. J., Dubois Y., Wurster J., Silk J., 2016, , 825, 83

Ripperda B., Liska M., Chatterjee K., Musoke G., Philippov A. A., Markoff S. B., Tchekhovskoy A., Younsi Z., 2022, , 924, L32

Roberts M. S., Whitehurst R. N., 1975, , 201, 327

Rossi P., Mignone A., Bodo G., Massaglia S., Ferrari A., 2008, , 488, 795

Rosswog S., 2020, , 498, 4230

Rubin V. C., Ford W. K. J., Thonnard N., 1980, , 238, 471

Russell H. R., McNamara B. R., Edge A. C., Hogan M. T., Main R. A., Vantyghem A. N., 2013, , 432, 530

Russell H. R., et al., 2016, , 458, 3134

Russell H. R., et al., 2017, , 836, 130

Russell H. R., et al., 2019, , 490, 3025

Ruszkowski M., Yang H. Y. K., Reynolds C. S., 2017, , 844, 13

Sabater J., et al., 2019, , 622, A17

Sadowski A., 2009, , 183, 171

Sadowski A., Narayan R., Penna R., Zhu Y., 2013, , 436, 3856

Sadowski A., Narayan R., McKinney J. C., Tchekhovskoy A., 2014, , 439, 503

Salim S., et al., 2007, , 173, 267

Salomé P., Combes F., Revaz Y., Downes D., Edge A. C., Fabian A. C., 2011, , 531, A85

Sancisi R., Thonnard N., Ekers R. D., 1987, , 315, L39

Sanders J. S., Fabian A. C., Dunn R. J. H., 2005, , 360, 133

Sanders R. L., et al., 2021, , 914, 19

Sani E., et al., 2018, Frontiers in Astronomy and Space Sciences, 5, 2

Sawala T., et al., 2015, , 448, 2941

Schaller M. e. a., 2018, SWIFT: SPH With Inter-dependent Fine-grained Tasking, Astrophysics Source Code Library (ascl:1805.020)

Schaller M., Dalla Vecchia C., Schaye J., Bower R. G., Theuns T., Crain R. A., Furlong M., McCarthy I. G., 2015, , 454, 2277

Schaller M., et al., 2024, ,

Schaye J., Dalla Vecchia C., 2008, , 383, 1210

Schaye J., et al., 2010, , 402, 1536

Schaye J., et al., 2015, , 446, 521

Schmidt M., 1963, , 197, 1040

Schmidt M., 1968, , 151, 393

Schmidt R. W., Fabian A. C., Sanders J. S., 2002, , 337, 71

Schwarzschild K., 1916, Abh. Konigl. Preuss. Akad. Wissenschaften Jahre 1906,92, Berlin,1907, 1916, 189

Sedov L. I., 1959, Similarity and Dimensional Methods in Mechanics

Shabala S. S., Deller A., Kaviraj S., Middelberg E., Turner R. J., Ting Y. S., Allison J. R., Davis T. A., 2017, , 464, 4706

Shakura N. I., Sunyaev R. A., 1973, , 500, 33

Sharma P., Quataert E., Hammett G. W., Stone J. M., 2007, , 667, 714

Shen X., Hopkins P. F., Faucher-Giguère C.-A., Alexander D. M., Richards G. T., Ross N. P., Hickox R. C., 2020, , 495, 3252

Shimwell T. W., et al., 2017, , 598, A104

Shulevski A., et al., 2019, , 628, A69

Sijacki D., Springel V., Di Matteo T., Hernquist L., 2007, , 380, 877

Sijacki D., Vogelsberger M., Kereš D., Springel V., Hernquist L., 2012, , 424, 2999

Sijacki D., Vogelsberger M., Genel S., Springel V., Torrey P., Snyder G. F., Nelson D., Hernquist L., 2015, , 452, 575

Singh V., Ishwara-Chandra C. H., Sievers J., Wadadekar Y., Hilton M., Beelen A., 2015, , 454, 1556

Smith M. D., Donohoe J., 2019, , 490, 1363

Smith andJustin Donohoe M. D., 2021, arXiv e-prints, p. arXiv:2101.03517

Snios B., et al., 2018, , 855, 71

Somerville R. S., Primack J. R., 1999, , 310, 1087

Spergel D. N., et al., 2003, , 148, 175

Springel V., 2005, , 364, 1105

Sternberg A., Soker N., 2008, , 389, L13

Stone J. M., Xu J., Hardee P., 1997, , 483, 136

Su K.-Y., et al., 2021, , 507, 175

Sun M., Voit G. M., Donahue M., Jones C., Forman W., Vikhlinin A., 2009, , 693, 1142

Suzuki Y. J., Koyaguchi T., 2010, , 37, L05302

Tabor G., Binney J., 1993, , 263, 323

Talbot R. Y., Bourne M. A., Sijacki D., 2020, arXiv e-prints, p. arXiv:2011.10580

Tchekhovskoy A., Bromberg O., 2016, , 461, L46

Tchekhovskoy A., Narayan R., McKinney J. C., 2010, , 711, 50

Tchekhovskoy A., Narayan R., McKinney J. C., 2011, , 418, L79

Thorne K. S., 1974, , 191, 507

Trayford J. W., et al., 2017, , 470, 771

Tremblay G. R., et al., 2015, , 451, 3768

Tremmel M., Karcher M., Governato F., Volonteri M., Quinn T. R., Pontzen A., Anderson L., Bellovary J., 2017, , 470, 1121

Tremmel M., et al., 2019, , 483, 3336

Turner J. S., 1986, Journal of Fluid Mechanics, 173, 431

Urry C. M., Padovani P., 1995, , 107, 803

Vantyghem A. N., et al., 2018, , 863, 193

Vogelsberger M., et al., 2014, , 509, 177

Voit G. M., Donahue M., 2015, , 799, L1

Voit G. M., Bryan G. L., Balogh M. L., Bower R. G., 2002, , 576, 601

Voit G. M., Kay S. T., Bryan G. L., 2005, , 364, 909

Volders L. M. J. S., 1959, , 14, 323

Volonteri M., Sikora M., Lasota J.-P., 2007, , 667, 704

Wadsley J. W., Keller B. W., Quinn T. R., 2017, , 471, 2357

Walg S., Achterberg A., Markoff S., Keppens R., Meliani Z., 2013, , 433, 1453

Wang S.-C., Yang H. Y. K., 2022, arXiv e-prints, p. arXiv:2201.05298

Wang J.-M., Zhou Y.-Y., 1999, , 516, 420

Ward S. R., Harrison C. M., Costa T., Mainieri V., 2022, , 514, 2936

Wardle J. F. C., Aaron S. E., 1997, , 286, 425

Webster B., Croston J. H., Harwood J. J., Baldi R. D., Hardcastle M. J., Mingo B., Röttgering H. J. A., 2021, , 508, 5972

Weinberger R., et al., 2017a, , 465, 3291

Weinberger R., Ehlert K., Pfrommer C., Pakmor R., Springel V., 2017b, , 470, 4530

Weinberger R., et al., 2018, , 479, 4056

Weinberger R., et al., 2023, , 523, 1104

Weinmann S. M., van den Bosch F. C., Yang X., Mo H. J., 2006, , 366, 2

Werner N., Urban O., Simionescu A., Allen S. W., 2013, , 502, 656

Werner N., McNamara B. R., Churazov E., Scannapieco E., 2019, , 215, 5

Whitaker K. E., van Dokkum P. G., Brammer G., Franx M., 2012, , 754, L29

White S. D. M., 1978, , 184, 185

Wiklind T., Combes F., Henkel C., 1995, , 297, 643

Wilman R. J., Edge A. C., Swinbank A. M., 2009, , 395, 1355

Wise M. W., McNamara B. R., Nulsen P. E. J., Houck J. C., David L. P., 2007, , 659, 1153

Xie F.-G., Yuan F., 2012, , 427, 1580

Yang W.-C., 2003, Handbook of Fluidization and Fluid-Particle Systems

Yang H. Y. K., Reynolds C. S., 2016, , 818, 181

Yang H. Y. K., Gaspari M., Marlow C., 2019, , 871, 6

Yang J., Gurvits L. I., Paragi Z., Frey S., Conway J. E., Liu X., Cui L., 2020, , 495, L71

York D. G., et al., 2000, , 120, 1579

Young P. J., Westphal J. A., Kristian J., Wilson C. P., Landauer F. P., 1978, , 221, 721

Young L. M., et al., 2011, , 414, 940

Yuan F., 2003, , 594, L99

Yuan F., Narayan R., 2014, , 52, 529

Zhang C., Zhuravleva I., Gendron-Marsolais M.-L., Churazov E., Schekochihin A. A., Forman W. R., 2022, arXiv e-prints, p. arXiv:2203.04259

ZuHone J. A., Markevitch M., Johnson R. E., 2010, , 717, 908

Zwicky F., 1933, Helvetica Physica Acta, 6, 110

de Bernardis P., et al., 2000, , 404, 955

van Putten M. H. P. M., 1996, , 467, L57